

GEOLOGIC FRAMEWORK FOR LATE CRETACEOUS MAGMATIC-HYDROTHERMAL  
MINERALIZATION IN THE TASEKO LAKES REGION, SOUTHWESTERN B.C.

by

Scott Kenneth Blevings

B.Sc., University of British Columbia, 2006

A THESIS SUBMITTED IN PARTIAL FULFILLMENT OF THE  
REQUIREMENTS FOR THE DEGREE OF

MASTER OF SCIENCE

in

The Faculty of Graduate Studies

(Geological Sciences)

THE UNIVERSITY OF BRITISH COLUMBIA

(Vancouver)

September 2008

© Scott Kenneth Blevings 2008

## ABSTRACT

The Taseko Lakes region is located in Southwestern British Columbia along the contact between the Coast Plutonic Complex (CPC) and the Southeast Coast Belt (SECB). Three separate generations of faults occur in the region: sub-vertical sinistral-reverse faults (D1), moderate- to high-angle south- and north-vergent contractional faults (D2) and large-scale dextral faults (D3). Several mineral deposits are located in the southern Taseko Lakes region. Three of these deposits were examined during this study: the Empress (porphyry Cu), Pellaire (gold-telluride) and Taylor-Windfall (high-sulphidation epithermal Au-Ag) deposits. The deposits were examined in order to characterize the known mineralization in the Taseko Lakes region and better understand the conditions and times at which mineralization took place.

The Empress deposit formed at approximately 88 to 87 Ma at depths of roughly 5 km when large volumes of high-temperature, oxidized magmatic-hydrothermal fluids from an unidentified source intrusion migrated laterally along a trough-shaped topographic low along the upper margin of an underlying intrusion – the Empress pluton. This horizontal flow produced subhorizontal-layered alteration and mineralization within the overlying Falls River succession.

The Taylor-Windfall deposit formed at about 89 to 87 Ma when magmatic-dominated, moderate- to low-temperature hydrothermal fluids ascended along faults and fractures. An initial high-temperature vapour phase produced a central core of vuggy-silica and corundum-andalusite alteration. A second phase of cooler, re-condensed vapours overprinted early high-temperature assemblages with lower temperature intermediate and advanced argillic alteration assemblages.

The Pellaire deposit formed at 85 Ma when mineralizing fluids migrated distally from a magmatic source along (D2) south-vergent contractional faults. Mineralization occurred when fluids crossed from the Falls River succession into the Mount McLeod granodiorite and were cooled and disturbed from chemical equilibrium, which resulted in the emplacement of quartz-veins in the south-vergent faults and deposition of ore minerals.

All three deposits formed from magmatic-dominated fluids (with variable meteoric input) between approximately 89 and 85 Ma. The similarities in ages, fluid compositions and sources between the deposits indicate they formed from similar magmatic-hydrothermal systems. The varying mineralization styles exhibited by the deposits in this study illustrate the variability of mineralizing styles that can occur in magmatic-hydrothermal systems. This variability arises largely due to differing characteristics of pre-existing geology and the location of the deposits with respect to the overall system.

# TABLE OF CONTENTS

ABSTRACT .....	ii
TABLE OF CONTENTS .....	iii
LIST OF TABLES.....	viii
LIST OF FIGURES .....	ix
ACKNOWLEDGEMENTS.....	xii
DEDICATION.....	xiii
CO-AUTHORSHIP STATEMENT .....	xiv

## CHAPTER I

### General Introduction

1.1 PURPOSE OF THIS STUDY .....	1
1.2 PREVIOUS GEOLOGICAL STUDIES AND MINERAL EXPLORATION IN THE TASEKO LAKES REGION.....	2
1.3 PROJECT METHODOLOGY .....	3
1.4 THESIS ORGANIZATION .....	3

## CHAPTER II

### Geology of the Southern Taseko Lakes Region, Southwestern British Columbia

2.1 INTRODUCTION .....	4
2.2 REGIONAL GEOLOGIC SETTING.....	5
2.2.1 Geologic Setting .....	5
2.2.2 Structural History.....	7
2.3 LITHOLOGIC UNITS .....	9
2.3.1 Twin Creek succession .....	9
2.3.2 Tchaikazan River succession .....	10
2.3.2.1 Sedimentary facies.....	10
2.3.2.2 Volcanic facies .....	11
2.3.3 Falls River succession.....	12
2.3.4 Taylor Creek Group .....	13
2.3.5 Powell Creek Formation .....	14
2.3.6 Mount McLeod Batholith .....	16
2.3.6.1 Mount McLeod granodiorite .....	16

2.3.6.2 Empress pluton .....	16
2.3.6.3 equigranular rhyolite-granite .....	17
2.3.6.4 porphyritic biotite-hornblende granite .....	17
2.3.7 Grizzly Cabin pluton .....	18
2.3.8 Tchaikazan Rapids pluton .....	18
2.3.9 Mount McLure pluton .....	19
2.3.10 Northwest Copper pluton .....	20
2.3.11 dikes .....	20
2.4 STRUCTURAL GEOLOGY .....	21
2.4.1 D1: Sinistral-Reverse Faults .....	21
2.4.2 D2: Contractional Faults .....	22
2.4.3 D3: Dextral Faults .....	23
2.4.4 Mount McLure fault .....	24
2.5 GEOCHRONOLOGY .....	26
2.5.1 <sup>40</sup> Ar- <sup>39</sup> Ar Geochronology .....	26
2.5.1.1 <sup>40</sup> Ar- <sup>39</sup> Ar samples .....	26
2.5.1.2 Age constraints on faults .....	30
2.5.2 U-Pb Geochronology .....	31
2.5.2.1 U-Pb samples .....	31
2.5.2.2 U-Pb interpretation .....	32
2.6 SUMMARY .....	34

### CHAPTER III

#### **Geologic Framework for Late Cretaceous Magmatic-Hydrothermal Mineralization in the Taseko Lakes Region, Southwestern British Columbia**

3.1 INTRODUCTION .....	58
3.1.1 Magmatic-hydrothermal systems .....	59
3.2 REGIONAL OCCURRENCES OF MINERALIZATION .....	62
3.2.1 Major rock units of the Taseko Lakes Region .....	62
3.2.2 Structural Geology of the Taseko Lakes Region .....	63
3.2.3 Regional Occurrences of Mineralization .....	63
3.3 DEPOSIT SCALE GEOLOGY FRAMEWORK .....	65
3.3.1 Methodology .....	65
3.3.1.1 Geological mapping and drill core logging .....	65

3.3.1.2 Petrographic studies.....	65
3.3.1.3 Short wavelength infrared analysis.....	65
3.3.1.4 X-ray diffraction .....	66
3.3.2 Introduction to deposits .....	66
3.3.2.1 Empress .....	66
3.3.2.2 Taylor-Windfall.....	67
3.3.2.3 Pellaire.....	68
3.3.3 Geologic Setting of Deposits .....	69
3.3.3.1 Empress .....	69
3.3.3.2 Taylor-Windfall.....	70
3.3.3.3 Pellaire.....	72
3.3.4 Alteration and Mineralization .....	73
3.3.4.1 Empress .....	73
3.3.4.2 Taylor-Windfall.....	77
3.3.4.3 Pellaire.....	79
3.3.5 Veins .....	80
3.3.5.1 Empress .....	80
3.3.5.2 Taylor-Windfall.....	82
3.3.5.3 Pellaire.....	82
3.3.6 Paragenesis.....	83
3.3.6.1 Empress .....	83
3.3.6.2 Taylor-Windfall.....	84
3.3.6.3 Pellaire.....	85
3.4 GEOCHRONOLOGY .....	86
3.4.1 Methodology .....	86
3.4.2 Empress Geochronology.....	86
3.4.2.1 <sup>40</sup> Ar- <sup>30</sup> Ar samples .....	86
3.4.2.2 U-Pb samples.....	88
3.4.2.3 Interpretation .....	89
3.4.3 Taylor-Windfall Geochronology .....	89
3.4.3.1 <sup>40</sup> Ar- <sup>30</sup> Ar samples .....	89
3.4.3.1 Interpretation .....	90
3.4.4 Pellaire Geochronology .....	90
3.4.4.1 <sup>40</sup> Ar- <sup>30</sup> Ar samples .....	90
3.4.4.2 U-Pb samples.....	91
3.4.4.3 Interpretation .....	92

3.4.5 Integration of Geochronological Data .....	92
3.5 FLUID INCLUSIONS.....	93
3.5.1 Empress Inclusions .....	93
3.5.2 Taylor-Windfall Inclusions.....	94
3.5.3 Pellaire Inclusions.....	96
3.6 ISOTOPES.....	98
3.6.1 Methodology .....	98
3.6.1.1 Carbonate isotopic analyses .....	98
3.6.1.2 Oxygen and hydrogen isotopic analysis .....	98
3.6.2 Empress Isotopes .....	99
3.6.2.1 Carbonate isotopes of calcite veins .....	99
3.6.2.2 Oxygen isotopes of quartz-veins .....	99
3.6.2.3 Oxygen isotopes of quartz-magnetite alteration.....	99
3.6.2.4 Oxygen and hydrogen isotopes of alteration minerals .....	100
3.6.3 Taylor-Windfall Isotopes.....	101
3.6.3.1 Oxygen isotopes of vuggy silica alteration.....	101
3.6.3.2 Oxygen and hydrogen isotopes of alteration minerals .....	101
3.6.4 Pellaire Isotopes.....	101
3.6.4.1 Oxygen isotopes of quartz veins.....	101
3.6.4.2 Oxygen and hydrogen isotopes of alteration minerals .....	102
3.7 FISSION-TRACK THERMOCHRONOLOGY .....	103
3.7.1 Methodology .....	103
3.7.2 Results.....	104
3.8 INTEPRETATION.....	106
3.8.1 Empress.....	106
3.8.1.1 Deposit classification.....	106
3.8.1.2 Alteration zonation .....	106
3.8.1.3 High water:rock ratios .....	108
3.8.1.4 Hydrothermal fluid sources .....	108
3.8.1.5 Hydrothermal fluid evolution .....	110
3.8.1.6 Hydrothermal fluid characteristics .....	112
3.8.1.7 Fluid flow directions.....	114
3.8.1.8 Structural controls .....	115
3.8.1.9 Summary .....	115
3.8.2 Taylor-Windfall .....	116
3.8.2.1 Structural controls .....	116

3.8.2.2 Hydrothermal fluid sources .....	117
3.8.2.3 Hydrothermal fluid evolution .....	117
3.8.2.4 Deposit classification.....	120
3.8.2.5 Summary .....	122
3.8.3 Pellaire .....	123
3.8.3.1 Structural controls .....	123
3.8.3.2 Hydrothermal fluid sources .....	123
3.8.3.3 Hydrothermal fluid evolution .....	124
3.8.3.4 Deposit classification.....	126
3.8.3.5 Summary .....	127
3.8.4 Integration of deposits .....	127
3.9 DISCUSSION.....	129
3.9.1 Magmatic-hydrothermal systems in the Taseko Lakes Region .....	129
3.9.2 Regional Comparisons.....	132
3.10 CONCLUSIONS .....	134

## **CHAPTER IV**

### **Conclusions and Recommendations for Future Research**

4.1 CONCLUSIONS .....	186
4.2 FURTHER WORK.....	189
REFERENCES .....	190

## **APPENDICES**

Appendix A: Short-wavelength infrared (SWIR) Spectra .....	201
Appendix B: Geochronological Data .....	204
Appendix C: Microthermometric Data .....	218

## LIST OF TABLES

### CHAPTER II

Table 2.1 Summary of geochronological age dates .....	44
---	----

### CHAPTER III

Table 3.1 Empress drill-hole data .....	138
Table 3.2 Summary of geochronological age data.....	144
Table 3.3 Carbon and oxygen isotope data for calcite veins at the Empress deposit.....	168
Table 3.4 Oxygen isotope data for quartz and magnetite samples.....	170
Table 3.5 Oxygen and hydrogen isotopic data for hydrous alteration minerals .....	172
Table 3.6 Summary of thermochronological data.....	174

### APPENDIX

Table B.1 $^{40}\text{Ar}$ - $^{39}\text{Ar}$ geochronological data.....	206
Table B.2 U-Pb laser-ablation geochronological data.....	215
Table C.1 Microthermometric data for Taylor-Windfall fluid inclusions .....	220
Table C.2 Microthermometric data for Empress fluid inclusions.....	221
Table C.3 Microthermometric data for Pellaire fluid inclusions .....	223

## LIST OF FIGURES

### CHAPTER II

Figure 2.1 Orogenic belts of southwestern British Columbia .....	35
Figure 2.2 Regional geology of the Taseko Lakes Region .....	36
Figure 2.3 Schematic summary of the tectonic setting and inferred sediment sources of Early to mid-Cretaceous rocks in the Tyaughton-Methow Basin .....	37
Figure 2.4 Geologic map of the Taseko Lakes Region.....	38
Figure 2.5 Geologic map and cross-section of the Twin Creeks and Pellaire areas .....	39
Figure 2.6 Photoplate of stratigraphic lithologies of the Taseko Lakes Region .....	40
Figure 2.7 Geologic map and cross-section of the Northwest Copper and Tchaikazan Valley areas .....	42
Figure 2.8 Geologic map of the Mount McLure area .....	43
Figure 2.9 U-Pb Concordia plots and weighted average plot for zircon analysis.....	45
Figure 2.10 Photoplate of the intrusive lithologies of the Taseko Lakes Region .....	47
Figure 2.11 $^{40}\text{Ar}$ - $^{39}\text{Ar}$ geochronology from the Taseko Lakes Region.....	49
Figure 2.12 Geologic map of the Twin Creeks sinistral-reverse shear zones showing locations of indicated photographs .....	51
Figure 2.13 Equal area, lower hemisphere stereonet plot showing orientations of poles to foliations from selected fault zones indicated in the Taseko Lakes Region .....	52
Figure 2.14 Geologic map showing locations of photographs of the main contractional fault in the Northwest Copper area .....	53
Figure 2.15 Geologic map showing locations of photographs of the dextral faults in the Tchaikazan Valley Area .....	54
Figure 2.16 Geologic map of the Mount McLure area showing locations of fault zone photographs .....	55
Figure 2.17 Cartoons illustrating the interpreted evolution of the Tchaikazan Fault system in the Mount McLure area .....	56
Figure 2.18 Summary of geochronological age data .....	57

### CHAPTER III

Figure 3.1 Regional geology of the Taseko Lakes Region .....	135
Figure 3.2 Geologic map of the Taseko Lakes Region.....	136
Figure 3.3 Cartoon illustrating deposit types potentially associated with magmatic-hydrothermal systems and schematic diagrams of porphyry and high-sulphidation epithermal deposits .....	137
Figure 3.4 Geologic map and cross-section of the Empress area .....	139

Figure 3.5 Geologic map of the Taylor-Windfall area modified Price (1986) .....	140
Figure 3.6 Geologic map and cross-section of the Taylor-Windfall area .....	141
Figure 3.7 Geologic and alteration maps and cross-section of the Pellaire property .....	142
Figure 3.8 Photoplate showing lithologic units of the Empress deposit .....	143
Figure 3.9 Ar-Ar plateau ages of lithologic and alteration units in the Taseko Lakes Region.....	145
Figure 3.10 Lithologic and alteration cross-sections through the Empress deposit .....	147
Figure 3.11 U-Pb data plots.....	148
Figure 3.12 Photoplate showing Taylor-Windfall area lithologic and alteration units .....	149
Figure 3.13 Photoplate of the Pellaire property geology .....	151
Figure 3.14 Photoplate showing alteration types of the Empress deposit.....	153
Figure 3.15 Photoplate showing the occurrence of chalcopyrite at the Empress deposit .....	156
Figure 3.16 Alteration and cross-section of the Taylor-Windfall area .....	157
Figure 3.17 Photoplate showing vein types of the Empress deposit .....	158
Figure 3.18 Interpreted paragenesis the Empress deposit.....	159
Figure 3.19 Interpreted paragenesis the Taylor-Windfall deposit .....	160
Figure 3.20 Interpreted paragenesis of the Pellaire deposit .....	161
Figure 3.21 Cartoons illustrating the interpreted evolution of the Pellaire deposit .....	162
Figure 3.22 Summary of the geochronological data for the Empress, Taylor-Windfall and Pellaire deposits .....	163
Figure 3.23 Cross-section of the Empress deposit showing locations of samples analyzed using microthermometry .....	164
Figure 3.24 Total melting temperature versus total homogenization temperature and temperature versus pressure/depth chart showing calculated isochores for fluid inclusions from all deposits .....	165
Figure 3.25 Photoplate showing Taylor-Windfall samples and fluid inclusions analyzed using microthermometry .....	166
Figure 3.26 Photographs of quartz-vein outcrop showing locations for Pellaire samples shown that underwent microthermometric analysis.....	167
Figure 3.27 Oxygen and carbon isotopic data for calcite vein samples at the Empress deposit.....	169
Figure 3.28 Oxygen isotope data from powdered quartz samples from all deposits and quartz-magnetite oxygen isotope geothermometry data from Empress quartz-magnetite alteration samples .....	171
Figure 3.29 Oxygen and hydrogen isotopic data from hydrous alteration minerals at all deposits .....	173
Figure 3.30 Mineral stability diagrams showing stability fields of selected alteration zones at the Empress deposit .....	175

Figure 3.31 Temperature-fS <sub>2</sub> diagram for the Fe-S-O system showing sulphidation states of ore-forming fluids and temperature-fO <sub>2(g)</sub> diagram for the Cu-Fe-S-O system under feldspar-stable conditions .....	176
Figure 3.32 Salinity-T <sub>h</sub> graph comparing L-V fluid inclusions from all deposits and curves limiting the stable existence of solutions with 1, 5 and 10% NaCl shown with isochores from each deposit.....	177
Figure 3.33 Cartoon cross-section illustrating the interpreted formation environment of the Empress deposit.....	178
Figure 3.34 Cartoons illustrating the potential scenarios resulting in epithermal-style alteration overprinting porphyry-style alteration .....	180
Figure 3.35 Cartoons illustrating the interpreted evolution of the Taylor-Windfall hydrothermal system .....	181
Figure 3.36 Cartoons illustrating the potential sources for mineralizing fluids at the Pellaire deposit...	182
Figure 3.37 Cartoon illustrating the interpreted formational settings of the Empress, Taylor-Windfall and Pellaire deposits .....	183
Figure 3.38 Geologic maps showing the present and proposed original geometries of the Empress and Taylor-Windfall deposits and Tchiakazan Fault.....	184
Figure 3.39 Pressure versus temperature graph with curves limiting the stable existence of saline fluids showing the interpreted P-T evolution of fluids for the Empress, Taylor-Windfall and Pellaire hydrothermal systems .....	185

## APPENDIX

Figure A.1 Sample SWIR spectra for indicated minerals and samples .....	202
---	-----

## ACKNOWLEDGEMENTS

Firstly, I would like to thank my supervisor Dr. Lori Kennedy and co-supervisor Dr. Ken Hickey for all of their guidance and advice throughout the course of this project. Without their input providing both the research projects and the research directions, this project would not have been possible. Galore Resources Inc. is thanked for both providing funding for the project and logistical support during fieldwork. GeoscienceBC is also thanked for providing funding for the project. Great Quest Metals Ltd. is thanked for permitting access to the Empress Deposit property and drill core. Nathan Cleven, Moira Cruickshanks, Gabe Jutras and Erin Looby are all thanked for all of their help and input during fieldwork. Thank you to Dan Marshall at Simon Fraser University for all his help and guidance with the fluid inclusion study in the project. Without his dedication the study would not have been successful. Claire Chamberlain's input and helpful advice throughout the course of this project has been a great support and is much appreciated. At UBC, Tom Ullrich is thanked for all his help and input in obtaining Ar-Ar dates for the project. Likewise, Janet Gabites is thanked for performing the carbonate stable isotope analyses. Thanks to Jim Mortensen for both being a dedicated committee member and obtaining the U-Pb dates for the project. Janet Gabites and Richard Friedman are also thanked for help in U-Pb data acquisition. Kerry Klassen at Queen's University is thanked for obtaining the oxygen and hydrogen stable isotopic data used in the project. Ray Donelick at Apatite to Zircon Inc. is thanked for the gathering and processing of thermochronological data. Stefan Wallier and Sasha Wilson are also thanked for their help in providing guidance for the fluid inclusion and XRD studies respectively. Thank you to my project partner Lucy Hollis for all of her helpful discussion and support throughout the course of this project. Finally thank you to all my friends and family for providing me with support when needed and making the past two years memorable and enjoyable.

## DEDICATION

*My Parents,  
for the camping trips.*

## CO-AUTHORSHIP STATEMENT

Dr. Lori Kennedy and Dr. Ken Hickey contributed significantly to all aspects of this project including fieldwork, research direction, interpretation and editing of previous manuscripts. Dr. Dan Marshall at Simon Fraser University contributed greatly to both the microthermometry and resulting data analysis and interpretation for the fluid inclusion study. Mineral separates were given to Tom Ullrich at UBC for Ar-Ar dating, and Bulk rock samples were given to Dr. Jim Mortensen, Dr. Richard Freidman and Janet Gabites also at UBC for U-Pb dating and to Ray Donelick at Apatite to Zircon, Inc. for thermochronological dating. Powdered calcite separates were given to Janet Gabites at UBC for carbonate C and O stable isotopic analysis. Likewise, powdered mineral separates and whole rock samples were given to Kerry Klassen at Queens University for oxygen and hydrogen stable isotopic analysis.

# CHAPTER I

## GENERAL INTRODUCTION

### 1.1 PURPOSE OF THIS STUDY

The relationship between deformation and mineralization occurrences in the Taseko Lakes region is poorly understood. This study is divided into two distinct parts: 1) The regional and structural geology of the Taseko Lakes region; and 2) Characterization of three mineral occurrences located within the Taseko Lakes region, proximal to the contact between the Coast Plutonic Complex (CPC) and southeast Coast Belt (SECB).

Regional and structural geology of the Taseko Lakes region (Part I): The purpose of this study is to identify and describe the lithologies and structural features present in the southern Taseko Lakes region. Detailed petrographic and structural studies, both in the field and lab, were undertaken to better understand the geology of the southern Taseko Lakes region. Geochronological studies were performed to place age constraints on identified lithologies and faults in the project area. The results of this study are presented in Chapter II. A summary of the implications of these results, specifically pertaining to what structural controls the faults or different lithologic units may impose on mineralization in the area are presented in Chapter III.

Mineral deposits of the Taseko Lakes region (Part II): The purpose of this phase of research is to characterize hydrothermal alteration and mineralization proximal to the contact between the Coast Plutonic Complex and southeast Coast Belt. This study integrated mapping, drill-core logging and sampling of three previously identified mineral occurrences in the southern Taseko Lakes region. Fieldwork was complemented by laboratory research to further understand the nature of the mineral occurrences and geologic features. This phase aims to: (1) Characterize the alteration and mineralization of three separate mineral deposits in the Taseko Lakes Area (Pellaire, Taylor-Windfall and Empress); (2) identify approximate P-T conditions of formation for observed alteration and mineralization; (3) determine geochronological ages for the observed mineralization in the region; (4) identify potential fluid sources for hydrothermal alteration; (5) propose genetic classifications for the deposits; and (6) determine the important geologic features governing the occurrence of mineralization in the region and (7) assess potential links between the deposits studied by placing them into a larger regional context. The results of this study are presented in Chapter III.

## **1.2 PREVIOUS GEOLOGICAL STUDIES AND MINERAL EXPLORATION IN THE TASEKO LAKES REGION**

The geology of the Taseko Lakes area was first described by Bateman (1914) and then by MacKenzie (1921). Tipper and Jeletzky completed the first geologic maps of the Taseko Lakes area (Tipper, 1963; Jeletzky and Tipper, 1968). Tipper later published the first geologic map of the entire Taseko Lakes area, at a 1:125,000 scale, in 1978 (Tipper, 1978). Subsequent regional and detailed mapping of the area has been completed by the British Columbia Geological Survey (Glover and Schiarizza, 1987; Glover et al., 1987, 1988a, b; Schiarizza and Garver, 1995; Schiarizza et al., 1997; Umhoefer and Schiarizza, 1996; Umhoefer et al., 2002). A regional stratigraphic and structural study of the southwestern Taseko Lakes area was conducted by Israel (2001) as a part of his M.Sc. research, which was later published (Israel et al. 2006).

Major deposits in the vicinity of Taseko Lakes include the Bralorne district gold deposits and the Prosperity Cu-Au deposit. Gold-bearing quartz veins were originally discovered in 1896 in the Bralorne area to the southeast of Taseko Lakes (Bellamy and Arnold, 1985). The Bralorne district mines were amalgamated by Pioneer Gold Mines of B.C. Ltd. in 1928. Since then, the district has produced >4 Moz of gold (Holtby, 1988). Mining operations at Bralorne ceased in 1971 (Bellamy and Arnold, 1985). The district has undergone subsequent exploration and is currently owned by Bralorne Pioneer Gold Mines Ltd. (Sanche, 2004). The Prosperity deposit was staked in the 1930's and was originally known as the Fish Lake deposit (Heinrich, 1991). Prosperity has since been extensively explored and developed, but never mined. It contains an estimated reserve 675 million tonnes of ore at 0.236% Cu and 0.434 g/t Au (Brommeland and Wober, 1999). Prosperity is currently owned by Taseko Mines Ltd.

The Taseko Lakes region has long been the focus of exploration for porphyry, epithermal and mesothermal-style mineralization. Between 1909 and 1920, many large, bog-iron deposits were discovered by prospectors in the Taseko Lakes area. Placer gold was discovered in the southeastern Taseko Lakes region in 1920 (Lane, 1983). Porphyry copper-gold mineralization was first discovered in the area in 1922 (Lambert, 1991), and mesothermal gold-bearing quartz veins were discovered in 1936. The region has since been explored for a variety of styles of copper and gold mineralization by a variety of companies and prospectors (Osborne, 1999). A government mineral assessment of the areas to the west of Taseko Lakes was carried out by McLaren (1990) in the late 1980's. Exploration properties in the Taseko Lakes region are

currently held by a variety of companies including Galore Resources Ltd., Great Quest Metals Ltd. and Valor Resources Ltd.

### **1.3 PROJECT METHODOLOGY**

Geological mapping, core logging and sampling in the field have been complemented by modern analytical techniques including: (1) petrographic work using transmitted and reflected light microscopes; (2) Ar-Ar and U-Pb geochronology; (3) thermochronological studies; (4) lithogeochemical analysis using short wavelength infrared spectral analysis (SWIR) and X-ray diffraction (XRD); (5) fluid inclusion analyses; and (6) oxygen, hydrogen and carbon stable isotopic analysis of veins and alteration samples at all three deposits studied. Detailed methodologies are described in the appropriate sections in subsequent chapters.

### **1.4 THESIS ORGANIZATION**

This thesis is presented in traditional format with four chapters. Chapter I is a brief introduction the project. Chapter II provides an overview of the background geology of the Taseko Lakes region with results from this study building on previous work. Chapter III presents the main findings of this study regarding the regional study of mineralization in the Taseko Lakes region. Chapter IV summarizes the main conclusions of the overall study and recommendations for future research. Finally, an appendix is also included with pertinent data from this study.

## **CHAPTER II**

### **GEOLOGY OF THE SOUTHERN TASEKO LAKES REGION**

#### **2.1 INTRODUCTION**

The Taseko Lakes Region is located in southwestern British Columbia, approximately 220 km north of Vancouver (Figure 2.1) and straddles the boundary between the southeast and southwest Coast geomorphologic belts. The region has undergone at least three phases of brittle, transpressional and contractional deformation and is dominated by intermediate volcanic, volcanoclastic, and clastic sedimentary rocks. Several mineral occurrences in the area are located within the Southeast Coast Belt (SECB) proximal to the contact of the Coast Plutonic Complex (CPC) (Figure 2.2). Despite the abundance of brittle faults dissecting the area, relationships between faulting and mineralization have not previously been investigated in detail. This chapter summarizes the observed lithologies, structural features observed during geologic mapping from this study, which builds on work from previous studies in the area including: McLaren (1990), Schiarizza et al. (1997) and Israel et al. (2006). Geochronological data from this study is presented for selected lithologic units and fault zones. The interpreted exhumation history of the region based on fission-track thermochronology is also described. Ultimately, this Chapter describes the interpreted geologic framework in which magmatic-hydrothermal mineralization in the Taseko Lakes Region took place.

## 2.2 REGIONAL GEOLOGIC SETTING

### 2.2.1 Geologic Setting

In the southern Canadian Cordillera, the southern Coast Belt separates the Intermontane superterrane to the east from the Insular superterrane to the west. The Intermontane superterrane is composed of several smaller terranes, including the Cache Creek, Quesnel, and Stikine terranes, and was accreted to the western margin of North America during the Early to Middle Jurassic (Monger et al., 1982). The Stikine Terrane bounds the southern Coast Belt to the east and consists of stratified Devonian to Jurassic volcanic arc rocks and associated coeval plutons (Monger et al., 1994).

The Insular superterrane is composed of smaller, dominantly Paleozoic terranes, including Wrangellia and Alexander terranes (Monger et al., 1982; Schiarizza et al., 1997; Israel et al., 2006), which were likely amalgamated by Middle Jurassic (Monger, 1999). The CPC has overprinted much of the eastern margin of the Insular superterrane. As a result, the nature and timing of the accretion of the Insular superterrane is poorly understood, although it was likely docked to the Intermontane superterrane by the Late Jurassic (Schiarizza and Garver, 1995).

The Taseko Lakes region straddles the boundary between the Southeast Coast Belt (SECB) and Southwest Coast Belt (SWCB), which together comprise the southern Coast Belt in the Canadian Cordillera (Monger and Journeay, 1994). The SECB consists mainly of several late Paleozoic to Mesozoic volcanic arcs and clastic basinal lithotectonic assemblages (Schiarizza et al., 1997). These assemblages were docked to ancestral North America by ~90 Ma (Israel et al., 2006). In the vicinity of Taseko Lakes, the SWCB consists predominantly of the Cretaceous plutonic rocks of the Coast Plutonic Complex (CPC) (Friedman and Armstrong, 1995). The study area lies on the southern margin of the SECB where it is intruded by the CPC (McLaren, 1990) (Figure 2.2).

In the Taseko Lakes Region, stratigraphic rocks of the SWCB consist of Early Cretaceous rocks of the Gambier Group. This is an assemblage of volcanic and sedimentary rocks that is transitional into similar rocks of the SECB (Umhoefer et al., 1994). The remainder of the SWCB is dominated by the CPC in the vicinity of Taseko Lakes. The CPC extends for 1500 km from Washington State, through British Columbia and into Alaska and the Yukon. It formed during the Cretaceous and early Tertiary as a coast-parallel Andean-type magmatic continental arc. The CPC is characterized by felsic to intermediate plutons that intruded the

continental rocks of the western North American continental margin (Symons et al., 2000). Intrusive rocks of the Taseko Lakes region are interpreted to be part of the CPC.

The SECB represents the geologic material present between the Insular and Intermontane superterrane at the time of the accretion of the Insular superterrane (Figure 2.3) (Monger and Journeay, 1994). The SECB consists of several smaller oceanic terranes, including the Bridge River, Cadwallader, and Methow terranes (Figure 2.2). Permian basement rocks in the Taseko Lakes are interpreted to belong to the Methow terrane. Cretaceous cover rocks at Taseko Lakes are correlated with Gambier Group rocks and were deposited along the western margin of the Tyaughton basin (Figure 2.3). The Gambier Group rocks overlie the terranes of the SECB. Therefore the Cretaceous cover rocks of the Taseko Lakes Region represent an overlap assemblage spanning the gap between the SECB and SWCB (Israel et al., 2006). The terranes of the SECB formed in the Tyaughton and Methow basins that once separated the Insular from the Intermontane prior to accretion during the Cretaceous (Umhoefer et al., 2002) (Figure 2.3).

The Tyaughton and Methow basins originally comprised a single basin, but were separated during the mid-Cretaceous due to uplift of the Bridge River Terrane with the Tyaughton basin situated to the west of the Bridge River Terrane and the Methow basin located to the east (Figure 2.3; Schiarizza et al., 1997). The Bridge River terrane consists of a Middle Mississippian to Middle Jurassic accretionary complex (Bridge River Complex) consisting of sedimentary and ophiolitic rocks that have undergone varying degrees of accretion-related metamorphism (Archibald et al., 1990). Sedimentary rocks of the Bridge River Complex are believed to have formed in the Bridge River Ocean, which was largely subducted beneath the North American Plate during the Middle Triassic to Middle Jurassic. Bridge River rocks are overlain by Jurassic to Cretaceous clastic sedimentary rocks of the Cayoosh Assemblage (Journeay and Mahoney, 1994). The majority of the Bridge River terrane currently lies to the southeast of the study area. The Cadwallader terrane is a Late Triassic volcanic arc that was originally situated to the east of the Bridge River Complex, but is now found throughout most of the length of the SECB (Rusmore, 1987; Umhoefer and Schiarizza, 1996). Both the Cadwallader and Bridge River terranes are overlain by Middle Jurassic to mid-Cretaceous sedimentary rocks that were deposited in the Tyaughton-Methow basin including the Early Cretaceous Relay Mountain and Late Cretaceous Taylor Creek Groups (Jeletzky and Tipper, 1968; McLaren, 1990). The Taylor Creek Group formed in the Tyaughton basin following the uplift and division of the two basins (Figure 3.3) (Garver, 1992). The volcanic and sedimentary rock of the SECB

are all intruded by Cretaceous to Tertiary, intermediate to felsic intrusives and locally overlain by Tertiary volcanic and sedimentary rocks (Schiarizza et al., 1997; McLaren, 1990).

The East Waddington Belt is interpreted to be an overlap assemblage linked to the SWCB (Figure 2.3; Umhoefer et al., 1994; 2002). It occurs mainly to the northwest of the study area and has been intensely structurally deformed (Umhoefer et al., 1994; Schiarizza et al., 1997). The East Waddington Belt consists of Early to mid-Cretaceous volcanic and sedimentary rocks correlated with rocks of the SWCB (Rusmore and Woodsworth, 1991). Mid- to Late Cretaceous contraction produced mainly north-vergent thrust faults, subsequently named the East Waddington Thrust Belt (Rusmore and Woodsworth, 1994).

### **2.2.2 Structural History**

The Taseko Lakes Region is characterized by an extensive system of northwest trending faults. Faults in the area are dominantly high-angle strike-slip and contractional faults that developed during at least three phases of deformation from the mid-Cretaceous to Tertiary (Schiarizza et al., 1997; Israel et al., 2006).

Steeply dipping, sinistral strike-slip faults are interpreted as the oldest structures in the area. Some sinistral faults may have been reactivated and overprinted by later phases of deformation, typically forming sinistral-reverse faults (Schiarizza et al., 1997). This deformational event is interpreted to have transported the SWCB southward prior to the docking of the SWCB with ancestral North America by roughly 90 Ma. Deformation likely formed in response to oblique subduction of oceanic crust beneath the western margin of North America (Israel et al., 2006). Sinistral-reverse fault zones in the Taseko Lakes Region are wide, but discontinuous along strike.

Contractional faults formed during the second phase of deformation in the mid- to Late Cretaceous (Journey and Friedman, 1993). This event is interpreted to coincide with the final collapse and uplift of the Bridge River ocean basin from 91 to 85 Ma (Garver, 1989; 1992). This deformational event produced the SWCB fold and thrust belt (Journey and Friedman, 1993), which consists of south to southwest verging thrust faults that occur mainly to the southeast of the study area in the SECB (Jeletzky and Tipper, 1968). In contrast, the East Waddington Thrust Belt occurs mainly to the northwest of the study area and is dominated by north to northeast-vergent thrust faults, interpreted to be back-thrusts to the larger south to southwest-vergent thrust faults in the SECB (Rusmore and Woodsworth, 1994; Umhoefer et al., 1994; Schiarizza et al.,

1997). North-vergent thrusting occurred slightly later than south-vergent thrusting in the SECB from 87 to 84 Ma (Monger and Journeay, 1994). The Taseko Lakes region hosts both north- and south-vergent thrust faults, although north-vergent thrusts are larger in scale.

Dextral strike-slip faults are the largest and most dominant structures in the region and cut all other faults (Schiarizza et al., 1997). The Yalakom Fault is the largest scale dextral fault in the region and at this latitude separates the SECB from the terranes of the Intermontane Belt to the north of the study area. Several smaller, parallel faults, including the Chita Creek, Tchaikazan, and Twin Creek faults, occur to the south of the Yalakom Fault. Together, the dextral faults are interpreted to comprise a large left-stepping dextral fault system. This system is estimated to have accommodated at least 115 km of cumulative dextral offset (Umhoefer and Schiarizza, 1996). An earlier, Late Cretaceous sinistral component of displacement on the Tchaikazan Fault has been proposed based on a sinistral offset of fault bounded Jurassic sedimentary rocks to the northwest of Taseko Lakes (McLaren, 1990; Schiarizza et al., 1997). Major dextral faulting during Eocene times affected the entire southern Coast Belt and northern Cascades (Israel et al., 2006).

## **2.3 LITHOLOGIC UNITS**

Regional geologic mapping in the Taseko Lakes Region was performed at the 1:10,000 scale. Mapping for this study was focused on the Twin Creeks, Pellaire, Northwest Copper, Tchaikazan Valley and Mount McLure areas (Figure 2.4). Stratigraphic units were divided based on previous work in the region (Jeletzky and Tipper, 1968; McLaren, 1990; Schiarizza et al., 1997; Israel et al., 2006). The lithologic units of the southern Taseko Lakes Region have been examined and described in detail in order to better understand the geologic history of the area and assess potential controls the different units may impose on hydrothermal alteration and mineralization in the region.

### **2.3.1 Twin Creek succession**

The Twin Creek succession was first identified by Israel (2001). Prior to this it was mapped as part of the Late Cretaceous Taylor Creek Group (LKTC) (Jeletzky and Tipper, 1968; McLaren, 1990). In the study area, the unit occurs as several fault-bound packages within the Twin Creeks area (Figure 2.5) and its true stratigraphic thickness is unknown. A minimum age for the unit has been interpreted as  $251 \pm 16$  Ma based upon a U-Pb zircon date from a cross cutting aplite/dacite dike (Israel et al., 2006). The Twin Creek succession represents the only Paleozoic rocks and subsequently the oldest rock units present in the study area. The succession is interpreted as Permian basement rocks to the Mesozoic Tyaughton basin (Israel et al., 2006).

The succession is comprised mainly of relatively mature, clastic sedimentary rocks. The majority of the unit is composed of black silty shales, often interbedded with muddy shales or sandstones. Together, the interbeds form fining-upwards sequences and are interpreted to represent incomplete turbidite sequences (Figure 2.6A). Sandstones also occur independently of the shales in the northwestern area of Twin Creeks and include arkosic and lithic wackes and arenites ranging from 10 to 30% matrix. They are generally rich in plagioclase and volcanic clasts, which commonly contain 10-30% subhedral hornblende crystals. Grain sizes range from 1-10mm but average 1-2mm in size. The matrix of selected samples is clay rich and often contains significant oxides.

Proximal to fault zones, shales become highly foliated and commonly develop anastomosing shear fabrics. The shales are significantly oxidized and take on a reddish-orange hue proximal to the Grizzly Cabin Pluton (Figure 2.6B). However, this is not observed proximal to the contact with the Mount McLeod Batholith where the development of micas is observed

along the contact. Planar quartz and calcite veins up to several cm thick in the Twin Creek succession are common in the northwestern part of Twin Creeks.

### **2.3.2 Tchaikazan River succession**

The Tchaikazan River succession was originally distinguished by Israel (2001). It was previously included in the Taylor Creek Group (LKTC) by McLaren (1990). It is the most prominent lithologic unit in the area and occurs in all of the Twin Creeks, Pellaire, Northwest Copper, and Tchaikazan Valley areas. The succession has been subdivided into sedimentary- and volcanic-dominated facies. However, no discernable contact between the two units has been observed as the two units always occur as separate fault bound lenses. A minimum depositional age for the unit is constrained by a U-Pb zircon age of  $102 \pm 2$  Ma obtained from a nearby cross-cutting intrusion (Israel et al., 2006). Fossil belemnites found in the lower sedimentary portion indicate the Tchaikazan River succession is Hauterivian in age (McLaren, 1990; Israel et al., 2006). It is interpreted to represent a transition between Gambier Group rocks and the Tyaughton Basin.

#### **2.3.2.1 Sedimentary facies**

The sedimentary facies of the Tchaikazan River succession occurs in the Twin Creeks and Pellaire areas (Figure 2.5). It is interpreted to be stratigraphically below the volcanic facies and estimated to be approximately 500 m thick (Israel et al., 2006). The sedimentary facies consists of fine to medium-grained clastic, volcanic dominated sedimentary rocks, as well as coherent andesitic flows and primary volcanic breccias. Sedimentary rocks are slightly more common than volcanic rocks in the sedimentary facies, but sedimentary and volcanic rocks are not interbedded at the outcrop scale.

The sedimentary rocks vary from fine, black, silty and muddy shales up to coarse-grained volcanic-rich sandstones. Beds of fine-grained, grey sandstones grading up into black siltstones and mudstones commonly occur with thickness generally at the 10-30 cm scale. Such gradational beds have been interpreted as incomplete turbidite sequences. Resedimented volcanic pebble to boulder conglomerates (Figure 2.6C) as well as medium to coarse-grained volcanoclastic sandstones (Figure 2.6D) are all common in the Tchaikazan sedimentary facies. Volcanoclastic rocks can contain intermediate-volcanic clasts as well as individual crystals of plagioclase,

quartz, and less commonly, clinopyroxene and olivine. Rare, more mature sandstones present in the area consist mainly of quartz and feldspar grains. This suggests some sediment input from distal continental sources as well as from nearby volcanic environments such as the Gambier Arc. Pyrite and arsenopyrite occur sporadically throughout the Tchaikazan sedimentary facies in concentrations up to several percent.

Southeast trending, vertical sinistral-reverse fault zones generally occur adjacent to the more sediment-dominated areas of the Tchaikazan sedimentary facies often resulting in strong foliation development within the finer clastic sediments. Anastomosing shear fabrics also typically developed within shale units proximal to and within fault zones. Silicification and carbonate alteration are common proximal to fault zones in both shales and coarser-grained sedimentary rocks. Chlorite alteration also occurs throughout the Tchaikazan sedimentary facies but is most often observed in the coarser grained sedimentary rocks.

### **2.3.2.2 Volcanic facies**

The volcanic facies of the Tchaikazan River succession is slightly more extensive than the sediment-dominated facies, occurring in all the Twin Creeks, Northwest Copper and Tchaikazan Valley areas (Figure 2.5, 2.7). The facies is predominantly composed of clastic and coherent intermediate to mafic volcanic rocks, less common volcanic-rich clastic sedimentary rocks and rare fine clastic marine sedimentary rocks. It is roughly 1000 m thick (Israel et al., 2006).

The volcanic rocks of the Tchaikazan volcanic facies are similar to those observed in the Tchaikazan sedimentary facies but more abundant. Coherent flows are andesitic in composition, with phenocryst contents ranging from 0% up to ~30%. Phenocrysts consist of hornblende and/or plagioclase in varying proportions. On average, hornblende phenocrysts are more abundant than plagioclase phenocrysts in the Tchaikazan volcanic facies, with typical compositions of phyrlic units ranging from 10-15% hornblende phenocrysts and 5-10% plagioclase phenocrysts. Rare units also contain as much as 20% olivine phenocrysts (Figure 2.6E) or 15% fine clinopyroxene phenocrysts, indicating variable, more mafic compositions of some coherent and volcanoclastic units. Porphyritic andesites are more common than purely aphanitic units in the volcanic facies. Coherent units containing up to 15% vesicles are also observed in both massive and phyrlic units. Vesicles typically occur as amygdules filled with chlorite and carbonate, and are slightly flattened (Figure 2.6F). Well developed columnar

jointing is reported in coherent andesite flows within the Tchaikazan River succession (Israel et al., 2006). Columnar jointing is indicative of a submarine depositional environment, which corroborates the hypothesis that Cretaceous-aged Taseko Lakes cover rocks were deposited into the Tyaughton Basin.

Volcaniclastic breccias are common but less abundant than coherent flow units in the volcanic facies. The volcaniclastic breccias have angular to subangular pebble-sized clasts that are andesitic in composition. Phenocryst contents of andesitic clasts vary in the same manner as the coherent units in the area. Matrix material is andesitic in composition with variable phenocryst contents. Breccia units vary from clast-rich coherent units with clast contents of less than 10% up to 90% in clast-supported breccias. Clast-supported breccias are monomictic and typically bound on either side by coherent flow units and thus are interpreted to be autobreccias. Many breccias possess similar matrix and clast compositions and appear coherent in hand sample, but a strong brecciated texture is clearly defined in thin section and such units are interpreted to be the fragmental portions of coherent lava flows.

Sedimentary rocks comprise a minority of the Tchaikazan volcanic facies and consist mainly of coarse lithic sandstones and fine clastic siltstones and mudstones. Coarser-grained units are common and are typically thicker (often greater than outcrop scale) than fine clastic sedimentary rocks. Coarser units are comprised of clast-rich medium to coarse-grained sandstones. Grains are lithic-dominated and suggest a volcanic provenance. Coarse units can also grade up to pebble-sized grain sizes but on average are comprised of sand-sized grains. Fine clastic sediments consist of fine, black silty to muddy shales (<10m thickness) interbedded with other volcanic units described above. The sedimentary rocks of the Tchaikazan River succession are interpreted to be of marine origin.

Clay alteration and weathering of all units are widespread throughout the study area. Zones of weak chlorite and carbonate alteration often occur proximal to fault zones. Within southeast trending, vertical fault zones, rocks can become silicified, giving them a cherty appearance.

### **2.3.3 Falls River succession**

The Falls River succession was originally distinguished by Israel (2001). Prior to this, it was included in the Taylor Creek Group (LKTC) by McLaren (1990). In the study area, it occurs in the southern parts of the Twin Creeks and Pellaire areas (Figure 2.7). A minimum age of

deposition for the Falls River unit is  $103.8 \pm 0.5$  Ma based on a U-Pb zircon age from the Mount McLeod Batholith of the CPC which cuts the unit (Israel et al., 2006). The succession consists of intermediate coherent and clastic volcanic units with less common clastic sedimentary rocks. Its stratigraphic thickness is estimated to be 1000 m (Israel et al., 2006).

The volcanic units of the Falls River succession are similar to those of the Tchaikazan succession but have more abundant plagioclase phenocrysts. Non-phyric units are also common (as in the Tchaikazan River succession) but plagioclase phenocryst contents range up to 40%. Typical compositions for porphyritic units range from 10-25% plagioclase phenocrysts and 5-10% hornblende phenocrysts. Volcanic breccias and conglomerates are also present as in the Tchaikazan River succession (Figure 2.6G, H). No vesicles, amygdules or olivine phenocrysts are observed in the Falls River succession. The lack of any olivine and the increased plagioclase to hornblende ratio in most rocks give the Falls River succession volcanic rocks a slightly more felsic appearance than those of the Tchaikazan River succession (Figure 2.6G). However, the variety of compositions present and the subtle differences between the respective lithologic units makes distinction between the Tchaikazan and Falls River successions difficult.

Sedimentary units are slightly less common in the Falls River succession than the Tchaikazan volcanic facies. However, units interpreted as fine-grained, clastic marine-deposited sedimentary rocks and resedimented volcanic rocks observed in the Falls River succession are very similar to those of the Tchaikazan volcanic facies.

Veining and alteration are common and increase in intensity proximal to east-southeast trending vertical fault zones in both the Twin Creeks and Pellaire areas (Figure 2.5). Veins are typically mm to cm scale and aren't deformed. They are composed of quartz and carbonate, and less commonly epidote and pyrite. Alteration is weak and alteration minerals are mainly limited to quartz and clay minerals.

### **2.3.4 Taylor Creek Group**

The Taylor Creek Group occurs to the north of the Tchaikazan Fault in the Northwest Copper and Tchaikazan Valley areas and extends beyond the study area to the north. It consists mainly of clastic marine sedimentary rocks (Figure 2.7, 2.8). Fossil evidence indicates an Albian age (113-97.5 Ma) for the Group (Garver, 1992). The unit is also intruded by the Tchaikazan Rapids Pluton ( $89.3 \pm 1.4$  Ma; Figure 2.9A, B; Table 2.1). The thickness of the Taylor Creek

Group is variable, but is interpreted to be less than 3000 m in the Tyaughton Basin (Garver, 1992).

In the Tchaikazan Valley area, Taylor Creek rocks are typically composed of grey, bedded, medium-grained sandstones (Figure 2.6I). Grains are mainly quartz and feldspar with rare larger lithic clasts (up to several mm). In this area, the Taylor Creek Group is inferred to be separated from the Tchaikazan Rapids pluton by a steeply dipping fault zone (Figure 2.7).

In the Northwest Copper area, the Taylor Creek Group occurs as interbeds of dark grey to black siltstones and fine- to medium-grained grey sandstones (Figure 2.6J). Scour surfaces and flame structures are visible, confirming the paleo-upwards direction. Sequences fine upwards from sandstone to siltstone and are interpreted as being incomplete turbidite sequences ranging from 10-50cm thickness. In this area, the Taylor Creek Group shares an irregular contact with the Tchaikazan Rapids Pluton confirming that the pluton intruded the sedimentary rocks. The sedimentary rocks are slightly oxidized proximal to the contact but no extensive contact metamorphism or alteration is observed.

### **2.3.5 Powell Creek Formation**

The Powell Creek Formation encompasses the majority of the Northwest Copper area to the south of the Tchaikazan Fault (Figure 2.7). The Formation was originally defined by McLaren (1990) and subsequent Ar-Ar dating of hornblende has provided ages from  $94.6 \pm 6.6$  Ma and 95.9 Ma at the base of the Formation to  $78.95 \pm 4.1$  Ma from the highest levels in the formation to the north of the study area (Maxson, 1996). The base is intruded by the Dickson-McClure batholith, supporting evidence that the base of the Formation must be older than  $92.4 \pm 0.3$  Ma (Parrish, 1992; Schiarizza et al., 1997). The Powell Creek Formation is the youngest stratigraphic unit in the Taseko Lakes Region and is believed to have a stratigraphic thickness of greater than 3000 m (Schiarizza et al., 1997).

The Formation consists exclusively of coherent andesitic units and associated volcanoclastic rocks. Volcanic breccias and conglomerates contain clasts ranging from pebble to boulder size and are generally compositionally similar to the coherent units in the area. Some clastic units show differential weathering patterns between clasts and matrix (Figure 2.6K, L). Breccias and conglomerates often bound coherent units on either side and have subsequently been interpreted as flow front units, suggesting a sub-aerial environment of deposition. However, other volcanoclastic units in the area display well-developed bedding planes defined by

gradational to sharp changes in grain size, which suggests a sub-aqueous depositional environment. Therefore, it is likely that the Powell Creek Formation was deposited in a coastal environment with both subaerial and submarine localities typical of a proximal volcanic arc setting.

Plagioclase phenocrysts are common in coherent flow units and the matrix and/or clasts of many volcanic breccias and conglomerates, with contents ranging from near absent up to over 30% of the rock. Hornblende phenocrysts are also present but are less common and less abundant than plagioclase, typically ranging from absent up to about 15% of the rock. Clasts can be either monomictic or polymictic with a uniformly intermediate volcanic composition, often ranging from non to highly-phyric andesite. The lack of differential weathering patterns between the clasts and matrix in some conglomerate and breccia suggests a uniform composition and subsequently short transport distance for the units. Other units showing differential weathering between clasts and matrix also commonly show at least a poorly developed bedding plane, suggesting a longer transport distance and at least some compositional variation within individual lithologies. Such units are likely resedimented volcanoclastic rocks. All volcanoclastic rocks observed in the area are matrix-supported. Rocks of the Powell Creek Formation from the Northwest Copper area are further described by Hollis et al. (2008).

The majority of the units observed in the Powell Creek Formation have a characteristic purple weathering colour. Most of the Powell Creek rocks inspected in thin section have at least a slight pervasive clay overprint. There are rare zones on the central ridge in the Northwest Copper Area that host strong argillic alteration, giving the rocks a highly weathered, yellow to white colour (Hollis et al., 2007). Closer to the main thrust fault in the area, small, planar zones of ankerite alteration are visible, and immediately proximal to the thrust fault is a pervasive zone of chlorite alteration on the Powell Creek (footwall) side.

A second inferred thrust fault cuts Powell Creek rocks in the northern part of the Northwest Copper area. On the north side of this fault, the Formation consists of immature clastic sedimentary rocks and purple porphyritic andesitic flows and conglomerates. Sedimentary rocks range from coarse-grained, lithic-dominated sandstones to pebble conglomerates. This package of rocks is similar to rocks south of the inferred thrust fault, but is more sediment dominated and interpreted to be stratigraphically higher in the Powell Creek Formation.

### **2.3.6 Mount McLeod Batholith**

The Mount McLeod Batholith is part of the CPC and bounds the study area to the south. In the study area, it occurs in the Twin Creeks, Pellaire, and Mount McLure areas (Figure 2.5, 2.8) and intrudes all observed stratigraphic units. It is dominated by relatively uniform granodiorite, but several other intrusive phases occur within the margins of the batholith.

#### **2.3.6.1 Mount McLeod granodiorite**

The majority of the batholith is composed of uniform, medium to coarse-grained biotite-hornblende granodiorite. Previous dating of concordant zircon and titanite fractions from the Pellaire area, obtained by Israel et al. (2006), have constrained a minimum crystallization age for the batholith of  $103.8 \pm 0.5$  Ma and  $101.1 \pm 0.3$  Ma respectively. A separate U-Pb date from zircon from the Mount McLure area yielded a date of  $83.2 \pm 2.6$  Ma (Figure 2.9C, D; Table 2.1).

The granodiorite is equigranular with crystal sizes ranging from 1-10mm and averaging 2-3mm. It is composed of approximately 35% euhedral plagioclase, 30% quartz, 15% euhedral K-feldspar, 10% anhedral biotite, and 10% subhedral hornblende. The granodiorite may also contain up to 3% of any combination of clinopyroxene, Fe-oxides, or pyrite. The quartz crystals occur interstitially to all other minerals, and the feldspars occur interstitially to the mafic minerals. The grain size of the batholith decreases slightly towards the margin of the igneous body. At Pellaire, the granodiorite can contain up to 20% cobble-sized, fine-grained mafic enclaves within the host granodiorite (Figure 2.10A). The oxides are a post-crystallization overprint of the host-rock. Areas of intense Cu- and Fe-Oxide alteration occur sporadically throughout the batholith in the study area. Sets of imbricated thrust faults also occur within the batholith in both the Twin Creeks and Pellaire areas. The Mount McLeod granodiorite intrudes all observed country rocks, but is cut by all other intrusive phases.

#### **2.3.6.2 Empress pluton**

The Empress pluton is composed of porphyritic granite and crops out in the northeastern part of the Mount McLure area. It is interpreted to be part of the same intrusive phase that underlies the Empress Deposit to the east (Blevings et al., 2008). It intrudes the Falls River succession and is inferred to cut the Mount McLeod granodiorite because of its finer grain size proximal to its contact with the granodiorite. Dating of concordant zircon fractions have yielded

a minimum crystallization age for the porphyritic granite of  $87.0 \pm 1.4$  Ma (Figure 2.9E, F; Table 2.1).

The porphyritic granite is coarsely porphyritic biotite granite consisting of roughly 30% subhedral feldspar, 10% anhedral biotite, and 10% anhedral quartz phenocrysts set in a fine-grained, quartz-feldspar-dominated groundmass. Phenocrysts range from 1-6 mm size, with feldspar and biotite being coarser on average than quartz phenocrysts. It commonly contains up to 1% Fe-oxide or pyrite.

### **2.3.6.3 Equigranular rhyolite-granite**

The equigranular rhyolite-granite unit outcrops in the eastern part of the Mount McLure area but is also occurs as dikes within the Mount McLeod granodiorite. No cross-cutting relationship is observed between the equigranular rhyolite-granite and the porphyritic granite phases. A minimum crystallization age for the equigranular rhyolite-granite is given by a biotite  $^{40}\text{Ar}$ - $^{39}\text{Ar}$  plateau age of  $91.45 \pm 0.51$  Ma (Table 2.1; Figure 2.11A).

The dikes and fringes of the equigranular rhyolite-granite intrusive phase are composed of equigranular, fine-grained biotite rhyolite. This unit also brecciates the Mount McLeod granodiorite (Figure 2.10B). It is composed of roughly 50% anhedral feldspar, 40% anhedral quartz, and 10% subhedral biotite with grain sizes ranging from about 0.1 to 0.8 mm (Figure 2.10C). This unit coarsens away from its margins with grain sizes increasing from <0.5 mm up to 2 mm. Minor chlorite alteration of biotite phenocrysts is also commonly observed.

### **2.3.6.4 Porphyritic biotite-hornblende granite**

The porphyritic biotite-hornblende granite unit occurs mainly as dikes and plugs in the eastern part of the Mount McLure area. It cuts all other intrusive phases in the Mount McLeod Batholith; however, it is cut by the Mount McLure pluton. A minimum crystallization age for the porphyritic biotite granodiorite is given by a biotite  $^{40}\text{Ar}$ - $^{39}\text{Ar}$  plateau age of  $98.7 \pm 2.2$  Ma (Table 2.1; Figure 2.11B).

The porphyritic biotite granodiorite consists of 50% feldspar, 34% quartz, 6% biotite, and 5% hornblende phenocrysts (Figure 2.10D). The majority of phenocrysts remain <1 mm in size, except feldspar and hornblende, which range from 1-4 mm in size. The variation in feldspar and hornblende phenocryst size gives the rock its porphyritic texture. The remaining 5% of the

modal composition is comprised of variable proportions of Fe-oxide and pyrite. Minor chlorite alteration of mafic phenocrysts is also commonly observed.

### **2.3.7 Grizzly Cabin pluton**

The Grizzly Cabin pluton occurs as an elongate, west-northwest trending lens in the northeastern part of the Twin Creeks area (Figure 2.5). It intrudes Permian rocks of the Twin Creek succession and Cretaceous-aged rocks of the Tchaikazan River succession. Abraded zircons from the pluton yield concordant U-Pb results suggesting an age of about 102-99 Ma (Israel et al., 2006).

The peripheral areas of the pluton are characterized by irregular intermingling layers of medium-grained quartz monzonite to monzodiorite and medium to fine-grained biotite-pyroxene diorite (Figure 2.10E). Mafic minerals are more abundant in the diorite layers than in the quartz monzonite layers (up to 50%). The central area of the pluton is composed of a single homogeneous phase of medium- to coarse-grained pyroxene diorite. The heterogeneous features could have resulted from a second, more mafic pulse of magma being injected into the magma body. The inner, hotter core of the pluton homogenized with the new batch of magma, whereas the cooler margins of the pluton did not, and the two phases remained immiscible during crystallization. More detailed study could better evaluate this hypothesis.

Country rocks proximal to the contact with the Grizzly Cabin Pluton display reddish-orange colours, suggesting they have been oxidized. This is interpreted to have arisen from the emplacement of the pluton.

### **2.3.8 Tchaikazan Rapids pluton**

The Tchaikazan Rapids pluton bounds the north side of the Tchaikazan Fault in the study area and is composed of plagioclase-hornblende porphyry (Figure 2.7). It is also bound to the north by the Taylor Creek Group and occurs in both the Northwest Copper area and the Tchaikazan Valley area. Previous dating of abraded zircon fractions by Israel et al. (2006), give a minimum age of crystallization for the intrusion in the Tchaikazan Valley area of  $76 \pm 13$  Ma. A U-Pb zircon date from the Northwest Copper area yielded an age of  $89.3 \pm 1.4$  Ma (Figure 2.9A, B; Table 2.1). From observations in the field, the intrusive rocks present on both the Northwest Copper and Tchaikazan Valley areas are interpreted to be part of the same intrusion.

The rock itself is comprised of approximately 50% aphanitic plagioclase and quartz-rich groundmass and 50% phenocrysts (Figure 2.10F). Plagioclase phenocrysts compose about 30% of the rock and generally occur as subhedral to euhedral lathes approximately 2-10mm in size (~4mm on average). About 15% of the rock is comprised by elongate hornblende lathes, 1-5 mm long (~2mm on average). The remaining 5% of the rock consists of rounded 2-3 mm-size quartz phenocrysts. Proximal to the Tchaikazan Fault in the Northwest Copper Area, the majority of the groundmass and plagioclase phenocrysts are extensively altered to clay minerals. Alternatively, proximal to the Tchaikazan fault in the Tchaikazan Valley area, the clay alteration is less significant, but the hornblende phenocrysts are significantly replaced by chlorite. Well developed fracture sets are also observed in the Tchaikazan Valley area.

### **2.3.9 Mount McLure pluton**

The Mount McLure pluton occurs mainly in the western part of the Mount McLure area (Figure 2.8) and consists of porphyritic plagioclase-clinopyroxene-hornblende diorite (Figure 2.10G). The diorite cuts both the Mount McLeod granodiorite (Figure 2.10H) and the Taylor Creek Group. Dating of concordant zircon fractions have yielded a minimum crystallization age for the porphyritic granite of  $86.0 \pm 1.3$  Ma (Figure 2.9G, H; Table 2.1). Hornblende from the pluton also yielded a  $^{40}\text{Ar}$ - $^{39}\text{Ar}$  plateau age of  $45.37 \pm 0.49$  Ma (Table 2.1; Figure 2.11C).

The pluton is comprised of approximately 20% plagioclase, 10% clinopyroxene, and 10% hornblende phenocrysts set in an aphanitic groundmass. Phenocrysts are subhedral to euhedral and vary in size from 1-4 mm, with plagioclase phenocrysts being slightly coarser on average than the mafic phenocrysts. The pluton may also contain up to 5% Fe-oxides.

The majority of the Mount McLure pluton is intensely altered to the point where the protolith is indiscernible. However, less altered zones preserve primary textures. Common alteration minerals include kaolinite, alunite, and halloysite. The presence of these alteration minerals indicates that altering fluids were relatively low temperature, reduced, and highly acidic (Hemley et al., 1969; Drews-Armitage, 1996). Least altered zones possess minor chlorite alteration of mafic phenocrysts and groundmass.

### 2.3.10 Northwest Copper pluton

The informally named Northwest Copper pluton occurs as a small magmatic plug, ~40m x 40m, in the northern part of the Northwest Copper area. It is a medium-grained hornblende-quartz-alkali-feldspar syenite (Figure 2.10I). The majority of the rock comprises subhedral to anhedral potassium feldspar crystals with less abundant finer-grained, angular quartz crystals. Epidote and chlorite replace hornblende and to a lesser extent plagioclase, in the relatively fresh, central zone of the pluton. The margins of the pluton are characterized by intense argillic alteration that completely overprints the original mineralogy and gives the rock a bleached appearance (Figure 2.10J). Examination of thin sections suggests that the pluton once contained significant amounts of pyrite that have subsequently weathered to Fe-oxides. No absolute age data is available on the pluton, however it intrudes the 96-79 Ma Powell Creek Formation (Maxson, 1996; Schiarizza et al., 1997).

### 2.3.11 Dikes

Dikes have been observed on both the Northwest Copper and Twin Creeks areas. Twin Creeks dikes consist of predominantly fine-grained to slightly porphyritic andesite. Hornblende from one such dike on Twin Creeks yielded a  $^{40}\text{Ar}$ - $^{39}\text{Ar}$  plateau age of  $65.07 \pm 0.93$  Ma (Table 2.1; Figure 2.11D). This dike was approximately 1-2m wide with a sub-horizontal orientation.

In addition, several dikes on Northwest Copper have been identified; all with roughly vertical orientations. They are extensively weathered, commonly occurring as subcrop, but are compositionally similar to the Tchaikazan Rapids Pluton (89.3 Ma, plagioclase-hornblende porphyry). A separate hornblende-phyric andesitic dike that cross-cuts bedded units within the Powell Creek Formation (Figure 2.10K) in the northern part of the Northwest Copper area yielded an age of  $22.19 \pm 0.59$  Ma from  $^{40}\text{Ar}$ - $^{39}\text{Ar}$  age of a hornblende mineral separate (Figure 2.11E; Table 2.1). This age is correlative with Pemberton Arc volcanism to the south of the study area (29 – 6.8 Ma) (Coish et al., 1998) and indicates volcanism was active in the area until at least Miocene time.

## 2.4 STRUCTURAL GEOLOGY

Several faults in the southern Taseko Lakes Region have been examined and described in order to better understand the deformational history of the area and assess potential controls the different faults may impose on hydrothermal alteration and mineralization in the region.

### 2.4.1 D1: Sinistral-Reverse Faults

The earliest phase of deformation identified in the Taseko Lakes Region is characterized by high-angle, northwest-trending, sinistral-reverse shear zones. The most extensively examined sinistral-reverse faults occur in the eastern part of the Twin Creeks area (Figure 2.12). At least three, parallel, vertical shear zones strike approximately  $130^\circ$  (Figure 2.13) and dip mainly subvertically towards the southwest. The shear zones are visible at surface on an east-facing slope above the Falls River where they outcrop as steep-sided gulleys that vary from about 10-100 m in width and are laterally continuous at the surface for at least 500 m (Figure 2.12A). At the bottom of the slope, the faults disappear under scree and are not traceable to the other side of the valley. The rocks within the shear zones consist of sheared interlayered andesitic and fine-grained clastic marine sedimentary rocks.

The fault zone consists of interlayered and variably sheared andesitic rocks and interbedded siltstone-sandstone. Deformation is preferentially focused into the sedimentary units in the fault zone (Figure 2.12C) which are highly fractured and foliated. Foliations in the sedimentary rocks consist of both bedding planes ( $S_0$ ) and cleavage planes ( $S_1$ ). Bedding planes are defined by variations in grain size (typically silt to mud) and cleavage planes are defined by layers of aligned white mica and less commonly biotite.

Alteration within the shear zones is variable and ranges from chlorite dominated to calcite-quartz dominated to absent. Vein densities range from less than 1% to nearly 30% of the bulk rock composition and their orientations are highly variable. Veins are generally comprised of quartz and calcite and only occur in andesitic rocks. Composite quartz-calcite veins (Figure 2.12D) and cross-cutting relationships observed in thin section suggest that multiple veining events occurred within the shear zone. Minor pyrite was observed in some shear zone samples; however no significant mineralization is present in any identified D1 faults.

Shear fabrics and kinematic indicators are visible in outcrop and give a sinistral high-angle dip-slip sense of movement (Figure 2.12B). Observed shear fabrics and shear-sense indicators in oriented thin sections, indicate the fault has both sinistral strike-slip and high-angle

dip-slip components, with the northern fault block being up-thrown (Figure 2.12B). This correlates with stratigraphic data that the northern wall of the fault is substantially older (Permian) than the southern wall (Cretaceous). Shear-sense indicators are present in thin sections oriented perpendicular to the main foliations in both the vertical (strike/dip = 210/90; Figure 2.12C) and horizontal (300/03; Figure 2.12D) planes confirming that deformation in the fault was oblique. In order for significant dip-slip to occur in such a steeply dipping fault, it is likely that the fault was reactivated following an initial sinistral deformational event. This reactivation resulted in the partial overprinting of sinistral shear-fabrics by dip-slip shear fabrics. The faults are interpreted to be reverse faults due to the sinistral to compressional regime under which they are interpreted to have formed (Journey and Friedman, 1993; Israel et al., 2006).

Mineral separates of muscovite, biotite and illite defining shear fabrics in the fault zone produced  $^{40}\text{Ar}$ - $^{39}\text{Ar}$  plateau ages of ~97-88 Ma (Table 2.1; Figure 2.11F, G, H, I). These ages may reflect the age of reactivation of the fault from an earlier deformational event.

## **2.4.2 D2: Contractional Faults**

North-vergent thrust faults are interpreted to have formed during the second phase of deformation in the Taseko Lakes based on correlations with regional deformation (Rusmore and Woodsworth, 1994; Schiarizza et al., 1997; Israel et al., 2006) and geochronological data from this study (Table 2.1). The main fault in the Northwest Copper area is the best studied of these faults (Figure 2.14). The fault zone dips steeply ( $>65^\circ$ ) to the south, and hosts mylonitic fabrics (Figure 2.14A, B). The fault is visibly continuous (but rarely accessible) over several kilometers as a slightly discoloured layer within well exposed, dark grey volcanic rocks.

The thrust fault hosts significant secondary chlorite and epidote. In some areas, the hanging wall of the fault also hosts dense quartz-epidote veining containing minor pyrite and chalcopyrite (Figure 2.14D). The presence of alteration and minor mineralization in and immediately around the fault zone suggests that the alteration is controlled by the fault, which acted as a fluid conduit. Dense dissolution seams substantiate that substantial amounts of fluids were likely present within the fault at the time of deformation (Figure 2.14B). The alteration and ductile style of deformation suggest that hydrothermal alteration and deformation occurred concurrently. Circulating hydrothermal fluids would have increasing the pore fluid pressure in the fault rocks, therefore reducing the effective stress required for deformation. Fluids altered competent minerals such hornblende and plagioclase to chlorite, epidote and white micas, which

subsequently reduced the rheological strength of the host rocks (Passchier and Trouw, 2005). Therefore hydrothermal fluids circulating through the fault zone could have aided in the generation of ductile shear fabrics and fault-controlled alteration.

Analysis of well developed shear-sense indicators such as S-C fabrics and sheared porphyroblasts/delta-structures (Figure 2.14C) suggest a reverse sense of displacement with the southern hanging wall moving up relative to the northern footwall. Contractional faults are common throughout the Southeast Coast Belt. Southwest-vergent thrust faults that imbricate rocks of the Tyaughton basin, Bridge River Complex, Cadwallader Terrane and Bralorne-East Liza and Shulaps Complexes typically occur to the southeast of the study area (Schiarizza et al., 1997). Such faults are interpreted to have developed from 91 to 86 Ma ((Leitch et al., 1989; Schiarizza et al., 1997). Other contractional fault systems have been observed to the southeast of the study area, including faults hosting the gold-quartz vein systems at the Bralorne and Pioneer mines, which also formed between 91 and 86 Ma and may have been reactivated from an earlier phase of sinistral deformation (Leitch et al., 1989; Schiarizza et al., 1997). Similar south-vergent contractional faults exist at the Pellaire deposit in the Taseko Lakes Region (See Chapter III); However, north to northeast-vergent thrust faults mainly occur to the northwest of the study area in the East Waddington Thrust Belt. Deformation in the EWB was active from 87 to 84 Ma, with the thrust faults interpreted as back thrusts to the larger scale southwest-vergent faults (Rusmore and Woodsworth, 1994; Umhoefer et al., 1994). North-vergent faults in the Taseko Lakes Region are interpreted to be related to those in the East Waddington Thrust Belt.

Gentle, large-scale E-W trending folds are also present in between the contractional faults on Northwest Copper as indicated bedding measurements within the Powell Creek Formation (Figure 2.7). The orientations of these folds correlate with N-S directed crustal shortening as expected from the D2 contractional deformational event.

An  $^{40}\text{Ar}$ - $^{39}\text{Ar}$  plateau age of  $60.53 \pm 0.33$  Ma (Table 2.1; Figure 2.11J) was attained from illite from fault zone material, and is younger than other dated contractional faults in the area.

### **2.4.3 D3: Dextral Faults**

The latest stage of brittle deformation evident in the area is characterized by large-scale dextral strike-slip faults (Figure 2.15), including the Tchaikazan and Twin Creeks faults. The Tchaikazan Fault system is exposed in the Tchaikazan Valley area and is characterized by parallel, relatively wide (~30-40m) zones of faulted material (Fig 2.17A, B). The Tchaikazan

Fault is believed to host the greatest amount of displacement of all the faults. No clear sense of shear could be determined at the outcrop. There is no significant alteration in the Tchaikazan Fault rocks. The absence of alteration in the Tchaikazan Fault implies that it formed after the main alteration and mineralization events in the area. The brittle deformation style also suggests that D3 faults formed at shallow depths relative to the other generations of faults in the region. Dextral movement on the Tchaikazan Fault is suspected from other outcrops observed by previous workers (McLaren, 1990; Schiarizza et al., 1997). Smaller scale faults in the Tchaikazan Valley area are interpreted to be antithetic to the larger faults (Figure 2.15C). The Twin Creeks Fault occurs in the southwestern part of the Twin Creeks and Pellaire areas (Figure 2.5) and is inferred to be a left-stepover associated with the Tchaikazan Fault (Israel et al., 2006).

The Tchaikazan Fault is interpreted to have formed during the initial phase of sinistral deformation, and was subsequently reactivated during the dextral phase of deformation (Schiarizza et al., 1997; Israel et al., 2006). It is a step-over fault related to the larger scale Yalakom Fault (Israel et al., 2006). The Yalakom fault was active from at least 77 to 67 Ma (Umhoefer and Schiarizza, 1996). However, other similar dextral-strike slip faults in the area including the Chita Creek and Fortress Ridge faults were also active from 47 to 44 Ma based on a cooling age from a syn-deformational intrusion (Schiarizza et al., 1997). Thus the dextral phase of deformation could have lasted from 77 to 44 Ma.

#### **2.4.4 Mount McLure fault**

The Mount McLure area hosts a prominent subvertical, south-southeasterly trending fault that is 50-100 m thick (Figure 2.16). Fault zone material consists of a sheared, silicified quartz-phyric unit. Foliations in the sheared unit are defined by slightly irregular interlayering of quartz-rich and illite-rich layers. Much of the deformed unit has been intruded by less-altered, undeformed, porphyritic diorite and porphyritic biotite-hornblende granite dikes (Figure 2.16A). The dikes are oriented parallel to the dominant foliation in the shear zone and are interpreted to have been intruded along pre-existing foliations.

The silicified quartz-phyric unit is interpreted to be a highly quartz-illite altered, foliated quartz-phyric granitoid. Foliations within the silicified quartz-phyric unit are defined by interlayering of quartz-rich and illite-rich layers and are typically wavy and folded (Figure 2.16B); however, no definitive shear sense is observed in outcrop. Roughly 10% mm-size, anhedral to euhedral quartz-phenocrysts and up to 3% cm-sized subrounded granodiorite clasts

occur in the unit. This suggests the protolith may have been the Mount McLeod granodiorite. Multiple generations of quartz veins cut quartz-illite layering in the sheared unit.

Fluids are known to promote strain softening in quartz (White, 1975). Therefore, if hydrothermal fluids were present synchronously with fault development, they may have aided in promoting ductile deformation. Quartz in the quartz-rich layers is very fine grained (Figure 2.16C), which suggests that dynamic recrystallization was occurring in the fault zone. Increases of pore pressure such that the fault rocks hydrofracture could have produced the observed quartz microveining (<1mm thickness) and compositional layering arising from small-scale foliation and fracture controlled alteration. Quartz microveins cross cut compositional layering and have variable orientations (Figure 2.16D). Clear kinematic indicators of displacement were not observed in outcrop or hand sample. Weak shear fabric geometries are observed in thin section but no conclusive sense of displacement was determined (Figure 2.16C). The subvertical, southeast trend of the fault correlates well with other strike-slip faults in the region. Foliation orientations are comparable with those in the Twin Creeks shear zones (Figure 2.13) and the faults may have initially developed during the same deformational phase (D1).

In the D1 faults studied, significant alteration and relatively ductile fabrics are observed. In order to attain ductile fabrics at brittle crustal levels, deformation can be aided by fluids and extremely fine grain sizes of host rocks (Passchier and Trouw, 2005). Both conditions could be attained from hydrothermal fluids altering primary host rock minerals to finer grained minerals. The presence of significant quartz veining in both Twin Creeks and Mount McLure faults supports this hypothesis (Figure 2.12D, 2.16D).

Possible correlations between this fault and the Tchaikazan Fault remain unclear due to the lack of exposure of the faults in the area. The geometry of the fault and its close proximity to the inferred location of Tchaikazan Fault suggest they may be related. There is no evidence that this Mount McLure fault underwent a phase of dextral deformation. However, the Tchaikazan Fault is interpreted to have undergone an initial phase of sinistral deformation prior to the dextral event (McLaren, 1990; Schiarizza et al., 1997). The Mount McLure fault may have developed during the initial sinistral deformation underwent subsequent deformation synchronously with a later hydrothermal alteration event. The relationship that the Mount McLure fault has with the Tchaikazan Fault is unclear, but is interpreted to be a separate strand or splay originating from the Tchaikazan Fault to the north of the Mount McLure area (Figure 2.17).

Illite from the foliated, silicified unit yielded a  $^{40}\text{Ar}$ - $^{39}\text{Ar}$  inverse isochron age of  $46.24 \pm 0.87$  Ma (Table 2.1; Figure 2.11K).

## 2.5 GEOCHRONOLOGY

### 2.5.1 $^{40}\text{Ar}$ - $^{39}\text{Ar}$ Geochronology

Mineral separates were picked from crushed samples and submitted for  $^{40}\text{Ar}$ - $^{39}\text{Ar}$  analysis. Dates from intrusive samples (07-SB-073, 07-SB-158, 07-SB-093, 06-SB-243, 06-SB-119) were obtained from primary igneous hornblende or biotite. All igneous samples yielded  $^{40}\text{Ar}$ - $^{39}\text{Ar}$  plateau ages (Figure 2.11 A, B, C, D, E). Hornblende has a closure temperature of  $500 \pm 50^\circ\text{C}$  (Hanes, 1991); thus the  $^{40}\text{Ar}$ - $^{39}\text{Ar}$  age from hornblende separates are interpreted to be close to the initial cooling ages of the intrusions. Biotite has a closure temperature of  $300 \pm 50^\circ\text{C}$  (Hanes, 1991) and therefore only constrains a minimum cooling age for the intrusive lithologies. The closure temperature for white mica (muscovite and illite for the purpose of this study) is largely dependant on grain-size and composition and has been shown to range from over  $400^\circ\text{C}$  for coarse-grained muscovite to less than  $200^\circ\text{C}$  for fine-grained illite (Dong et al., 1997; Markley et al., 2002). The results are summarized in Table 2.1 and the full data set is included in Appendix B. The plateau age plots are shown in Figure 2.13.

#### 2.5.1.1 $^{40}\text{Ar}$ - $^{39}\text{Ar}$ samples

**06-SB-025-1** (location: 457 014 mE, 5 663 244 mN) is a polymictic granular clast-rich volcanoclastic sandstone from the Tchaikazan River sedimentary facies. It was sampled from a sinistral-reverse shear zone on the Twin Creeks area (Figure 2.12). It consists of roughly 25% anhedral to rounded, 1 to 4 mm-sized clasts (~10% quartz, 5% plagioclase, 5% calcite and 5% fine grained aggregates of calcite, clay and feldspar). The remainder of the sample is comprised of a clay and phyllosilicate-dominated groundmass. The alignment of phyllosilicates (biotite and muscovite) in the groundmass defines prominent shear banding. Pressure shadows and asymmetries of shear fabrics around clasts indicate a sinistral-reverse shear sense. Deformation twinning and overprinting of calcite on plagioclase clasts is common. Mineral separates of biotite and illite were dated from this sample using  $^{40}\text{Ar}$ - $^{39}\text{Ar}$  geochronology and generated plateau ages of  $88.96 \pm 0.6$  Ma (biotite; Figure 2.11F) and  $88.15 \pm 0.57$  Ma (illite; Figure 2.11G). There is significant variability in the ages of the highest-temperature steps in the biotite plateau, therefore the biotite age may not be entirely accurate. High-temperature steps for the illite plateau are all within error; therefore the illite age is interpreted to be valid.

**06-SB-030** (location: 456 794 mE, 5 663 455 mN) is a dark grey siltstone from the Twin Creeks Succession. It was sampled from a sinistral-reverse shear zone on the Twin Creeks area (Figure 2.12). It possesses 2% subrounded quartz crystals and 2% subangular plagioclase crystals (both are 1 to 2 mm in size). The remainder of the rock consists of a clay dominated groundmass with well-developed shear fabrics defined by the alignment of phyllosilicates. Asymmetries of shear fabrics indicate a sinistral-reverse shear sense. Calcite commonly overprints plagioclase crystals. Mineral separates of biotite and muscovite were dated from this sample using  $^{40}\text{Ar}$ - $^{39}\text{Ar}$  geochronology and generated plateau ages of  $91.98\pm 0.75$  Ma (biotite; Figure 2.11H) and  $96.77\pm 0.92$  Ma (muscovite; Figure 2.11I) respectively. The muscovite and biotite plateaus show accurate steps with low variability at high temperatures, therefore the ages are interpreted to be reliable.

**06-SB-082-4** (location: 448 391 mE, 5 669 397 mN) is a clast-rich mylonite taken from the main north-vergent contractional fault on Northwest Copper (Figure 2.14). It consists of 20% subrounded fine grained aggregate clasts that are typically 1 to 5 mm in size. The remainder of the rock is comprised of clay-chlorite dominated groundmass with well developed mylonitic shear-fabric. The foliation in the sample is defined by alignment and interlayering of fine-grained chlorite and illite. Alignment of illite and chlorite also define shear-fabrics in the sample. Assymetries of shear-fabrics around porphyroblasts, sheared porphyroblasts and pressure-shadows all indicate a top-left (contractional) shear sense. Dissolution seams are also common and are cut by shear bands. Rare voids are infilled by fine-grained quartz aggregates. Illite from shear-fabrics in the groundmass was dated using  $^{40}\text{Ar}$ - $^{39}\text{Ar}$  geochronology and generated a plateau age of  $60.53\pm 0.33$  Ma (Figure 2.11J). High-temperature steps for this sample are all within error, therefore the age is interpreted to be valid.

**06-SB-119** (location: 450 763 mE, 5 673 397 mN) is a light-grey, moderately hornblende-phyric andesite dike taken from a zone of rubbly outcrop in the northern part of the Northwest Copper area. It consists of 10% needle-shaped hornblende phenocrysts and 5% euhedral clinopyroxene phenocrysts (Figure 2.10K). Phenocrysts are 0.5 to 3 mm in size and set in a groundmass dominated by very-fine grained plagioclase lathes and fracture biotite crystals. A mineral separate of hornblende was dated using  $^{40}\text{Ar}$ - $^{39}\text{Ar}$  geochronology and generated a plateau age of  $22.19\pm 0.59$  Ma (Figure 2.11E). There is a slight saddle shape to the plateau for

this sample, indicative of Ar-loss (T. Ullrich, personal communication, 2008), therefore the age of the sample may not be entirely accurate.

**06-SB-243** (location: 456 786 mE, 5 664 955 mN) is a grey, moderately hornblende-phyric andesite dike taken from the Twin Creeks area. It consists of 10% euhedral to subhedral hornblende phenocrysts that are 1 to 2 mm in size. The remainder of the rock is dominated by fine-grained plagioclase lathes less than 0.5 mm in size. The dike is roughly one meter thick and cuts fresh, medium-grained sandstone of the sedimentary facies of the Tchaikazan River succession. A mineral separate of hornblende was dated using  $^{40}\text{Ar}$ - $^{39}\text{Ar}$  geochronology and generated a plateau age of  $65.07 \pm 0.93$  Ma (Figure 2.11D). There is significant error associated with the majority of steps in the plateau for this sample, indicating a low level of confidence in the precision of the age.

**07-SB-073** (location: 468 683 mE, 5 659 184 mN) is a weakly clay-chlorite altered, fine grained felsic dike from the Mount McLure area. The dike is roughly 10 cm thick cutting through the Mount McLeod granodiorite and is interpreted to be part of the same intrusive phase as the equigranular rhyolite-granite described above. The dike consists of 50% anhedral feldspar crystals, 40% anhedral quartz crystals and 10% subhedral biotite crystals (all 0.1 to 0.8 mm in size) (Figure 2.10C). Feldspar and biotite crystals are slightly overprinted by clay and chlorite. A mineral separate of biotite from the dike was dated using  $^{40}\text{Ar}$ - $^{39}\text{Ar}$  geochronology and generated a plateau age of  $91.45 \pm 0.51$  Ma (Figure 2.11A). The plateau is composed of highly accurate and precise steps, therefore the age is likely very reliable.

**07-SB-093** (location: 469 480 mE, 5 659 272 mN) is a least-altered sample of the Mount McLure pluton (weak to moderately clay-chlorite altered, porphyritic plagioclase-hornblende diorite) (Figure 2.10G) taken from the Mount McLure area. The sample consists of 20% subhedral plagioclase phenocrysts, 10% subhedral to euhedral hornblende phenocrysts, 5% euhedral clinopyroxene phenocrysts and 5% anhedral quartz phenocrysts. Phenocrysts range from 0.5 to 5mm in size, with mafic phenocrysts typically being moderately chloritized and slightly smaller than plagioclase phenocrysts. Phenocrysts are set in a fine-grained quartz-feldspar dominated groundmass. A mineral separate of hornblende was dated using  $^{40}\text{Ar}$ - $^{39}\text{Ar}$  geochronology and generated a plateau age of  $45.37 \pm 0.49$  Ma (Figure 2.11C). The plateau is composed of highly accurate and precise steps, therefore the age is likely very reliable. This age

is significantly younger than the corresponding U-Pb age from this study for the Mount McLure pluton. It is unlikely that the hornblende in the sample could have been thermally reset (requires temperatures of  $500 \pm 50^\circ\text{C}$  (Hanes, 1991)) because there is no high-temperature metamorphism or alteration observed in the area. Therefore, it must have come from a separate intrusive phase than the U-Pb sample. This suggests that either the Mount McLure pluton is comprised of multiple intrusive phases, or the hornblende Ar-Ar sample is from a dike that is compositionally and texturally very similar to the rest of the pluton. Widespread, intense alteration in the Mount McLure pluton obscures internal intrusive relationships within the pluton.

**07-SB-102-1** (location: 469 717 mE, 5 658 560 mN) is a sheared, highly quartz-clay altered, quartz-phyric granite taken from the main fault in the Mount McLure area (Figure 2.16). It consists of 10% mm-sized, anhedral to euhedral quartz phenocrysts and clasts. Weak compositional layering is defined by separate layers of more quartz-rich and illite-rich material. Weak shear-fabrics defined by alignment of illite crystals and compositional variations are visible, but no clear shear-sense is apparent. A mineral separate of illite was dated using  $^{40}\text{Ar}$ - $^{39}\text{Ar}$  geochronology and generated an inverse isochron age of  $46.24 \pm 0.87$  Ma (Figure 2.11K). Ages were unable to be determined from plateau or isochron plots for this sample. Only four steps were used in the calculation of the inverse isochron age, therefore only a low level of confidence is associated with the age.

**07-SB-158** (location: 470 341 mE, 5 659 468 mN) is a fine to medium grained, slightly porphyritic biotite granite taken from the Mount McLure area (Figure 2.10D). It consists of 50% subhedral feldspar, 35% anhedral quartz, 6% anhedral biotite, 4% subhedral hornblende and 5% angular grains of Fe-oxides and pyrite. Feldspar crystals range from 0.5 to 4 mm size, with the larger feldspar crystals giving the rock a slightly porphyritic texture. Other minerals are 0.2 to 1 mm in size. Mafic minerals possess a slight chlorite-overprint. A mineral separate of biotite was dated using  $^{40}\text{Ar}$ - $^{39}\text{Ar}$  geochronology and generated a plateau age of  $98.7 \pm 2.2$  Ma (Figure 2.11B). The highest temperature step in the plateau does not match the rest of the plateau steps, therefore there is some uncertainty regarding the precision of the age.

### 2.5.1.2 Age constraints on faults

#### *Sinistral faults*

Four mineral separates (muscovite, illite and two biotite) from two samples obtained from one of the sinistral shear zones on Twin Creeks were submitted for  $^{40}\text{Ar}$ - $^{39}\text{Ar}$  analysis (06-SB-025-1 and 06-SB-030). These separates yielded plateau ages ranging from approximately 88 to 97 Ma that are largely not within error of each other (Figure 2.11 F, G, H, I). However, the mineral separates used have variable closure temperatures (Hanes, 1991; Markley et al., 2002), and the minerals with higher closure temperatures have generated older ages. Therefore, there is a possibility that the dates obtained only reflect subsequent hydrothermal events or cooling histories of the fault rather than the timing of deformation across the fault. However, from the lack of widespread, intense alteration or deformation in the fault zone, it is unlikely that temperatures in the fault zone exceeded those required to exceed the closure temperature for biotite ( $300 \pm 50^\circ\text{C}$ ). It is more likely that the faults were reactivated and these ages reflect the reactivation ages of the fault, rather than the initial deformation. The muscovite separate from sample 06-SB-030 generated the oldest age ( $96.77 \pm 0.92$  Ma) which is interpreted to be a minimum age constraint on the initial deformational age of the fault. The Grizzly Cabin pluton intrudes the Twin Creek succession relatively parallel to these faults. This suggests that the faults may have aided emplacement of the pluton and therefore initial deformation took place prior to 99 to 102 Ma (Israel et al., 2006).

#### *Contractional faults*

An illite separate from the Northwest Copper contractional fault (Sample 06-SB-082-4) was also submitted for  $^{40}\text{Ar}$ - $^{39}\text{Ar}$  analysis and produced a  $^{40}\text{Ar}$ - $^{39}\text{Ar}$  plateau age of  $60.53 \pm 0.33$  Ma (Figure 2.11J). This age is younger than expected for the D2 deformational event correlated with East Waddington Belt deformation. The Northwest Copper fault hosts significant hydrothermal alteration. Since illite has a relatively low closure temperature that is largely dependant on grain size (Markley et al., 2002), the age from the Northwest Copper Fault may reflect a more recent hydrothermal event rather than the deformational age of the fault. However, the Northwest Copper Fault may have also been reactivated during subsequent deformational events such as the D3 dextral event. This age could also represent the primary age of deformation on the Northwest Copper Fault and thus represent a younger phase of contractional deformation not previously documented in the Taseko Lakes Region.

### *Mount McLure fault*

An illite mineral separate from the Mount McLure fault (sample 07-SB-102-1) was submitted for  $^{40}\text{Ar}$ - $^{39}\text{Ar}$  analysis and yielded an inverse isochron age of  $46.24 \pm 0.87$  Ma. This age correlates with the interpreted ages of deformation on the major dextral faults (D3) in the region including the Yalakom and Tchaikazan Faults (Schiarizza et al., 1997).

Ages from both the Northwest Copper and Mount McLure Fault indicate that significant deformation also occurred during 60 to 45 Ma. This overlaps with the interpreted age of D3 dextral deformation in the region (Schiarizza et al., 1997). Neither fault exhibits characteristics indicative of other dextral faults in the region, such as an east-southeasterly trend. Therefore, the D3 deformational event could have given rise to more than just dextral faulting.

## **2.5.2 U-Pb Geochronology**

Four bulk samples of intrusive lithologies were submitted for U-Pb laser ablation dating for the purposes of this study (06-SB-GEO-2, 07-SB-GEO-09, 07-SB-GEO-02 and 07-SB-GEO-08). All samples yielded dateable zircon fractions. Results from this study are summarized in tables 2.1 and 3.2, Concordia plots are shown in figures 2.9 and 3.14 and the full data set and analytical methodology is included in Appendix B.

### **2.5.2.1 U-Pb samples**

**06-SB-GEO-2** (location: 450 078 mE, 5 675 682 mN) is from the Tchaikazan Rapids pluton taken from the Northwest Copper Area. It is composed of 30% subhedral to euhedral plagioclase phenocrysts ranging from 2 to 10 mm in size and 15% elongate hornblende lathes ranging from 1 to 5 mm in size (Figure 2.10F). Hornblende is largely replaced by chlorite and plagioclase possesses a slight clay overprint. The remainder of the rock consists of very fine grained quartz-feldspar dominated groundmass. A zircon mineral separate was dated using U-Pb geochronology and generated a concordant age of  $89.3 \pm 1.4$  Ma (Figure 2.9). The majority of analyses yielded similar values, therefore there is reasonable confidence in the age.

**07-SB-GEO-02** (location: 471 890 mE, 5 661 590 mN) is from the Empress pluton taken from drill-core at the Empress deposit. The sample is coarsely-porphyritic granite consisting of

40% euhedral to subhedral feldspar phenocrysts, 2 to 10 mm in size, 10% biotite phenocrysts 0.5 to 2 mm in size and 5% pyrrhotite grains 0.5 to 1 mm in size. The phenocrysts are set in a fine grained quartz-feldspar dominated groundmass that is slightly overprinted by carbonate and clay minerals. A zircon mineral separate was dated using U-Pb geochronology and generated a concordant age of  $87.0 \pm 1.4$  Ma. The majority of analyses possess large errors, therefore the age has a low precision.

**07-SB-GEO-08** (location: 466 760 mE, 5 660 115 mN) is a relatively fresh sample of the Mount McLure pluton (weak to moderately clay-chlorite altered, porphyritic plagioclase-hornblende diorite) (Figure 2.10G) taken from the Mount McLure area. The sample consists of 20% subhedral plagioclase phenocrysts, 10% subhedral to euhedral hornblende phenocrysts, 5% euhedral clinopyroxene phenocrysts and 5% anhedral quartz phenocrysts. Phenocrysts range from 0.5 to 5mm in size, with mafic phenocrysts typically being moderately chloritized and slightly smaller than plagioclase phenocrysts. Phenocrysts are set in a fine-grained quartz-feldspar dominated groundmass. A zircon mineral separate was dated using U-Pb geochronology and generated a concordant age of  $86.0 \pm 1.3$  Ma. The majority of analyses yielded similar values, therefore there is reasonable confidence in the age.

**07-SB-GEO-09** (location: 468 272 mE, 5 659 568 mN) is from the Mount McLeod granodiorite (Figure 2.10A), sampled from the Mount McLure area. It is coarse-grained and composed of 60% subhedral feldspar, 18% anhedral quartz, 10% anhedral biotite, 8% anhedral to subhedral hornblende, 2% elongate clinopyroxene lathes and 2% irregular Fe-Oxide blebs. Mafic minerals are variably replaced by chlorite. A zircon mineral separate was dated using U-Pb geochronology and generated a concordant age of  $83.2 \pm 2.6$  Ma. The majority of analyses possess large errors; therefore the age has a low precision.

### **2.5.2.2 U-Pb interpretation**

Sample 06-SB-GEO-2 was obtained from the Tchaikazan Rapids pluton to the north of the Northwest Copper Area. The sample yielded a concordant zircon age of  $89.3 \pm 1.4$  Ma (Figure 2.9A, B). The Tchaikazan Rapids pluton intrudes the Taylor Creek Group, confirming that the Group is older than  $\sim 90$  Ma. Conversely, the Tchaikazan Rapids pluton is cut by the Tchaikazan Fault, confirming that the fault was active more recently than 89 Ma.

Sample 07-SB-GEO-08 was obtained from the Mount McLure pluton in the Mount McLure area. The sample yielded  $86.0 \pm 1.3$  Ma (Figure 2.9G, H). The Mount McLure pluton intrudes both the Falls River succession and Mount McLeod Batholith in the Mount McLure area, substantiating that both units are mainly older than 86 Ma. The Mount McLure pluton is cut by the Mount McLure fault, which indicates that the fault was active past 86 Ma.

Sample 07-SB-GEO-09 was obtained from the Mount McLeod granodiorite in the Mount McLure area. The sample yielded an age of  $83.2 \pm 2.6$  Ma (Figure 2.9C, D). Sample 07-SB-GEO-02 was obtained from the Empress pluton to the east of the Mount McLure area on the Empress property (Figure 2.4). The sample yielded an age of  $87.0 \pm 1.4$  Ma (Figure 2.9E, F). These dates are significantly younger than previous dates of the Mount McLeod granodiorite ( $103.8 \pm 0.5$  Ma and  $101.1 \pm 0.3$  Ma; Israel et al., 2006), indicating intrusive activity was occurring in the Mount McLeod batholith over an extended period of time. The Mount McLeod Batholith intrudes country rocks of the Falls River succession, which confirms that the succession has a minimum age of  $\sim 104$  Ma. Conversely, the Batholith is cut by the Twin Creeks Fault (D3), the Mount McLure fault and both north and south-vergent (D2) thrust faults (see chapter III). Due to the variety of intrusive phases present within the batholith, more extensive mapping and geochronological dating is required to better understand the formational history of the Mount McLeod Batholith.

These ages all represent the crystallization age of the respective intrusions and are relatively synchronous with much of the hydrothermal activity in the region (see chapter III; Leitch et al. 1989; Hollis et al., 2008). More detailed isotopic studies could better assess genetic links between mineralization and the intrusive phases in the region.

## 2.6 SUMMARY

Country rocks in the Taseko Lakes Region consist of sub-greenschist facies intermediate volcanic and clastic sedimentary rocks. The Tchaikazan River and Falls River successions identified by Israel et al. (2006) host strikingly similar mainly volcanic, volcanoclastic and resedimented volcanic rocks and are difficult to differentiate in the field. The Twin Creeks succession and Taylor Creek Group are composed of fine- to medium-grained clastic sedimentary rocks. The Powell Creek Formation is the youngest stratigraphic unit in the region and consists of coherent to volcanoclastic intermediate volcanic rocks.

Intrusive units in the Taseko Lakes Region are typically intermediate in composition but may be equigranular or porphyritic with variable percentages of typical granitoid forming minerals. Isotopic ages from intrusive units in this study indicates that the majority of magmatism in the area occurred from roughly 80 to 90 Ma. Dikes samples indicate that magmatic activity continued in the area until almost 20 Ma. Plutons observed in this study all intrude the surrounding country rocks. This corroborates that the country rocks in the region are mostly older than 90 Ma (McLaren, 1990; Umhoefer et al., 1994).

Age data from the sinistral/dip-slip faults in this study indicate they were active from roughly 96 to 88 Ma. This overlaps with the expected age range for D1 deformation in the SECB from previous studies (Schiarizza et al., 1997; Israel et al., 2006). Therefore, the shear zones observed in the Twin Creeks Area are interpreted to have formed from the initial sinistral, transpressional phase of deformation in the SECB.

Samples from the Northwest Copper and Mount McLure faults yielded ages younger than expected for D1 or D2 deformational events. The ages did overlap with the interpreted age of D3 dextral deformation (Umhoefer and Schiarizza, 1996; Israel et al., 2006). However, neither fault exhibits any characteristics clearly indicative of dextral offset. The Northwest Copper fault is interpreted to be a contractional fault. The sense of movement on the Mount McLure fault is unclear. Therefore, the D3 deformational event may have caused more than just dextral-style deformation in the SECB.

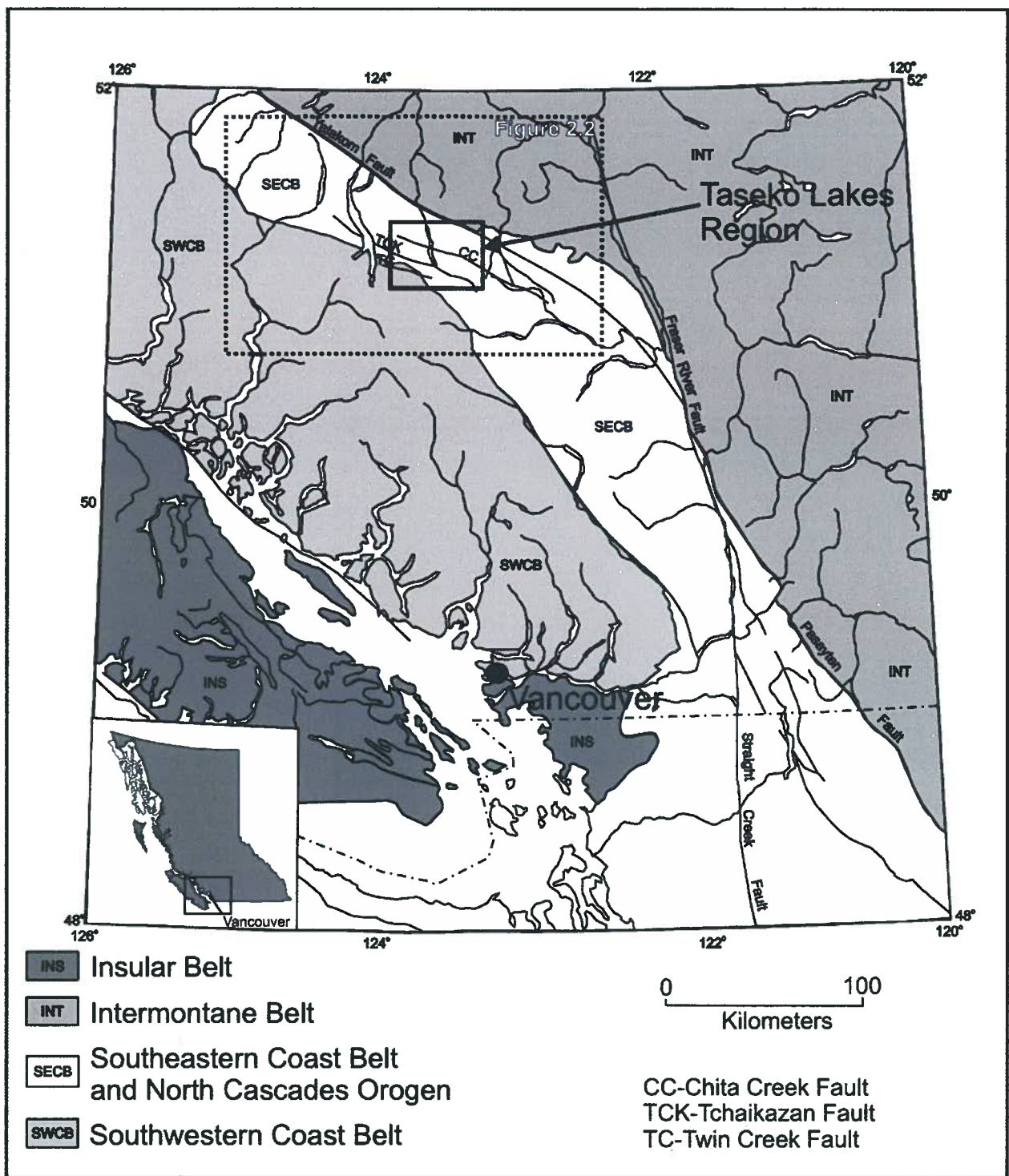


Figure 2.1 Orogenic belts of southwestern British Columbia (modified from Israel, 2001) showing the location of the Taseko Lakes region. Inset box indicates the area of Figure 2.2.

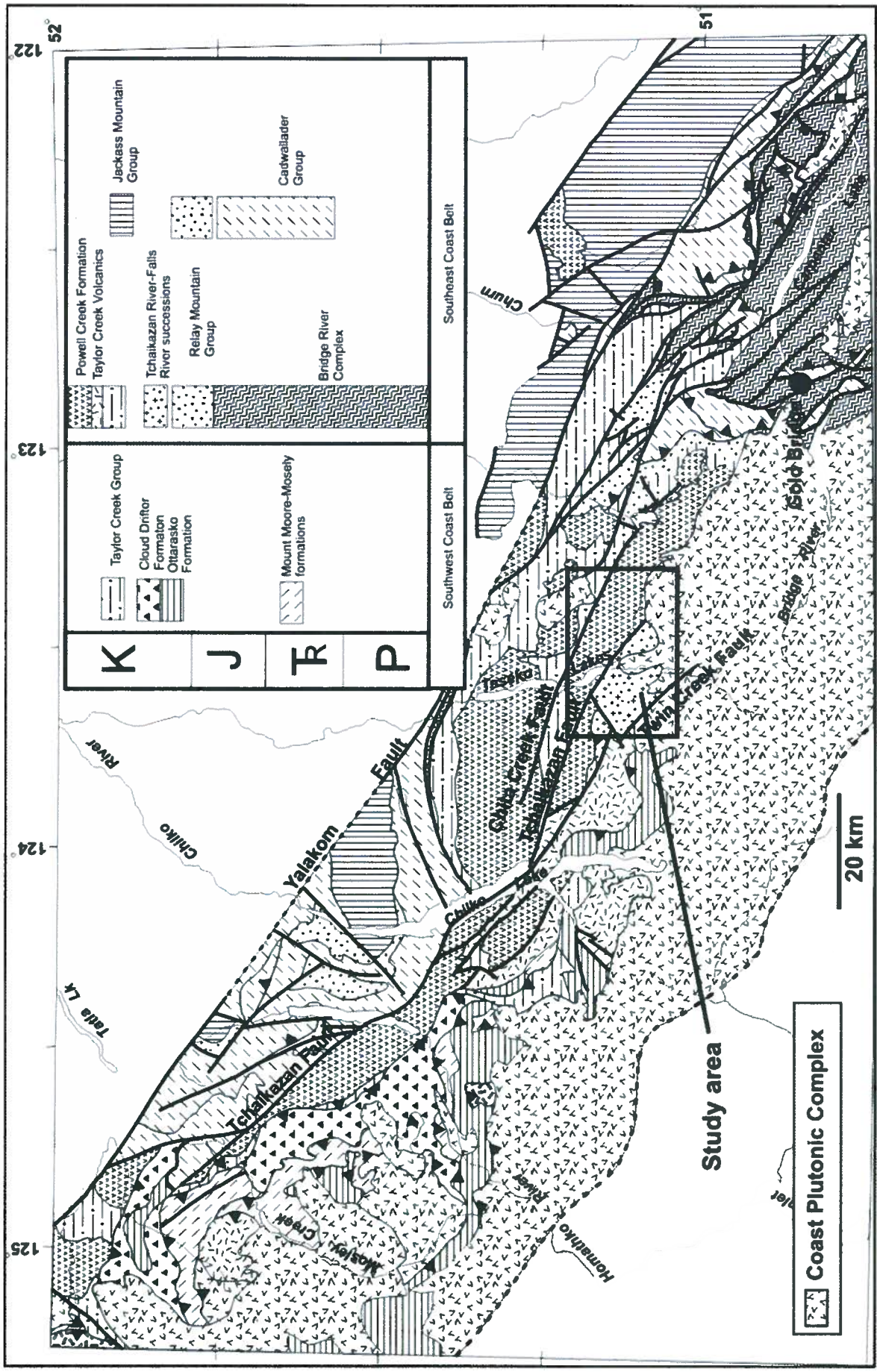


Figure 2.2 Regional geology of the Taseko Lakes Region showing the location of major faults, towns and the study area (modified from Israel et al., 2006). The location of Figure 2.4 is indicated by the solid box.

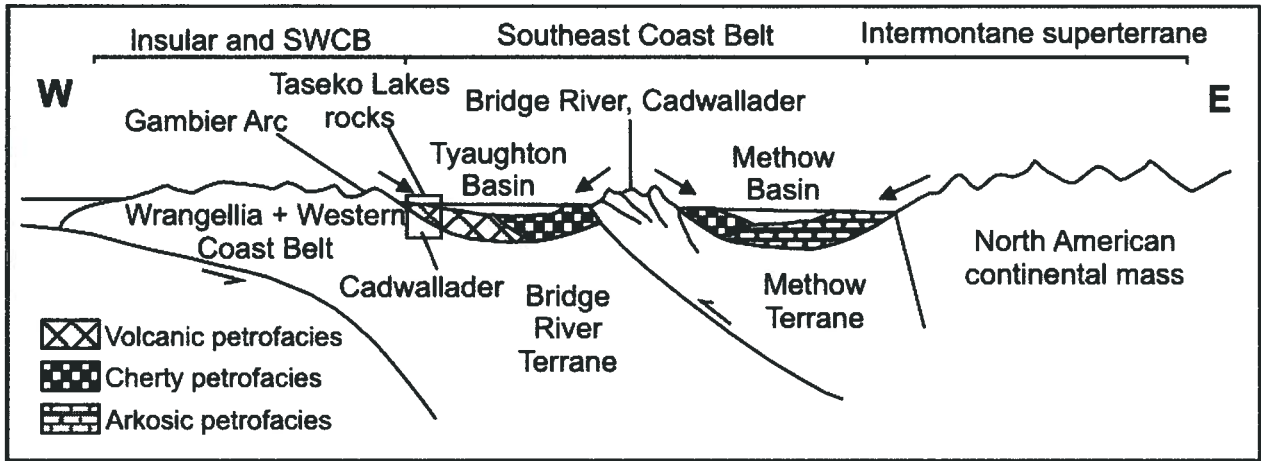


Figure 2.3 Schematic summary of the tectonic setting and inferred sediment sources of Early to mid-Cretaceous rocks in the Tyaughton-Methow basin (From Garver, 1992; Schiarizza et al., 1997). Location of Taseko Lakes rocks origin from Israel et al. (2006).

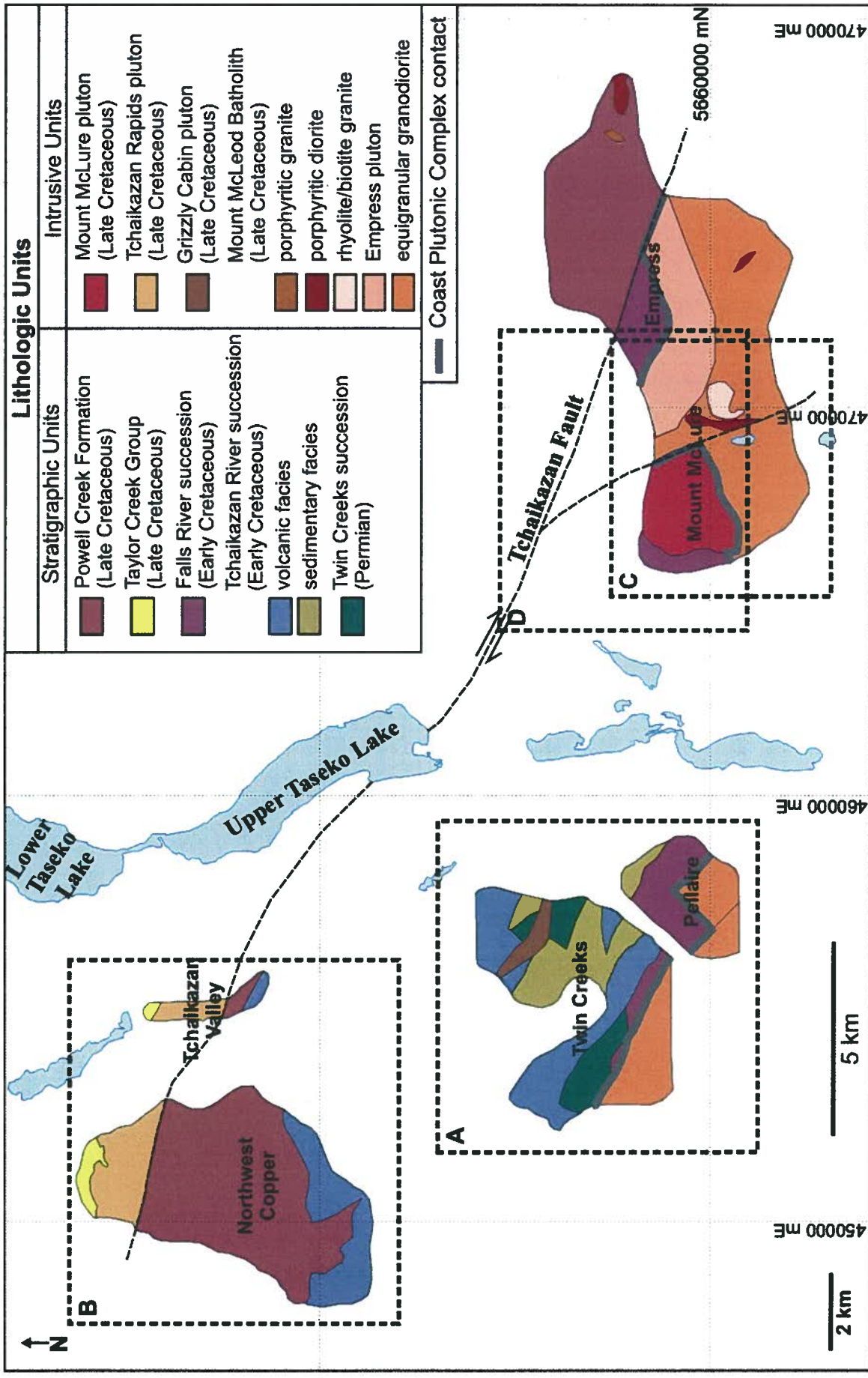
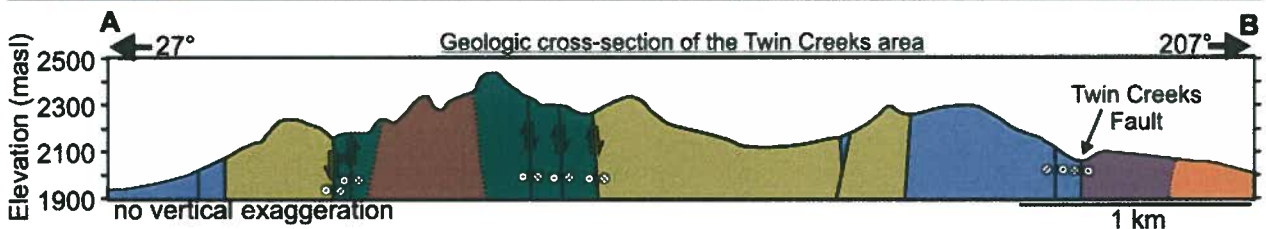
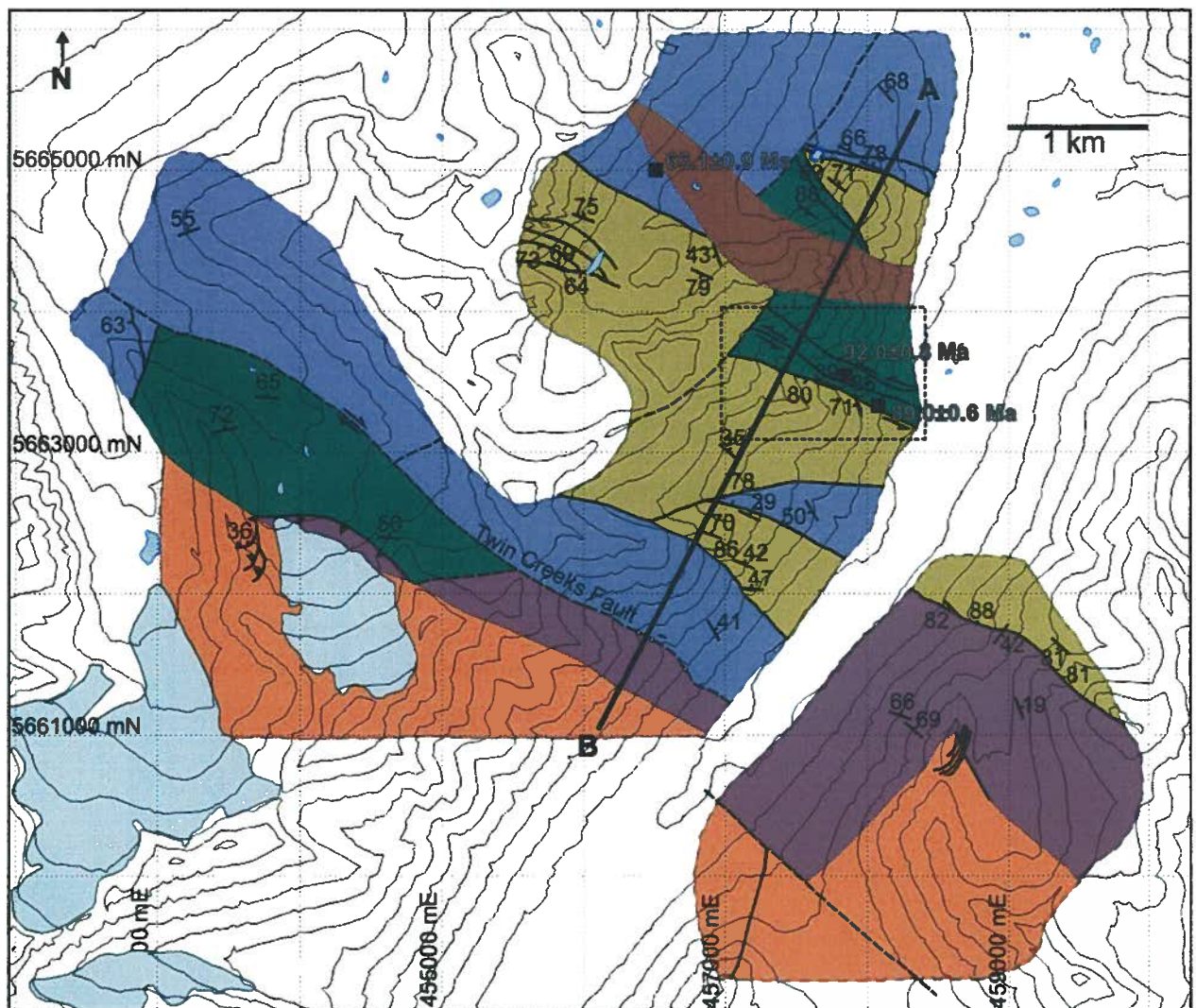


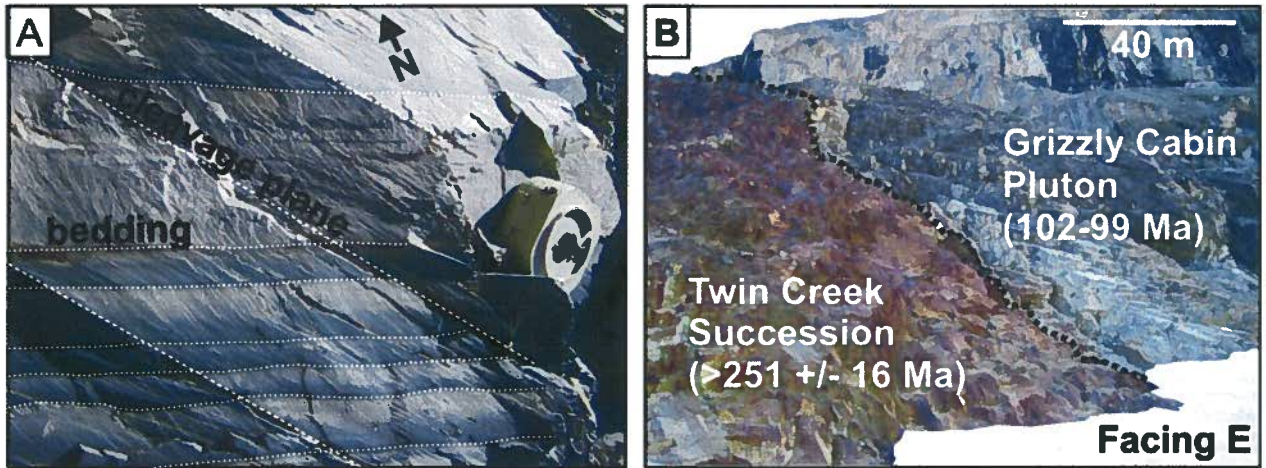
Figure 2.4 Location map of the Taseko Lakes Region showing locations and geology of properties studied and the Tchaikazan Fault. Locations of subsequent geologic maps are indicated by the lettered boxes: A – Figure 2.5; B – Figure 2.8; C – Figure 2.7; D – Figure 2.17. UTM coordinates are in NAD 83 Zone 10.



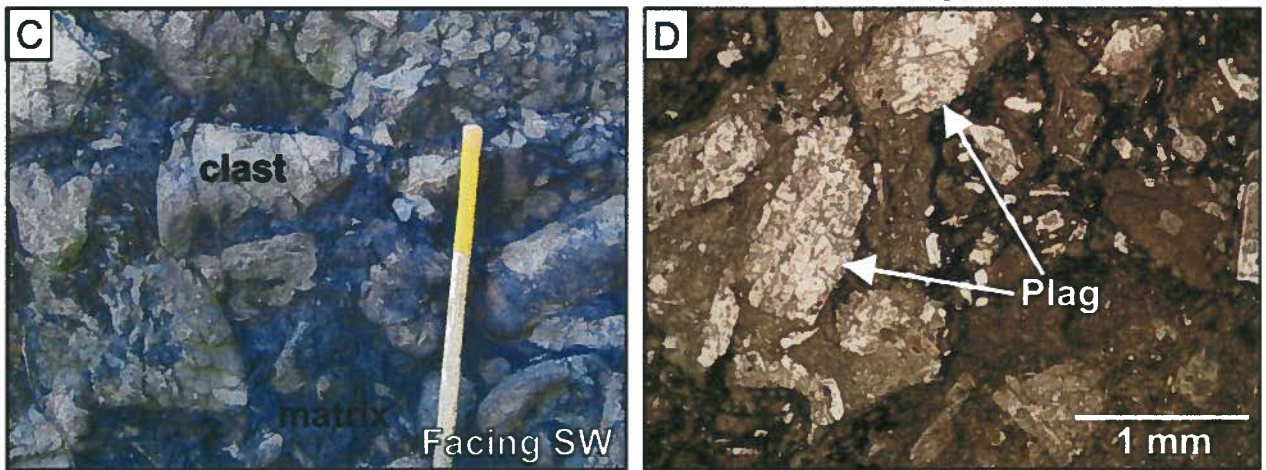
Lithologic Units		Map Symbols
<b>Stratigraphic Units</b>	<b>Intrusive Units</b>	\ bedding — observed fault - - - inferred fault ..... contact - - - extent of mapping area ■ Ar-Ar sample
■ Falls River Succession (Early Cretaceous) ■ Tchaikazan River Succession (Early Cretaceous) ■ volcanic facies ■ sedimentary facies ■ Twin Creeks Succession (Permian)	■ Grizzly Cabin pluton (Late Cretaceous) ■ Mount McLeod Batholith (Late Cretaceous) ■ equigranular granodiorite	

Figure 2.5 Geologic map and cross-section of the Twin Creeks and Pellaire areas. The location of the cross-section is indicated by line AB on the map. The location of the Twin Creeks Fault is also indicated. The dashed box indicates the location of the map shown in Figure 2.12. Locations and ages of geochronological samples from this study are indicated. UTM coordinates are in NAD 83 Zone 10. (contour interval = 100 m). Mapping was aided by previous work from Israel et al. (2006).

## Twin Creeks succession



## Tchaikazan River succession - sedimentary facies



## Tchaikazan River succession - volcanic facies

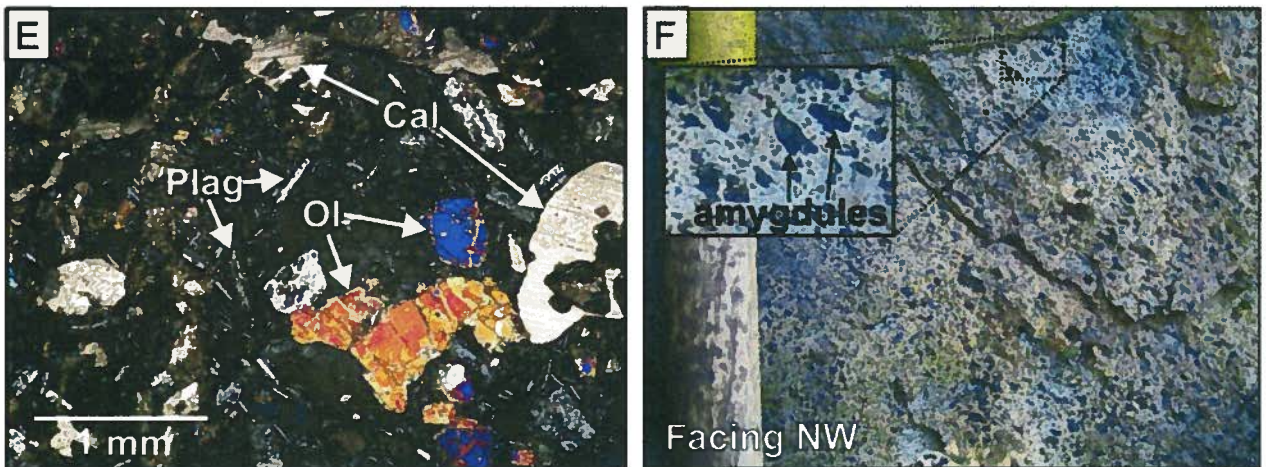
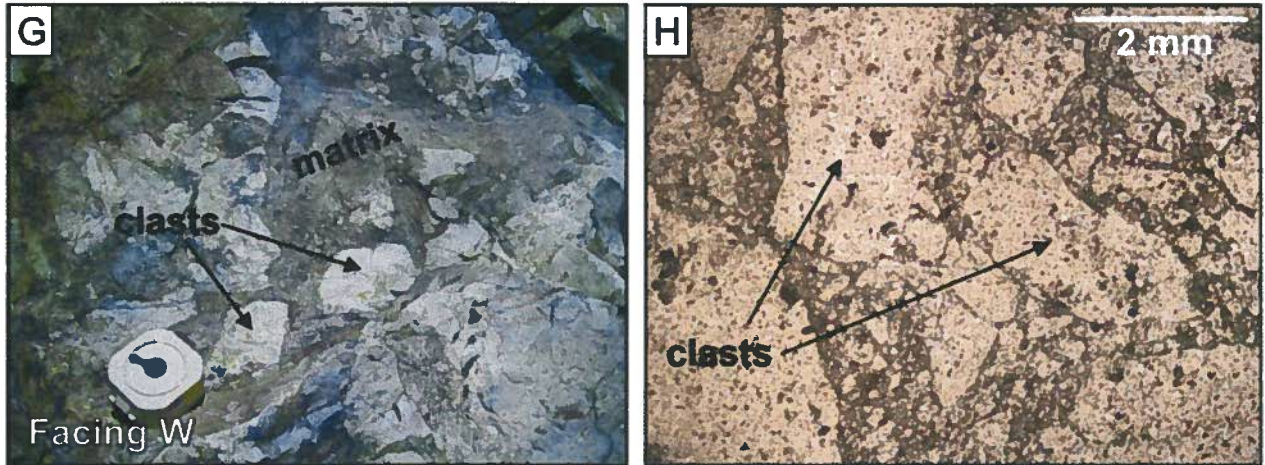
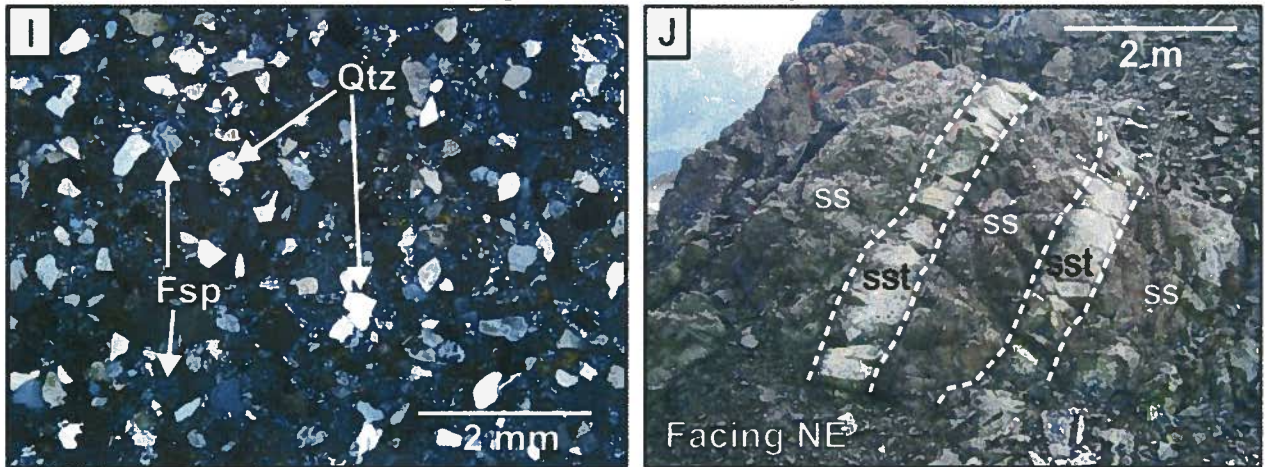


Figure 2.6 Photoplate of stratigraphic lithologies of the Taseko Lakes Region: A) Interbedded, fining-upwards sandstone(light grey)-mudstone(dark grey) sequences, interpreted to be incomplete turbidite sequences. Cleavage planes cross-cutting bedding planes are also indicated. B) Contact between oxidized Twin Creeks succession (left) and the Grizzly Cabin Pluton (right). C) Volcanic boulder breccia showing differential weathering between the clasts and matrix suggestive of resedimentation D) Plane-polarized light photomicrograph of plagioclase phyrlic microbreccia (field of view = 3.9mm). E) Cross-polarized light photomicrograph of olivine, plagioclase phyrlic clastic andesite unit with calcite infilling void space (field of view = 3.9mm). F) Amygdule-rich coherent andesite unit. Abbreviations: Cal = calcite, Ol = olivine, Plag = plagioclase.

## Falls River succession



## Taylor Creek Group



## Powell Creek Formation

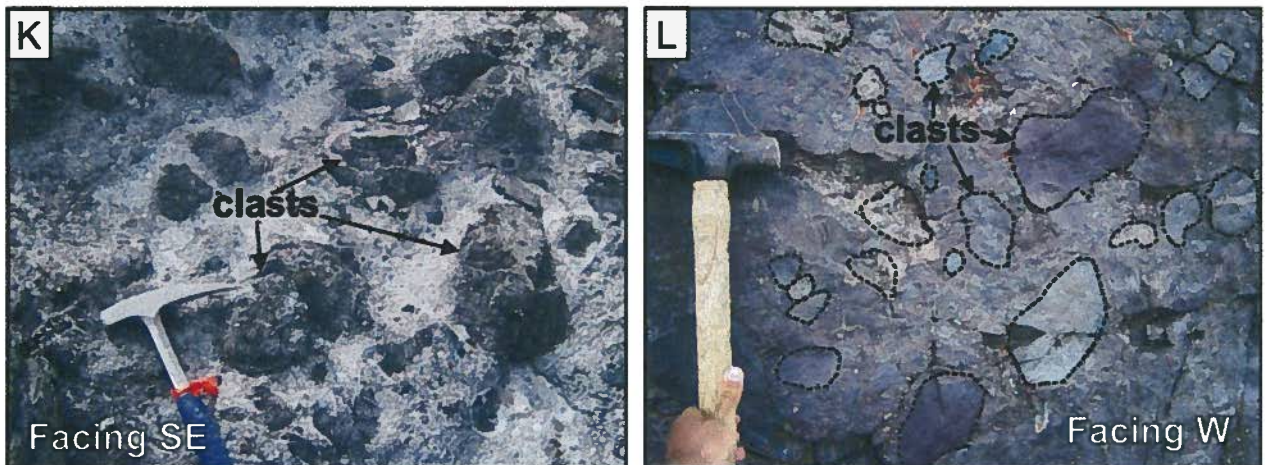
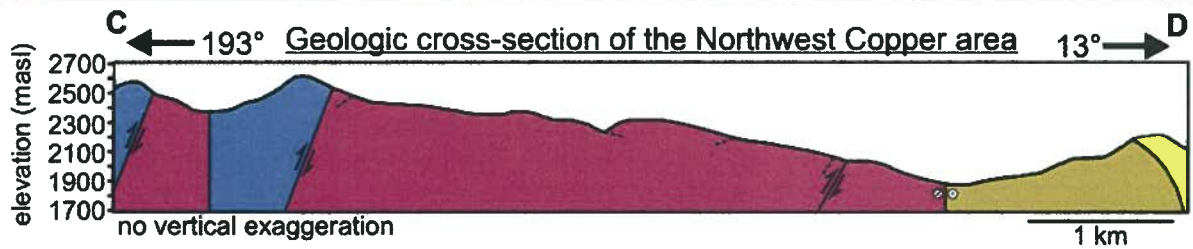
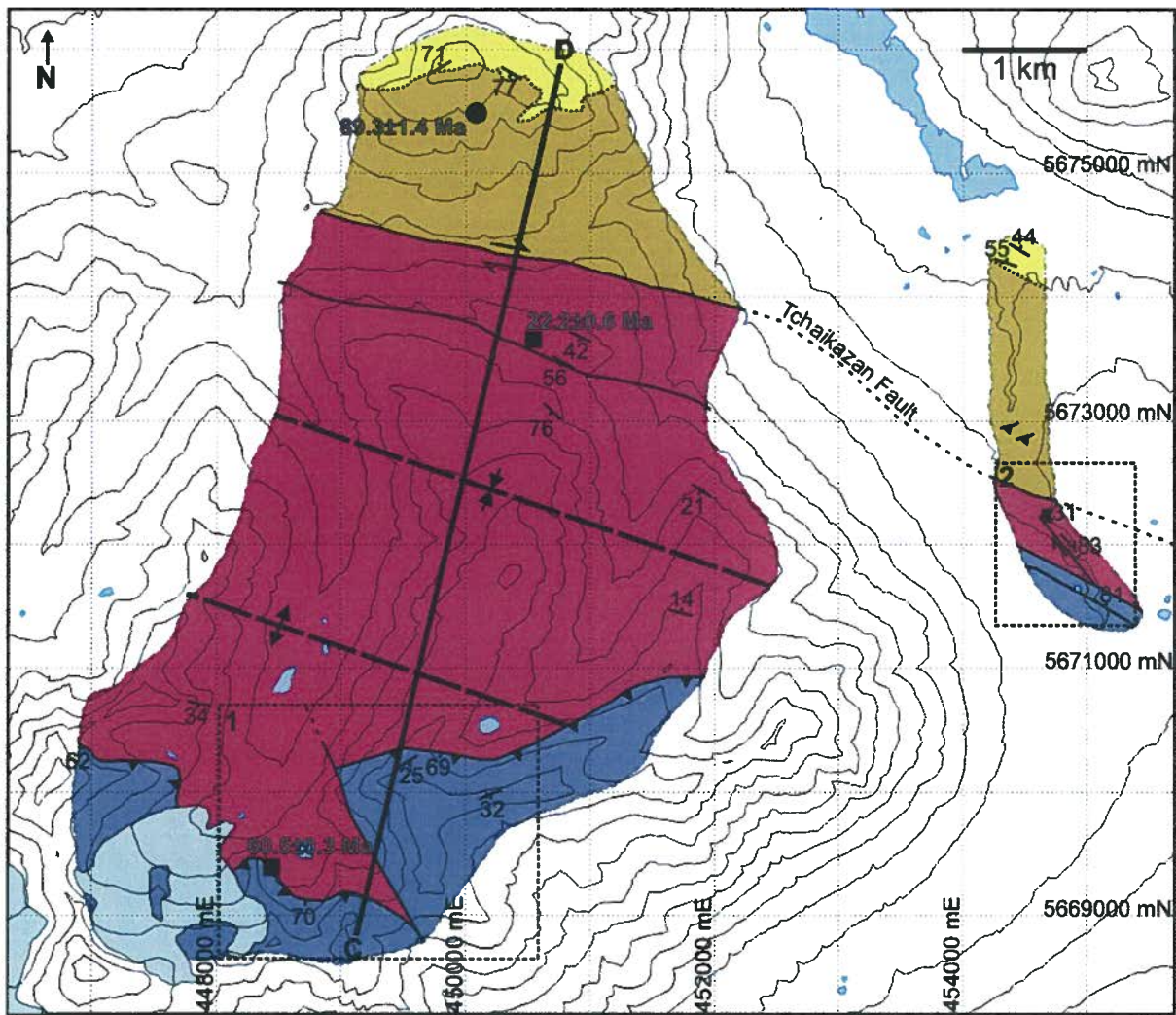


Figure 2.6 (cont'd) G) Felsic to intermediate volcanic breccia with compositionally similar clasts and matrix. H) Plane-polarized light photomicrograph of an intermediate volcanic granular to pebble breccia (field of view = 3.9mm). I) Cross-polarized light photomicrograph of a medium grained, quartz-feldspathic wacke of the Taylor Creek Group (field of view = 7.8mm). J) Interbeds sandstone-siltstone in the Taylor Creek Group. K) Intermediate, volcanic boulder conglomerate showing differential weathering between clasts and matrix. L) Intermediate volcanic conglomerate exhibiting no differential weathering between clasts and matrix. Abbreviations: Fsp = feldspar, Qtz = quartz, ss = siltstone, sst = sandstone.



Lithologic Units		Map Symbols
<b>Stratigraphic Units</b>	<b>Intrusive Units</b>	\ bedding — observed fault - - inferred fault ..... contact --- axial trace - - - extent of mapping area - - - bedding (in x-section)
■ Powell Creek Formation (Late Cretaceous) ■ Taylor Creek Group (Late Cretaceous) Tchaikazan River Succession (Early Cretaceous) ■ volcanic facies	■ Tchaikazan Rapids pluton (Late Cretaceous)	
<b>Geochronological samples</b>		
	● U-Pb sample ■ Ar-Ar sample	

Figure 2.7 Geologic map and cross-section of the Northwest Copper and Tchaikazan Valley areas. The location of the cross section is indicated by line CD on the map. Box 1 indicates the location of the map shown in Figure 2.15 and box 2 indicates the location of the map shown in Figure 2.14. Locations and ages of geochronological samples from this study are indicated. UTM coordinates are in NAD 83 Zone 10. (contour interval = 100 m). Mapping was aided by previous work from Israel et al. (2006).

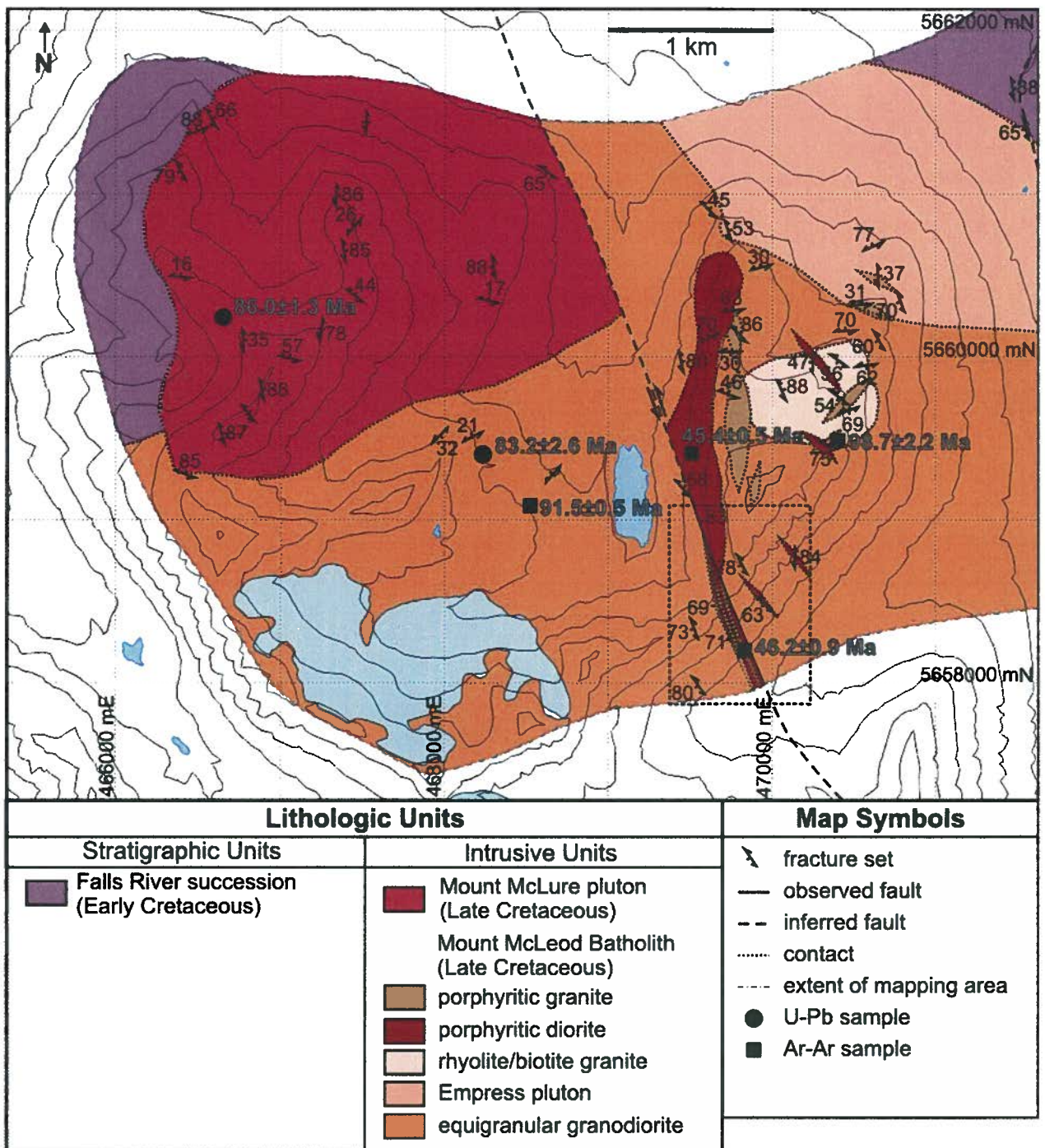


Figure 2.8 Geologic map of the Mount McLure area. The dashed box indicates the location of the map shown in Figure 2.13. Locations and ages of geochronological samples from this study are indicated. UTM coordinates are in NAD 83 Zone 10. (contour interval = 100 m)

Table 2.1 Summary of geochronological age dates

Sample	Property	Dating Method	Description	Mineral Separate	Age±2σ (Ma)	Age type
Northwest						
06-SB-GEO-2	Copper	U-Pb	Tchaikazan Rapids pluton	zircon	89.3±1.4	concordant
07-SB-GEO-09	Mount McLure	U-Pb	Mount McLeod granodiorite	zircon	83.2±2.6	concordant
07-SB-GEO-02	Mount McLure	U-Pb	porphyritic granite	zircon	87.0 ± 1.4	concordant
07-SB-GEO-08	Mount McLure	U-Pb	Mount McLure pluton	zircon	86.0 ± 1.3	concordant
07-SB-073	Mt. McLure	<sup>40</sup> Ar- <sup>39</sup> Ar	rhyolite dyke cutting granodiorite	biotite	91.45±0.51	plateau
			porphyritic biotite-hornblende granite	biotite	98.7±2.2	plateau
07-SB-158	Mt. McLure	<sup>40</sup> Ar- <sup>39</sup> Ar		biotite	98.7±2.2	plateau
07-SB-093	Mt. McLure	<sup>40</sup> Ar- <sup>39</sup> Ar	Mount McLure pluton	hornblende	45.37±0.49	plateau
06-SB-243	Twin Creeks	<sup>40</sup> Ar- <sup>39</sup> Ar	andesite dike	hornblende	65.07±0.93	plateau
Northwest						
06-SB-119	Copper	<sup>40</sup> Ar- <sup>39</sup> Ar	hornblende phyrlic dike	hornblende	22.19±0.59	plateau
Twin Creeks						
06-SB-025-1	Twin Creeks	<sup>40</sup> Ar- <sup>39</sup> Ar	sinistral shear zone (D1)	biotite	88.96±0.6	plateau
06-SB-025-1	Twin Creeks	<sup>40</sup> Ar- <sup>39</sup> Ar	sinistral shear zone (D1)	illite	88.15±0.57	plateau
06-SB-030	Twin Creeks	<sup>40</sup> Ar- <sup>39</sup> Ar	sinistral shear zone (D1)	biotite	91.98±0.75	plateau
06-SB-030	Twin Creeks	<sup>40</sup> Ar- <sup>39</sup> Ar	sinistral shear zone (D1)	muscovite	96.77±0.92	plateau
07-SB-102-1	Mt. McLure	<sup>40</sup> Ar- <sup>39</sup> Ar	Mount McLure fault	illite	46.24±0.87	inverse isochron
Northwest						
06-SB-082-4	Copper	<sup>40</sup> Ar- <sup>39</sup> Ar	thrust fault (D2)	illite	60.53±0.33	plateau

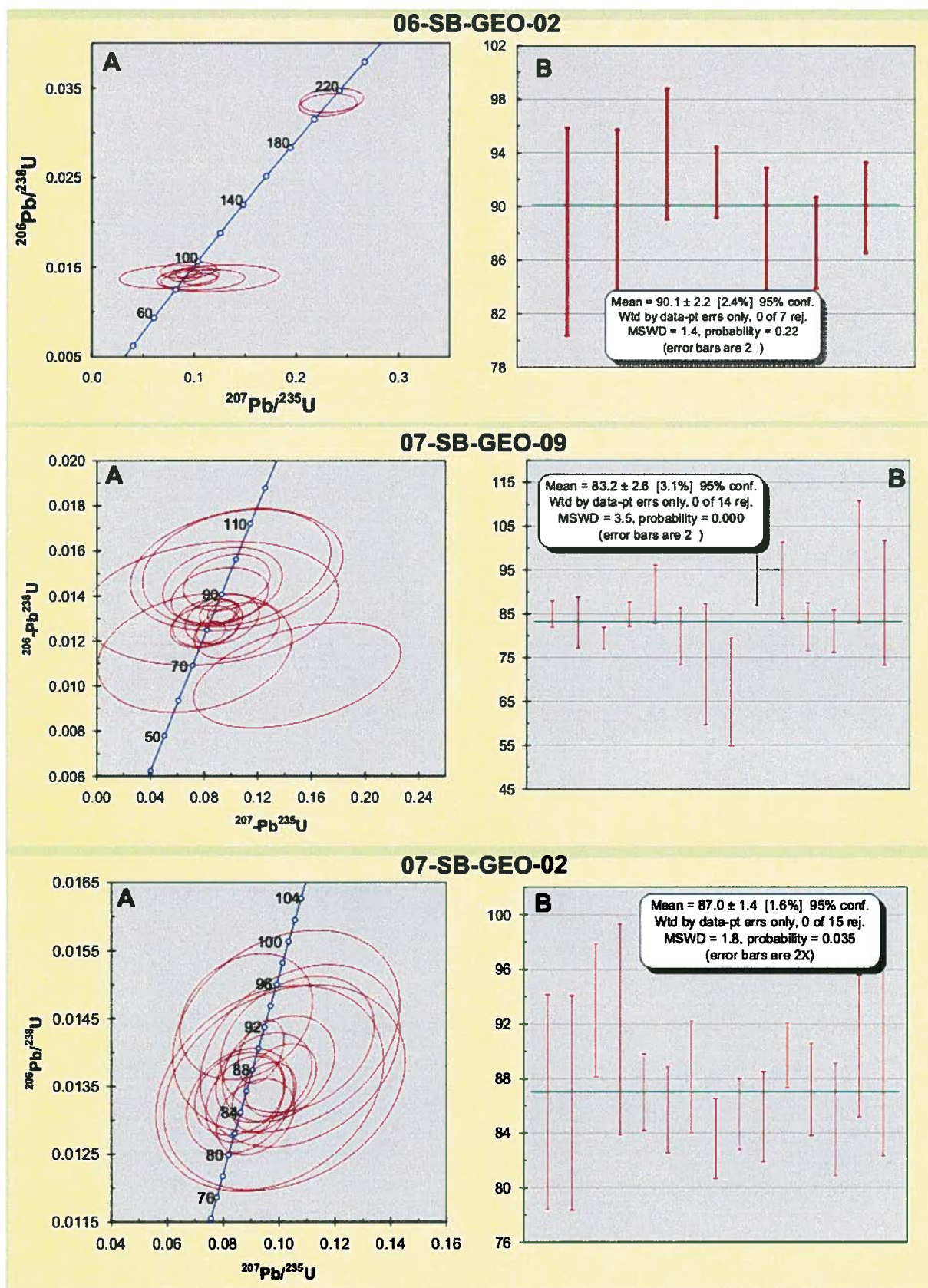


Figure 2.9 U-Pb data for samples indicated showing: A) U-Pb Concordia plots for zircon analysis (data presented in appendix and data point ellipses are  $2\sigma$ ) Ellipses represent the statistical 'concordia age' as calculated by ISOPLOT. The black line with white circles represents the Concordia curve with time (Ma) markers. B) Weighted average plots. Plots, ages, and errors were calculated using the ISOPLOT program of Ludwig (2003).

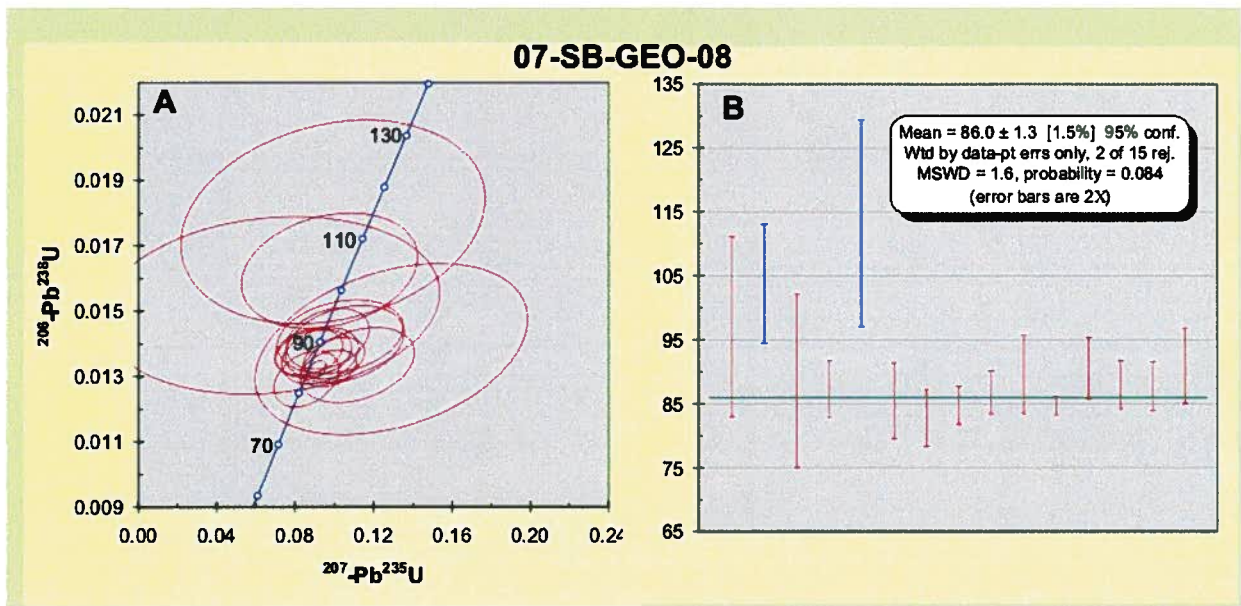
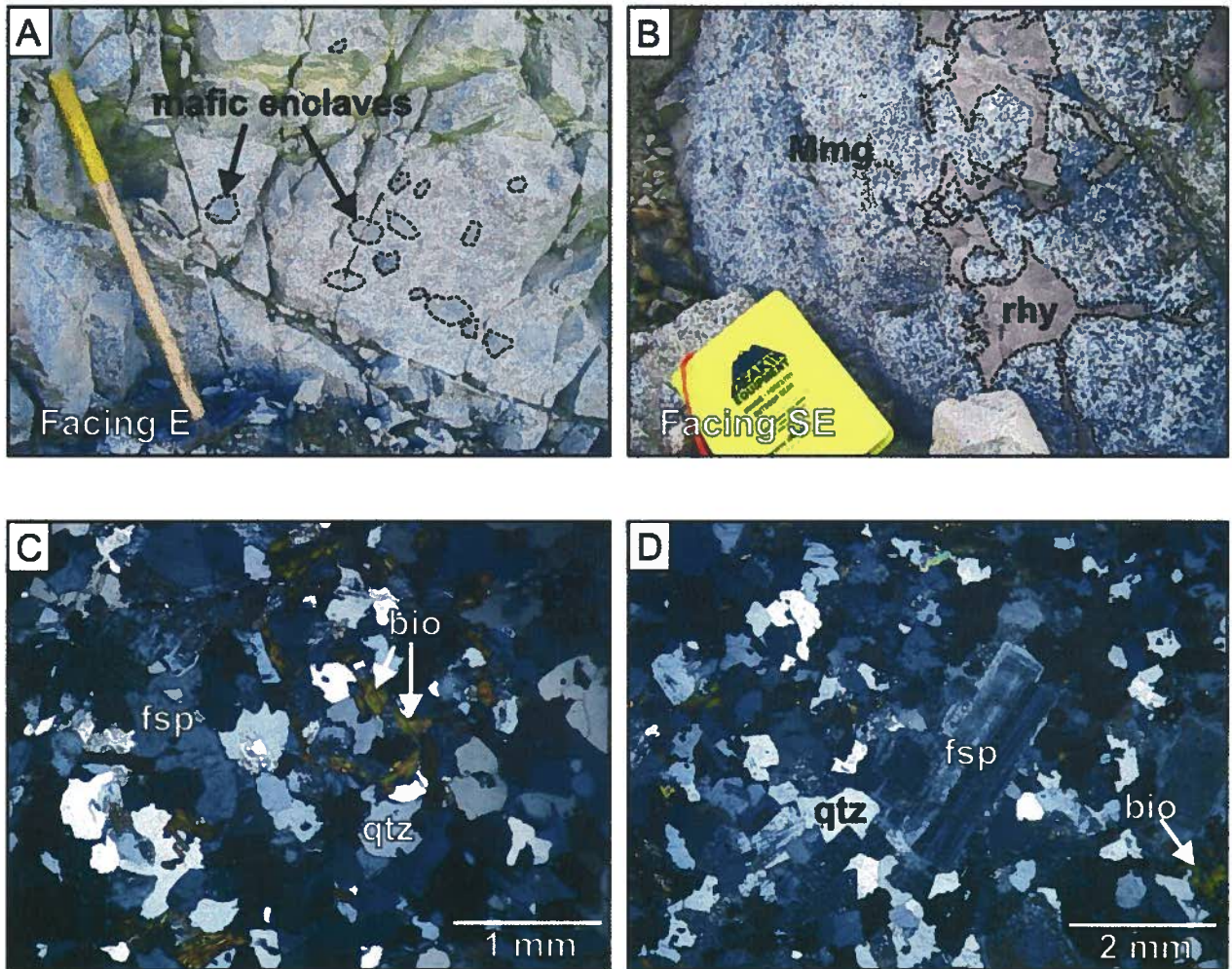
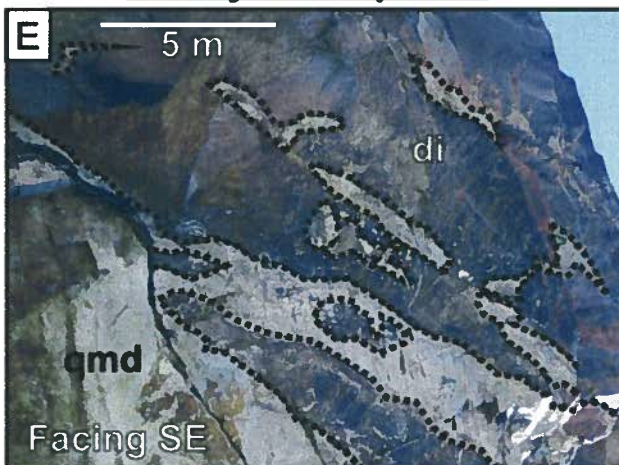


Figure 2.9 U-Pb data for samples indicated showing: A) U-Pb Concordia plots for zircon analysis (data presented in appendix and data point ellipses are  $2\sigma$ ) Ellipses represent the statistical 'concordia age' as calculated by ISOPLOT. The black line with white circles represents the Concordia curve with time (Ma) markers. B) Weighted average plots. Plots, ages, and errors were calculated using the ISOPLOT program of Ludwig (2003).

## Mount McLeod Batholith



### Grizzly Cabin pluton



### Tchaikazan Rapids pluton

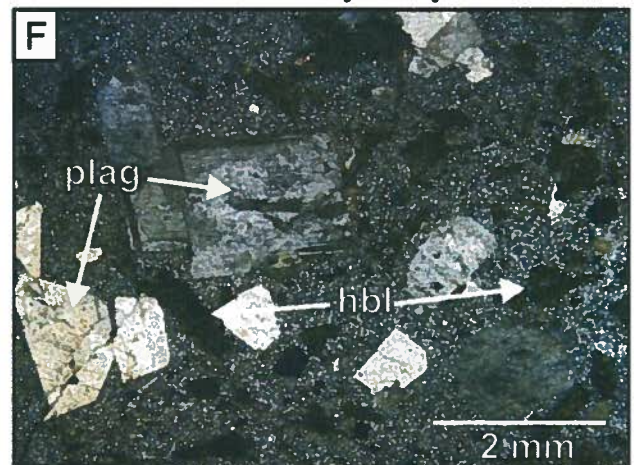
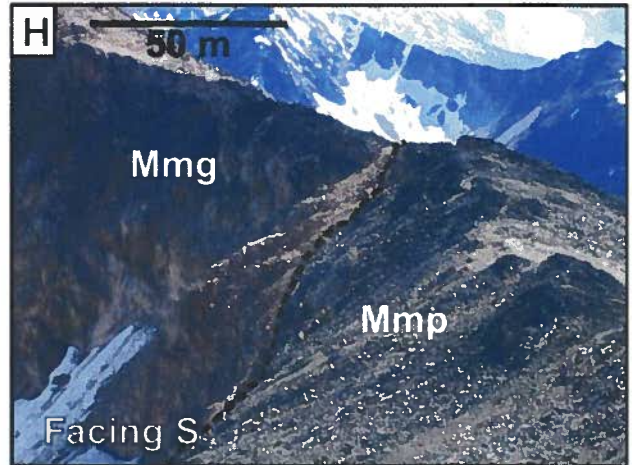
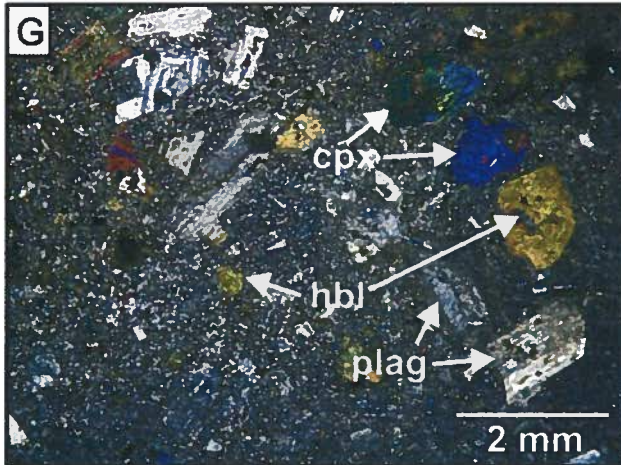
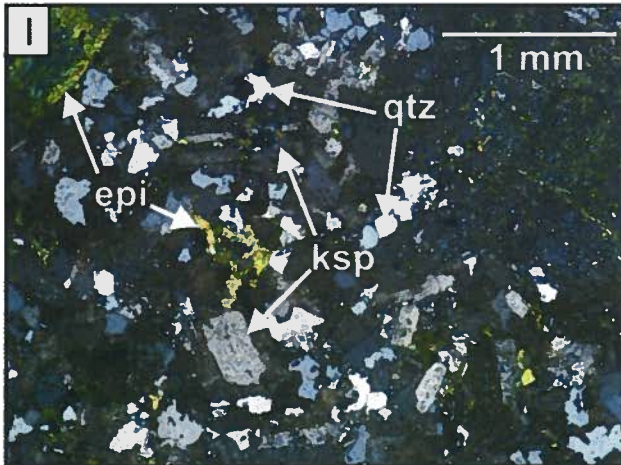


Figure 2.10 Photoplate of the intrusive lithologies of the Taseko Lakes Region: A) Cobble-sized mafic enclaves within equigranular granodiorite. B) Equigranular rhyolite (rhy) brecciating the Mount McLeod granodiorite (MMg) proximal to their contact. C) Cross-polarized light photomicrograph of a fine grained, equigranular biotite rhyolite dike from within the Mount McLeod granodiorite (field of view = 3.9 mm). D) Cross-polarized light photomicrograph of the slightly porphyritic biotite granite (field of view = 7.8mm). E) Cliff face of the Grizzly Cabin Pluton showing intermingling layers of separate intermediate intrusive lithologies. F) Cross-polarized light photomicrograph of a plagioclase-hornblende porphyry of the Tchaikazan Rapids Pluton (note: chlorite has replaced much of the hornblende) (field of view = 7.8mm). Abbreviations: bio = biotite, di = diorite, fsp = feldspar, hbl = hornblende, MMg = Mount McLeod granodiorite, qmd = quartz monzodiorite, qtz = quartz, plag = plagioclase, rhy = rhyolite.

## Mount McLure pluton



## Northwest Copper pluton



## dikes

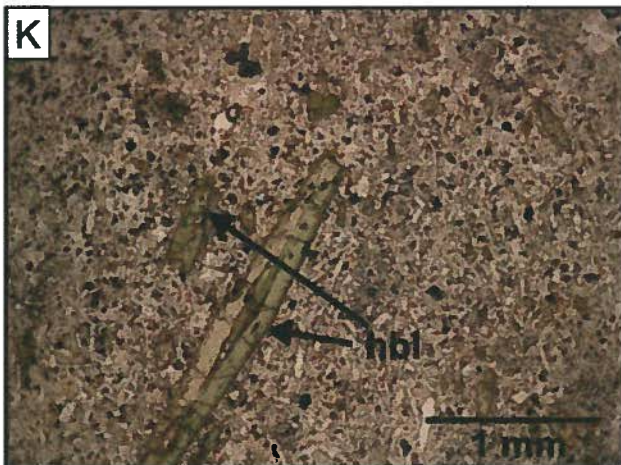


Figure 2.10 (cont'd) G) Cross-polarized light photomicrograph of the porphyritic plagioclase-clinopyroxene-hornblende diorite of the Mount McLure pluton (field of view = 7.8mm). H) Contact between the Mount McLure pluton (bottom) and the Mount McLeod granodiorite (top). I) Cross-polarized light photomicrograph of an epidote altered, medium-grained quartz-alkali feldspar syenite from the Northwest Copper Pluton (field of view = 3.9mm). J) Boulders of highly-clay altered Northwest Copper Pluton quartz-alkali feldspar syenite. K) Plane-polarized light photomicrograph of a plagioclase-clinopyroxene-hornblende phyrlic andesite dike that cross-cuts the Powell Creek Formation (field of view 3.9mm). Abbreviations: bio = biotite, cpx = clinopyroxene, epi = epidote, hbl = hornblende, Mmg = Mount McLeod granodiorite, Mmp = Mount McLure pluton, Plag = plagioclase, Qtz = quartz.

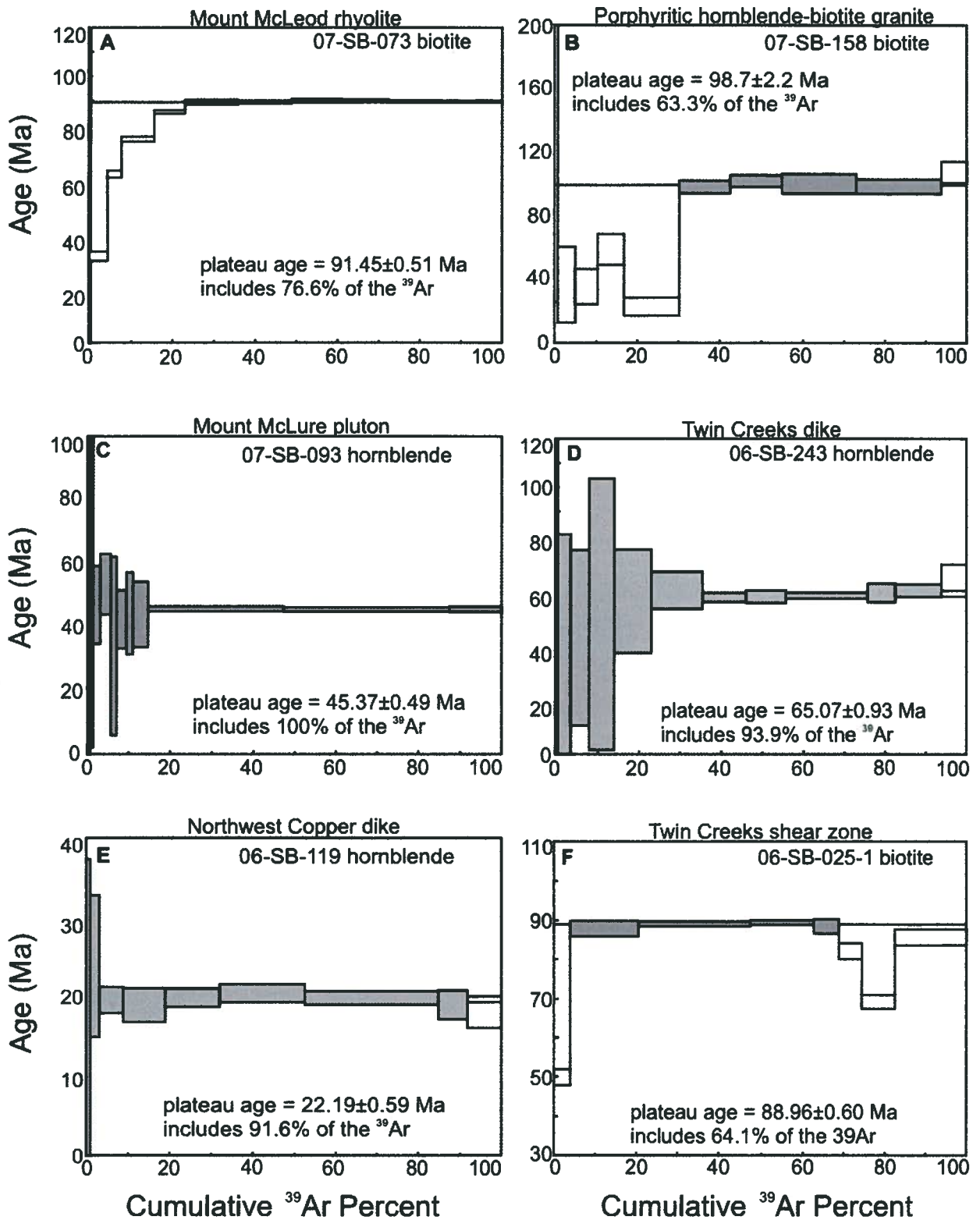


Figure 2.11 A) to F)  $^{40}\text{Ar}$ - $^{39}\text{Ar}$  geochronology from the Taseko Lakes Region. The grey shaded boxes are included in the age calculation while the white boxes are rejected steps. Errors in box heights given at  $2\sigma$ . See text for analytical description and appendix A for complete data set.

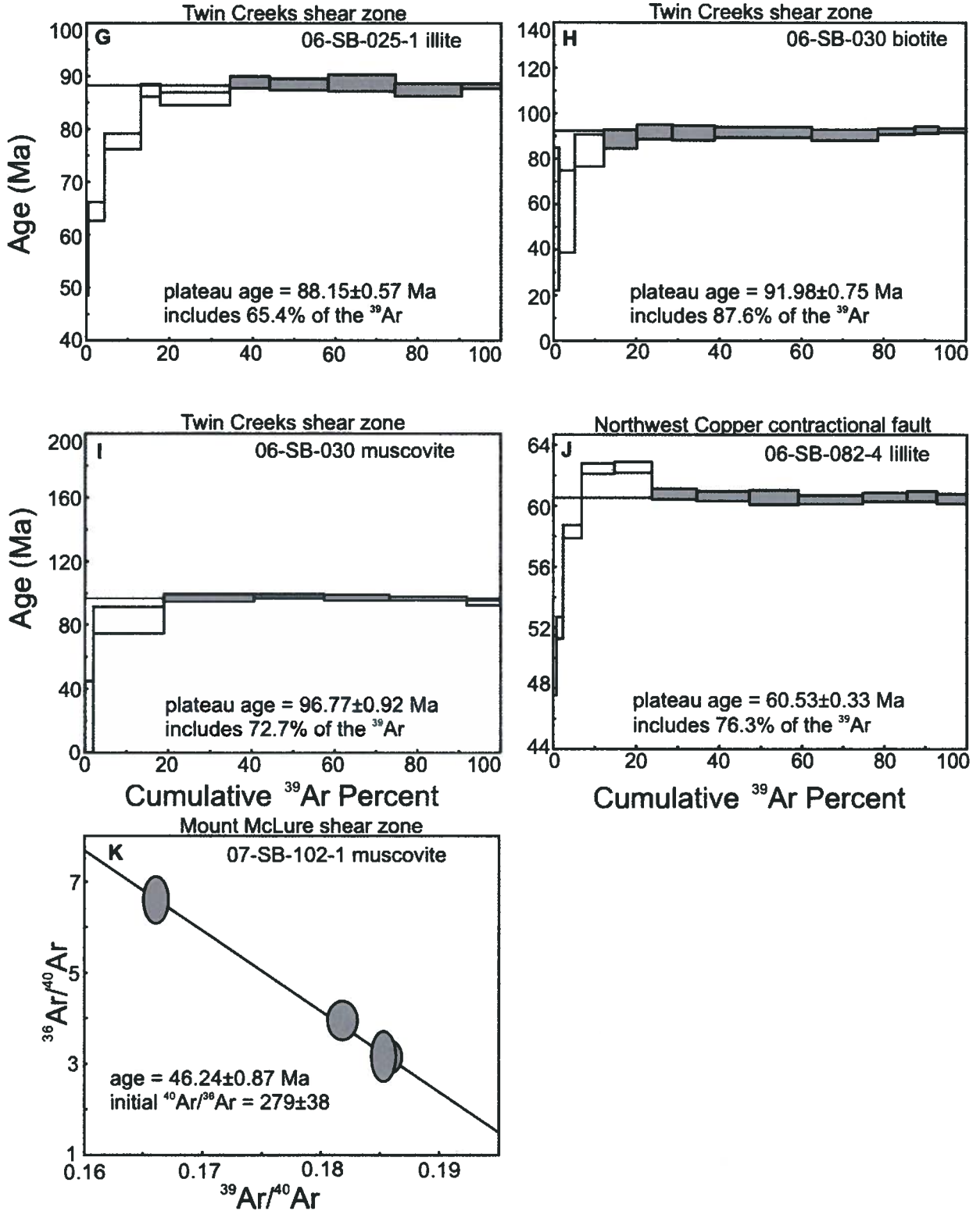


Figure 2.11 (cont'd) G) to J)  $^{40}\text{Ar}$ - $^{39}\text{Ar}$  geochronology from the Taseko Lakes Region. The grey shaded boxes are included in the age calculation while the white boxes are rejected steps. Errors in box heights given at  $2\sigma$ . K) Inverse isochron plot for  $^{40}\text{Ar}$ - $^{39}\text{Ar}$  geochronology data. Data point error ellipses are  $2\sigma$ . See text for analytical description and appendix A for complete data set.

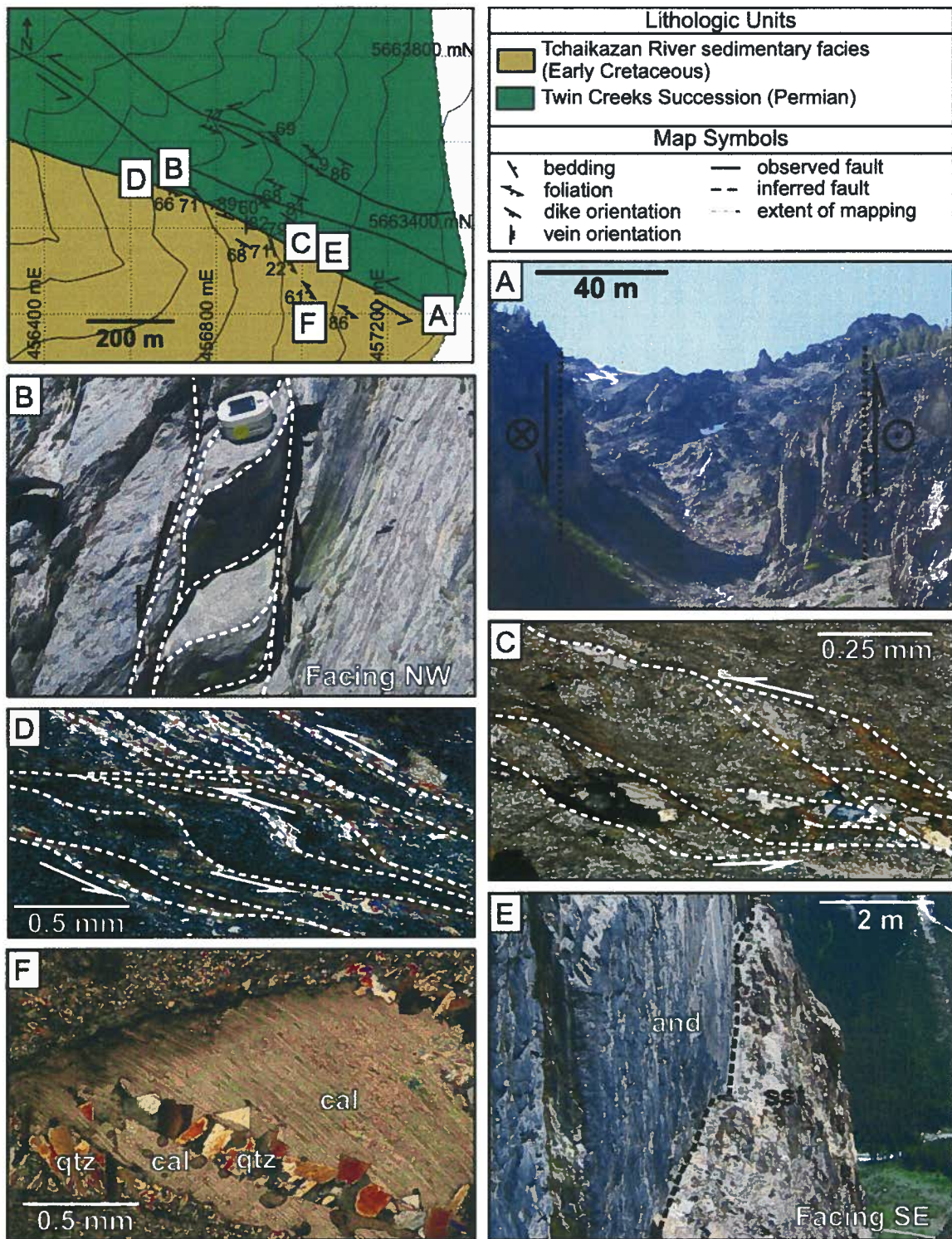


Figure 2.12 Geologic map of the Twin Creeks sinistral-reverse shear zones (location indicated by dashed box on Figure 2.5) showing locations of indicated photographs: A) View of the shear zone from below showing the approximate boundary of the shear zone and the interpreted sense of movement. B) Shear fabrics in outcrop indicating sinistral-reverse shear-sense. C) Cross-polarized light photomicrograph of micaceous shear fabrics cutting through quartz-clay dominated host rock, indicating top-left shear-sense. Section is oriented in the 210/90 plane, therefore the top-left shear sense corresponds to right-side up dip-slip deformation on the fault. D) Cross-polarized light photomicrograph of micaceous shear fabrics cutting through clay-carbonate dominated host rock, indicating top-left shear-sense. Section is oriented in the 300/03 plane, therefore the top-left shear sense corresponds to sinistral strike-slip deformation on the fault. E) contact between coherent, less deformed andesite (left) and more deformed clastic sedimentary rocks (right). F) Cross-polarized light photomicrograph showing a composite quartz-calcite vein (field of view = 2.0mm). Abbreviations: and = andesite, cal = calcite, qtz = quartz, sst = sandstone/siltstone.

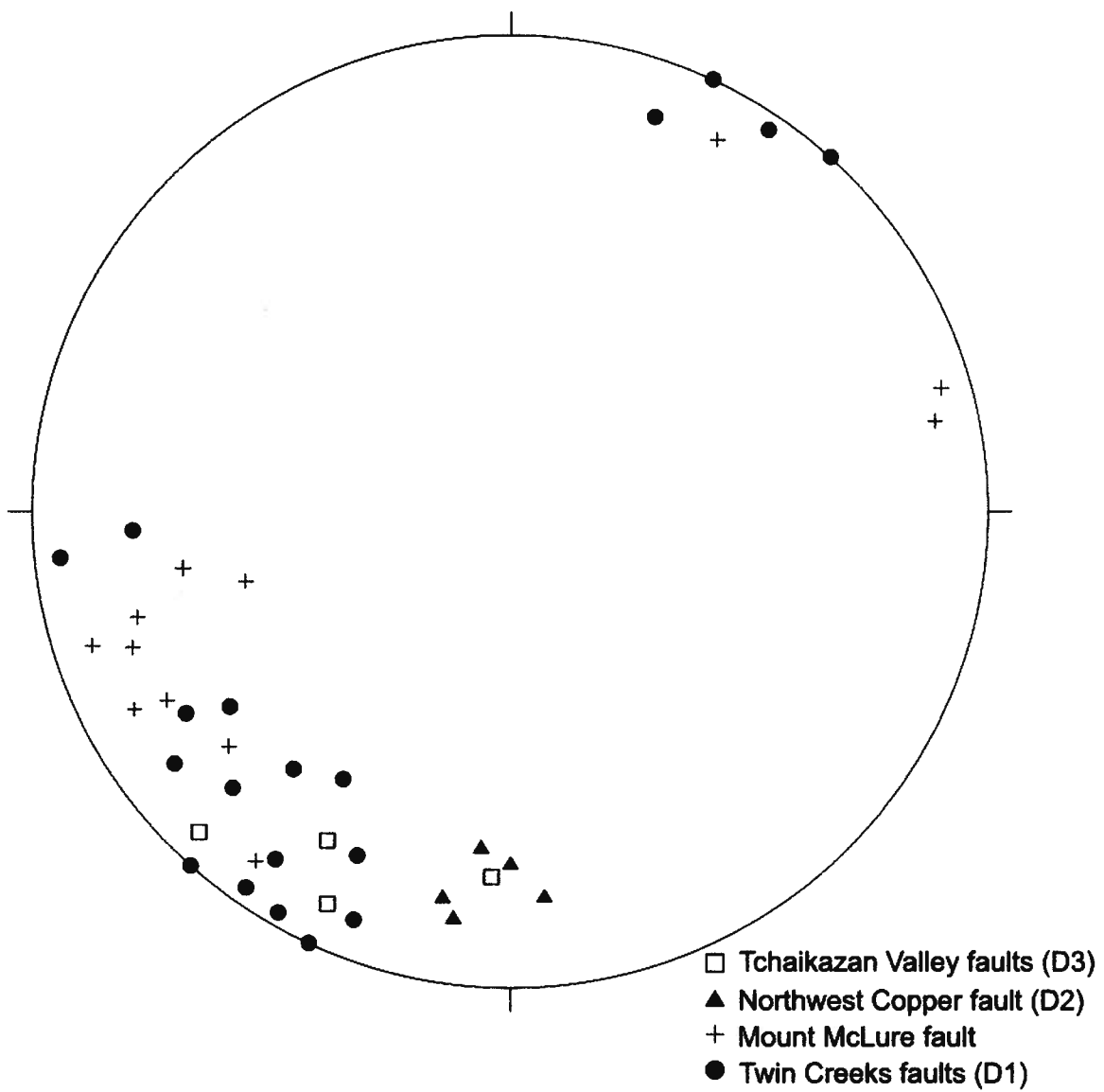


Figure 2.13 Equal-area, lower hemisphere stereonet plot showing orientations of poles to foliations from selected fault zones indicated in the Taseko Lakes Region.

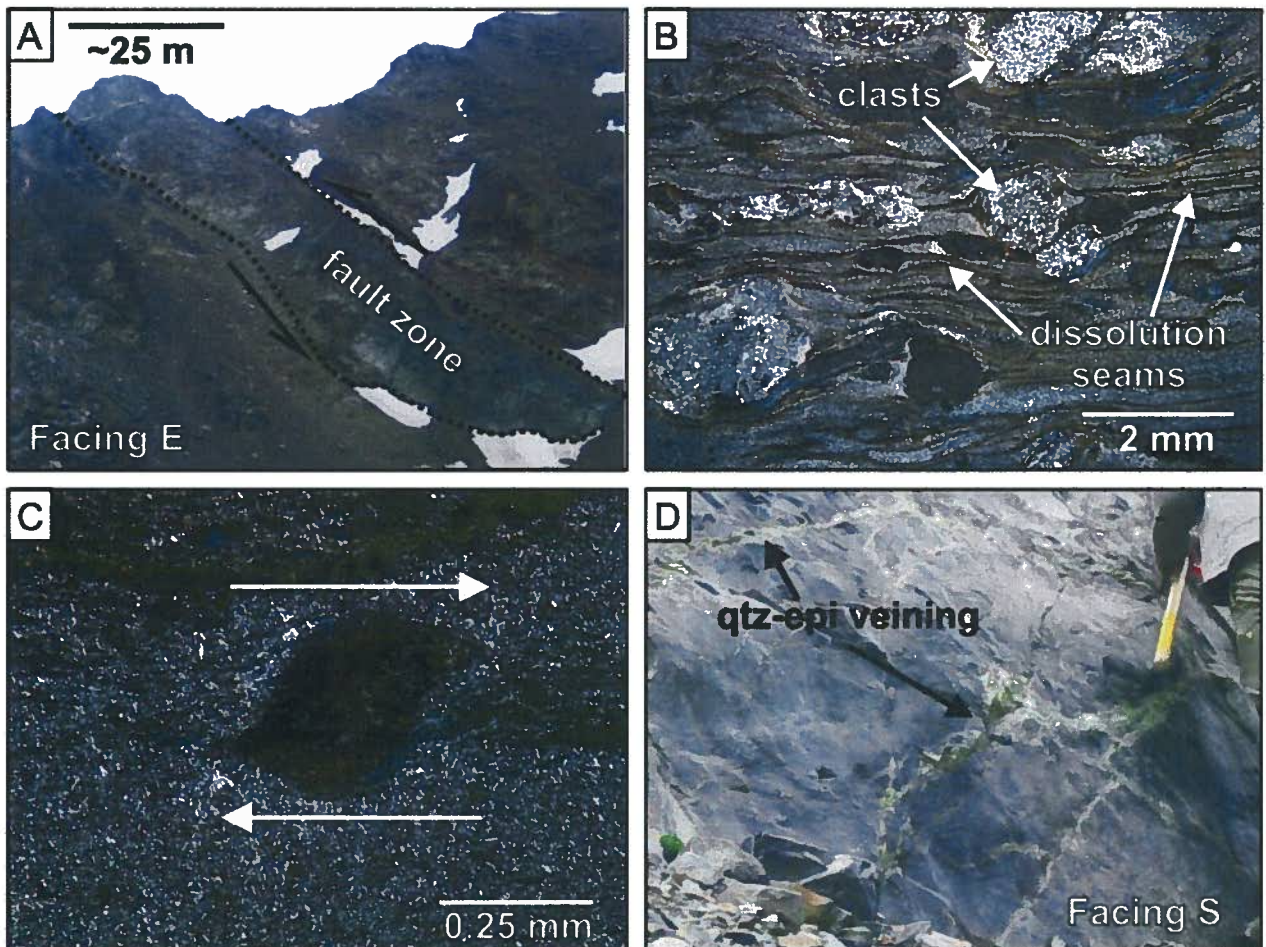
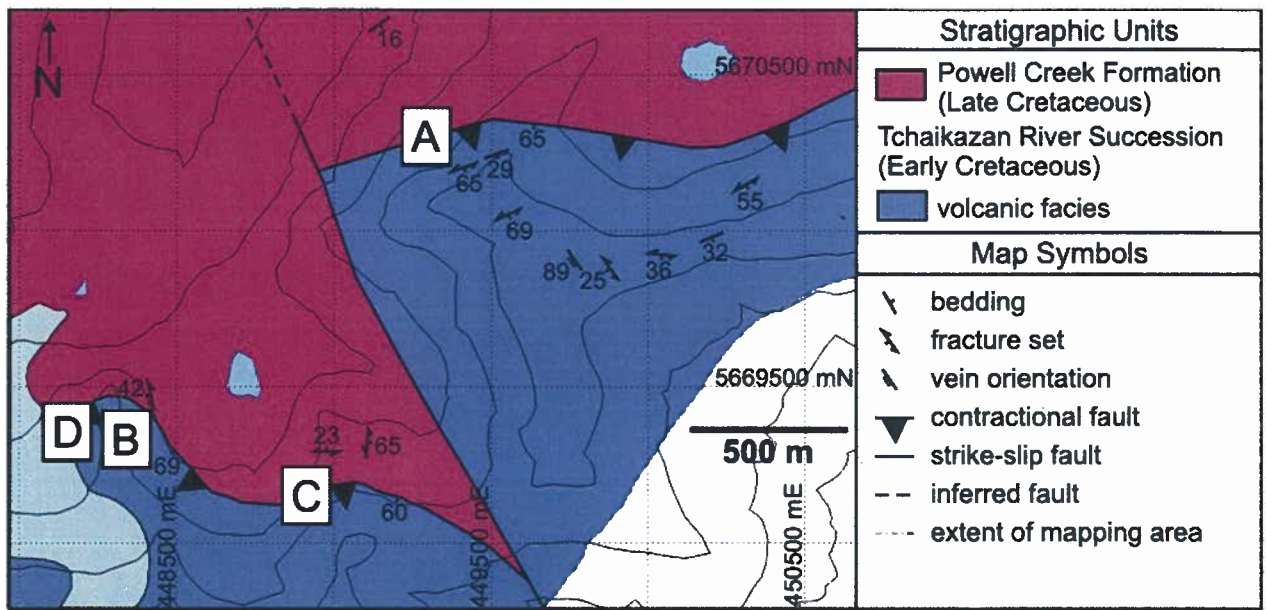
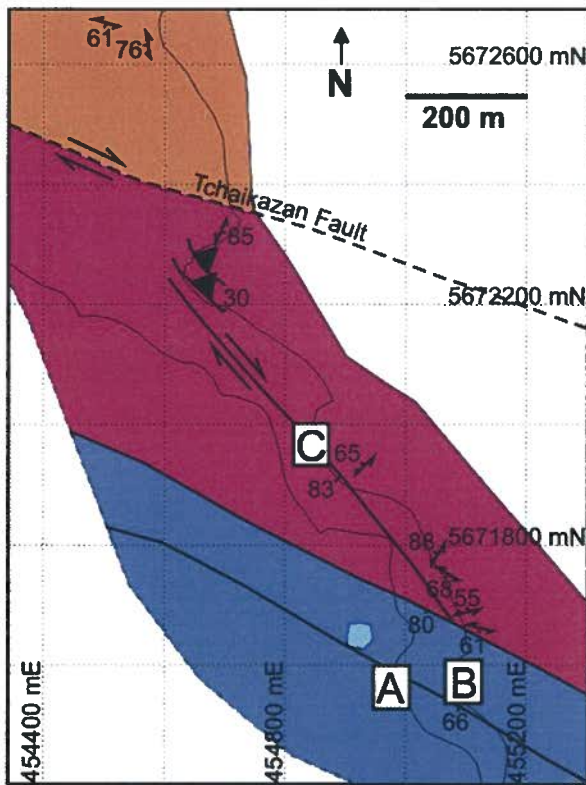


Figure 2.14 Geologic map showing locations of the photographs of the main contractional fault in the Northwest Copper Area: A) View of the thrust fault from below showing the approximate location of the fault and the interpreted sense of movement. B) Cross-polarized light photomicrograph of the mylonite in the fault showing shear bands, dissolution seams and rotated clasts (field of view = 7.8mm). C) Cross-polarized light photomicrograph of a sheared porphyroblast within the mylonite showing a top-side right sense of movement in the plane of the section, equating to contractional deformation on the fault (orientation: 005/90, field of view = 1.0mm). D) Stockwork quartz-epidote-pyrite veining in the hanging wall of the thrust fault. Abbreviations: epi = epidote, qtz = quartz.



Stratigraphic Units	
	Powell Creek Formation (Late Cretaceous)
	Tchaikazan River Succession (Early Cretaceous)
	volcanic facies
Intrusive Units	
	Tchaikazan Rapids pluton (Late Cretaceous)
Map Symbols	
	fracture set
	observed fault
	inferred fault
	extent of mapping area

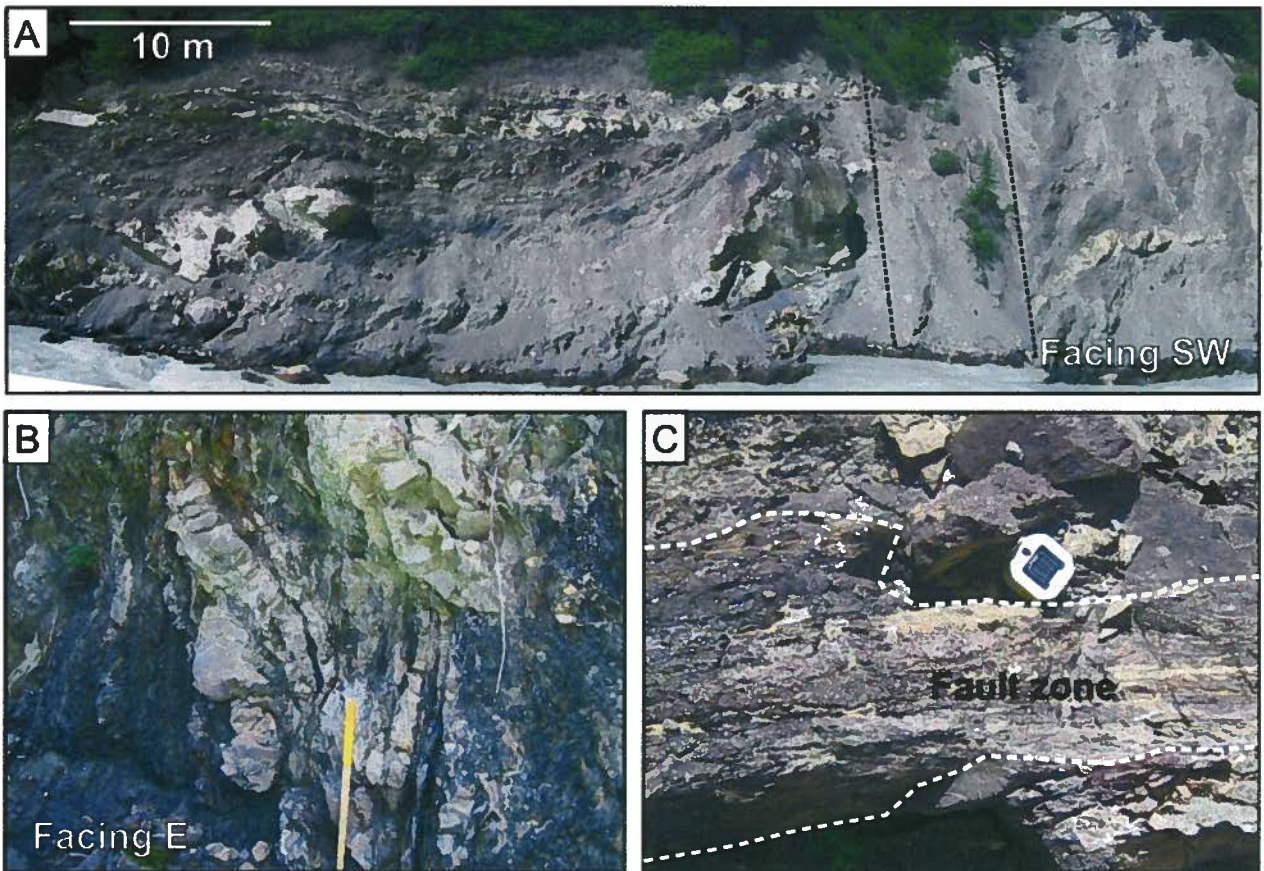
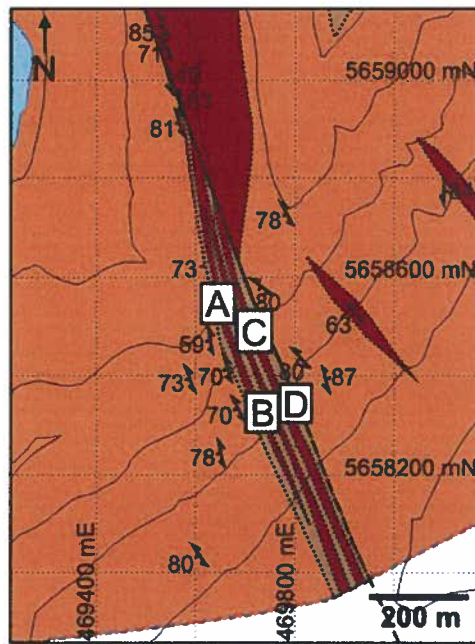


Figure 2.15 Geologic map showing locations of the photographs of the dextral faults in the Tchaikazan Valley Area: A) View of one of the main faults in the Tchaikazan Valley area. B) A rubbly outcrop characteristic of faults formed during the D3 event. C) A small, possibly antithetic fault of the larger-scale WNW trending faults in the area.



Intrusive Units	
Mount McLeod Batholith (Early Cretaceous)	
	porphyritic granite
	porphyritic diorite
	equigranular granodiorite
Map Symbols	
	foliation
	observed fault
	inferred fault
	contact
	extent of mapping area

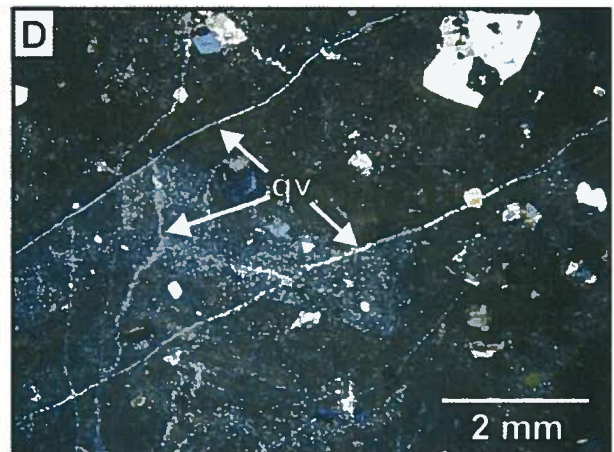
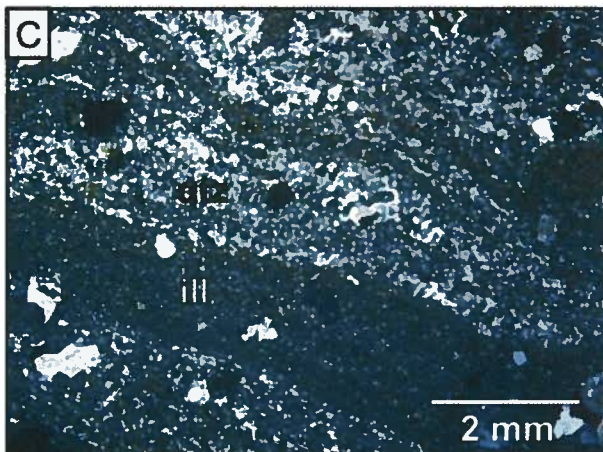


Figure 2.16 Geologic map of the Mount McLure area (location indicated by dashed box on Figure 2.8) showing locations of fault zone photographs: A) Contact between a silicified, sheared, quartz-phyric unit (sqp) and porphyritic biotite-hornblende granite (pbg). B) Well developed, slightly folded foliations within the silicified quartz-phyric unit. C) Cross-polarized light photomicrograph showing layering of quartz-rich and illite-rich layers within the silicified quartz-phyric unit (section orientation = 282/18; field of view = 2.0mm). D) Cross-polarized light photomicrograph multiple generations of quartz veins cutting quartz-illite layering (orientation = 354/90; field of view = 2.0mm). Abbreviations: ill = illite, pbg = porphyritic biotite-hornblende granite, qtz = quartz, qv = quartz vein, sqp = silicified quartz-phyric unit.

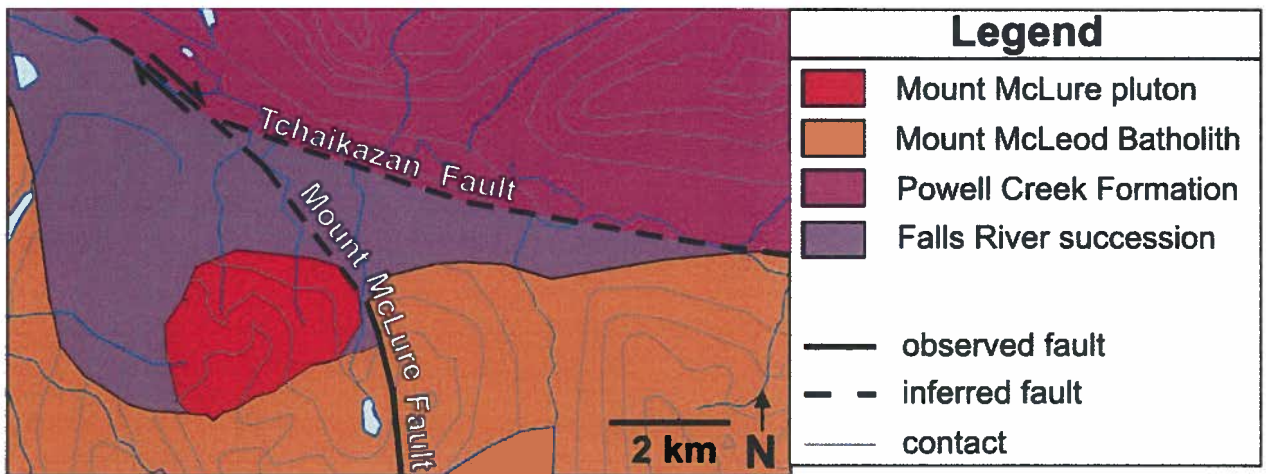
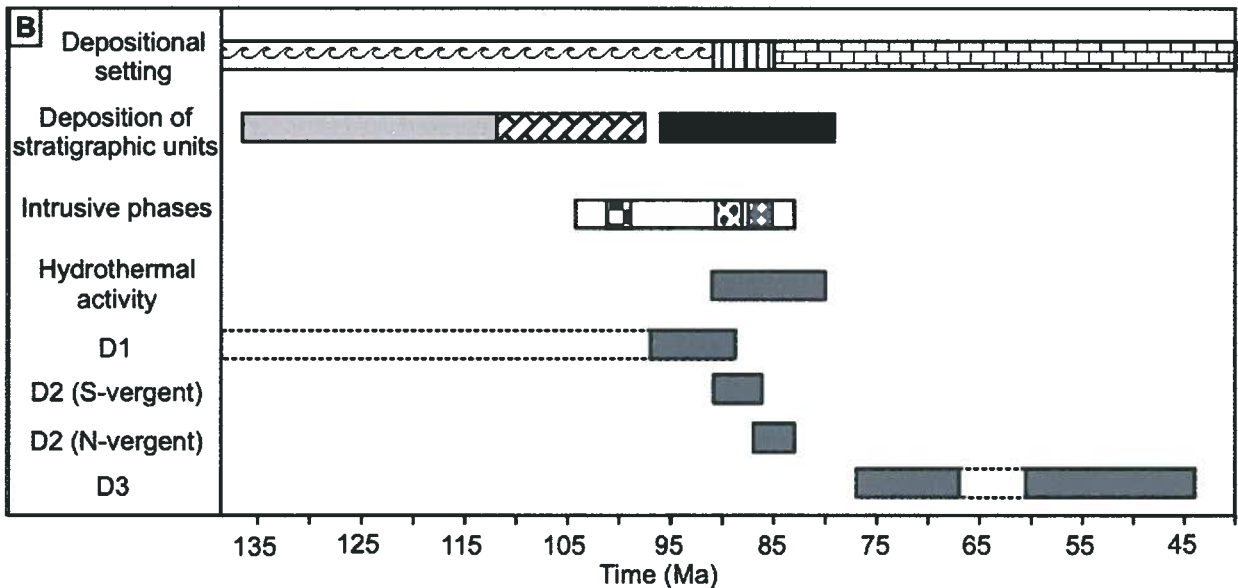
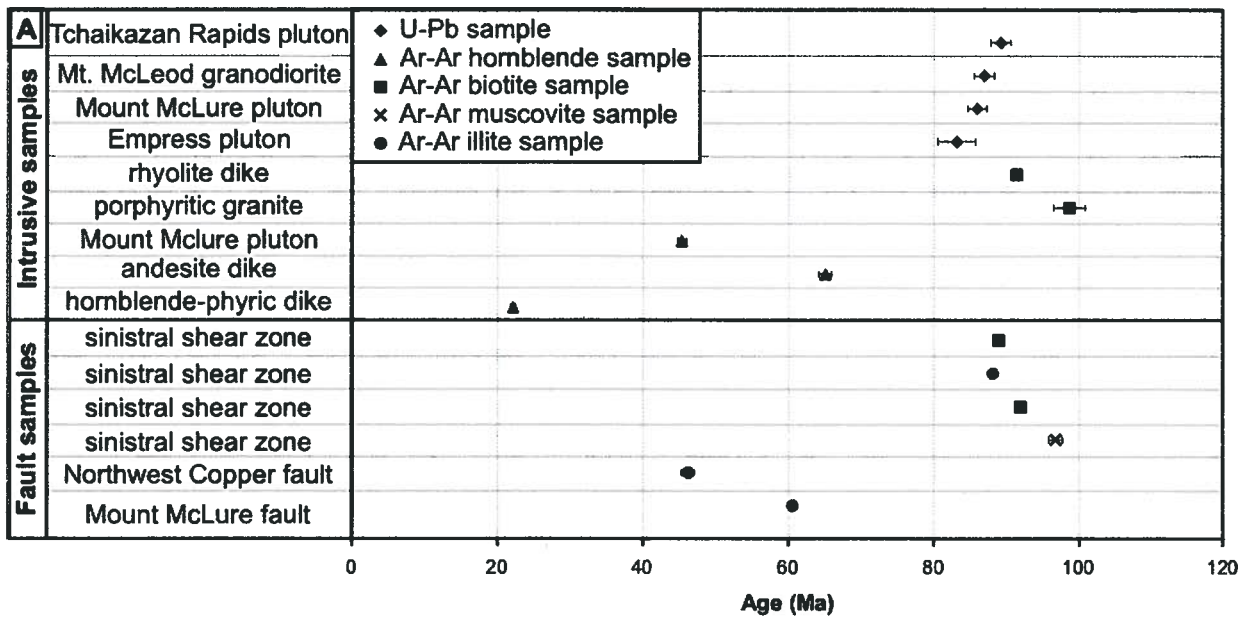


Figure 2.17 Cartoon illustrating the interpreted geometry Mount McLure-Tchaikazan Fault system in the Mount McLure area.



depositional settings	stratigraphic units	intrusive phases
submarine	Tchaikazan and Falls River successions	Mount McLeod Batholith
coastal	Taylor Creek Group	Grizzly Cabin pluton
subaerial	Powell Creek Formation	Tchaikazan Rapids pluton
		Mount McLure pluton

Figure 2.18 A) Summary of geochronological age data. (2 $\sigma$  error bars included). B) A summary of the interpreted ages of stratigraphic deposition, intrusive phases, hydrothermal alteration events (see chapter III) and D1 (sinistral), D2 (contractional) and D3 (dextral) deformational phases in the Taseko Lakes Region. (Ages after this study and Leitch et al., 1991; Rusmore and Woodsworth, 1994; Schiarizza et al., 1997; Israel et al., 2006)

## CHAPTER III

# GEOLOGIC FRAMEWORK FOR LATE CRETACEOUS MAGMATIC-HYDROTHERMAL MINERALIZATION IN THE TASEKO LAKES REGION, SOUTHWESTERN BRITISH COLUMBIA

### 3.1 INTRODUCTION

The Coast Plutonic Complex (CPC) is a massive, chain of overlapping batholith located along the western margin of the Canadian Cordillera. The CPC is interpreted to have formed as a result of the subduction of oceanic crust beneath the western margin of North America from approximately 90 to 45 Ma (Rusmore and Woodsworth, 1991a; Schiarizza et al., 1997; Symons et al., 2000). Many porphyry and epithermal deposits occur along the margins of the CPC.

The Southeast Coast Belt (SECB) is situated on the eastern margin of the CPC in the southern Canadian Cordillera. The SECB hosts several prospective and past-producing mineral deposits, including the Bralorne Mining District and Prosperity deposits. All mineralization previously studied in the region is hydrothermal in origin, and includes porphyry, epithermal and mesothermal styles of mineralization.

The Taseko Lakes Region straddles the boundary between the CPC and the SECB (Jeletzky and Tipper, 1968; Schiarizza et al., 1997) (Figure 3.1). Several smaller and less developed mineral occurrences are present in the vicinity of Taseko Lakes, close to the contact between the CPC and SECB (Figure 3.2) (McLaren, 1990). These occurrences are all hydrothermal in origin and include the Hub, Northwest Copper, Charlie, Pellaire, Taseko-Empress (from here onwards referred to as Empress), and Taylor-Windfall.

The origin, characterization and factors governing the occurrence of these deposits are poorly understood and potential connections between the mineral deposits in the region and the CPC have not been explored. It is unclear whether the CPC-SECB plays a fundamental role in the formation of mineral deposits in the region.

The purpose of this study is to characterize the alteration and mineralization of the Pellaire, Empress and Taylor-Windfall deposits. Pressure-temperature-compositional (P-T-X) conditions and sources of hydrothermal fluids responsible for mineralization at the deposits have been determined in order to propose genetic classifications and to better understand the geologic environments in which the deposits formed. Isotopic ages of alteration and lithologies at the

deposits have been attained to better understand the geologic and hydrothermal history of the region. From this data, the Pellaire, Empress and Taylor-Windfall deposits have been placed into geologic context and it is discussed if they could be part of the same magmatic-hydrothermal system, and ultimately places the deposits into context with respect to a larger overall magmatic-hydrothermal system within the geologic framework of the Taseko Lakes Region.

### **3.1.1 Magmatic Hydrothermal Systems**

Porphyry Cu deposits are large, relatively low-grade, epigenetic Cu deposits that are spatially and genetically related to felsic to intermediate porphyritic intrusions (Lowell and Guilbert, 1970; McMillan and Panteleyev, 1988). Alteration is typically characterized by concentric zones of potassic, phyllic, propylitic and overprinting advanced argillic assemblages (Figure 3.3B), with most mineralization occurring within potassic and phyllic zones (Lowell and Guilbert, 1970; Gustafson and Hunt, 1975). Porphyry Cu deposits can be subdivided into oxidized or reduced styles based on the redox state of mineralizing fluids (Rowins, 1999). Oxidized porphyries can be further subdivided into calc-alkalic and alkalic porphyries, based on the geochemistry of the mineralizing intrusion (Barr et al., 1976).

Epithermal deposits form in volcanic environments as a result of circulating hydrothermal fluids (Figure 3.3A; Buchanan, 1981; Hedenquist and Arribas, 1999) and are typically classified as either high sulphidation or low sulphidation systems based on the interpreted chemistry of the mineralizing fluids (White and Hedenquist, 1995). Sulphidation refers to the redox state of sulphur present in the mineralizing fluid (Hedenquist, 1987). Low sulphidation epithermal systems form from geothermal fluids that are relatively distant from a heat source (generally magmatic) to hot-spring types of environments. Mineralizing fluids associated with low-sulphidation epithermal systems are relatively low temperature (~100-250°C), have near neutral pH's and are reduced, with sulphur occurring as H<sub>2</sub>S (White and Hedenquist, 1995). High sulphidation epithermal systems form in proximal, sub-volcanic environments from ascending magmatic fluids (Figure 3.3A, C). These fluids are typically low to moderate temperature (~200-300°C), acidic and oxidized with sulphur occurring as both SO<sub>2</sub> and H<sub>2</sub>S (Hedenquist, 1987; Zhang et al., 1989). Transitional systems also exist between high and low sulphidation systems, and classified as intermediate sulphidation epithermal deposits (Richards, 2007).

Vein-hosted Au deposits encompass all epigenetic, structurally-hosted Au vein systems (Groves et al., 1998). They occur in a wide range of geologic settings in terranes of all ages, and form from a variety of processes. Gold-telluride deposits are an example of vein-hosted gold deposits that occur as sheeted vein systems or open-space filling within mafic breccia bodies (Kelley et al., 1998). Many gold-telluride deposits form from magmatic hydrothermal fluids and may be spatially associated with porphyry systems. Previous studies indicate there may also be genetic links between gold-telluride and porphyry deposits wherein gold-telluride deposits are distal expressions of the central porphyry systems, similar to epithermal systems (Figure 3.3A) (Spry et al., 1996). It is suggested that some gold-telluride deposits form from fluids that have migrated distally along faults from a magmatic source and undergone significant rock buffering with little interaction with external fluids (Alderton and Fallick, 2000). This method of formation is analogous to low-sulphidation epithermal systems, but lacks an external fluid input. However there is evidence that ore deposition occurs when fluids migrate across lithologic contacts, thus disrupting chemical equilibrium (Spry et al., 1996; Alderton and Fallick, 2000). Therefore, boiling is not necessary for ore deposition in these systems and it is not essential that gold-telluride deposits form at shallow (epithermal) depths.

Mesothermal or orogenic Au deposits occur in regional metamorphic terrains and are another example of vein-hosted Au deposits. They form during compressional to transpressional deformation at convergent plate margins in accretionary and collisional orogens (Groves et al. 1998; 2003). Mineralization commonly occurs in quartz veins hosted in contractional faults that cut supracrustal rocks and felsic intrusions (Leitch et al., 1989). Such deposits can form over a wide range of P-T conditions, ranging from 180°C at <100 MPa to 700°C at 500 MPa, and between depths ~2-15 km (Groves et al., 1998). Fluids responsible for mineralization ascend along faults from deeper sources; however debate remains over whether they are metamorphic or magmatic in origin (Boyle, 1979; Jia and Kerrich, 1999; Hart et al., 2008).

Hydrothermal ore deposits, such as those described above, form from the dissolution, transport and re-precipitation of specific elements or chemical species of economic interest (Kesler, 2005; Heinrich, 2007). Genetic links exist between hydrothermal ore deposits based on deposits sharing a common source of fluids or chemical species transported by the fluids. Destabilization of ore-bearing complexes within hydrothermal fluids is the key process required for ore deposition. This destabilization arises from changes in the chemical properties of ore-bearing fluids (Gammons and Williams-Jones, 1997). The chemical properties of hydrothermal fluids are pressure and temperature dependent, thus changes required for ore deposition may

occur due to only cooling or depressurization of a simple fluid phase (Shimizu et al., 1998; Yardley, 2005). However, more commonly there is more than one fluid phase present in a hydrothermal system. Reactions between hydrothermal fluids and wall rocks also commonly occur in hydrothermal systems. Such processes may also aid ore deposition depending on the compositions and physical properties of the host rocks in hydrothermal systems. Interaction between hydrothermal fluids may be classified under two broad processes: mixing of contrasting fluids, or separation of immiscible fluid phases (boiling). Both these processes act as driving mechanisms for precipitation of ore minerals and selective enrichment of specific elements (Heinrich, 2007).

Magmatic-hydrothermal systems develop from the exsolution of hydrothermal fluids of fluids during the emplacement of felsic to intermediate magmas at shallow crustal levels. These magmas develop from the partial melting of the crust due to subduction processes. Therefore porphyry and some epithermal systems (mainly high-sulphidation systems) typically form adjacent to subduction zones in subvolcanic environments. When porphyry and epithermal systems intersect, epithermal-style alteration and mineralization typically overprints porphyry-style mineralization (Williams-Jones and Heinrich, 2005). However, examples exist where spatially associated porphyry and epithermal systems were active synchronously (Arribas et al., 1995). Exposed porphyry-epithermal systems indicate that these hydrothermal systems may continue over a depth interval of >6km (Dilles and Einaudi, 1992). Evidence from previous studies suggests that gold-telluride deposits may be distal expressions of porphyry-epithermal systems (Spry et al., 1996). Therefore, magmatic-hydrothermal systems can be thought of as overall systems that may contain porphyry, low-sulphidation epithermal, high-sulphidation epithermal and gold-telluride deposits (as well as other types of deposits) in specific settings (Figure 3.3). Thus, markedly differing styles of alteration and mineralization may occur in the same overall magmatic-hydrothermal system depending on the proximity to the magmatic source and pre-existing geologic framework. Orogenic Au deposits also occur in orogenic belts, but are linked to compressional deformation during collisional orogens, and may or may not be related to magmatism.

## **3.2 REGIONAL GEOLOGIC SETTING**

### **3.2.1 Major rock units of the Taseko Lakes Region**

The Permian Twin Creeks succession is the only Paleozoic unit in the Taseko Lakes Region. It is interpreted to be part of the basement rocks upon which the nearby Cadwallader and Tyaughton Basins were built (Rusmore and Woodsworth, 1991b; Israel et al., 2006).

Early Cretaceous cover rocks of the Taseko Lakes Region are interpreted to be part of an overlap assemblage between the SWCB and SECB deposited in the western margin of the Tyaughton Basin (Schiarizza et al., 1997; Israel et al., 2006). The Early Cretaceous Tchaikazan River and Falls River successions are composed of submarine coherent, volcanoclastic and sedimentary rocks and are interpreted to be derived from the Gambier Arc to the west. The Taylor Creek Group also exhibits a dominantly submarine depositional history, but contains no primary volcanic units. This suggests little volcanism was active in the proximity of the western Tyaughton basin during the deposition of the Taylor Creek Group (113-97.5 Ma; Garver, 1992). The Taylor Creek Group is also interpreted to have been deposited more distally to the Gambier Arc than the Tchaikazan and Falls River successions.

The Powell Creek Formation has both subaerial (indicated by pyroclastic surge and flow front breccia units) and subaqueous (indicated by rare bedded sedimentary and resedimented volcanic units) depositional characteristics, suggesting a coastal depositional environment typical of many volcanic island arcs. The Powell Creek Formation is the youngest stratigraphic unit (96 to 79 Ma) in the region, indicating that the area emerged from the Tyaughton Basin during the Late Cretaceous, and remained above sea level thereafter. This demonstrates that the Tyaughton-Methow basin was uplifted during contractional deformation from 91 to 85 Ma (Garver, 1989; 1992). Therefore it is expected that it should exhibit both submarine and subaerial characteristics.

Intrusive lithologies in the Taseko Lakes Region are part of the CPC, which formed as a result of the subduction of oceanic crust beneath the western margin of North America during Late Cretaceous to Eocene time (Symons et al., 2000). Miocene dikes in the area are likely linked to Pemberton Arc volcanism (Coish et al., 1998).

### **3.2.2 Structural Geology of the Taseko Lakes Region**

At least three generations of faulting occurred in the Taseko Lakes region, producing three unique styles of faults: D1 sinistral-reverse faults, D2 contractional faults and D3 dextral faults.

D1 sinistral-reverse faulting took place as a result of oblique subduction of oceanic crust beneath western North America (Schiarizza et al., 1997). This deformation caused the southward translation of the SWCB to its current location adjacent to the SECB (Monger et al., 1994; Schiarizza et al., 1997). D1 faults host cataclastic fabrics likely due to rheological weakening of fault zone materials and/or high fluid flow through fault zones during deformation. These faults were likely reactivated during 97 to 88 Ma following the initial sinistral deformation event.

D2 contractional faulting formed from 91 to 84 Ma during a period of more margin-perpendicular subduction (Umhoefer et al., 1994; Schiarizza et al., 1997). D2 deformation resulted in the closure and uplift of the Tyaughton-Methow Basin and can be subdivided into early south-vergent faults (91 to 86 Ma) (Schiarizza et al., 1997) and late north-vergent faults (87 to 84 Ma) (Umhoefer et al., 1994).

D3 faults are characterized by strongly brittle-style deformation and host no significant observed mineralization or alteration. Most D3 faults are dextral faults and are the most prominent faults in the region. They are interpreted to have been active during the Eocene and are linked to the larger scale Yalakom Fault system to the north of the study area (Umhoefer and Schiarizza, 1996). This system also arose as a result of oblique subduction of oceanic crust beneath the western margin of North America (Schiarizza et al., 1997). Evidence from this study indicates that contractional and sinistral faulting may have also been active in the area during the Tertiary (see chapter II).

### **3.2.3 Regional Occurrences of Mineralization**

Many significant Cu and Au deposits occur in the vicinity of Taseko Lakes within the SECB and Intermontane Belts. The Bralorne Mining District is located approximately 50 km to the southeast of the Taseko Lakes area, and represents British Columbia's largest historical Au producer. The Bralorne mining area produced 130 metric tons of Au over a 70 year span (Leitch et al., 1991). The Bralorne deposits and similar examples to the south are vein-hosted, mesothermal Au deposits. Gold occurs in quartz veins located within steeply dipping, reverse faults located within Permian, pre-mineralization intrusions (Bellamy and Arnold, 1985; Leitch et al., 1989; Sanche, 2004). Studies by Leitch et al. (1991) and Ash (2001) concluded that Au

mineralization formed from ~92-86 Ma and may be linked to sinistral or contractional deformation in the region. However, recent work by Hart et al. (2008) indicates that gold mineralization took place at 68 to 64 Ma and may be linked to dextral strike-slip faulting. Multiple, overprinting mineralizing events have also been postulated for the Bralorne Mining District (Sanche, 2004).

The Prosperity deposit, formerly known as the Fish Lake deposit, is a developed porphyry Cu-Mo-Au prospect. It occurs approximately 30 km north of the Taseko Lakes region and has a reserve of 675 million tonnes of ore at 0.236% Cu and 0.434 g/t Au (Brommeland and Wober, 1999). A possible inferred age of mineralization of  $77.2 \pm 2.8$  Ma was attained from a whole-rock age of a hornfels unit containing secondary biotite (Wolfhard, 1976). Mineralization occurs predominantly in veins and along fractures and is believed to be accommodated in part by displacement along the nearby Yalakom Fault which may have been active from 77-70 Ma (Heinrich, 1991; Schiarizza et al., 1997; Brommeland and Wober, 1999).

## **3.3 DEPOSIT SCALE GEOLOGIC FRAMEWORK**

### **3.3.1 Methodology**

#### **3.3.1.1 Geological mapping and drill core logging**

During the 2006 field season, the Northwest Copper, Twin Creeks, Tchaikazan Valley and Pellaire areas were mapped at the 1:5,000 and 1:10,000 scales. Exposure in the area ranges from 10% to greater than 50%). During the 2007 field season, the Mount McLure area was mapped at 1:10,000 scale, while the Empress, Taylor-Windfall and Pellaire areas were mapped at 1:5,000 and smaller scales (similar exposure levels to the other areas). This was complemented by core logging of seven diamond drill-holes (approximately 1000m of core from the Empress deposit and 150m of core from the Taylor-Windfall deposit). Approximately 660 hand specimens were sampled in the field from both drill core and outcrop.

#### **3.3.1.2 Petrographic studies**

Samples of 175 representative rock and vein types from the study area were submitted for polished thin sections. An additional 17 oriented samples of fault zone and foliated rocks were also submitted for polished thin sections. The purpose of this was to investigate (1) the mineralogy and textures of the sedimentary, extrusive and intrusive igneous rocks, (2) microstructural characteristics of oriented samples, (3) secondary alteration and (4) paragenesis of all secondary deformation, veining and alteration events. All rocks were classified using the nomenclature of the International Union of the Geological Sciences based on observations from hand samples and petrography.

#### **3.3.1.3 Short wavelength infrared analysis**

Short wavelength infrared (SWIR) analysis can be performed on samples in the field with the use of the portable infrared mineral analyzer (PIMA). A PIMA allows for rapid identification of hydrothermal and clay minerals, which ultimately allows the mapping of zones of hydrothermal alteration when individual mineral species are indiscernible (Herrmann et al., 2001). The short wavelength infrared range consists of electromagnetic wavelengths from 1300 to 2500 nm. This range incorporates fundamental absorption features of  $\text{OH}^-$ ,  $\text{H}_2\text{O}$ ,  $\text{CO}_3^{2-}$ ,  $\text{NH}_4^+$ ,  $\text{AlOH}$ ,  $\text{FeOH}$  and  $\text{MgOH}$ . From the relative magnitude of these absorption features, relative

abundances of many hydrothermal alteration minerals can be estimated (Thompson et al., 1999; Bierwirth et al., 2002).

A total of 537 SWIR measurements were taken on 129 outcrop samples, and 185 drill core samples for this project were made using a TerraSpec® SWIR spectrometer from Analytical Spectral Devices, Inc. (ASD) (ASD, 2006) using RS<sup>3</sup> software (ASD, 2005). Calibrations were made approximately every 20 to 30 measurements using a white reference standard, and multiple measurements were made in order to check for heterogeneities in the sample and legitimize the results. Spectra attained from these measurements were compared against reference spectra using SpecMin Pro software (SII, 2002). Sample spectra from this study are presented in Appendix A.

#### **3.3.1.4 X-ray diffraction**

Six powder samples were analyzed by XRD and subsequently compared with results from the SWIR analyses. Samples were crushed and saturated with ethanol then smeared on a thin section plate and left to dry. These were analyzed in a Siemens D5000 Diffractometer with a Vantech-1 detector. Diffraction took place at 0.2° increments from 2θ angles from 3° to 80°. The analysis was controlled using XRD Commander control software. Processing and analysis of \*.raw files was performed using EVA software. Identification of clay minerals and other mineral phases was completed according to methods described in Brindley and Brown (1980).

### **3.3.2 Introduction to deposits**

#### **3.3.2.1 Empress**

The Empress deposit was classified as a porphyry Cu deposit by Lambert (1991). The goal of this study was to characterize the alteration and mineralization at the deposit and place temperature, depth, compositional and age constraints on the conditions of formation. Six drill-holes from the 1989 and 1990 exploration programs (89-3, 89-6, 90-17, 90-19, 90-22 and 90-30) on the property by Westpine Metals Ltd. were logged and sampled in detail (Table 3.1). Geology was mapped at a 1:10 000 scale.

The Empress deposit is located 12 km southeast of Upper Taseko Lake in the SECB (Figure 3.2; 3.7). The area in and around the Empress deposit was actively explored between 1969 and 1976 as a porphyry Cu-Mo target by Scurry Rainbow Oils Ltd., Sumitomo Metals

Mining Canada Ltd., and Quintana Minerals Corp. (Lambert 1991; Osborne 1999). In 1985, the property was explored for its epithermal Au potential by Esso Resources Canada, Ltd. Westpine Metals, Ltd., carried out subsequent work on the property during 1988-1991, 1993 and 1998 (Lambert, 1991; Osborne, 1994; 1999). A zone of hydrothermal alteration extends outwards from the contact with the CPC into rocks of the SECB. Alteration and lithologies of the Empress area are described in detail by Lambert (1991) and Osborne (1999). No outcrop is exposed in the vicinity of the deposit, therefore information is limited to examination of drill core. The Empress deposit contains 10,048,000 tonnes of 0.61 percent Cu and 0.79 grams per tonne Au and chalcopyrite is the predominant ore mineral (Osborne, 1999). The property is currently owned by Great Quest Metals, Ltd.

### **3.3.2.2 Taylor-Windfall**

The Taylor–Windfall deposit is classified as a vein-hosted epithermal Au-Ag deposit (Lane, 1983). For this study, the area surrounding the deposit was mapped at 1:5,000 and 1:10,000 scales to characterize the intense alteration zones present in the vicinity of the deposit and identify structural controls on alteration and mineralization. Underground workings at the Taylor–Windfall deposit were inaccessible during fieldwork; therefore sampling and mapping were restricted to limited surface exposures. One drill-hole (84-03) from Westmin Resources 1984 exploration program was also examined. Results from field and laboratory provided insights into the conditions of formation of Taylor–Windfall and possible links with the Empress deposit.

Placer Au was discovered on the Taylor-Windfall property by E.J. Taylor in 1920. A small-scale, underground mining operation was performed during the 1930's resulting in three levels of underground workings. Production ceased during World War II, but recommenced in 1952-53. In 1983 and 1984, Westmin Resources Ltd. conducted geologic mapping, sampling and diamond drilling in the immediate mine area (Lane, 1983).

A detailed study of the alteration and mineralization of the Taylor-Windfall deposit was performed by Price (1986) as a part of her M.Sc. research. Price mapped two levels of underground workings, the immediate surface area and assisted in logging 800 m of diamond drill-core. A sample map and cross-section from Price (1986) is presented in Figure 3.5. Price described the Taylor-Windfall area being comprised of coherent to volcanoclastic andesitic units that have undergone variable amounts of hydrothermal alteration (mainly intermediate and

advanced argillic alteration). Petrographic and lithogeochemical studies were performed following fieldwork in an attempt to describe the Taylor-Windfall prospect in sufficient geologic detail to postulate its origin. Price (1986) identified a high-temperature alteration assemblage overprinted by a retrograde alteration assemblage at Taylor-Windfall. Price concluded that Taylor-Windfall bears similarities to both porphyry and epithermal systems.

The deposit is located in the gulley surrounding Battlement Creek (Figure 3.6), 15 km southeast of Upper Taseko Lake (Figure 3.2). Production records show that 14,525 grams of Au and 156 grams of Ag were recovered from 555 tonnes of ore over 5 years. Hydrothermal alteration is dominated by minerals characteristic of advanced argillic alteration and silicification (Price, 1986). Known mineralization is largely restricted to two discrete vein types: sulfide-dominated and tourmaline-dominated (Lane, 1983). Historical reserves suggest that the remaining veins host approximately 1000 tons of ore at 0.4 ounces of Au per ton (Price, 1986). The property is presently owned by Galore Resources Ltd.

### **3.3.2.3 Pellaire**

The Pellaire deposit is classified as a polymetallic vein-hosted deposit (Holtby, 1988). This deposit was mapped at a 1:5,000 scale to determine structural controls on mineralization and collect samples of veins and wallrock for laboratory analyses in order to place constraints on temperature, depth and age of mineralization.

The Pellaire deposit is a past-producing, Au-Ag deposit located 7 km south-southwest of Upper Taseko Lake (Figure 3.2). The deposit is located along the contact between the Falls River succession and the Mount McLeod Batholith (Figure 3.7) (Hollis et al., 2007). Mineralization occurs in quartz veins hosted in south-vergent thrust faults (Pezzot, 2005). Hydrothermal alteration is not intense or widespread but is dominated by quartz, muscovite, illite, ankerite and jarosite. Probable geological reserves are 30,841 tonnes grading 22.9 grams per tonne Au and 78.8 grams per tonne Ag (Holtby, 1988).

Au-bearing quartz veins at the Pellaire deposit were first discovered in 1936 by prospectors A. Pelletier and A.J. Allaire. The two formed Hi Do Gold Mines Ltd. in 1937 and continued to develop the property. During 1945-1947, Pellaire Mines Ltd. established the first road to the property and drove 5 separate adits. Silver Standard Mines Ltd. carried out a resampling program of the Pellaire veins in 1973. In 1980-1981, Lord River Gold Mines drove

two more adits on the property. Subsequent drilling and adit development was performed by Lord River Gold Mines in 1984, Consolidated Silver Standard Mines Ltd. in 1987 (Holtby, 1988). Mine development and regional sampling were performed by Pellaire Mines Ltd. in 1996 and 1997 (Smith, 1998)). Valor Resources Ltd. currently owns the Pellaire property and most recently performed a geophysical exploration program in 2005 (Pezzot, 2005).

### **3.3.3 Geologic Setting of Deposits**

#### **3.3.3.1 Empress**

The Empress Deposit is interpreted to be hosted within the Falls River succession and is underlain by porphyritic granite, herein named the Empress pluton. The deposit is located in a forested area near the bottom of the Taseko Valley. Outcrop in the area surrounding the deposit occurs in the gully at Granite Creek about 200 meters west of the deposit, as well as on the ridge to the southeast of the deposit (Figure 3.4).

Rocks exposed around Granite Creek and its immediate surroundings are predominantly coherent andesite and dacite with phenocryst contents ranging from 5-40%, consisting of feldspar, biotite and quartz in decreasing abundance. Quartz phenocrysts are absent in the andesitic units. The majority of the rocks exposed at the surface have undergone only minor carbonate and chlorite alteration, whereas more intensely altered rocks occur in the center of the gully (Figure 3.8A). The altered rocks contain illite and minor pyrite and chalcopyrite. This alteration zone is inferred to be centered on a fault extending up the center of Granite Creek. No bedding was observed in outcrop during mapping, so the orientation of any potential pre-existing layering in the country rocks at Empress is unknown. Biotite from an undeformed dacitic dike near Granite Creek yielded a  $^{40}\text{Ar}$ - $^{39}\text{Ar}$  plateau age of  $53.8 \pm 1.3$  Ma (Table 3.2; Figure 3.9A).

The ridge to the south of Empress is underlain by the Mount McLeod Batholith. The majority of the rock on the ridge is a coarse-grained, equigranular hornblende-biotite granodiorite that has undergone only minor chlorite alteration of the mafic minerals. The Mount McLeod granodiorite intrudes porphyritic granite on the northwestern margin of the ridge. The porphyritic granite is composed of up to 50% coarse feldspar, biotite, hornblende and quartz phenocrysts set in a fine-grained, feldspar-quartz-dominated groundmass. Plagioclase phyric andesitic dikes with meter-scale thicknesses are also present on the ridge and cut the granodiorite with subvertical orientations (Figure 3.8B). Hornblende phenocrysts from one of the andesite

dikes yielded a  $^{40}\text{Ar}$ - $^{39}\text{Ar}$  plateau age of  $61.1 \pm 7.4$  Ma (Table 3.2; Figure 3.9B). Discrete, m-scale zones of brecciation cemented by megacrystic biotite occur within the granodiorite (Figure 3.8C). Biotite from one such breccia zone yielded a  $^{40}\text{Ar}$ - $^{39}\text{Ar}$  plateau age of  $87.93 \pm 0.59$  Ma (Table 3.2; Figure 3.9C). Outcrop-scale zones of Fe and Cu-oxide alteration occur sporadically throughout the Mount McLeod Batholith.

At Empress, the host country rock lithologies are obscured by the intense alteration (Figure 3.10A). In contrast, the pluton which underlies the deposit, termed the Empress pluton, is only moderately altered with primary textures still easily visible. The Empress pluton is a porphyritic biotite granite (Figure 3.8D). The porphyritic granite observed on the ridge above the deposit to the southeast is very similar in composition to the Empress pluton and is interpreted to be a part of the same intrusive phase. Inspection of drill core suggests that the contact of this pluton is relatively flat-lying in the vicinity of the deposit (Table 3.1; Figure 3.10), forming a slight trough at the deposit that increases in elevation towards the southeast. Porphyritic dikes, inferred to be part of the same intrusive phase as the Empress pluton, are also observed in drill core. At the deposit, alteration within the pluton is typically comparable to that of the overlying country rock, but lower in intensity. A U-Pb zircon age of  $87.0 \pm 1.4$  Ma (Table 3.2; Figure 3.11A, B) was obtained from the Empress pluton.

Feldspar-phyric andesite dikes, similar to the andesite dikes that occur on the ridge to the south of the Empress deposit, and fine-grained biotite rhyolite dikes are observed in drill core. Both sets of dikes have undergone less alteration than the country rocks. Biotite from a rhyolite dike located to the west of Empress, inferred to be of the same generation as the dikes at Empress, yielded a  $^{40}\text{Ar}$ - $^{39}\text{Ar}$  plateau age of  $91.45 \pm 0.51$  Ma (Table 3.2; Figure 3.9D).

### **3.3.3.2 Taylor-Windfall**

The Taylor-Windfall deposit is hosted within the Upper Cretaceous Powell Creek Formation (Figure 3.6). Rocks proximal to the deposit are variably altered, and in some cases, the protolith is indiscernible. The Powell Creek Formation consists of andesitic coherent and associated volcanoclastic rocks. Volcanic breccias and conglomerates range from pebble to boulder-sized and are generally compositionally similar to the coherent units. Some clastic units show differential weathering patterns between clasts and matrix. Breccias and conglomerates often bound coherent units on either side and are interpreted as flow front units, suggesting a sub-aerial environment of deposition. Pyroclastic deposits exhibiting strong bedding are

observed (Figure 3.12A). Other volcanoclastic units in the area display well developed bedding planes defined by gradational to sharp changes in grain size which suggests a subaqueous environment of deposition. Bedded clastic sedimentary rocks occur to the west of Taylor-Windfall in the Powell Creek Formation. Thus the Powell Creek Formation is interpreted to be deposited in both subaerial and submarine settings typical of a volcanic island arcs. Proximal to Taylor-Windfall, bedding is prominent in many volcanoclastic units in the area and typically absent in coherent volcanic units. It is consistently striking and dipping 260/30 (Figure 3.6B).

The Powell Creek Formation which hosts the Taylor-Windfall deposit is estimated to have a stratigraphic thickness up to 3 km (Schiarizza et al., 1997). Since Taylor-Windfall (~88 Ma; see geochronology section) formed synchronously with the Powell Creek Formation (~96-79 Ma; Maxson, 1996), Taylor-Windfall could not have formed at depths greater than 3 km unless thrust stacking occurred during the D2 deformational event.

The best exposures in the field area are located on the ridges above Battlement Creek to the north and east; the latter is known as Battlement Ridge. A porphyritic plagioclase-olivine diorite intrusion cuts the Powell Creek Formation along the center of the ridge. A large porphyritic plagioclase diorite dike cuts the ridge to the north of Granite Creek and is prominently visible from the valley below (Figure 3.12B). Another intrusive plug of porphyritic granite containing 5% rounded quartz eyes cuts across the crest of Battlement Ridge.

Bedding attitude in the vicinity of Taylor-Windfall is 250/30 (strike and dip) (Figure 3.6B). The majority of faults in the Taseko Lakes Region are steeply dipping; however, a fault that hosts quartz-alunite alteration on Battlement Ridge is a low-angle south-dipping fault oriented relatively parallel to bedding. No obvious foliations or shear fabrics occur in the fault zone, but due to its shallow dip, it is best correlated with the contractional deformational event in the region (91 to 85 Ma; Garver, 1992). However, this zone of intense alteration could potentially have been generated by focused, bedding parallel fluid flow. There are three common fracture set orientations with one oriented relatively parallel to bedding (strike and dip: 250/30) and the other sets occurring orthogonal to bedding (065/75, 340/90). No evidence for significant fracture parallel displacement across these fractures was observed. The northeast trending fractures (strike and dip: 065/75) exhibit the strongest control on alteration and are consistent with orientations of the mineralized veins at the deposit (Price, 1986), which have strike lengths of 20 to 100 m. Alteration halos surrounding fractures are dm scale thicknesses, while fracture spacings are typically dm to m scale. A high angle fault is inferred to run down the middle of

Battlement Creek from the intense, but confined alteration present in the gully. The fault is not observed in outcrop.

### 3.3.3.3 Pellaire

On the Pellaire property, the Falls River succession consists of intermediate, coherent and clastic volcanic units with lesser amounts of sedimentary rocks, typified by siltstone and shale.

In the vicinity of the Pellaire deposit, the Mount McLeod Batholith consists of medium- to coarse-grained, hornblende granodiorite. The Mount McLeod granodiorite is equigranular, ranging from 1-10 mm grain sizes and an average of about 2-3 mm. It is composed of ~40 % quartz, 30% euhedral plagioclase, 15 % subhedral hornblende, 10 % euhedral potassium-feldspar, 3 % hematite and magnetite, and 2 % subhedral biotite. Quartz occurs interstitially to all other minerals, and feldspar occurs interstitially to mafic minerals. Minor oxide minerals are also observed in the Mount McLeod granodiorite. In some outcrops on Pellaire, the Mount McLeod granodiorite contains up to 20 % cobble-sized, fine-grained mafic enclaves (Figure 3.13A). Grain size of the granodiorite decreases slightly towards the margin. It intrudes the Falls River Succession on the western flank of the Pellaire Ridge (Figure 3.13B); however, the contact between the two units is brecciated and faulted on the crest and eastern flank of the ridge. Areas of significant clay alteration and oxidation occur sporadically throughout the Batholith in the study area. Discrete zones of intense Cu- and Fe-oxide alteration are commonly observed in the Mount McLeod Batholith.

Basaltic dikes intrude the Mount McLeod granodiorite and are cut and slightly offset by faults hosting the Au-bearing quartz veins at Pellaire (Figure 3.13C). The dikes are composed of fine-grained, moderately clinopyroxene-phyric olivine tholeiite and dip steeply to sub-vertically to the west. Basalt dikes on Pellaire are no greater than one meter thick.

North-dipping faults within the Falls River succession and Au-bearing quartz-veins within the Mount McLeod granodiorite are both oriented with strikes and dips of ~240/50 (Figure 3.7). Fault-hosted quartz veins steepen southwards with dips increasing to 70-75°. Faults generally have dm-scale thicknesses and relatively uniform orientations, also steepening towards the south (Figure 3.7). Weak shear fabrics indicated a contractional sense of displacement across the fault. Illite from the fault gouge of a south-vergent fault yielded a  $^{40}\text{Ar}$ - $^{39}\text{Ar}$  plateau age of  $84.52 \pm 0.58$  Ma (Table 3.2; Figure 3.9J).

A later phase of deformation at Pellaire produced faults oriented 320/60 that cut the quartz veins and faults described above. One such fault separates the Mount McLeod granodiorite from the hydrothermal breccia zone, thus obscuring the nature of the original contact between the two units.. North-vergent faults possess dm-scale thicknesses, but no clear sense of displacement was observed in outcrop. Other reported north-vergent thrust faults were active in the area from 87-84 Ma (Rusmore and Woodsworth, 1991b).

### **3.3.4 Alteration and Mineralization**

#### **3.3.4.1 Empress**

Six alteration types were distinguished at Empress from drill core (Figure 3.10B), aided by short-wavelength infrared (SWIR) and X-ray Diffraction (XRD) analysis. The alteration types include quartz-dominated, potassium-silicate, quartz-magnetite, quartz-sericite, quartz-chlorite, sodic and advanced argillic alteration. Alteration intensity in the country rock prevents identification of the original lithologies. The fine-grained and gradational nature between quartz-sericite, sodic and advanced argillic alteration typically prevents identification of alteration types in hand sample. The purpose of alteration mapping is to gain insight into the size, geometry and P-T-X conditions of the Empress system during mineralization and to identify potential controls imposed on the hydrothermal system.

Drill core logged at the Empress deposit was not oriented; as a result, limited information is available on structural orientations at the deposit. However, the majority of alteration layering observed in subvertical drill holes was near perpendicular to the drill core axis, suggesting a dominantly sub-horizontal trend to the layering of the deposit. Vertical drill-holes show similar patterns of alteration, also suggesting a dominantly sub-horizontal layering of alteration zones at the deposit (Figure 3.10B).

#### *Quartz-dominated alteration*

Quartz-dominated alteration is characterized by a rock comprising 90% or greater of quartz. Grain size in this type of alteration is variable and is uniform to highly inequigranular (Figure 3.14A). In quartz-dominated alteration, two or more generations of quartz locally coexist in the same rock. Quartz phases vary from milky to clear, and from light to dark grey (Figure 3.14B). These variations in appearance are attributed to differences in grain size and inclusion

abundance. Quartz occurs as either separate zones of blotchy or patchy, uneven alteration, or as one or more phase brecciated by a later phase. The matrices of breccias contain variable amounts of clay and carbonate. Quartz-dominated breccias lack a pervasive foliation and shear fabric, and are interpreted to be hydrothermal and not tectonic in origin. Quartz is brecciated, cut and overprinted by most other alteration phases, suggesting that quartz-dominated alteration formed early in the system when fluids were hot.

#### *Potassium-silicate alteration*

Moderate potassium-silicate alteration occurs in the Empress pluton, most primary textures in the rock are preserved. It is characterized by extensive recrystallization of hornblende to biotite and slight to moderate K-feldspar alteration of the groundmass, giving the rock a pink colour (Figure 3.14C). Biotite from the potassium-silicate alteration zone within the Empress pluton yielded a  $^{40}\text{Ar}$ - $^{39}\text{Ar}$  plateau age of  $87.87 \pm 0.47$  Ma (Table 3.2; Figure 3.9E). Minor biotite in the pluton has been replaced by chlorite. Rare, fine-grained rutile occurs with biotite in potassium-silicate alteration.

#### *Quartz-magnetite alteration*

Quartz-magnetite alteration is characterized by >10% magnetite and occurs within zones of otherwise quartz-dominated alteration. Generally, magnetite has an interstitial occurrence with respect to quartz that can grade into a net-texture, with concentrations typically ranging from 10-40%. Discrete zones of intense magnetite alteration may contain up to 90% massive magnetite (Figure 3.14D). Magnetite also occurs interlayered with quartz (Figure 3.14E), as the cement in magnetite-cemented quartz-clast-rich breccias (Figure 3.14F), or as veins that cut quartz-dominated alteration. Hematite is commonly intermixed with magnetite. Rare rutile occurs disseminated within quartz-magnetite alteration. The contact between the Empress pluton and overlying country rock is typically marked by a sharp zone of intense magnetite alteration.

#### *Quartz-sericite/Intermediate argillic alteration*

Quartz-sericite alteration consists of >10% sericite and occurs in an otherwise quartz-dominated (Figure 3.14G) or quartz-magnetite dominated rock. Sericite is a general term used to describe both fine-grained muscovite and illite. Zones within the Empress pluton also show significant sericite overprint of feldspar phenocrysts and groundmass (Figure 3.14H). Coarser-grained muscovite occurs intermittently throughout quartz-sericite dominated alteration.

Undeformed, euhedral muscovite crystals indicate that there is no significant penetrative deformation of the deposit following alteration. Sericite occurrence may be uniform or occur as small blebs and patches (Figure 3.14I) with zones locally containing up to 80% sericite. Quartz-sericite alteration shows gradational changes into all other alteration types. Sericite is commonly intermingled with quartz-dominated and quartz-chlorite alteration, occurring as irregular interlayering or as small blebs <5 mm size. Muscovite from quartz-sericite alteration yielded a  $^{40}\text{Ar}$ - $^{39}\text{Ar}$  plateau age of  $86.66 \pm 0.50$  Ma (Table 3.2; Figure 3.9F).

#### *Sodic alteration*

Sodic alteration at Empress consists of at least 30% sodium-rich minerals including albite (Figure 3.14J), paragonite and montmorillonite. Intense sodic alteration is comprised of close to 100% sodium-rich minerals. Sodic minerals typically occurred intermixed with other alteration minerals such as quartz, magnetite, sericite and chlorite. Early alteration minerals such as quartz and magnetite are overprinted by sodic alteration (Figure 3.14J), however overprinting relationships are less clear for sericite and chlorite. Paragonite and montmorillonite are always very fine grained and unrecognizable in hand sample. They were identified through SWIR analysis. Advanced argillic alteration is spatially associated with sodic alteration at Empress.

#### *Advanced argillic alteration*

Advanced argillic alteration consists of at least 30% aluminous fine grained minerals superimposed on other alteration types. Advanced argillic minerals occur as uniform to blotchy overprints of feldspars, magnetite, sericite and chlorite, and can comprise close to 100% of host rocks in zones of intense alteration. In the Empress pluton, small (<1 m) zones of advanced argillic alteration are restricted to moderate kaolinite-dickite overprinting of groundmass and feldspar phenocrysts (Figure 3.14K). Advanced argillic alteration minerals include any combination of andalusite (Figure 3.14L), pyrophyllite, dickite, kaolinite with rare topaz, nacrite and halloysite. Quartz, Fe-oxides, siderite and sodic alteration minerals often occur with advanced argillic minerals and can occur in the matrix of hydrothermal breccias. Carbonates are the only mineral phases observed to overprint advanced argillic alteration and are interpreted as the latest alteration mineral.

#### *Quartz-chlorite alteration*

Quartz-chlorite alteration consists of at least 10% chlorite in an otherwise quartz-dominated host rock. Chlorite overprints quartz-dominated, quartz-magnetite (Figure 3.14M) and quartz-sericite (Figure 3.14N) alteration, occurring as uniform disseminations, or as patches and blebs within other types of alteration. Minor chlorite is commonly present in other alteration types, and overprints most other alteration minerals. Chlorite alteration may grade in as veinlets and occur as halos to magnetite veins (Figure 3.14O). It is also commonly associated with minor carbonate minerals (Figure 3.14P). Chlorite frequently occurs with magnetite, hematite, and siderite resulting in gradational changes from quartz-magnetite to quartz-chlorite alteration.

Quartz-chlorite altered rocks in drill-core resemble some chlorite-altered rocks observed in outcrop along Granite Creek. Since the majority of rocks around Granite Creek are significantly less altered than the rocks at the Empress deposit, quartz-chlorite alteration is interpreted to be the least-intense alteration type at the Empress deposit.

### *Mineralization*

Chalcopyrite is the dominant ore mineral at the Empress deposit. Pyrrhotite is less common, and bornite and molybdenite are rare. Ore grade is inferred to vary directly with chalcopyrite abundance, with the highest chalcopyrite grades occurring in quartz-magnetite alteration. The northern area of the deposit hosts more extensive mineralization than the southern area. The mode of Au occurrence is unknown, but is spatially associated with Cu at the deposit (Lambert, 1991). Pyrite and less commonly pyrrhotite are also associated with high grade zones. Pyrite commonly cuts or brecciates pyrrhotite and is inferred to have formed after pyrrhotite. Pyrrhotite and rare bornite are restricted to zones of potassium-silicate and quartz-magnetite alteration. Rare molybdenite occurs in quartz-dominated and quartz-sericite alteration zones.

Chalcopyrite commonly occurs interstitially, disseminated (Figure 3.15A), or within veinlets (Figure 3.15B). Chalcopyrite abundance ranges from about 2 to 5 %, but may be present in concentrations up to 40%. Chalcopyrite occurs with pyrrhotite (Figure 3.15C), pyrite (Figure 3.15D), and magnetite (Figure 3.15E). Pyrite occurs as inclusions within chalcopyrite and is observed to be brecciated by chalcopyrite in some areas (Figure 3.15D). Pyrite and chalcopyrite occur interstitially or as cement in quartz-dominated or quartz-magnetite breccias (Figure 3.15E). Sulphides are locally observed to be cut or replaced by muscovite (Figure 3.15F) and all later phases of alteration. The majority of mineralization is interpreted to have occurred sometime during the latter phase of quartz-dominated and quartz-magnetite alteration phases,

and the early part of the quartz-sericite alteration phase. This is within the range of typical porphyry systems.

### **3.3.4.2 Taylor-Windfall**

Alteration at the Taylor Windfall deposit is generally fracture controlled, resulting in large variations in alteration style and intensity at the outcrop scale. Distinguishing and delineating separate alteration zones is complicated due to small scale variations in alteration styles. Consequently, contacts on the alteration map shown in Figure 3.16 are only approximate. Price (1986) performed more detailed mapping of the property (Figure 3.5).

#### *Vuggy silica ± pyrite alteration*

A central zone of vuggy silica ± pyrite alteration (Figure 3.12C, D) occurs at the mine site, proximal to the mineralized veins. Vugs are mm to cm size and comprise 5-10 % of the rock. Vugs may contain euhedral pyrite crystals up to several mm in size. The remainder of the rock is composed of quartz of variable grain size (Figure 3.12D). The zone of vuggy silica alteration is the only massive alteration unit and exhibits no obvious structural control.

#### *Tourmaline alteration*

Tourmaline occurs in veins and as disseminations of up to 10% of the rock in quartz-sericite alteration surrounding the central vuggy silica zone (Figure 3.12E). Tourmaline is commonly associated with pyrite and forms rims to cm-size round blebs referred to as orbicules in previous studies (Price, 1986) (Figure 3.12F). Orbicules consist of pyrite-tourmaline rims but possess no internal textures. Orbicule centers are typically compositionally identical to the rock surrounding the orbicules, which is generally dominated by argillic minerals. Drill core studied was not oriented, but tourmaline veinlets typically have relatively uniform orientations with respect to core axes.

#### *Quartz-sericite ± chlorite ± pyrite and advanced argillic alteration*

Interlayered zones of quartz-sericite-pyrite ± chlorite ± pyrite (Figure 3.12G) and advanced argillic alteration surround the central vuggy silica zone. Advanced argillic alteration minerals were detected through SWIR analysis and include kaolinite, dickite, palygorskite, paragonite, pyrophyllite and halloysite. All alteration styles mentioned are typically controlled

by fractures. For example, quartz-sericite-pyrite may occur proximal to a central fracture, with a quartz-chlorite-sericite halo. In drill core, zones of sericite, chlorite and other advanced argillic alteration also form blotchy, uneven alteration (Figure 3.12H). Weak, background chlorite  $\pm$  carbonate alteration is present outside of the quartz-chlorite-sericite alteration zone. Illite from near the central vuggy silica altered zone yielded a  $^{40}\text{Ar}$ - $^{39}\text{Ar}$  plateau age of  $89.3 \pm 0.54$  Ma (Table 3.2; Figure 3.9G).

#### *Hydrothermal breccias*

Quartz-illite-palygorskite cemented breccias are observed at surface exposures with m-scale thicknesses (Figure 3.12I). The breccias are dominantly monomictic and poorly sorted, which is suggestive of short-transport distance of clasts. Cement grades outward as stockwork veining, but dominates the breccias zones at their cores. Palygorskite is an alteration mineral commonly associated with hydrothermal vein systems (Post and Crawford, 2007). Illite from the matrix of a hydrothermal breccia produced a  $^{40}\text{Ar}$ - $^{39}\text{Ar}$  plateau age of  $87.7 \pm 1.1$  Ma (Table 3.2; Figure 3.9H).

#### *Quartz-alunite alteration*

Intense quartz-alunite alteration is observed on Battlement Ridge and is confined to a zone <50 m thick surrounding a low-angle fault zone of unknown kinematics (Figure 3.12J). The rocks immediately surrounding the fault zone are bright orange in colour due to the presence of alunite, and grade out into a purely silicified zone before alteration returns to background levels. The porphyritic plagioclase-olivine diorite and porphyritic granite intrusions have undergone this alteration, indicating they pre-date to the alteration event.

#### *Quartz-dickite alteration*

Rocks on the ridge to the north of Battlement Creek hosts mainly weak background, chlorite alteration except for a large porphyritic plagioclase diorite dike that cuts the ridge (Figure 3.12B). The dike is moderately silicified and hosts significant dickite alteration of feldspars, but alteration is confined exclusively to the dike and not the surrounding rocks.

#### *Mineralization*

The known mineralization at Taylor-Windfall is hosted in two veins; one of these is sulphide dominated, and the other is tourmaline-dominated. Mineralized veins are not exposed at

the surface, and the underground mine workings were inaccessible during this study. As a result, the following vein descriptions are taken from Price (1986). The tourmaline-dominated vein varies from 10-20 cm thickness and is comprised of open space filling of tourmaline, chlorite, pyrite, tennantite, sphalerite, chalcopyrite, galena, rare earth element phosphate and minor tetradymite, Au and enargite. The main sulphide vein has largely been mined out. It is approximately 20 cm wide and possesses similar mineralogy to the tourmaline-dominated vein but with greater amounts of sphalerite, tennantite and REE-phosphate. Native Au is present in trace amounts and is spatially associated with tennantite. Pyrite is the only mineral which forms discrete layers within the veins, and is the only significant sulphide observed in outcrop or drill core. It occurs within vugs in vuggy silica alteration, disseminated throughout quartz-sericite alteration and as rims to orbicules (Figure 3.12F). Rare chalcopyrite is present in drill core. Ore minerals described by Price (1986) at Taylor-Windfall, particularly enargite and tennantite, are typical of high sulphidation epithermal systems (White and Hedenquist, 1995).

### **3.3.4.3 Pellaire**

#### *Alteration*

Alteration on Pellaire is not as intense or widespread as at Empress or Taylor-Windfall. It is limited to discrete zones of moderate alteration wherein the majority of the primary textures in the host rocks are preserved.

A zone of quartz-carbonate alteration occurs in the Falls River succession along the western flank of Pellaire Ridge extending outward from the Mount McLeod Batholith (Figure 3.7). Quartz, siderite, ankerite and minor muscovite are associated with this style of alteration, which obliterates most, but not all primary textures in the host rocks (Figure 3.13H). There is a thin zone of contact metamorphism and intense silicification of the Falls River Succession immediately adjacent to the Mount McLeod granodiorite contact.

A zone brecciation, interpreted to be hydrothermal in origin, separates the Falls River succession from the Mount McLeod Batholith on the eastern flank of the Pellaire Ridge (Figure 3.13I). The contact between the hydrothermal breccia and the granodiorite is faulted; however, the contact between the breccia and Falls River Succession is not. Alteration within the hydrothermal breccia is dominated by muscovite, illite, ankerite, siderite and jarosite. Alteration minerals are abundant in the breccia matrix, and less intense in the clasts of the breccia and surrounding rocks of the Falls River succession. Pyrite and minor chalcopyrite occur in

granodiorite clasts in andesitic clasts or in the matrix of the breccia. The presence of jarosite (a weathering product of sulphides) within the breccia matrix also suggests the breccia may have hosted more significant mineralization at one time (Bladh, 1982). Illite from the cement of the hydrothermal breccia yielded a  $^{40}\text{Ar}$ - $^{39}\text{Ar}$  plateau age of  $85.16 \pm 0.65$  Ma (Table 3.2; Figure 3.9I). Similar alteration minerals occur immediately surrounding the Au-bearing quartz veins within the Mount McLeod granodiorite.

Regional, background alteration in the Falls River succession and basalt dikes consists of slight to strong chlorite alteration of mafic and plagioclase phenocrysts, as well as slight clay or carbonate alteration of the groundmass in porphyritic and volcanoclastic units. Basaltic dikes display a moderate chlorite overprint of their groundmass and are commonly cut by chlorite veinlets. Negligible alteration is observed in the Mount McLeod granodiorite.

### *Mineralization*

Access was not gained to the underground workings on Pellaire for this study. As a result, the following description of mineralization is taken from Holtby (1988) and Pezzot (2005). Mineralization at the Pellaire deposit occurs in quartz veins hosted within the Mount McLeod Batholith. Ore minerals include galena, sphalerite, pyrite, chalcopryrite and tellurides. Au occurs as Au-telluride or as inclusions in pyrite. Sulphides in veins occur as void fill, but are weathered out at the surface, where only limonite and Cu-oxides are observed. Weathering of sulphide has given the quartz veins a stained, rusty appearance at surface exposures. Minor pyrite and chalcopryrite are disseminated in granodiorite clasts within the hydrothermal breccia zone. Sulphides are limited to <2% in the breccia, however, significant jarosite, a weathering product of sulphides (Bladh, 1982), occurs in the breccia matrix.

## **3.3.5 Veins**

### **3.3.5.1 Empress**

Veining is common in the Empress deposit, with alteration minerals typically grading from micro-vein infill into massive or brecciated textures. This is typically observed in quartz-dominated, quartz-magnetite and quartz-chlorite alteration, while other veins cut host alteration.

#### *Quartz veins*

Two generations of quartz veins have been identified at the Empress deposit: early and late quartz veins. The designation of “early” and “late” refers to the timing of emplacement of the quartz vein generation relative to each other and does not reflect their timing relative to mineralization or other processes that occurred at the Empress deposit.

Early quartz-veins most commonly occur in quartz-dominated and quartz-sericite alteration but may be present in all alteration types (Figure 3.17A). Vein thicknesses vary from less than 1 mm to greater than 10 cm and may be overprinted by sericite, chlorite, sodic or advanced argillic alteration minerals (Figure 3.17B) which likely formed after vein emplacement. Main-stage quartz veins have syntaxial textures or form composite veins hosting pyrite, chalcopyrite, molybdenite, muscovite or biotite in the vein centers. The presence of ore minerals within early veins suggests they formed synchronously with mineralization. Quartz-sericite-pyrite ± chalcopyrite veins cut potassic and phyllic alteration in the upper parts of many porphyry deposits (Gustafson and Hunt, 1975)

A second generation of quartz veins cut all other veins and alteration types. Late quartz veins are significantly thinner (<0.5cm) than main-stage quartz veins, host no mineralization and mainly occur in quartz-chlorite alteration. Their lack of ore minerals and lack of spatial association to the central Empress alteration zones indicate that late quartz veins have no significant connection to mineralization.

#### *Fe-oxide veins*

Fe-oxide veins are mainly developed in quartz-dominated, quartz-magnetite and quartz-sericite alteration. Veins are mm-scale thicknesses and composed of variable proportions of magnetite and hematite, with magnetite veining largely confined to zones of quartz-magnetite alteration. Hematite veins are often overprinted by siderite (Figure 3.17C). Fe-oxide veining can grade into breccias. Rare magnetite veins possess chlorite halos. Fe-oxide veinlets most commonly cut quartz-chlorite alteration.

#### *Chlorite ± calcite veins*

Chlorite veins occur in all alteration types except advanced argillic alteration. Vein thickness is restricted to mm-scale and often show composite textures with central calcite cores rimmed by chlorite (Figure 3.17D) and cut all mineralization and early alteration and vein phases (Figure 3.17E). Calcite may also occur independently of chlorite in veins and is observed to cut all alteration and mineralization phases.

### *Gypsum veins*

Gypsum veining is restricted to the quartz-sericite (Figure 3.17F), quartz-chlorite, sodic and advanced argillic alteration zones. They are generally 2-5 mm thick with regular orientations and spacings, and cut all other vein types except for late quartz veins. Gypsum veins are typically originally emplaced as anhydrite veins in porphyry systems during the waning stages of the hydrothermal system and later hydrated to gypsum by infiltrating ground waters (Gustafson and Hunt, 1975; Hezarkhani and Williams-Jones, 1998). Anhydrite is associated with late, feldspar-destructive alteration in most porphyry systems (Proffett, 2003).

#### **3.3.5.2 Taylor-Windfall**

Mineralization at Taylor-Windfall is hosted in a sulphide-rich and a tourmaline-rich vein. Price (1986) reports that both veins dip subvertically to the southeast and possess zones of open space filling textures up to 5 cm in thickness and the main tourmaline vein is sheared at one of the levels of underground workings. Tourmaline veinlets up to 2 mm thickness occur in quartz-sericite-pyrite-dominated alteration in drill core with typical vein densities of about 2 mm/5 cm. Pyrite occurs in both tourmaline veinlets and in the cores of siderite veins up to 5 mm thick. Illite fracture coating occurs with variable orientations. Chlorite veinlets up to mm scale thickness are present in quartz-chlorite-sericite alteration.

#### **3.3.5.3 Pellaire**

Five separate quartz veins were identified at the surface at Pellaire. A total of 10 veins have been identified from previous work, five of which have been at least partially mined out (Pezzot, 2005). At the surface, veins dip moderately to steeply towards the northwest (Figure 3.7), with thicknesses varying from ~30 cm - 2 m (Figure 3.13D). Brecciation of the hangingwall granodiorite overlying the veins is confined to within about 0.5 m from the veins (Figure 3.13E) and grades down to stockwork veining (Figure 3.13F). The lower contacts of the veins are faulted. The quartz veins extend into the hydrothermal breccia from the granodiorite (Figure 3.13G), but not into the Falls River succession. Veins in the hydrothermal breccia are offset by the fault separating the granodiorite from the breccia zone. Quartz veins cut basaltic dikes at Pellaire. Cu and Fe-oxides occur along the vein-dike contacts.

Similarities in orientations between the shallow, north-dipping faults within the Falls River succession and the quartz veins within the Mount McLeod granodiorite suggest the veins were emplaced into faults that extended into the granodiorite. The geometries of the faults are characteristic of an imbricate fan fault system (Figure 3.7), suggesting contractional deformation, which must have continued following vein emplacement as indicated by the faulted lower contacts of the quartz veins. Upper margins of veins are generally marked by brecciation of the hangingwall, with no indication of offset between the vein and the hangingwall.

### **3.3.6 Paragenesis**

#### **3.3.6.1 Empress**

Multiple overprinting relationships are observed between the different alteration units at Empress. Early, high-temperature alteration phases consist of quartz-dominated, quartz-magnetite and potassium silicate alteration. Quartz-dominated alteration must have formed at least partially before magnetite as indicated by the presence of magnetite-cemented quartz-dominated breccias (Figure 3.9E). However, in other areas, quartz and magnetite likely formed synchronously and occur as uniform to blotchy alteration. Potassium-silicate alteration is interpreted to have formed at the same time as quartz-magnetite alteration from similar fluids. The contrasting alteration styles between quartz-magnetite and potassium-silicate alteration is attributed to the physical and compositional differences between the Falls River succession (quartz-magnetite) and Empress pluton (potassium-silicate) protoliths. The pluton likely possessed greater potassium and lower permeability than the andesitic rocks of the Falls River succession. This caused higher, less alkaline fluid flow in the overlying country rocks.

The majority of mineralization occurs within high-temperature alteration zones, interstitially to quartz and magnetite (Figure 3.15E). Therefore, the bulk of mineralization likely formed after the high-temperature alteration assemblages, but before the majority of the moderate and lower temperature alteration assemblages.

Sodium-rich minerals (albite and paragonite) as well as potassium-rich minerals (muscovite and illite) typically occur interstitially to quartz and are interpreted to have formed after the bulk of the quartz-dominated alteration. Compositional differences between sodic and quartz-sericite alteration could be attributed to variable fluid compositions or variable host-rock compositions. The intensity of alteration at Empress prevents identification of original lithologies. Advanced argillic minerals such as andalusite, pyrophyllite, dickite and kaolinite

overprint all other alteration types. The fine-grained occurrence of sodic, quartz-sericite and advanced argillic alteration minerals inhibits the observation of textural relationships between the alteration zones. Advanced argillic, sodic and quartz-sericite alteration all possess both moderate to high temperature alteration minerals (eg. andalusite, albite and muscovite) and low temperature alteration minerals (eg. pyrophyllite, dickite, kaolinite, paragonite, montmorillonite and illite). It is interpreted that the higher temperature alteration minerals formed first in these alteration zones and were later overprinted by lower temperature mineral assemblages as the system cooled.

Chlorite occurs mainly around the periphery of the Empress deposit. It overprints muscovite and illite and occurs interstitially to magnetite and hematite (Figure 3.14 M, N). Chlorite is a late, retrograde overprint of alteration minerals at Empress. However, less altered rocks from Granite Creek, to the west of the deposit host similar alteration to some of the quartz-chlorite alteration at Empress. Therefore, some chlorite alteration may predate the Empress hydrothermal system and was overprinted by Empress alteration assemblages. Calcite and gypsum veining and alteration cut and replace all other alteration assemblages and are interpreted to have formed entirely post-mineralization.

A summary of the interpreted paragenesis of Empress is provided in Figure 3.18.

### **3.3.6.2 Taylor-Windfall**

High-temperature advanced argillic assemblages reported by Price (1986) and vuggy silica alteration at Taylor-Windfall are interpreted to be the earliest alteration phases at the deposit, although no cross-cutting relationships were observed in the field. The occurrence of pyrite within vugs in vuggy silica alteration indicates that vuggy silica formed prior to pyrite, which is mainly associated with tourmaline and quartz-sericite/intermediate argillic alteration. Price (1986) interpreted that high-temperature advanced argillic alteration was the earliest alteration phase and was overprinted by all subsequent alteration assemblages.

No tourmaline was observed in the central vuggy silica zone, but was commonly observed in the surrounding intermediate to advanced argillic alteration. Tourmaline typically occurs with pyrite (Figure 3.12) and within the mineralized veins at Taylor-Windfall (Price, 1986), and is interpreted to have formed with mineralization, but after the early, high temperature alteration phases.

Quartz-sericite/intermediate argillic and advanced argillic alteration assemblages occur around the central vuggy silica zone and may overprint tourmaline-pyrite alteration. Therefore these assemblages formed at least partly after mineralization. The intermediate and advanced argillic assemblages typically occur intermixed (Figure 3.12H) and formed synchronously. Retrograde alteration assemblages, such as illite, dickite and kaolinite, likely overprinted early higher temperature alteration minerals, such as pyrophyllite and muscovite, as fluids cooled.

Chlorite occurs as background alteration around the Taylor-Windfall deposit and intermixed with lower temperature alteration assemblages at the deposit. It may have been present at the deposit prior to mineralization and was overprinted by the intense alteration observed at Taylor-Windfall. However, it also occurs as a retrograde overprint on some micaceous minerals around the deposit and therefore also formed after mineralization at the deposit.

A summary of the interpreted paragenesis of the Taylor-Windfall deposit is provided in Figure 3.19.

### **3.3.6.3 Pellaire**

Alteration at Pellaire is not as intense or widespread as at Taylor-Windfall or Empress. All observed alteration assemblages at Pellaire are moderate to low temperature. Vein emplacement, mineralization, brecciation and alteration are all interpreted to have formed synchronously. Contractional faulting is inferred to have been active before, during and after the hydrothermal system at Pellaire was active. This is based on the similarities in orientations between the mineralized veins and observed contractional faults, and the faulted contacts of the veins and hydrothermal breccia. A summary of the interpreted paragenesis of the Pellaire deposit is provided in Figure 3.20.

## 3.4 GEOCHRONOLOGY

### 3.4.1 Methodology

Detailed analytical methodologies for  $^{40}\text{Ar}$ - $^{39}\text{Ar}$  geochronology and U-Pb geochronology in this study are described in Appendix B. The results are summarized in Table 3.2, and age plots are shown in Figure 3.12 and 3.14.

### 3.4.2 Empress Geochronology

#### 3.4.2.1 $^{40}\text{Ar}$ - $^{39}\text{Ar}$ samples

Six sets of mineral separates from the vicinity of the Empress deposit were submitted for  $^{40}\text{Ar}$ - $^{39}\text{Ar}$  isotope geochronology. Three samples were analyzed to date primary lithologic units, and three samples were analyzed to date secondary alteration minerals.

**07-SB-006-2** (location: 472 966 mE, 5 660 479 mN) is a chlorite-carbonate altered, plagioclase-phyric andesite taken from the ridge to the southeast of the Empress deposit. It is from a dike approximately one meter thick that cross-cuts the Empress pluton (Figure 3.9B) and consists of 5% euhedral, mm-sized plagioclase phenocrysts and 3% subhedral, mm-sized hornblende phenocrysts. The phenocrysts are set in a fine-grained groundmass dominated by plagioclase lathes which are variably overprinted by chlorite and calcite. Hornblende phenocrysts are also variably altered to chlorite. A mineral separate of hornblende was dated using  $^{40}\text{Ar}$ - $^{39}\text{Ar}$  geochronology and generated a plateau age of  $61.1 \pm 7.4$  Ma (Table 3.2; Figure 3.9B). The Plateau age has a low precision due to the low K content of the hornblende dated. This is likely attributed to significant chlorite replacement within the sample. This dike is interpreted to be of the same generation as the andesitic dikes that cut the Empress deposit. Despite the large error associated with the age, it corroborates that andesite dikes at Empress were emplaced post-mineralization.

**07-SB-008** (location: 473 597 mE, 5 660 791 mN) is a chlorite altered, megacrystic biotite-cemented pebble to boulder granodiorite breccia obtained from the ridge to the southeast of the Empress deposit (Figure 3.8C). The zone of brecciation is approximately 2 meters thick. The sample is composed of 70% clasts of the Mount McLeod granodiorite, which is a coarse-grained, equigranular granodiorite consisting of 50% subhedral feldspar, 25% anhedral quartz, 15%

anhedral biotite, 8% subhedral hornblende and up to 2% disseminated pyrite. Biotite and hornblende are variably altered to chlorite. The granodiorite clasts are cemented by subhedral biotite crystals between 0.5 and 2 cm in size. These crystals are typically fractures and moderately altered to chlorite. A mineral separate of biotite from the breccia cement was dated using  $^{40}\text{Ar}$ - $^{39}\text{Ar}$  geochronology and generated a plateau age of  $87.93\pm 0.59$  Ma (Table 3.2; Figure 3.9C). Only the final step yielded an erroneous age for the sample, all other steps generated accurate ages. This age is interpreted to reflect the age of alteration and mineralization.

**07-SB-016** (location: 471 561 mE, 5 661 666 mN) is a chlorite-carbonate altered, moderately feldspar-quartz-biotite phyric dacite sampled from the gulley surrounding Granite Creek, to the west of the Empress deposit. It consists of 20% subhedral to euhedral feldspar phenocrysts, 10% subhedral quartz phenocrysts and 8% subhedral biotite phenocrysts. Phenocrysts are typically 0.5 to 2 mm in size, with feldspars variably overprinted by carbonate and biotite variably altered to chlorite. A mineral separate of primary igneous biotite was dated using  $^{40}\text{Ar}$ - $^{39}\text{Ar}$  geochronology and generated a plateau age of  $53.8\pm 1.3$  Ma (Table 3.2; Figure 3.9A). The final two steps of the plateau age are high error, but the rest of the steps are reasonable. The plateau age is younger than expected for country rocks in the region. Ca/K ratios from the sample indicate that some hornblende may have been present with the biotite (T. Ullrich, personal communication, 2008). This suggests that hornblende may be replaced by biotite and therefore the age of the biotite represents a later hydrothermal event rather than the age of the host rocks. An alternate explanation is that the dacitic unit is a younger dike that intruded the country rocks of the Falls River succession. No contacts were observed between the dacite and the surrounding units. Judging from the lack of significant alteration in the majority of rocks surrounding Granite Creek, the unit is interpreted to be a dike.

**07-SB-073** (location: 468 683 mE, 5 659 184 mN) is a slightly clay-chlorite altered, fine grained biotite rhyolite sampled from west of the Empress deposit. The rhyolite is from a dike roughly 10 cm thick cutting through the Mount McLeod granodiorite. The dike is equigranular and consists of 50% anhedral feldspar crystals, 40% anhedral quartz crystals and 10% subhedral biotite crystals (all 0.1 to 0.8 mm in size). Feldspar and biotite crystals are slightly overprinted by clay and chlorite. A mineral separate of biotite from the dike was dated using  $^{40}\text{Ar}$ - $^{39}\text{Ar}$  geochronology and generated a plateau age of  $91.45\pm 0.51$  Ma (Table 3.2; Figure 3.9D). Low temperature steps generated young ages, indicative of Ar-loss, while higher temperature steps all

yielded highly accurate and precise ages. The rhyolite dike is interpreted to be of the same generation as the rhyolite dikes observed at the Empress deposit. Therefore, this age indicates that rhyolite dikes were emplaced prior to mineralization at the Empress deposit.

**07-SB-CS-013** (location: 471 890 mE, 5 661 590 mN) is an intensely muscovite-altered rock (Figure 3.17F) sampled from drill-core at the Empress deposit. It consists of 88% medium-grained muscovite, 4% anhedral quartz, 4% angular magnetite grains and 2% amorphous pyrite. Muscovite crystals are typically subhedral needles and radiating blades. The sample is also cut by wavy Fe-Oxide veins up to 0.5 mm thick. A muscovite mineral separate was dated using  $^{40}\text{Ar}$ - $^{39}\text{Ar}$  geochronology and generated a plateau age of  $86.66\pm 0.50$  Ma (Table 3.2; Figure 3.9F). The plateau age generated accurate and precise ages for all steps. This age likely reflects the age of quartz-sericite alteration at Empress.

**07-SB-CS-102** (location: 471 930 mE, 5 661 480 mN) is a potassium-silicate-altered, porphyritic granite of the Empress pluton obtained from drill-core at the Empress deposit (Figure 3.14C). The sample consists of 65% subhedral to euhedral feldspar phenocrysts, 20% anhedral quartz crystals, 10% anhedral biotite crystals and 5% angular Fe-Oxide blebs. Feldspar phenocrysts range from 2 to 6 mm in size and give the rock its porphyritic texture, while the rest of the minerals range from 0.2 to 2 mm in size. Biotite has replaced hornblende in the sample and is also in turn slightly altered to chlorite. A biotite mineral separate was dated using  $^{40}\text{Ar}$ - $^{39}\text{Ar}$  geochronology and generated an accurate plateau age of  $87.87\pm 0.47$  Ma from all heating steps (Table 3.2; Figure 3.9E). This age likely reflects the age of potassium-silicate alteration at Empress which is interpreted to have formed synchronously with mineralization.

#### **3.4.2.2 U-Pb samples**

One bulk sample of the Empress pluton was submitted for U-Pb isotope geochronology in order to constrain the crystallization age of the pluton.

**07-SB-GEO-02** (location: 471 890 mE, 5 661 590 mN) is part of the Empress pluton taken from drill-core at the Empress deposit (Figure 3.14C). The sample is coarsely-porphyritic granite consisting of 40% euhedral to subhedral feldspar phenocrysts, 2 to 10 mm in size, 10% biotite phenocrysts 0.5 to 2 mm in size and 5% pyrrhotite grains 0.5 to 1 mm in size. The phenocrysts

are set in a fine grained quartz-feldspar dominated groundmass that is slightly overprinted by carbonate and clay minerals. A zircon mineral separate was dated using U-Pb geochronology and generated a concordant age of  $87.0 \pm 1.4$  Ma (Table 3.2; Figure 3.11A, B).

### **3.4.2.3 Interpretation**

Felsic dikes were intruded into Falls River succession country rocks at 91-92 Ma, followed by emplacement of the Empress pluton at ~87-88 Ma. Both intrusive phases pre-date the hydrothermal system at Empress. Ages of secondary alteration minerals at Empress indicate that the hydrothermal system was active at 88-86 Ma relatively synchronously with the emplacement of the Empress pluton. This suggests that the Empress pluton may be genetically related to mineralizing fluids at Empress. However, the less intense but variable alteration within the Empress pluton, sharp, well-defined contact between the pluton and overlying rocks and well developed alteration zonation parallel to this contact, all indicate that at least the outer carapace of the pluton must have crystallized prior to mineralization in the vicinity of the deposit. Mineralizing fluids could still have been exolved from elsewhere in the pluton. Post mineralization andesite dikes were later intruded at ~61 and 54 Ma.

### **3.4.3 Taylor-Windfall Geochronology**

#### **3.4.3.1 $^{40}\text{Ar}$ - $^{39}\text{Ar}$ samples**

Two sets of mineral separates from the vicinity of the Taylor-Windfall deposit were submitted for  $^{40}\text{Ar}$ - $^{39}\text{Ar}$  isotope geochronology to date secondary alteration minerals.

#### *Sample descriptions*

**07-SB-020-2** (location: 457 336 mE, 5 662 001 mN) is a quartz-sericite-chlorite cemented, andesitic hydrothermal pebble breccia obtained from the gulley surrounding Battlement Creek near the Taylor-Windfall deposit. The zone of brecciation is approximately 1 meter thick. The zone is cement-dominated at its center and grades down into veining in the surrounding feldspar-phyrlic andesite interpreted to be part of the Powell Creek Formation. Clasts are typically angular and range from sand to boulder-sized. The cement is dominated by fine-grained quartz, sericite, alunite and chlorite. A mineral separate of sericite, which may have contained other clay minerals indistinguishable from illite, was dated using  $^{40}\text{Ar}$ - $^{39}\text{Ar}$  geochronology. It generated a

plateau age of  $87.1 \pm 1.1$  Ma (Table 3.2; Figure 3.9H). The plateau is saddle shaped which is indicative of excess argon (T. Ullrich, personal communication, 2008), and possesses only three accurate steps. Therefore, there is not a high level of confidence in the age, which is interpreted to represent formation of the hydrothermal breccia and should reflect the age of mineralization.

**07-SB-023-3** (location: 475 613 mE, 5 662 113 mN) is a layered quartz-illite-altered rock sampled from near the Taylor-Windfall minesite from a small area within the central zone of vuggy silica alteration. The layers are typically mm-scale in thickness and are composed exclusively of fine-grained quartz or illite with minor pyrite. The entire outcrop is strongly silicified and light yellow in colour. A mineral separate of illite from one of the illite layers was dated using  $^{40}\text{Ar}$ - $^{39}\text{Ar}$  geochronology and generated a plateau age of  $89.3 \pm 0.54$  Ma (Table 3.2; Figure 3.9G). The plateau age is not terribly well constrained because the sample was too radiogenic (T. Ullrich, personal communication, 2008). This represents the age of formation of quartz-illite alteration at Taylor-Windfall and is interpreted to reflect the age of mineralization.

### **3.4.3.2 Interpretation**

The  $^{40}\text{Ar}$ - $^{39}\text{Ar}$  ages obtained from Taylor-Windfall samples indicate that the Taylor-Windfall hydrothermal system was active from  $\sim 87$ - $89$  Ma, and thus overlapped with deposition of the Powell Creek Formation ( $\sim 96$ - $79$  Ma; Maxson, 1996).

## **3.4.4 Pellaire Geochronology**

### **3.4.4.1 $^{40}\text{Ar}$ - $^{39}\text{Ar}$ samples**

Two sets of mineral separates from the vicinity of the Pellaire deposit were submitted for  $^{40}\text{Ar}$ - $^{39}\text{Ar}$  isotope geochronology. One sample was intended to date alteration associated with mineralization, and the other to date displacement along one of the shallow dipping faults.

**07-SB-136-7** (location: 457 702 mE, 5 661 037 mN) is a highly quartz-carbonate-muscovite-alunite altered rock taken from a south-vergent fault on the eastern flank of the Pellaire Ridge. The fault is hosted within andesite belonging to the Falls River succession, and alteration intensity sharply decreases away from the fault. Primary textures are indiscernible in the sample and grain sizes vary from 0.1 to 1 mm in size. Mineral occurrence is relatively uniform,

consisting of roughly 40% quartz, 30% carbonates, 15% muscovite and 15% alunite. Alunite appears to overprint muscovite and both occur as euhedral, elongate lathes. A mineral separate of muscovite was dated using  $^{40}\text{Ar}$ - $^{39}\text{Ar}$  geochronology and generated a plateau age of  $84.52 \pm 0.58$  Ma (Table 3.2; Figure 3.9J). The plateau is reasonable and only the final two steps are inaccurate, potentially because the sample was highly radiogenic (T. Ullrich, personal communication, 2008). This age is interpreted to correspond to the contractional deformational event at the deposit, which was likely synchronous with the hydrothermal event at Pellaire.

**07-SB-173-1** (location: 457 696 mE, 5 660 944 mN) is a strongly muscovite-chlorite altered, coarse-grained equigranular granodiorite taken from a clast of the hydrothermal breccia on the eastern flank of Pellaire Ridge (Figure 3.13B). The granodiorite is from the Mount McLeod granodiorite and consists of 60% subhedral feldspar, 35% anhedral quartz and 5% amorphous pyrite. There is a pervasive muscovite on all minerals with muscovite crystals forming needles and radiating crystals up to 0.5 mm in size. There is also a weak chlorite overprint on some feldspar crystals. Granodiorite clasts in the hydrothermal breccia are typically subrounded and cobble- to boulder-sized. Muscovite is a prominent mineral in the cement of the breccia. A muscovite mineral separate was dated using  $^{40}\text{Ar}$ - $^{39}\text{Ar}$  geochronology and generated a plateau age of  $85.16 \pm 0.65$  Ma (Table 3.2; Figure 3.9I). All steps in the plateau are accurate and precise. The breccia is interpreted to have formed during the main hydrothermal event at Pellaire and likely represents the age of mineralization at the deposit.

#### **3.4.4.2 U-Pb samples**

One bulk sample of the Mount McLeod granodiorite, taken from east of Pellaire, was submitted for U-Pb isotope geochronology. It was intended to assess variability in crystallization ages from within the Mount McLeod Batholith by comparing the data with previous ages from Israel et al. (2006).

**07-SB-GEO-09** (location: 468 272 mE, 5 659 568 mN) is a sample of the Mount McLeod granodiorite taken from the Mount McLure area. It is coarse-grained and composed of 60% subhedral feldspar, 18% anhedral quartz, 10% anhedral biotite, 8% anhedral to subhedral hornblende, 2% elongate clinopyroxene lathes and 2% irregular Fe-Oxide blebs. Mafic minerals are variably replaced by chlorite. A zircon mineral separate was dated using U-Pb

geochronology and generated a concordant age of  $83.2 \pm 2.6$  Ma (Table 3.2; Figure 3.11C, D). There is significant error and variability with much of the data, therefore the accuracy of this age may be relatively low. Previous dating of the Mount McLeod Batholith in the Pellaire area generated ages of  $103.8 \pm 0.5$  Ma and  $101.1 \pm 0.3$  Ma (Israel et al., 2006). These ages suggest magmatism was active in the Mount McLeod Batholith for as much as 20 My. At Pellaire, the granodiorite is interpreted to have been emplaced prior mineralization at Pellaire and is not genetically related to the hydrothermal fluids responsible for the deposit.

#### **3.4.4.3 Interpretation**

The Falls River succession is the oldest unit in the Pellaire area and was deposited into the Tyaughton Basin during the Early Cretaceous. The succession was intruded by the Mount McLeod batholith at 104 Ma, which was subsequently intruded by a series of basaltic dikes (Figure 3.21A). Regional contractional deformation related to the closure and uplift of the Tyaughton-Methow Basin from 91 to 87 Ma (Figure 3.21B; Monger and Journeay, 1994) producing south-vergent thrust faults on Pellaire, which acted as permeable conduits for deeper seated fluids responsible for mineralization. This contractional deformation continued and overlapped with north-vergent faulting at the deposit; which correlates with deformation associated with East Waddington Thrust Belt to the northwest of the study area from 87 to 84 Ma (Figure 3.21C, D) (Rusmore and Woodsworth, 1994). Mineralization appears to be synchronous with contractional deformation at 85 Ma (Figure 3.21C) with fluids potentially migrating along either set of faults. A U-Pb date for zircons from the Mount McLeod Batholith from east of Pellaire yielded an age of  $83.2 \pm 2.6$  Ma (Table 2.2, Figure 3.11C, D) This is younger than data from Israel et al. (2006) of a U-P zircon age of the Mount McLeod Batholith near Pellaire of  $103.8 \pm 0.5$  Ma. This indicates that the Batholith was active for at least 20 My.

#### **3.4.5 Integration of Geochronological Data**

The ages of alteration minerals at Empress and Taylor-Windfall overlap. Therefore, the two systems are interpreted to have been active synchronously (~90-86 Ma). Geochronological data also indicates that Pellaire was active during the Late Cretaceous, but is slightly younger than the Empress and Taylor-Windfall deposits (~86-84 Ma). A summary of geochronological data for the three deposits is provided in Figure 3.22.

## 3.5 FLUID INCLUSIONS

Complete microthermometric analytical methodology and results for this study are presented in Appendix C.

### 3.5.1 *Empress Inclusions*

Microthermometric studies were performed on two main-stage quartz veins from the Empress Deposit in order to obtain approximate pressure-temperature-compositional (P-T-X) conditions of the hydrothermal system and ultimately mineralization. Main-stage quartz veins were selected because they contain ore minerals, which petrography suggests formed synchronously with ore deposition. The absence of inclusions showing crystal growth zonation prevented positive identification of primary inclusions.

Early quartz vein samples (07-SB-CS-044 - Figure 3.23A, and 07-SB-CS-117- Figure 3.23B) were collected, inspected for fluid inclusions and subsequently underwent microthermometric analysis in order to obtain P-T-X estimates of the hydrothermal system.

Early quartz vein samples from Empress inspected for fluid inclusions contain pyrite-chalcopyrite-muscovite (07-SB-CS-044) and pyrite-chalcopyrite-molybdenite (07-SB-CS-117) as well as biotite and Fe-oxide veining. The presence of ore minerals and high temperature alteration minerals within the veins indicates the veins formed synchronously with the high temperature alteration phase associated with mineralization. Quartz grain sizes vary from 0.1-5 mm, with coarser grains hosting larger inclusions appropriate for microthermometric analysis. Inclusion occurrence in finer grains is generally too dense to study individual inclusions. Coarser grains possess fewer inclusions, allowing for easier study of individual inclusions. Four types of fluid inclusions were identified in Empress samples:

- 1) Fine, monophasic liquid-rich inclusions are the most abundant type of inclusion and occur as planar arrays, which cross grain boundaries and cut all other inclusion types. They are interpreted as secondary and the youngest generation of inclusions. Monophasic inclusions are relatively round, less than 5  $\mu\text{m}$ , and unsuitable for microthermometry.

- 2) Relatively rare inclusions containing liquid, vapour and birefringent, accidental solids (L-V-S) were observed in one Empress sample (07-SB-CS-044; Figure 3.23C). Such inclusions are irregularly shaped and range from 10-30  $\mu\text{m}$ . Solid crystal contents within L-V-S inclusions are variable from 5-25 vol. %. Likewise vapour contents are variable from absent to 20 vol. %. Solid-bearing inclusions contained anywhere from one to five salt crystals. Some inclusions

possess cubic, halite crystals. Unfortunately, all solid-bearing inclusions either didn't exhibit phase changes during cooling or decrepitated at low temperatures during heating. As a result, microthermometric data obtained from these inclusions was unusable.

3) Liquid-vapour (L-V) inclusions are common in the Empress samples studied (Figure 3.23D) and assumed to be comprised mainly of H<sub>2</sub>O and NaCl. They are round to oval-shaped and vary from 3-30 μm in size, most are 5-10 μm in size. Vapour contents vary from 5-10 vol. %.  $T_{m(\text{ice})}$  measurements for L-V inclusions ranged from -17 to -0.1°C (mean =  $-4.7 \pm 3.5^\circ\text{C}$ , n = 43). The melting temperatures for ice correspond to salinities between 0.2 and 20.3 wt. % NaCl equiv. (mean =  $7.0 \pm 4.3$  wt % NaCl equiv., n = 43). L-V inclusions always homogenized into the liquid phase with  $T_{h(\text{total})}$  occurring between 128 and 263°C (mean =  $158.9 \pm 20.7^\circ\text{C}$ , n = 42) (Figure 3.24A).

4) Liquid-vapour-CO<sub>2</sub> (L-V-CO<sub>2</sub>) inclusions were also observed, but less common than liquid-vapour inclusions at the Empress Deposit (Figure 3.23E). L-V-CO<sub>2</sub> inclusions are inferred to be characterized by the H<sub>2</sub>O-NaCl-CO<sub>2</sub> system and are oval to irregular in shape and 5-30 μm in size, with most between 10-15 μm. Vapour contents vary from 10-25 vol. %.  $T_{m(\text{ice})}$  measurements for L-V-CO<sub>2</sub> inclusions range from -2.1 to -0.2°C (mean =  $-1.4 \pm 0.7^\circ\text{C}$ , n = 6) and  $T_{m(\text{clathrate})}$  measurements vary from 0.5 to 5.5°C (mean =  $2.7 \pm 1.6^\circ\text{C}$ , n = 7).  $T_{h(\text{total})}$  measurements range from 139 to 148°C (mean =  $143 \pm 3.5^\circ\text{C}$ , n = 5) (Figure 3.24A). The CO<sub>2</sub>-rich vapour phase always homogenized into the liquid phase. Salinity was calculated to be 5.33 wt. % NaCl equiv and  $X_{\text{CO}_2}$  to be 0.022 for L-V- CO<sub>2</sub> inclusions using the clathrate program of Bakker (2002).

Isochores were calculated for both L-V and L-V-CO<sub>2</sub> inclusions (Figure 3.24B). The L-V-CO<sub>2</sub> isochore yields higher trapping temperatures than L-V isochores.

### **3.5.2 Taylor-Windfall Inclusions**

A microthermometric study was performed on a sample (07-SB-023-2) of vuggy silica-altered rock obtained near the main mine site at Taylor-Windfall (Figure 3.25A) to establish P-T-X conditions of the hydrothermal system. No quartz veins were observed in outcrop or drill core. Although the vuggy silica zone is not associated with any mineralization, it hosts abundant pyrite within vugs. Therefore the vuggy silica zone formed prior to the majority of pyrite in the system, and likely pre-dates mineralization. A second sample of vuggy silica-altered rock (07-SB-023-3)

was also inspected for fluid inclusions but none were suitable for microthermometric analysis and will not be further discussed.

In the sample of vuggy silica-altered rock inspected for fluid inclusions, only areas immediately surrounding vuggy cavities contained inclusions appropriate for study (Figure 3.25B, C). Other areas contained dense concentrations of impurities, mineral inclusions and fluid inclusions, which obstructed vision and prevented study of individual fluid inclusions. This is contrasted by sparse fluid inclusions in crystals immediately surrounding vuggy cavities (Figure 3.25C). No crystal growth zonation patterns were evident from the inclusions, or under cathodoluminescence, so no fluid inclusions could be confidently identified as primary inclusions. Three types of inclusions were identified at Taylor-Windfall:

1) Monophase liquid inclusions at Taylor-Windfall are usually round, less than 4  $\mu\text{m}$  in size and not suitable for microthermometry. They occur randomly or form weak planar arrays, which do not cross grain boundaries, but cut all other inclusion types. Monophase inclusions are inferred to be late.

2) L-V inclusions are the most common fluid inclusion type appropriate for microthermometry (Figure 3.25D) and are typically round and 5-15  $\mu\text{m}$  in size. Their occurrence is random and isolated. Vapour contents vary from 5-10 vol. % in L-V inclusions.  $T_{m(\text{ice})}$  measurements for L-V inclusions ranged from -4 to 0°C (mean =  $-1.6 \pm 1.2^\circ\text{C}$ ,  $n = 18$ ), corresponding to salinities between 0 and 6.4 wt. % NaCl equiv. (mean =  $2.6 \pm 1.9$  wt % NaCl equiv.,  $n = 18$ ). L-V inclusions always homogenized into the liquid phase with  $T_{h(\text{total})}$  occurring between 100 and 168°C (mean =  $135.6 \pm 19.8^\circ\text{C}$ ,  $n = 18$ ) (Figure 3.24A).

3) L-V-CO<sub>2</sub> inclusions are significantly less common than L-V inclusions at the Taylor-Windfall Deposit (Figure 3.25E), generally oval-shaped and 5-15  $\mu\text{m}$  size, with most between 5 and 10  $\mu\text{m}$ . Vapour contents vary from 5-20 vol. %.  $T_{m(\text{ice})}$  measurements for L-V-CO<sub>2</sub> inclusions range from -2.0 to -0.8°C (mean =  $-1.3 \pm 0.5^\circ\text{C}$ ,  $n = 6$ ), while  $T_{m(\text{clathrate})}$  measurements vary from 0.1 to 1.8°C (mean =  $0.8 \pm 0.5^\circ\text{C}$ ,  $n = 12$ ) and  $T_{h(\text{total})}$  measurements from 108 to 132°C (mean =  $117.2 \pm 8.2^\circ\text{C}$ ,  $n = 5$ ) (Figure 3.24A). The CO<sub>2</sub>-rich vapour phase always homogenized into the liquid phase. Salinity was calculated to be 5.44 wt. % NaCl equiv and  $X_{\text{CO}_2}$  to be 0.019 for L-V-CO<sub>2</sub> inclusions using the clathrate program of Bakker (2002).

Isochores were calculated for both L-V and L-V-CO<sub>2</sub> inclusions (Figure 3.24B). The L-V-CO<sub>2</sub> isochore yielded higher trapping temperatures than L-V isochores.

### 3.5.3 Pellaire Inclusions

Microthermometric analyses were performed on four samples (07-SB-136-1, 07-SB-139-3, 07-SB-172-3 and 07-SB-172-7) from three separate quartz veins at Pellaire. Although no mineralization is evident at surficial exposures, all veins are reported to be mineralized at depth (Pezzot, 2005). Samples from the upper contact and the center of the largest vein at Pellaire (Figure 3.26A, B, C) were analyzed to assess variance across the width of the vein due to changes in fluid conditions during vein formation. Samples from two other veins (Figure 3.26D, E, F, G) were analyzed to assess variance between separate quartz veins at the deposit. The samples were all studied in an attempt to obtain approximate P-T-X conditions of the hydrothermal system. The absence of crystal growth patterns observed under transmitted light or cathodoluminescence prevented positive identification of any primary inclusions.

Fluid inclusions were examined in 14 doubly polished sections from five separate quartz veins at Pellaire. Most samples contained similar fluid inclusion assemblages. Four sections were selected for microthermometric analysis based on the vein they came from and inclusions they contained. Quartz vein samples from Pellaire contain minor oxides and have grain sizes from 0.5-2 mm size. Three types of fluid inclusions were identified.

1) Monophase liquid inclusions are abundant at Pellaire and form planar arrays (Figure 3.26H), which crosscut grain boundaries and are interpreted to be late. Monophase inclusions are round, typically 1-2  $\mu\text{m}$  in size and were not analyzed for microthermometry.

2) L-V inclusions observed at Pellaire have variable shapes and range from 5-20  $\mu\text{m}$  in size (average  $\sim 10$   $\mu\text{m}$ ) (Figure 3.26I). Their occurrence can be random, clustered or slightly planar. Planar arrays are not observed to cross grain boundaries. Vapour contents range from 5-10 vol. %.  $T_{\text{m(ice)}}$  measurements for L-V inclusions range from -9 to  $0^{\circ}\text{C}$  (mean =  $-3.3 \pm 1.4^{\circ}\text{C}$ ,  $n = 79$ ), corresponding to salinities of 0-12.8 wt. % NaCl equiv. (mean =  $5.1 \pm 2.2$  wt % NaCl equiv.,  $n = 79$ ). L-V inclusions always homogenized into the liquid phase with  $T_{\text{h(total)}}$  occurring between 125 and  $240^{\circ}\text{C}$  (mean =  $186.1 \pm 33.5^{\circ}\text{C}$ ,  $n = 71$ ) (Figure 3.24A).

3) L-V-CO<sub>2</sub> inclusions are more common than L-V inclusions at Pellaire, and have variable shapes and range from 5-25  $\mu\text{m}$  size (Figure 3.26J). Vapour contents vary from 10-25 vol. %.  $T_{\text{m(ice)}}$  measurements for L-V-CO<sub>2</sub> inclusions range from -10.9 to  $-0.1^{\circ}\text{C}$  (mean =  $-2.9 \pm 2.5^{\circ}\text{C}$ ,  $n = 21$ ) while  $T_{\text{m(clathrate)}}$  measurements vary from 3 to  $13^{\circ}\text{C}$  (mean =  $8.5 \pm 1.7^{\circ}\text{C}$ ,  $n = 133$ ) and  $T_{\text{h(total)}}$  measurements from 185 to  $325^{\circ}\text{C}$  (mean =  $246.1 \pm 34.2^{\circ}\text{C}$ ,  $n = 111$ ) (Figure 3.24A). The CO<sub>2</sub>-rich vapour phase always homogenized into the liquid phase. Salinity was calculated to

be 4.62 wt. % NaCl equiv and  $X_{\text{CO}_2}$  to be 0.027 for L-V-CO<sub>2</sub> inclusions using the clathrate program of Bakker (2002).

Isochores were calculated for both L-V and L-V-CO<sub>2</sub> inclusions (Figure 3.24B). L-V-CO<sub>2</sub> inclusions were trapped at higher trapping temperatures than L-V inclusions. Similarities in fluid inclusion characteristics observed between the samples analyzed, suggest vein-forming fluids at Pellaire were relatively uniform in composition through time and space.

## **3.6 ISOTOPES**

### **3.6.1 Methodology**

#### **3.6.1.1 Carbonate isotopic analyses**

Analyses were carried out by Janet Gabites at the University of British Columbia using the gas bench and a Delta PlusXL mass spectrometer in continuous flow mode. The  $\delta^{13}\text{C}$  (V-PDB) and  $\delta^{18}\text{O}$  (V-SMOW) results are corrected to V-PDB and V-SMOW based on an average of multiple analyses of NBS standards 18 & 19.

Samples were acidified with 99% Phosphoric Acid in helium-flushed sealed vials, and the headspace gas was measured in a helium flow. The analyses were corrected for fractionation using repeat analyses of UBC internal carbonate standards BN 13, BN 83-2, H6M. These have been calibrated against NBS international standards NBS 18 & 19. Fractionation corrections for equivalent  $\delta^{18}\text{O}$  and  $\delta^{13}\text{C}$   $\text{H}_2\text{O}$  isotopic values at 250°C were aided by Beaudoin and Therrien (2008).

#### **3.6.1.2 Oxygen and hydrogen isotopic analysis**

Oxygen isotopic compositions of 7 quartz samples and 2 whole rock samples were performed by Kerry Klassen at Queen's University in January 2008. Additional analyses on 13 hydrous silicate samples for oxygen and hydrogen isotopes and three pairs of quartz-magnetite mineral pairs were performed in May 2008. Analyses were carried out using a Bromine Pentafluoride extraction line and a Finnigan Mat 252 Mass spectrometer. Detailed methodology is described by Johns et al. (2006).  $\delta^{18}\text{O}$  and  $\delta\text{D}$  results have been corrected to Vienna standard mean ocean water (VSMOW). Fractionation corrections for equivalent  $\delta^{18}\text{O}$  and  $\delta\text{D}$   $\text{H}_2\text{O}$  isotopic values were aided by Beaudoin and Therrien (2008). Fractionation corrections were calculated at 300°C for quartz veins, 700°C for quartz alteration samples, and the following temperatures for hydrous alteration minerals: biotite (500°C), muscovite (350°C), illite and paragonite (250°C) and kaolinite and chlorite (200°C). These temperatures correspond to the estimated formational temperatures of the alteration minerals.

## **3.6.2 Empress Isotopes**

### **3.6.2.1 Carbonate isotopes of calcite veins**

Six calcite mineral separates from carbonate veins sampled from drill core were submitted for stable isotopic analysis of carbon and oxygen. Carbonate veins are dominantly composed of calcite but may also contain minor siderite and dolomite. Complete  $\delta^{18}\text{O}$  (V-SMOW) and  $\delta^{13}\text{C}$  (V-PDB) values for Empress samples are included in Table 3.3. Average  $\delta^{18}\text{O}$  (V-SMOW) values of 9.53‰ (std. dev = 1.92‰, n = 6), and  $\delta^{13}\text{C}$  (V-PDB) values of -9.46‰ (std. dev. = 1.37‰, n = 6) were generated for calcite from Empress calcite veins.

The  $\delta^{13}\text{C}$  and  $\delta^{18}\text{O}$   $\text{H}_2\text{O}$  data from calcite veins at Empress falls predominantly in between the field for primitive igneous rocks (i.e., the magmatic field of Sharp, 2006) and meteoric water values on a  $\delta^{13}\text{C}$  versus  $\delta^{18}\text{O}$  diagram (Figure 3.27). This suggests that the calcite veins at Empress precipitated from mixed magmatic and meteoric fluids.

### **3.6.2.2 Oxygen isotopes of quartz-veins**

Three quartz vein samples from drill core were submitted for stable isotopic analysis of oxygen, all of which contained significant sulphides (pyrite  $\pm$  chalcopyrite  $\pm$  molybdenite). The quartz veins yielded an average  $\delta^{18}\text{O}$  (V-SMOW) values of 8.5‰ (std. dev. = 0.1‰, n = 3). Three samples of quartz from quartz-magnetite alteration were also analyzed for oxygen isotopes and generated average  $\delta^{18}\text{O}$  (V-SMOW) values of 9.2‰ (std. dev. = 2.8‰, n = 3). Complete results for  $\delta^{18}\text{O}$  of quartz samples are available in Table 3.4.

$\delta^{18}\text{O}$   $\text{H}_2\text{O}$  isotopic evidence indicates that quartz-vein-forming fluids at Empress were dominantly meteoric in origin, while quartz from quartz-magnetite alteration formed from magmatic-dominated fluids (Figure 3.28A) (Ohmoto and Rye, 1979; Rollinson, 1993).

### **3.6.2.3 Oxygen isotopes of quartz-magnetite alteration**

Three pairs of quartz-magnetite mineral separates from Empress drill core were analyzed for their oxygen isotopic compositions in order to constrain temperatures and sources of fluids responsible for quartz-magnetite alteration. Oxygen isotope fractionation between mineral pairs that formed in equilibrium can provide information about the temperature at which the minerals

formed. Quartz-magnetite is one such mineral pair where quartz is typically enriched in  $\delta^{18}\text{O}$  relative magnetite (Perry et al., 1973).

Quartz-magnetite mineral pairs from samples 07-SB-CS-052, 07-SB-CS-123 and 07-SB-CS-150 generated  $\Delta^{18}\text{O}$  (VSMOW)<sub>(quartz-magnetite)</sub> values of 5.8‰, 0.5‰ and 6.2‰ respectively (Table 3.4). The fractionation factor for sample 07-SB-CS-123 is too low to generate a useable temperature from quartz-magnetite fractionation geothermometry. This is a sample of layered quartz-magnetite alteration. It is interpreted that the quartz and magnetite must not have formed in equilibrium in this sample; magnetite was likely deposited after the quartz as in magnetite-cemented quartz breccias at Empress. The other fractionation factors of 5.8‰ and 6.2‰ correspond to equilibrium temperatures of approximately 707°C and 678°C respectively using equations from Chiba et al. (1989) (Figure 3.28B). There is no observed textural evidence to suggest that quartz and magnetite in these samples did not form in equilibrium. Therefore, the isotopic values indicate that minimum peak temperature for quartz-magnetite alteration at Empress was approximately 700°C. This is also interpreted to be the overall peak temperature for the Empress hydrothermal system, which is relatively high temperature for porphyry systems (Gammons and Williams-Jones, 1997).

#### **3.6.2.4 Oxygen and hydrogen isotopes of alteration minerals**

Nine samples of hydrous alteration minerals were submitted for isotopic analysis of oxygen and hydrogen. Minerals from the potassium silicate (biotite), quartz-sericite (muscovite, illite), quartz-chlorite (chlorite), sodic (paragonite) and advanced argillic (kaolinite) alteration zones were submitted in order to assess variance in the isotopic composition between alteration minerals in the different alteration zones. This was done in order to determine likely sources for fluids responsible for the different alteration types and better understand the alteration paragenesis of the Empress deposit. A summary of oxygen and hydrogen isotopic data is provided in Table 3.5.

$\delta^{18}\text{O}$  and  $\delta\text{D}$   $\text{H}_2\text{O}$  isotopic evidence indicates that the majority of alteration minerals analyzed (biotite, muscovite, paragonite and chlorite) formed from magmatic fluids (Figure 3.29). Kaolinite and illite values fall between the magmatic field and meteoric water line from Rollinson (1993) and likely formed from a mixture of magmatic and meteoric waters. Muscovite and illite samples are enriched in  $\delta\text{D}$  relative to other alteration minerals, while kaolinite is depleted in both  $\delta\text{D}$  and  $\delta^{18}\text{O}$  compared to other alteration minerals at Empress.

### **3.6.3 Taylor-Windfall Isotopes**

#### **3.6.3.1 Oxygen isotopes of vuggy silica alteration**

One sample of quartz from vuggy silica-altered rock was submitted for stable isotopic analysis of oxygen. This sample yielded a  $\delta^{18}\text{O}$  (V-SMOW) value of 11.1‰ (Table 3.4).

The vuggy silica-altered sample from Taylor-Windfall generated  $\delta^{18}\text{O}$   $\text{H}_2\text{O}$  value that is transitional between magmatic and meteoric waters (Figure 3.28A). Therefore, it is interpreted that vuggy silica alteration at Taylor-Windfall formed from magmatic fluids partially diluted with meteoric waters typical of high-sulphidation epithermal systems.

#### **3.6.3.2 Oxygen and hydrogen isotopes of alteration minerals**

Two samples of hydrous alteration minerals from Taylor-Windfall were submitted for isotopic analysis of oxygen and hydrogen, with the goal of better constraining sources of hydrothermal fluids. An illite mineral separate taken from drill-core within quartz-sericite alteration generated a  $\delta^{18}\text{O}$  value of 10.0‰ (V-SMOW) and  $\delta\text{D}$  value of -82‰ (V-SMOW), while paragonite taken from immediately surrounding the vuggy silica alteration zone yielded a  $\delta^{18}\text{O}$  value of 7.8‰ (V-SMOW) and  $\delta\text{D}$  value of -72‰ (V-SMOW) (Table 3.5).

$\delta^{18}\text{O}$  and  $\delta\text{D}$   $\text{H}_2\text{O}$  isotopic evidence indicates that illite and paragonite formed from mainly magmatic fluids (Figure 3.29). The values fall on the periphery of the magmatic field from Rollinson (1993), which indicates there may have been some input of meteoric waters.

### **3.6.4 Pellaire Isotopes**

#### **3.6.4.1 Oxygen isotopes of quartz veins**

Three quartz vein samples and two wall-rock samples from Pellaire were submitted for stable isotopic analysis of oxygen. Samples were obtained from the upper contact and approximate center of the largest observed vein at Pellaire (Figure 3.13D) in order to assess isotopic variance across the width of the vein. Another sample was acquired from near the center of a separate quartz vein to evaluate isotopic variation between the veins. Samples taken from the margin and center of the largest vein generated  $\delta^{18}\text{O}$  (V-SMOW) values of 8.7‰ and 9.4‰, while the separate vein generated a value of 9.6‰ (Table 3.4).

$\delta^{18}\text{O}$  values from quartz veins indicate vein-forming fluids at Pellaire had a largely meteoric source (Figure 3.28A). There is no significant isotopic variation between the veins analyzed, but the  $\delta^{18}\text{O}$  value from the main vein margin is less than the sample taken from the center of the vein suggesting rock-buffering of vein forming fluids may have occurred.

#### **3.6.4.2 Oxygen and hydrogen isotopes of alteration minerals**

Two samples of hydrous alteration minerals from Pellaire were submitted for isotopic analysis of oxygen and hydrogen in order to better constrain the source of hydrothermal fluids at Pellaire. A muscovite mineral separate from the hydrothermal breccia on Pellaire generated a  $\delta^{18}\text{O}$  value of 6.1‰ (V-SMOW) and  $\delta\text{D}$  value of -77‰ (V-SMOW), while a separate muscovite separate taken from a south-vergent fault zone yielded a  $\delta^{18}\text{O}$  value of 5.5‰ (V-SMOW) and  $\delta\text{D}$  value of -66‰ (V-SMOW) (Table 3.5).

$\delta^{18}\text{O}$  and  $\delta\text{D}$   $\text{H}_2\text{O}$  isotopic values of Pellaire muscovite samples lie in between the magmatic field and meteoric water line from Rollinson (1993) (Figure 3.29). The values also fall within the metamorphic water field, indicating a potential input of metamorphic fluids into the hydrothermal system.

## 3.7 FISSION-TRACK THERMOCHRONOLOGY

### 3.7.1 Methodology

The fission-track dating methods are thermochronological methods that are used to constrain thermal histories of rocks (Reiners and Brandon, 2006). Fission tracks are defects in crystal lattices due to ionization damage resulting from the fission decay of  $^{238}\text{U}$  (Fleischer et al., 1975). Thermally activated diffusion allows for defects to migrate and anneal. However, below a certain temperature, the rate of damage due to fission decay exceeds the rate of damage annealing and fission tracks are retained (Ketcham et al., 1999). The low temperature thermal sensitivity of fission track thermochronometers means that they typically record the cooling history of a rock rather than the crystallization age of its minerals. In orogenic settings, these cooling ages can be applied to understand the uplift and erosional history of an area (Reiners and Brandon, 2006).

Bulk samples of intrusive lithologies were crushed and separated by ALS Chemex in Vancouver, B.C. Crushed samples were then sent to Ray Donelick at Apatite to Zircon, Inc. in Viola Idaho. Apatite mineral separates were dated using fission track dating methods. Detailed methodology is described by Reiners and Brandon (2006).

In this study, two thermochronometers [zircon fission track (ZFT) and apatite fission track (AFT)] have been implemented to understand the cooling history of the rocks in the Taseko Lakes Region. These thermochronometers have unique thermal retentions. As a result, each system has distinctive effective closure temperatures for specified cooling rates. For a cooling rate of  $10^{\circ}\text{C Myr}^{-1}$ , the effective closure temperatures for the thermochronometers applied in this study are: ZFT  $\sim 230^{\circ}\text{C}$  (Brandon et al., 1998) and AFT  $\sim 120^{\circ}\text{C}$  (Ketcham et al., 1999). These closure temperatures are only approximate and are variable depending on mineral compositions and alpha-damage of crystals (Reiners et al., 2004). If a constant geothermal gradient is used, effective closure temperatures correspond to effective closure depths for each thermochronometer. If a geothermal gradient of  $30^{\circ}\text{C/km}$  (typical of volcanic arc-environments) is assumed for the Taseko Lakes Region, approximate effective closure depths for the two thermochronometers in this study are: ZFT  $\sim 8\text{km}$  and AFT  $\sim 4\text{km}$ . Therefore, cooling age dates provided by the separate thermochronometers correspond to the times at which the rocks were exhumed above these depths. Depth constraints can then be applied to the rocks at given ages based on which thermochronometers were below their effective closure temperatures and which did not retain their decay products until a later time.

### 3.7.2 Results

Three samples from the Empress Area were analyzed using the four thermochronometers described above. 07-SB-GEO-02 is part of the Empress pluton taken from drill-core at the Empress deposit from an elevation of 1425m and generated thermochronological dates of: ZFT =  $94.7 \pm 9.2$  Ma; AFT =  $33.3 \pm 5.0$  Ma; (Table 3.6). 07-SB-GEO-04 is a sample of the Mount McLeod granodiorite taken from the ridge to the southeast of the Empress deposit from an elevation of 2000 m: ZFT =  $94.7 \pm 9.6$  Ma; AFT =  $40.8 \pm 4.8$  Ma; (Table 3.6). 07-SB-GEO-12 is also a sample of the Mount McLeod granodiorite taken from the ridge to the southeast of the Empress deposit from an elevation of 2600 m and produced thermochronological dates of: ZFT =  $92.5 \pm 9.0$  Ma; AFT =  $55.6 \pm 6.6$  Ma; (Table 3.6).

AFT data indicates the rocks underlying the Empress deposit did not cool below 120°C until 33 Ma. Likewise, rocks on the ridge to the south of Empress did not cool below 120°C until roughly 55 Ma and indicate they were buried to at least 4km depth prior to 55 Ma. Since this sample was taken from approximately 1km in elevation above the Empress deposit, it suggests that Empress must have been buried to a depth of 5km if the elevation difference between the two samples is accounted for.

The ages generated from ZFT data are within error of the interpreted age of the Empress hydrothermal system, and emplacement of the Empress pluton. Therefore, the ZFT dates are interpreted to reflect the cooling age of the Empress pluton. Since the overall system cooled relatively rapidly below 230°C, the ambient temperature must have been below 230°C, and Empress must not have been buried to depths greater than roughly 8 km.

Pellaire, like Empress, is hosted in the Falls River Succession. Previous regional stratigraphic studies indicate the Falls River succession was overlain by the Late Cretaceous Taylor Creek Group and Powell Creek Formation. The Taylor Creek group has an estimated thickness of 2-4 km (Garver, 1992), the Powell Creek Formation is approximately 3-4 km thick (Maxsom, 1996; Schiarizza et al., 1997) and the Falls River Succession is roughly 1 km thick (Israel et al., 2006). The Powell Creek Formation was actively being deposited during mineralization at Empress and Pellaire. Therefore a thickness of 2-3 km is assumed for the Formation at the time of mineralization. The Falls River succession should have been between roughly 4 and 8 km depth based on the known thickness of overlying stratigraphy during the Late Cretaceous. Thermochronological data, which indicates that Empress formed at roughly 5 to 8 km depth is supported by known stratigraphic constraints (Figure 3.35).

However, contractional deformation in the region could have resulted in deeper burial of the succession. Contractional deformation occurred in the Taseko Lakes Region from 91 to 84 Ma (Umhoefer et al., 1994; Schiarizza et al., 1997). The Empress deposit is interpreted to have formed at approximately 87-88 Ma. Therefore, contractional deformation continued after mineralization had occurred at Empress. This contractional deformation could have resulted in deeper burial of the Empress system following mineralization as a result of the thrusting of material overtop of the deposit. The thermochronological data likely reflect the maximum burial depth of the system, which may have been reached following the mineralizing event. Therefore, if contractional deformation is taken into account, Empress may have formed at depths shallower than 5km.

## **3.8 INTERPRETATION**

### **3.8.1 Empress**

#### **3.8.1.1 Deposit classification**

Previous studies have interpreted the Empress deposit to be an oxidized, calc-alkalic porphyry Cu deposit (Lambert, 1991; Osborne, 1994, 1999). Relative timing of alteration, mineralization, veining and dike emplacement are presented in Figure 3.18. Although Empress exhibits porphyry-style alteration and mineralization, the parts of the deposit examined in this study possess several characteristics atypical of most porphyry deposits: 1) sub-horizontal alteration zonation, 2) complete replacement of host rocks, and abundant quartz alteration, 3) lack of high temperature fluid inclusions, and 4) the presence of both potassium-rich and sodium-rich alteration zones.

#### **3.8.1.2 Alteration zonation**

Alteration zonation at the Empress deposit is characterized by sub-horizontal layering, rather than the more typical concentric shells expected for porphyry deposits (Figure 3.3) (Lowell and Guilbert, 1970; Holiday and Cooke, 2007). The most important physical factors determining the evolution of hydrothermal system are the magmatic heat supply and the permeability structure (Hurwitz et al., 2003). Permeability controls in the Empress system must have forced hydrothermal fluids to migrate laterally.

Pre-existing anisotropies in the country rock (e.g., bedding), are interpreted to be responsible for the layered quartz-magnetite alteration may have also imposed controls on hydrothermal fluid flow. Foliations in altered rocks at Empress were rare and no foliations were observed in the rocks in Granite Creek. Anisotropies may have been present in the Empress host rocks, however have been obliterated by the intense alteration. Fluids may have been focussed existing anisotropies in the Falls River succession, but it is unlikely that host rock anisotropies alone were able to effectively focus lateral fluid flow at Empress.

Fractures that migrate outwards from source intrusions in porphyry deposits commonly occur as a result hydrofracturing of the crystallized carapace of the intrusion due to overpressuring of hydrothermal fluids contained within the intrusion (Driesner and Geiger, 2007). Hydrofractures create the permeability required by fluids to migrate out of the source intrusion into the surrounding country rocks. Shallow dips to fractures would have focused fluids laterally. No regular fracture sets were observed in Empress drill core. However, the intense

alteration at Empress suggests that any fractures present at the start of the hydrothermal system would have subsequently annealed.

Hydrothermal fluids are typically more buoyant than host rocks, and therefore upward flow is expected. In order to maintain a lateral fluid flow in a hydrothermal system, either upward flow must be impeded, or conditions favouring horizontal flow exist. Impermeable flat-lying boundaries such as well developed bedding in host rocks, flat lying impermeable sills or overlying rock units could act as impermeable layers and prevent fluid ascent. Alternatively, fluid flow in compressional stress regimes is commonly parallel to the primary compressive stress, which is subhorizontal in most fold and thrust belts (Husson and Moretti, 2002). Topographic variations, which are common in fold and thrust belts, may also drive hydraulic gradients, causing lateral fluid flow (Oliver, 1986). Contractional deformation as interpreted for the SECB during the Late Cretaceous (Rusmore and Woodsworth, 1991b) can create flat lying permeable conduits such as faults which allow for lateral fluid flow. If a large permeable conduit such as a fault was present to the south of the deposit, it could also have provided the hydraulic head required to drive fluid flow from the source intrusion, through the country rocks at the deposit, to the conduit to the south of the deposit.

The flat contact of the underlying, less-altered, low permeability Empress pluton is interpreted to have controlled lateral fluid flow. In the upper crust, country rocks typically possess much higher permeabilities than crystallizing intrusions (Dreisner and Geiger, 2007). Alteration is significantly less intense in the Empress pluton and suggests that fluids were not able to effectively infiltrate the pluton and were subsequently focused through the overlying rocks. Alternatively, if fluids were exolved from a separate part of the Empress pluton and experienced negligible mixing with external fluids and buffering by wallrocks, they would have remained in relative equilibrium with the rocks of the Empress pluton. The variety of alteration types observed in the Empress pluton (potassium-silicate, quartz-sericite, advanced argillic) indicate that hydrothermal fluids at the Empress deposit were not in chemical equilibrium with the Empress pluton. The deposit sits within a trough on top of the Empress pluton (Figure 3.4). If fluid ascent was prevented, or magmatic fluids were less buoyant than overlying fluids, magmatic fluids would have likely pooled and been further concentrated in this trough.

Potentially only a small part of a larger overall system has been examined at Empress. This suggests that on a larger scale, fluid flow may have been more vertical, but the zone observed at Empress possess locally horizontal flow.

### **3.8.1.3 High water-rock ratios**

Extensive replacement of primary rock components entirely by quartz requires very high water-rock ratios (Reed, 1997). This typically requires water:rock ratios of >1:1 (Reed, 1997; Dreisner and Geiger, 2007), which in turn requires high permeabilities of host rocks. Once temperatures reach 350 to 400°C, quartz-rich rocks behave ductilely and their permeabilities decrease substantially (Fournier, 1999). The lack of regional metamorphism in the Taseko Lakes Region indicates that country rocks never reached these conditions. The rocks at the Empress deposit were likely heated during the emplacement of the Empress pluton. There is no evidence suggesting that the Empress pluton directly exolved significant volumes of fluids at the deposit, however, fluids could have been released from the overlying rocks resulting from contact metamorphism. These fluids then would have migrated upwards, away from the Empress pluton, causing some alteration in the overlying rocks. This may be how quartz-chlorite alteration developed at the deposit. This style of alteration can take place at relatively low temperatures (<350°C), allowing host rocks to maintain high permeabilities.

If the Empress pluton did not exolve any fluids at the Empress deposit, heat transfer would have been conductive between the pluton and Falls River succession. Conductive heat transfer is much slower than advective heat transfer (Dreisner and Geiger, 2007), thus if timescales were relatively short between the emplacement of the Empress pluton and the infiltration of hydrothermal fluids at the Empress deposit, heat transfer between the pluton and overlying rocks would not have been extensive. Therefore, country rocks at the Empress deposit were at a relatively low temperature (<350°C) prior to the infiltration of magmatic-hydrothermal fluids. Permeable, subhorizontal fractures emanating from the source intrusion and focusing of fluids by the impermeable underlying Empress pluton allowed for high volumes of fluids to infiltrate the Empress system and produce the intense and widespread silicification observed at the deposit. The presence of pre-existing fractures at the deposit would have greatly increased the permeability of the system and aided in the accommodation of high fluid flux.

### **3.8.1.4 Hydrothermal fluid sources**

Fluid inclusion and stable isotopic evidence indicates that Empress was dominated by an initial magmatic fluid. Magmatic fluids were responsible for high-temperature (quartz-dominated and quartz-magnetite) alteration. As these fluids cooled and increased in acidity they then formed quartz-sericite and finally advanced argillic alteration.

Oxygen and hydrogen isotopic data from biotite samples indicate that initial high-temperature alteration formed from magmatic fluids. All later alteration minerals are more depleted in  $\delta^{18}\text{O}$ , which suggests that there was an input of meteoric water into the system, which diluted the magmatic fluids. Moderate temperature alteration minerals such as muscovite and paragonite still possess a magmatic isotopic signature, but low temperature alteration minerals (illite and kaolinite) possess isotopic signatures in between that of magmatic and meteoric waters. A progressive input of meteoric water into the system occurred as it cooled. The isotopic signatures from alteration minerals at Empress are broadly magmatic, indicating there was only limited mixing of magmatic fluids with meteoric water.

Oxygen isotopic data from samples of quartz from high temperature quartz-magnetite alteration shows that high-temperature fluids at Empress were magmatic, whereas isotopic evidence suggests that fluids responsible for main-stage quartz veins had a significant meteoric component. The presence of significant  $\text{CO}_2$  in fluid inclusions from main-stage quartz veins at Empress indicates that there was also a significant magmatic component. Likewise, carbon and oxygen isotopic data from calcite veins shows that carbonate veins at Empress formed from mixed magmatic-meteoric fluids.

Sodic alteration and quartz-sericite alteration are interpreted to have formed relatively synchronously. Quartz-sericite alteration (muscovite and illite) is significantly more enriched in  $\delta\text{D}$  relative to sodic (paragonite) and advanced argillic (kaolinite) alteration. Since fluids are interpreted to have initially been exclusively magmatic, and meteoric water input was not extensive, there must have been some segregation of existing fluids into separate sodium-rich and potassium-rich phases at Empress to generate the discrepancies in isotopic signatures of the lower temperature alteration phases.

The chlorite separate analyzed for oxygen and hydrogen isotopes also exhibits a magmatic isotopic signature, and is interpreted to have formed from relatively cool magmatic-dominated fluids around the periphery of the hydrothermal system. These fluids may also have had a minor meteoric component.

Isotopic and fluid inclusion evidence indicates that the Empress hydrothermal system consisted of an initial magmatic fluid phase followed by a gradual input of meteoric water into the system which cooled and diluted the magmatic-hydrothermal fluids. Mineralization at Empress is interpreted to be genetically related to the Empress pluton, which is one of the intrusive phases of the CPC.

### 3.8.1.5 Hydrothermal fluid evolution

Potassium-silicates, quartz and magnetite are all alteration minerals characteristic of high-temperature potassic alteration (Lowell and Guilbert, 1970; Ulrich and Heinrich, 2001). Therefore, quartz-dominated, quartz-magnetite and potassium silicate alteration comprise the high temperature alteration assemblages at the Empress deposit. Brecciation of quartz-dominated and quartz-magnetite alteration by magnetite was likely aided by the dissolution of primary components coupled with high pore-fluid pressures of hydrothermal fluids that leached host lithologies.

The abundance of magnetite at Empress suggests that initial hydrothermal fluids responsible for quartz-magnetite alteration were relatively oxidized and high-temperature (Simon et al., 2000). Quartz-magnetite oxygen isotope geothermometry indicates that fluids responsible for quartz-magnetite alteration were roughly 700°C. This was likely the peak temperature for the hydrothermal system and other alteration assemblages formed at temperatures lower than this.

Potassic alteration forms in the cores of porphyry systems as a result of the infiltration of hydrothermal fluids, which are sulphide-undersaturated but capable of dissolving most rock-forming components. The absence of potassium feldspar within intensely altered country rock at Empress indicates that fluids were at least mildly acidic ( $\text{pH} < 6$ ) (Figure 3.30A). Silicification of host rocks reduced their buffering capacities (Hedenquist and Hemley, 1985) and permitted fluids to increase in acidity. This is consistent with the lack of potassium-silicate alteration in the Falls River succession. If fluids weren't able to effectively infiltrate the Empress pluton, the buffering capacity of the pluton would have remained high, allowing for the formation of potassium-silicate alteration. Whereas fluids in the Falls River succession would have increased in acidity as they cooled if they were not buffered by host rocks (Giggenbach, 1997; Reed, 1997). Increased fluid acidity would have prevented the formation of potassium feldspar (Brimhall and Ghiorso, 1983; Gammons and Williams-Jones, 1997).

Quartz-sericite alteration at Empress correlates with phyllic alteration typical of porphyry systems. Phyllic alteration forms during the cooling of magmatic fluids responsible for potassic alteration (Harris and Golding, 2002). Cooling of magmatic fluids may or may not be coupled by mixing with external fluids (Gustafson and Hunt, 1975). Fluids cooled to  $<300^\circ\text{C}$  to produce illite (Figure 3.30B, C) (Hedenquist et al., 1998). Cu-Fe sulphides commonly precipitate between 550 and  $300^\circ\text{C}$  (Field et al., 2005), therefore most ore deposition likely occurred prior

to phyllic alteration. This is consistent with the predominant association of mineralization to quartz-magnetite and quartz-dominated alteration.

Sodic alteration results from sodium-rich fluids (possessing a high  $a(\text{Na}^+/\text{K}^+)$ ) and facilitates the formation of the sodium-rich minerals (albite, paragonite and montmorillonite) (Figure 3.30C). Albite forms first when fluids were hot, and was likely overprinted by paragonite and montmorillonite as fluids cooled.

Advanced argillic alteration requires high acidity fluids. Highly acidic fluids may result from cooling of magmatic fluids in the absence of host-rock buffering (Harris and Golding, 2002) and/or from the dissolution of sulphides in the central alteration zones by infiltrating fluids, resulting in the production of  $\text{H}_2\text{SO}_4$  (Brimhall and Ghiorso, 1983). Advanced argillic alteration overprints mineralization at Empress as indicated by a lack of sulphides present in the alteration zone. A  $\text{pH} < 4$  is required for the formation of kaolinite and dickite (Drews-Armitage, 1996). The presence of andalusite within the advanced argillic alteration zone implies that peak temperatures for fluids must have been at least  $360^\circ\text{C}$  (Figure 3.30B, C). At these temperatures, confining pressures could not have exceeded 200 MPa to form andalusite (Figure 3.30D). Dickite-kaolinite assemblages form at lower temperatures ( $200\text{-}300^\circ\text{C}$ ) and indicate that fluids were at quartz saturation (Hedenquist and White, 2005). Pyrophyllite is an intermediate between andalusite and kaolinite-dickite, and formed as fluids cooled from  $350$  to  $200^\circ\text{C}$  (Sand et. al, 1957; Ames et. al, 1991).

In porphyry systems, chlorite preferentially replaces mafic minerals due to the infiltration of low temperature ( $<300^\circ\text{C}$ ), low acidity fluids through the hydrothermal system (Dilles and Einaudi, 1992). The abundance of quartz in quartz-chlorite alteration requires high water-rock ratios during formation (Reed, 1997). The absence of epidote, albite, actinolite and carbonates in quartz-chlorite alteration indicates that this style of alteration does not correspond to the propylitic alteration zone (Martinez-Serrano, 2002).

The association of Cu-sulphides with the high-temperature alteration zones suggests that ore deposition occurred at predominantly potassic (high temperature) alteration conditions and transitional conditions between potassic and phyllic alteration. The presence of magnetite, pyrite and pyrrhotite in mineralized zones indicates that fluids were oxidized at the time of ore deposition (Figure 3.31A, B) (Barton and Skinner, 1979). Oxidized porphyry systems are more common than reduced porphyry systems (Rowins, 1999).

Ore deposition in porphyry systems can result from buffering of fluids by wallrocks, boiling of fluids due to sharp drops in confining pressure or from dilution, mixing or cooling of

fluids (McMillan and Pantelyev, 1988; Gammons and Williams-Jones, 1997; Seedorf and Einaudi, 2004). The abundance of quartz and lack of potassium-feldspar associated with mineralized zones suggests that little buffering of fluids occurred during ore deposition. There is no evidence from fluid inclusions or vein textures that fluids boiled at Empress. Mineralization occurs predominantly in the “potassic” alteration zone at Empress, which is interpreted to have formed from predominantly magmatic fluids (Dilles and Einaudi, 1992), giving no indication that fluid mixing occurred during ore deposition. Precipitation of Cu-bearing sulphides is interpreted to have resulted from cooling of ore-bearing fluids alone. Cooling of the system favoured the precipitation of pyrite over pyrrhotite, because pyrite is favoured by lower temperatures (Seedorff and Einaudi, 2004), which explains the restricted occurrence of pyrrhotite relative to pyrite.

#### **3.8.1.6 Hydrothermal fluid characteristics**

Quartz-sericite-pyrite ± chalcopyrite veins, similar to early Empress quartz veins, cut potassic and phyllic alteration in many porphyry deposits (Gustafson and Hunt, 1975). Such veins are typically formed by fluids of low to intermediate salinity (Hedenquist et al., 1998; Watanabe and Hedenquist, 2001). This is consistent with the fluid inclusion assemblages observed in main-stage quartz veins at Empress.

No observed fluid inclusions in Empress quartz veins homogenized into the vapour phase during heating. This indicates that fluids responsible for early quartz vein formation at Empress were liquid. Therefore, confining pressures likely remained high (i.e. above hydrostatic) during the hydrothermal event at Empress (Figure. 3.45B; Ahmad and Rose, 1980). Based on best estimates from previous regional stratigraphic studies, the Falls River succession was likely overlain by 3.5-6 km of volcanic and sedimentary rocks during the Late Cretaceous (Garver, 1992; Maxson, 1996; Schiarizza et al., 1997). Therefore, Empress likely formed at 3.5-6 km depth. If a lithostatic pressure gradient (33 MPa/km; Hagemann and Brown, 1996) is assumed for the Empress system these depths correspond to pressures from 100-200 MPa. If the stated pressure constraints are applied to calculated isochores, L-V-CO<sub>2</sub> inclusions were trapped at temperatures from 280-340°C, which are too low to represent peak temperatures for any “normal” porphyry systems. Therefore fluid inclusions at Empress are interpreted to have formed after peak hydrothermal conditions and only place minimum temperature constraints on the system. Isochores calculated for L-V inclusions yielded lower temperatures than for L-V-CO<sub>2</sub> inclusions, indicating L-V inclusions formed after L-V-CO<sub>2</sub> inclusions. Isochores also

suggest the hydrothermal system was active to temperatures as low as 190°C. This is corroborated by the presence of kaolinite in the system.

Halite saturated inclusions commonly occur in porphyry deposits and are interpreted to be trapped at high temperatures (>450°C; Hedenquist et al., 1998). Halite-saturated inclusions are not observed at Empress. Therefore either vein-forming fluids did not reach 450°C or high salinity inclusions were destroyed during lower temperature recrystallization. Some porphyry systems possess only low to moderate salinity (5 to 10% NaCl) and CO<sub>2</sub>-rich inclusions (Larson, 1987), which are abundant at Empress. Homogenization temperatures exhibited by Empress inclusions are lower than typical for potassium-silicate zones for porphyry Cu deposits (Figure 3.32A; Vila et al., 1991) and likely formed during the later stages of the hydrothermal system. Even so, such fluids can be derived directly from magmas at high temperatures (up to 700°C) if boiling does not occur (Ahmad and Rose, 1980). Low- to moderate salinity liquids in porphyry systems can also form from the condensation of a low-salinity vapour phase due to cooling (Heinrich, 2007). In other porphyry systems, CO<sub>2</sub>-rich fluid inclusions are also reportedly associated with low to moderate-salinity inclusions as they are in the Empress deposit (John, 1989; Ren et al., 1995). CO<sub>2</sub> preferentially partitions into the vapour phase during phase separation of liquid fluids (Williams-Jones and Heinrich, 2005). Therefore, if main-stage quartz veins at Empress formed from liquids previously condensed from vapour, it is expected that these fluids would contain an increased concentration of CO<sub>2</sub>.

The absence of high-temperature or high-salinity fluid inclusions in early-quartz veins at Empress indicates that these veins either formed after peak hydrothermal conditions, or high temperature fluid inclusions were destroyed during retrograde processes in the veins. High-temperature, hypersaline fluids were likely present in the Empress hydrothermal system, however are not preserved in any observed samples. Veins similar to main-stage quartz veins at Empress cut upper parts of many porphyry copper deposits (Gustafson and Hunt, 1975; Hedenquist et al., 1998), and typically possess only low- to moderate-salinity aqueous fluid inclusions. Williams-Jones and Heinrich (2005) propose that such veins form from aqueous fluids previously condensed from a vapour phase. A vapour phase is produced when an initial one-phase high salinity magmatic fluid undergoes two phase separation into a low-salinity vapour phase and a high-salinity aqueous phase. Boiling in the porphyry environment occurs at high temperatures (>450°C) due to decreases in confining pressure resulting from expansion and hydrofracturing of host rocks. CO<sub>2</sub>, sulphur species and metals all preferentially enter the vapour phase during phase separation (Heinrich, 2007). Previous fluid inclusion microanalyses of

porphyry ore samples show that vapour-like fluids of low to intermediate salinity and density (~1-10 wt% NaCl eq.) can carry up to percentage-level concentrations of copper and several ppm gold at high temperature and pressure (Heinrich, 2005). As the vapour phase cools, it precipitates metals and sulphur species as ore minerals and once again condenses, leaving a low- to moderate-salinity, potentially CO<sub>2</sub>-rich aqueous fluid, much like the inclusions observed in main-stage quartz veins at Empress. If boiling had not occurred in the Empress system, aqueous inclusions would likely possess higher salinities. Vapour-rich inclusions were not observed in Empress samples, therefore no vapour phase was present during the trapping of Empress inclusions in main-stage quartz veins. The presence of CO<sub>2</sub>-rich inclusions supports that L-V-CO<sub>2</sub> fluid inclusions are part of a previously condensed vapour phase. Empress fluids must have boiled and the vapour phase later re-condensed prior to trapping in order to produce the observed fluid inclusion assemblages. Boiling was triggered by drops in pressure caused by hydrofracturing and thermal expansion of the country rocks (Williams-Jones and Heinrich, 2005). Therefore, main-stage quartz veins were emplaced after peak conditions when magmatic vapours had cooled sufficiently to re-condense (280-340°C based on isochore data).

### **3.8.1.7 Fluid flow direction**

Based on the distribution of higher temperature sulphide minerals (pyrrhotite and bornite), hydrothermal fluids likely flowed southeastward and upward through the trough created by the upper margin of the Empress pluton (Figure 3.33). This indicates the fluids originated from a source intrusion to the northwest. Limited drilling has been performed to the northwest of the deposit, therefore the unidentified source intrusion maybe be located within a few hundred meters of the deposit.

Quartz-chlorite alteration is interpreted to be the least intense alteration type at the Empress deposit. It either formed due to the heating of external fluids as they migrated proximal the hydrothermal system at Empress, or it pre-dates mineralization and is overprinted by all later alteration types. In either case, it serves as a marker for areas of low hydrothermal fluid flow. Much of the quartz-chlorite alteration occurs in the upper part of the deposit. This is consistent with the idea that fluids pooled in the trough created by the upper margin of the Empress deposit. Therefore it is expected hydrothermal fluid flow volumes should have decreased away from the pluton contact. The southeastern part of the deposit is also dominated by quartz-chlorite alteration, indicating that high volumes of hydrothermal fluids were also not able to infiltrate that part of the system. Fluid flow was dominantly directed to the southeast, Empress fluids had

largely ceased to migrate by the time fluids reached the southeastern part of the system. Since high fluid flows and water-rock ratios are expected for the Empress system, it is unlikely that fluid flow could stop so abruptly without the influence external influences. Either a separate generation of fluids migrated to the northwest and prevented continued migration of Empress fluids, or perhaps Empress fluids lacked the pressure head or buoyancy required to climb the steepening contact of the underlying Empress pluton. Fluids could have also escaped along an unidentified permeable structure to the south of the deposit.

### **3.8.1.8 Structural controls**

The Tchaikazan Fault occurs roughly 500 meters to the north of the deposit. Dextral deformation on the Tchaikazan is interpreted to have occurred between 77 and 44 Ma (Umhoefer and Schiarizza, 1996; Schiarizza et al., 1997). Therefore it is possible that the intrusive body associated with mineralization at Empress has been partially or completely faulted away by the Tchaikazan Fault. The Tchaikazan Fault is postulated to have been reactivated from Early Cretaceous sinistral deformation (Schiarizza et al., 1997). If the Tchaikazan Fault was present at the time of mineralization at Empress, fluids would likely have escaped along the fault zone and not generated the alteration and mineralization at Empress. Therefore either the Tchaikazan formed after mineralization during the initial sinistral deformation phase, or the Tchaikazan fault strand near the Empress deposit did not form until the later dextral phase of deformation.

### **3.8.1.9 Summary**

In summary, Empress is interpreted to be an oxidized, relatively deep (~5 km) and high temperature (700°C) porphyry system that formed when high volumes of magmatic-hydrothermal fluids migrated away from a source intrusion of the CPC. These fluids were highly focused a combination of pre-existing fractures in the Falls River succession and by a pre-existing, underlying, low permeability intrusion. There was a gradual influx of meteoric water into the hydrothermal system, which cooled and increased the acidity of hydrothermal fluids at Empress. A summary of the genesis of the Empress deposit is illustrated in Figure 3.33.

## **3.8.2 Taylor-Windfall**

### **3.8.2.1 Structural controls**

The alteration at Taylor-Windfall is dominantly structurally controlled. Alteration is largely restricted to the Battlement Creek gully, which is interpreted to be a fault that acted as a permeable conduit for hydrothermal fluids. Reported vein orientations (Price, 1986) are similar to orientations of repeated fracture sets in the vicinity of Taylor-Windfall. Therefore, these fracture sets were likely present at the time of mineralization and acted as permeable conduits producing uneven alteration patterns observed at the outcrop scale, as well as accommodating emplacement of mineralized veins. Fractures pre-dating mineralization at Taylor-Windfall (87-89 Ma) must be associated with the initial phase of sinistral deformation (>90 Ma; see Chapter II), rather than successive (D3 - dextral) deformational events which formed after alteration Taylor-Windfall. Open space filling textures in veins (Price, 1986) support the hypothesis that veins were emplaced along pre-existing fractures. The central zone of vuggy silica alteration is the only alteration zone that exhibits no significant fracture control. Therefore either fractures weren't present in this alteration zone, or they were sealed and recrystallized during the alteration event. The inferred fault in Battlement Creek could potentially have been connected with the fault on Battlement Ridge, which allowed high-acidity fluids to migrate and produce the quartz-alunite alteration observed on Battlement Ridge.

The Powell Creek Formation is the youngest observed stratigraphic unit in the region and has a maximum observed thickness of 3 km. Therefore, if maximum stratigraphic depth constraints of 3km are applied, the Taylor-Windfall system formed at hydrostatic pressures of up to 30 MPa or lithostatic pressures of up to 100 MPa. Most epithermal deposits form in the top 2 km of the crust, corresponding to hydrostatic pressures of 20 MPa or less (White and Hedenquist, 1990; Sillitoe, 1995).

The Taylor-Windfall deposit is interpreted to have formed from hydrothermal fluids migrating upwards around a central fault/fracture zone. The Powell Creek Formation hosts the Taylor-Windfall deposit and upper parts of the Formation were still being deposited at the time of mineralization. Therefore, it is possible that the central fault at Taylor-Windfall did not breach the surface because it was overlain by younger rocks of the Powell Creek Formation. If this were the case, pressures in the fault zone may have been above hydrostatic. As fluids continued to ascend along pre-existing faults, they could have generated the intense, fault-controlled quartz-alunite alteration observed on Battlement Ridge. Further geochronological and isotopic analyses

are required to assess possible links between Battlement Ridge alteration and the Taylor-Windfall system.

### **3.8.2.2 Hydrothermal fluid sources**

Stable isotope data from high-sulphidation epithermal systems indicate that vapour phases responsible for early advanced argillic alteration, as well as aqueous fluids of similar low to intermediate salinity but liquid-like density commonly show a magmatic isotopic signature (Rye et al., 1992; Hedenquist et al., 1998; Heinrich, 2005; Williams-Jones and Heinrich, 2005). This is consistent with the hypothesis that both fluid phases at Taylor-Windfall had a common, magmatic source. Oxygen and hydrogen isotopic data from Taylor-Windfall corroborates that fluids were dominantly magmatic, but also indicates that at least some mixing with meteoric waters occurred. CO<sub>2</sub>-rich fluid inclusions often occur with low-salinity inclusions in epithermal deposits as they do in the Taylor-Windfall deposit (de Ronde and Blattner, 1988; Ren et al., 1995). The controls on the occurrence of CO<sub>2</sub>-rich inclusions are not fully characterized, but indicate a magmatic source for fluids (John, 1989). Therefore, Taylor-Windfall is interpreted to have formed from magmatic-dominated fluids that partially mixed with meteoric waters during fluid migration.

Taylor-Windfall (89-88 Ma) formed at the same time that the CPC was being emplaced (90-45 Ma; Symons et al., 2000). Fluid inclusion and isotopic evidence suggests that hydrothermal fluids responsible for alteration at Taylor-Windfall were magmatic in origin. Magmatic fluids in the Taseko Lakes Region at the time of mineralization at Taylor-Windfall were likely genetically related to one of the intrusive phases of the CPC.

### **3.8.2.3 Hydrothermal fluid evolution**

Tourmaline is generally regarded as an alteration mineral associated with porphyry systems; however, it can also occur in high-sulphidation epithermal systems (Richards, 2007). Therefore, the presence of tourmaline at Taylor-Windfall is not inconsistent with the interpretation that it is a high sulphidation epithermal system.

The formation of advanced argillic alteration minerals such as pyrophyllite, kaolinite, dickite and alunite indicates that hydrothermal fluids at Taylor-Windfall were moderate to low temperature and highly acidic (Brimhall and Ghiorso, 1983). Vuggy silica alteration requires fluids with pH < 2 in order to remove aluminum from the system (White and Hedenquist, 1990). Pyrophyllite-kaolinite-dickite assemblages indicate that the peak temperatures of the fluids must

have been at least 300°C (Figure 3.30B) (Hedenquist and White, 2005). Rare hydrothermal muscovite also supports that at least locally, peak temperatures must have reached 300°C. More widespread occurrence of illite and paragonite indicates that temperatures were largely below 300°C, with fluids possessing moderate acidities and high  $a(\text{Na}^+/\text{K}^+)$  ratios at some time during the alteration event. Advanced argillic alteration often overprints quartz-sericite alteration if fluids increase in acidity over time, typically as a result of boiling of fluids in epithermal systems (Brimhall and Ghiorso, 1983; Figure 3.25).

Alunite forms from highly acidic hydrothermal fluids and is stable from 200-380°C (Hemley et al, 1969). Based on SWIR analyses, alunite on Battlement Ridge is rich in sodium, indicating fluids responsible for alunite alteration may have had some seawater or connate water component. Barren lithocaps commonly overlie epithermal systems and are characterized by intense quartz-alunite alteration (Buchanan, 1981; Brathwaite et al., 2001). The quartz-alunite alteration zone on Battlement Ridge above and to the east of Taylor-Windfall is interpreted to be part of a barren lithocap, and possibly part of the same hydrothermal system as Taylor-Windfall. Further geochemical and geochronological study is required to further assess this potential link.

Assuming confining pressures of <100 MPa, average trapping temperatures of 230-280°C for L-V-CO<sub>2</sub> inclusions and 100-220°C for L-V inclusions are indicated from calculated isochores (Figure 3.24B). L-V-CO<sub>2</sub> inclusions fall in the typical range for high sulphidation epithermal systems ( $T_h = 200\text{-}300^\circ\text{C}$ , salinity = 0-3 wt. % NaCl equiv.) (Zhang et al., 1989; Evans, 1993), and could have been in equilibrium with mineralizing fluids. The L-V inclusions have salinities typical of epithermal systems (0-3 wt. % NaCl equiv.); however, their homogenization temperatures are slightly lower than normal for such systems (Figure 3.32A) (de Ronde and Blattner, 1988; Zhang et al., 1989; Vila et al., 1991). This suggests that L-V inclusions were not in equilibrium with mineralizing fluids and are secondary inclusions. L-V inclusions represent fluids from later stages of the hydrothermal system and indicate that the system was still active to temperatures potentially as low as 100°C. This is supported by the presence of low temperature clay assemblages such as kaolinite and halloysite at Taylor-Windfall. If a single, main hydrothermal phase is assumed for Taylor-Windfall, isochore data indicates fluids became depleted in CO<sub>2</sub> over time.

The lack of vapour-rich inclusions or L-V inclusions that homogenized to the vapour phase indicates that fluids responsible for the vuggy silica alteration did not undergo boiling. Boiling of fluids is generally expected for high-sulphidation epithermal systems and is regarded

as an important mechanism for ore deposition (Gammons and Williams-Jones, 1997; Shimizu et al., 1998). Boiling is triggered by sharp drops in fluid pressures to hydrostatic conditions as fluids are ejected into fractures (Ahmad and Rose, 1980). However, isochores from both L-V and L-V-CO<sub>2</sub> inclusions at Taylor-Windfall indicate that confining pressures of less than 5 MPa are required to intersect a two-phase boiling curve (Figure 3.32B). There is no evidence to suggest that fluids responsible for vuggy silica alteration at Taylor-Windfall reached boiling, the system likely maintained confining pressures of >5 MPa, corresponding to depths >500 m. Inspection of vein samples would provide more insight into the possibility of boiling in the system. Although boiling is an efficient mechanism for precipitating Au from epithermal fluids, cooling of fluids in the absence of boiling can cause this deposition (Shimizu et al., 1998).

Previous studies of high-sulphidation epithermal systems indicate that ore deposition is associated with aqueous liquids of moderate acidity and low to intermediate salinity that postdates acid leaching of wallrocks (Stoffregen, 1987; Arribas et al., 1995; Hedenquist et al., 1998; Heinrich, 2005). If this were the case at Taylor-Windfall, vuggy silica and high-temperature advanced argillic alteration formed from high-acidity vapours prior to mineralization. These alteration phases were not overprinted by later aqueous fluids because all mobile elements had already been leached from the host rocks. However, the vuggy silica core could have been recrystallized during later hydrothermal fluid influx, which would explain the lack of vapour-rich fluid inclusions present in observed vuggy-silica samples. As the aqueous liquids cooled they would have superimposed progressively more acidic alteration assemblages towards the vuggy silica core, and retrograde lower temperature advanced argillic assemblages (pyrophyllite, dickite, kaolinite) on top of the pre-existing high-temperature assemblages (andalusite, corundum). In fresher host rocks, the moderate acidity, low temperature aqueous fluids produced quartz-sericite alteration, producing the intermixed quartz-sericite and low-temperature advanced argillic alteration observed at Taylor-Windfall. Quartz-sericite cemented breccias were generated in zones of localized high fluid pressures, possibly arising from sealing of fractures due to silica deposition.

Recent studies of epithermal systems suggest that differences in sulphidation state and alteration style are not due varying fluid sources, but rather differences in the P-T evolution of hydrothermal fluid phases (Williams-Jones and Heinrich, 2005). Phase separation of fluids can greatly affect the physiochemical characteristics of hydrothermal fluids. Thus mineralization styles are greatly affected by the histories of mineralizing fluids.

Vapour-derived partially rock-reacted, aqueous liquid, such as the proposed second fluid phase at Taylor-Windfall, is postulated to be a highly effective agent for producing high-grade epithermal gold deposits, and is capable of transporting at least 1ppm gold to temperatures as low as 150°C. Fracture zones surrounded by advanced argillic, feldspar-destructive alteration assemblages (kaolinite, pyrophyllite, andalusite ± muscovite) are effective channelways for such gold transporting, vapour-derived liquids due to the low reactive capacity of these alteration assemblages (Hedenquist et al., 1998; Heinrich, 2005). This allows internal equilibria to drive the condensed fluids to a very low pH during fluid-buffered cooling (Williams-Jones and Heinrich, 2005). Deposition of gold from the fluids can occur when fluids migrate into isolated fractures, consistent with the mineralization and open-space filling textures hosted by veins at Taylor-Windfall as described by Price (1986). Sealing of fractures by silica deposition within the vuggy silica zone, coupled with the low buffering capacity of vuggy silica alteration explains why mineralization is absent in the vuggy silica zone. Sealing of fractures due to silica deposition can also allow pressures to increase from hydrostatic to lithostatic, thus inhibiting boiling of hydrothermal fluids (Figure 3.32B, Ahmad and Rose, 1980; Hedenquist and Arribas, 1999). Alternatively, gold-deposition may also occur during sudden boiling of fluids from rapid decreases in pressure, consistent with the sector-collapse hypothesis (Heinrich, 2005), although no evidence supporting boiling was observed in this study or that of Price (1986).

#### **3.8.2.4 Deposit classification**

Price (1986) interpreted the Taylor-Windfall deposit to be characteristic of a porphyry system based on the alteration assemblages observed at the deposit. Price identified a high temperature corundum-andalusite alteration assemblage. Temperatures of >400°C are required to form this type of advanced argillic alteration (Hemley et al., 1980), which is higher than typical for high-sulphidation epithermal systems. A summary of Taylor-Windfall alteration minerals and their interpreted formational temperatures are provided in Figure 3.27.

The Taylor-Windfall deposit exhibits many characteristics typical of high-sulphidation epithermal systems such as: a core of vuggy silica surrounded by white mica, pyrophyllite and kaolinite-alunite assemblages, mineralization associated with advanced argillic alteration assemblages and the presence of abundant pyrite and typical high sulphidation ore minerals (Figure 3.4B; Stoffregen, 1987; Reyes, 1990; White and Hedenquist, 1990). Similar alteration zonation has been documented for other high-sulphidation epithermal systems (Hedenquist et al., 1998; Squire et al., 2007). Conversely, it also has some properties atypical of many high

sulphidation epithermal systems, which include: high temperature advanced argillic alteration assemblages (Price, 1986), restriction of mineralization exclusively to veins, and widespread occurrence of illite.

Corundum and andalusite were not identified in this study, likely because access was not gained to the underground mine workings at Taylor-Windfall. Corundum and andalusite are not characteristic high-sulphidation epithermal alteration minerals. Epithermal systems will typically overprint porphyry systems at a given erosional level (Sillitoe, 1994). Structurally controlled, upward-flaring advanced argillic alteration zones may overprint potassic alteration and copper mineralization in the roofs of porphyry deposits (Figure 3.34A; Gustafson and Hunt, 1975; Hedenquist et al., 1998; Ulrich and Heinrich 2001; Watanabe and Hedenquist, 2001). The corundum-andalusite, high-temperature alteration assemblage is interpreted as an earlier phase of porphyry style alteration at Taylor-Windfall. All other alteration is attributed to later epithermal fluids, which overprinted the higher temperature porphyry-style alteration. Williams-Jones and Heinrich (2005) propose that an overall system evolution can occur as a source intrusion crystallizes and partial melts retreat to deeper crustal levels. Late epithermal-stage fluids are exolved at greater depths and migrate up through and overprint the pre-existing porphyry system (Figure 3.34B). The high-temperature advanced argillic alteration zone (corundum and andalusite) is the only porphyry-style alteration assemblage reported at Taylor-Windfall, and it may represent the roof of a porphyry system present at depth.

Alternatively, sector collapse of a volcanic edifice may cause telescoping of superimposed alteration types, reducing their depth range by instantaneous increases in pressure, temperature, and subsequently, chemical gradients (Figure 3.34C; Sillitoe, 1994). If such an event took place at Taylor-Windfall, a rapid change from high-temperature porphyry-style alteration assemblages to lower temperature epithermal-style alteration could have arisen from rapid drops in pressure and temperature of migrating fluids.

A final possible explanation for the high temperature alteration at Taylor-Windfall is that it formed from an initial vapour-dominated fluid phase followed by a cooler liquid phase (Figure 3.34D). Boiling and re-condensation of magmatic-hydrothermal fluids has been proposed for many porphyry systems (Heinrich, 2005; 2007; Dreisner and Geiger, 2007), thus if high-sulphidation epithermal systems are thought of as shallower extensions of porphyry systems (Williams-Jones and Heinrich, 2005), they should possess similar types of fluids. If a high temperature, high acidity vapour phase was generated at depth, and migrated significant distances, at least part of the vapour phase would cool sufficiently to re-condense. This would

result in a vapour phase and a condensed aqueous fluid phase with similar compositions, but contrasting temperatures and densities. Vapour phases are less dense/more buoyant than liquid phases, therefore, the vapour phase ascended more rapidly due to the greater buoyancy. The rapid ascent permitted minimal cooling and interaction with wall rocks, and so the vapour was still at high temperatures and high acidities when it reached Taylor-Windfall. In Contrast, the greater density of the re-condensed phase would have slowed its ascent permitting greater cooling and wallrock interaction. The re-condensed phase would have reached the Taylor-Windfall area after the vapour phase and generated retrograde low-T advanced argillic alteration that overprints the earlier high-T assemblages.

Taylor-Windfall has a widespread occurrence of illite. High-sulphidation epithermal systems are generated by fluids with acidities too high to form illite (White and Hedenquist, 1990). However, widespread illite often occurs in intermediate-sulphidation epithermal systems (Figure 3.35A; Richards, 2007). Buffering of fluids by host rocks can reduce fluid acidities, permitting the formation of illite and muscovite, which typically form at pH's from 4-6 (Figure 3.30A; Gammons and Williams-Jones, 1997). No minerals indicative of low-sulphidation epithermal systems such as adularia and chalcedony are observed at Taylor-Windfall. The presence of advanced argillic alteration minerals such as pyrophyllite, kaolinite and dickite at Taylor-Windfall are indicative of high-sulphidation systems.

Taylor-Windfall exhibits no evidence that mineralizing fluids underwent boiling, and there are no robust depth constraints on the system. Therefore, mineralization did not necessarily occur in the top 1.5 km of the crust as required for epithermal systems (Buchanan, 1981). Taylor-Windfall possesses an early phase of high-temperature alteration indicative of porphyry systems that has been overprinted by lower-temperature alteration phases characteristic of high- to intermediate-sulphidation epithermal systems. Epithermal overprints of porphyry-systems have been observed and postulated for many previously studied deposits (Milu et al., 2004; Heinrich, 2005; Wallier et al., 2006). Thus, Taylor-Windfall can be thought of as forming in the porphyry-epithermal continuum, likely somewhere in between the two end members. This corroborates observations by Price (1986) that Taylor-Windfall possesses both porphyry and epithermal characteristics.

### **3.8.2.5 Summary**

Taylor-Windfall is interpreted to have formed when magmatic-hydrothermal fluids, exolved from a Late Cretaceous pluton, ascended along pre-existing faults and fractures. An

initial vapour dominated fluid produced high temperature vuggy silica and advanced argillic alteration at Taylor-Windfall. This fluid phase was followed by a low-salinity condensed vapour phase which recrystallized vuggy silica alteration and overprinted high-temperature advanced argillic assemblages with low temperature advanced argillic and quartz-illite alteration. Mineralization occurred when the condensed-vapour phase migrated into pre-existing fractures and was possibly aided by sudden boiling due to rapid pressure drops. Vapour and condensed-vapour phase fluids may have originally been part of the same magmatic-fluid phase, with physiochemical differences between the fluid phases explained by repeated phase separations of fluids and subsequent difference in P-T evolution of the separate phases (Figure 3.35). Mineralization may have occurred at intermediate depths between porphyry and epithermal systems.

### **3.8.3 Pellaire**

#### **3.8.3.1 Structural controls**

Contractional faults at Pellaire are relatively small scale, with observed displacements of only a few meters. Because of this it is unlikely that these faults are continuous over distances of several kilometers as needed to transport fluids from both distal magmatic or metamorphic sources. South-vergent contractional faults at Pellaire are interpreted to be part of a larger-scale imbricate fan system. Therefore, the overall fault system could be continuous for distances required to source distal fluids. Alternatively, south-vergent faults could have intersected a pre-existing fault at depth which could have acted as a conduit for fluid transport.

#### **3.8.3.2 Hydrothermal fluid sources**

Oxygen and hydrogen isotopic data from alteration minerals at Pellaire indicate that hydrothermal fluids were either a mixture of magmatic and meteoric fluids or were metamorphic in origin. However, the abundance of CO<sub>2</sub>-rich inclusions and salinities of L-V and L-V-CO<sub>2</sub> inclusions at Pellaire indicate that hydrothermal fluids had a magmatic source (John, 1989; Zhang et al., 1989). CO<sub>2</sub>-rich fluid inclusions often occur with low-salinity inclusions in epithermal deposits (de Ronde and Blattner, 1988; Ren et al., 1995).

Late Cretaceous cover rocks of the Taseko Lakes Region (which includes the Falls River succession) have not undergone significant metamorphism. Therefore, if ore-forming fluids at Pellaire are interpreted to be derived from a metamorphic source, they must have originated from

deeper rocks that underwent higher grade metamorphism. Cretaceous cover rocks at Taseko Lakes are interpreted to overlie the Cadwallader Terrane (Israel et al., 2006). The Cadwallader Terrane is part of the SECB and comprises Upper Triassic mafic volcanic and sedimentary rocks that have typically undergone greenschist facies metamorphism. However, much of the metamorphism that occurred in the SECB is interpreted to have occurred during the Eocene (Schiarizza et al., 1997). Therefore, mineralization at Pellaire pre-dates regional metamorphism, and mineralizing fluids were likely not metamorphic in origin, and Pellaire does not meet the classifications for an orogenic Au deposit.

The origin of mineralizing fluids at Pellaire is not well constrained. However, it is clear that structural and lithologic controls were the paramount factors in the concentration of gold and silver at Pellaire, rather than the processes leading to the generation of hydrothermal fluids.

### **3.8.3.3 Hydrothermal fluid evolution**

Alteration at Pellaire is dominated by moderate-temperature, carbonate-rich mineral assemblages. Pellaire fluid inclusions are also moderate temperature and rich in CO<sub>2</sub>, which are the type of fluids expected to generate the observed alteration. Therefore, Pellaire L-V-CO<sub>2</sub> inclusions are interpreted to be primary inclusions and likely represent the peak hydrothermal conditions. There is no evidence suggesting that Pellaire fluids boiled at any point during their evolution.

The hydrothermal breccia separating the granodiorite from the Falls River succession on the eastern flank of Pellaire Ridge is interpreted to have formed either as a result of permeability contrast between the Mount McLeod granodiorite and the Falls River succession or from faulting along the contact between the two lithologic units. This contrast resulted in overpressuring of circulating hydrothermal fluids which caused brecciation of both host lithologies. The presence of hangingwall brecciation above the quartz-veins suggests overpressuring of hydrothermal fluids occurred during vein emplacement. Silicification and quartz-carbonate alteration observed on the western flank of Pellaire Ridge is similar to alteration in the hydrothermal breccia. The two alteration styles likely formed during the same event; however, fluid pressures on the western flank of the ridge were not sufficiently high to cause fracturing and brecciation. Breccia veins occur in shallow mesothermal Au deposits under brittle deformation regimes (<10 km depth; Colvine et al., 1988) as expected for Pellaire.

The presence of hydrothermal muscovite within the hydrothermal breccia matrix implies that breccia forming fluids exceeded 300°C and possessed relatively high K<sup>+</sup>/H<sup>+</sup> ratios to

produce significant illite and muscovite (Figure 3.30A) (Hemley, 1959; Hedequist et al., 1998). Sulphides likely remained in the granodiorite clasts in the breccia due to the lower permeabilities of the clasts compared to the breccia matrix. Ankerite and siderite often occur as gangue minerals associated with Fe-sulphides in hydrothermal systems, supporting the hypothesis that the breccia originally contained more significant sulphides.

The mineralizing fluids were able to infiltrate the granodiorite along permeable south-vergent faults. The south-vergent contractional faults are relatively small-scale and could have terminated within the granodiorite resulting in the trapping of ore-forming fluids. Since mineralization occurs in veins that are hosted within the Mount McLeod granodiorite, the granodiorite must pre-date mineralization, and mineralizing fluids would have cooled within the granodiorite. Cooling of vein-forming fluids resulted in deposition of silica and ore minerals (White and Hedenquist, 1995). The Mount McLeod granodiorite contains greater amounts of potassium feldspar than the rocks of the Falls River succession. Therefore, the granodiorite likely hosts a greater buffering capacity than the Falls River Succession (Dilles and Einaudi, 1992). Potassium feldspar in the granodiorite wallrocks could have reacted with mineralizing fluids and reduced their acidities which resulted in Au deposition (Gammons and Williams-Jones, 1997). Ore deposition likely occurred as a result of cooling of hydrothermal fluids and/or buffering of fluids by granodiorite wallrock.

Mesothermal deposits typically form under lithostatic pressures at depths greater than 1.5 km, corresponding to pressures above 50 MPa (Hagemann and Brown, 1996). Stratigraphic constraints indicate that Pellaire was at a maximum depth of ~6 km of rock at the time of mineralization (Garver, 1992; Maxson, 1996; Schiarizza et al., 1997), corresponding to a maximum lithostatic pressure of 200 MPa. Trapping temperatures for Pellaire fluid inclusions were attained for both L-V and L-V-CO<sub>2</sub> inclusions based on calculated isochores and stated pressure constraints (Figure 3.24B). The P-T conditions indicated by L-V-CO<sub>2</sub> inclusions indicate trapping temperatures of 300-450°C, which overlap with other documented mesothermal systems (T = 280-350°C, P > 100 MPa, salinity = 3-6 wt. % NaCl equiv.) (Zhang et al., 1989; Leitch et al., 1991; Boer et al., 1995). L-V inclusions are lower temperature, secondary inclusions, suggesting fluids decreased in CO<sub>2</sub> content as they cooled. There is no evidence that fluids boiled at Pellaire.

### 3.8.3.4 Deposit classification

Pellaire is a vein-hosted Au-telluride deposit. However it remains unclear whether it is distally related to a magmatic-hydrothermal system (i.e., an epithermal-style, Au-telluride deposit), or if it's more closely related to metamorphic dehydration of deeper crust as a result of contractional deformation (i.e., an orogenic Au deposit) (Figure 3.36). Gold-telluride deposits are interpreted to be distal, fault controlled epithermal-type systems (Spry et al., 1996). Pellaire is interpreted to have formed at depths of approximately 5 km based on stratigraphic correlations, which is too deep for typical epithermal systems. Gold-telluride systems show evidence of rock-buffering of fluids, but lack significant external fluid input, unlike typical low-sulphidation epithermal systems (Alderton and Fallick, 2000). Orogenic Au deposits typically form in metamorphic rocks and depths greater than 5 km (Groves et al., 1998). Metamorphic and magmatic fluids have similar stable isotopic signatures, making it difficult to discern between the two sources.

Previous studies on epithermal-style gold-telluride deposits indicate that mineralizing fluids are low temperature (~200°C) and low salinity (~1% NaCl) (Spry et al., 1996). Orogenic Au deposits can form from fluids at a wide range of P-T conditions (180-700°C and depths ~2-15 km; Groves et al., 1998); therefore fluid P-T conditions are not an effective method of classifying a deposit as an orogenic Au deposit. From this study, Pellaire fluids were likely ~350°C and 3-6 wt. % NaCl, indicating that Pellaire either formed deeper or more proximal to its heat and fluid source than the more epithermal-style gold telluride deposits in other studies. These fluid characteristics are similar to those of the Bralorne deposits (Leitch et al., 1991; Ash, 2001).

Since ore deposition at Pellaire, as with other Au-telluride deposits, is interpreted to have been triggered by fluid migration across lithologic contacts rather than due to boiling, the system need not have been at shallow, epithermal depths. Greater depths of formation are also consistent with formational temperatures indicated by fluid inclusions, which are also greater than typical for distal epithermal systems. Therefore, Pellaire is interpreted to have formed in the distal part of a magmatic-hydrothermal system from fluids that migrated along D2 contractional faults. Ore deposition occurred when fluids migrated from Falls River Succession, which they were in relative equilibrium with, into the Mount McLeod Granodiorite, which they were not in equilibrium with. Since orogenic Au deposits can potentially have magmatic fluid sources, Pellaire could potentially be classified as a orogenic Au deposit, however a more general Au-

telluride classification is preferred for Pellaire due to its similarities with both epithermal and mesothermal systems.

### **3.8.3.5 Summary**

The Pellaire gold-telluride deposit formed at approximately 85 Ma when mixed magmatic-meteoric hydrothermal fluids migrated along south-vergent contractional faults. Ore deposition occurred once the fluids passed from the Falls River succession into the Mount McLeod Batholith. Faulting or fluid overpressuring caused localized brecciation along the contact between the Batholith and country rocks. Fluids were then cooled and/or buffered by the Mount McLeod granodiorite resulting in the emplacement of mineralized quartz veins at the deposit. Mineralization is interpreted to have occurred synchronously with contractional deformation, which continued after vein emplacement was complete. A summary of the interpreted genesis of the Pellaire deposit is illustrated in Figure 3.21.

### **3.8.4 Integration of deposits**

The Empress, Taylor-Windfall and Pellaire deposits host markedly differing styles of mineralization that are all interpreted to have formed from magmatic-hydrothermal systems. However, many similarities exist between the alteration minerals, isotopic characteristics and fluid inclusions of the three deposits. For example, all the deposits host an early generation of L-V-CO<sub>2</sub> inclusions, followed by a lower temperature phase of low to moderate salinity L-V inclusions, followed finally by abundant, monophasic liquid-rich inclusions. Isotopic evidence from alteration minerals at the deposits all suggest that fluids responsible for mineralization in all the systems were magmatic but underwent varying degrees of mixing with meteoric waters. The similarities in fluid inclusions and isotopes suggest that comparable fluids were present at Empress, Taylor-Windfall and Pellaire. Magmatism in the region at the time of mineralization was characterized by the emplacement of the CPC. Therefore, all the deposits in this study are interpreted to have formed from magmatic fluids evolved from the CPC. Since fluids in all three systems were likely broadly compositionally similar, the differences in the characteristics of the deposits are likely attributed to the variable P-T conditions and geologic settings in which the deposits formed.

Relatively close (~3 km) spatial association between Taylor-Windfall and Empress, coupled with similarities in geochronological age data for the mineralization of the deposits

(Empress at 87-88 Ma vs. Taylor-Windfall at 87-89 Ma Table 3.2) supports the hypothesis that the deposits have a genetic relationship (Figure 3.37). Calculated isochores for the Empress and Taylor-Windfall deposits are similar, suggesting that variations in trapping temperatures between the two deposits can be attributed to differences in depths of formation and proximity to fluid and heat sources (Figure 3.32B). Fluid inclusion and isotopic compositions indicate fluids were dominantly magmatic with some meteoric input. Further isotopic and geochemical study is required to better assess similarities and potential genetic links between fluids at Taylor-Windfall and Empress.

Pellaire lacks a close spatial association to other identified deposits and is slightly younger than Empress and Taylor-Windfall. Therefore at least two separate generations of mineralization took place in the southern Taseko Lakes Region – one responsible for Empress and Taylor-Windfall, the other for Pellaire. Pellaire formed from magmatic fluids that migrated distally from a central magmatic source along contractional and possibly other deeper seated faults. There was some meteoric fluid input into the system, but fluids likely reached relative equilibrium with the surrounding rocks judging from the low level intensity of alteration in the Falls River succession. This equilibrium was disturbed when fluids migrated across the lithologic contact between the Mount McLeod Batholith and Falls River Succession, which resulted in ore deposition within contractional fault zones.

Pellaire and Empress likely formed in comparable geologic environments (~5km depth, along the CPC-SECB contact), but exhibit markedly contrasting styles of mineralization and alteration. Their presence demonstrates the potential variations in mineralization due to the proximity of hydrothermal systems to the central magmatic source (Empress: proximal; Pellaire: distal) as well as the potential of the CPC-SECB contact to focus hydrothermal fluids and concentrate economic minerals.

Mineralization in the Taseko Lakes Region occurred synchronously with contractional faulting which was active from 91-85 Ma (Journeay and Friedman, 1993). Pellaire illustrates an implicit connection between contractional faulting and mineralization. Other mineral occurrences in the region associated with contractional may exist. Significant alteration is hosted within both contractional and strike-slip fault zones throughout the region (see chapter II; Hollis et al., 2007). Extensive regional alteration implies hydrothermal fluids were widespread, likely evolving from multiple sources and multiple events.

## 3.9 DISCUSSION

### 3.9.1 Magmatic-hydrothermal systems in the Taseko Lakes Region

The Empress, Taylor-Windfall and Pellaire deposits are all interpreted to be linked to magmatic-hydrothermal systems likely centered on crystallizing calc-alkaline intrusions, with each deposit forming in separate parts of the overall systems (Figure 3.37). Empress formed proximal to the crystallizing intrusion at depths of >5km. Taylor-Windfall formed above the crystallizing intrusion at shallow depths (<1.5km) at the top of the hydrothermal system. Pellaire formed distally away from the intrusion at depths of approximately 5km. Geochronological data indicates that Pellaire formed after Empress and Taylor-Windfall, likely during a separate generation of magmatism and shares no direct genetic relationship with the other deposits. Empress and Taylor-Windfall potentially formed during the same generation of magmatism and possibly were part of the same overall hydrothermal system.

Empress, Taylor-Windfall and Pellaire all possess isotopic evidence that meteoric waters mixed with magmatic-hydrothermal fluids during the evolution of the hydrothermal systems. Taylor-Windfall is interpreted to have formed in roughly the top kilometer of the crust, therefore it is likely that meteoric waters would be present at such shallow depths. Pellaire and Empress are both interpreted to have formed at depths of approximately 5 kilometers, where it is less likely that meteoric waters would be present. However, the abundances of steeply-dipping fault zones in the Taseko Lakes Region would have permitted significant draw-down of meteoric waters from shallow depth during hydrothermal circulation. The region is interpreted to have been a marginal marine setting during the Late Cretaceous (Israel et al., 2006), therefore it is expected that seawater may have also been present at the time of mineralization. But isotopic data provides no evidence that any significant input of seawater occurred in any of the hydrothermal systems.

Radiometric dates of alteration minerals from both Taylor-Windfall and Empress are within error of each other. Hydrothermal systems in permeable host rocks with high water:rock ratios like Empress and Taylor-Windfall are believed to be active for relatively short time scales ( $\sim 10^3$ - $10^4$  years; Hayba and Ingebritsen, 1997; Driesner and Geiger, 2007). The emplacement and crystallization of large magmatic bodies occurs over longer timescales than these ( $\sim 10^5$ - $10^6$  years). Therefore there is potential that multiple hydrothermal systems can be generated from the same source intrusion (synchronously or successively). Because of this and the analytical uncertainties associated with radiometric dating techniques, it is not possible to prove that

Taylor-Windfall and Empress formed during the same specific hydrothermal event. However, it appears that both systems shared a common source intrusion and are relatively coeval on longer timescales. Any direct genetic link between the deposits is based on the assumption that they are the same age. Ages from the Pellaire deposit slightly overlap with those of the Empress deposit, but are not within error of ages from the Taylor-Windfall deposit (Figure 3.22).

If Empress and Taylor-Windfall are assumed to have formed synchronously, they must have been separated by a minimum vertical distance of 3 km based on the thickness of the Taylor Creek Group which separates the host rocks of the two deposits (Powell Creek Formation and Falls River succession). Telescoping of magmatic-hydrothermal systems has been observed over vertical intervals of over 6 km (Dilles and Einaudi, 1992), therefore the two systems were situated close enough vertically to potentially be part of the same hydrothermal system.

It is unlikely that the same exact fluids were responsible for both the Empress and Taylor-Windfall systems. However, if fluids at both deposits were originally exolved from the same magma, they would have shared the same physiochemical properties. If the fluids then underwent similar P-T evolutions, they would continue to share similar properties.

The Tchaikazan Fault is inferred to be located between the Empress and Taylor-Windfall. Eocene offset along the fault is interpreted to be dextral (Schiarizza et al., 1997, Israel et al., 2006), indicating that Taylor-Windfall and Empress may have shared a closer spatial relation at one time. A maximum of 7-8 km of dextral offset is estimated for the Tchaikazan Fault (Mustard and van der Heyden, 1994). Since Taylor-Windfall and Empress are located relatively close to the interpreted terminus of the Tchaikazan Fault (Figure 3.1), displacement across the fault in the vicinity of the deposits was likely less than 7-8 km. If the displacement were closer to 3 or 4 km, the deposits would originally have been positioned much closer to each other than they presently are (Figure 3.38). The Powell Creek Formation, hosts Taylor-Windfall, and is located stratigraphically above the Falls River Succession, which hosts Empress. The two deposits are currently at roughly the same elevation. Therefore, dip slip was likely also associated with deformation on the Tchaikazan Fault, and Taylor-Windfall was located above the Empress deposit, based on their stratigraphic positions. If the deposits formed in the same system, Taylor-Windfall should overlie Empress (Figure 3.37). The available data indicates the deposits were at least part of the same generation of mineralization in the region, and could be directly related.

The contact between the CPC and SECB in the vicinity of Empress has an east-southeast trend, which is relatively parallel to the interpreted trend of the Tchaikazan Fault. Other prospective showings occur to the east of Empress along the CPC-SECB contact (Osborne,

1999). Therefore, if multiple mineral occurrences were generated along the upper contact of the Empress pluton, Taylor-Windfall could be related to any of the occurrences on the south-side of the Tchaikazan Fault depending on the magnitude of displacement accommodated.

Pellaire is a gold-telluride deposit has characteristics typical of both mesothermal and epithermal Au deposits. Since ore deposition at Pellaire occurred as a result of fluids migrating across lithologic boundaries, its depositional mechanism is relatively independent of depth. This is why it does not fit traditional epithermal or mesothermal classifications – both of which are based on depths of formation. Pellaire represents a distal hydrothermal-magmatic style of mineralization that requires high permeability conduits cross-cutting sharp contacts between compositionally unique units. Pellaire is interpreted to have formed at approximately 5km, which would have helped maintain fluid temperatures higher than typical for epithermal systems. Other gold-telluride deposits are interpreted to have formed at epithermal depths (Alderton and Fallick, 2000), therefore it is possible that Pellaire could have formed at lower temperatures and shallower depths and this style of mineralization is largely independent of depth.

Mineralization at Pellaire (~85 Ma) is interpreted to have occurred synchronously with contractional deformation in the Taseko Lakes Region (91-84 Ma; Umhoefer et al., 1994; 2002; Schiarizza et al., 1997). Just as faults aided fluid migration by providing high-permeability conduits for fluid flow, fluids likely aided deformation along faults by maintaining high fluid pressures within fault zones.

Pellaire illustrates both the significance of the CPC-SECB contact for mineral potential as well as the potential for fault-controlled mineralization in the Taseko Lakes Region. Although the Mount McLeod Batholith has no genetic relationship to mineralization at Pellaire, its contrasting permeability and composition to the country rocks which it intrudes (in this case the Falls River succession) provides prospective zones in which mineralizing fluids could be focused and trapped. The role of the south-vergent faults at Pellaire indicates that mineralization in the Taseko Lakes Region can be controlled by contractional faults. Fault-hosted mineralization further illustrates the importance of fluid focusing due to permeability variations of host structures and lithologies in the concentration of ore minerals.

The similarities in ages and shared genetic association of the deposits in this study to magmatic-hydrothermal systems indicate that magmatic-hydrothermal activity in the region was widespread during the Late Cretaceous. Fluids at all three deposits may have initially been very similar, but evolved different due to variations in transport distances, cooling histories and phase separations (Figure 3.39). The variable characteristics and geologic settings of the deposits also

suggest that such overall hydrothermal systems were much larger than the scale of the individual deposits as has been proposed for other magmatic-hydrothermal systems (Dilles and Einaudi, 1992; Dilles et al., 1995; Hedenquist et al., 1998). If one or more large-scale magmatic hydrothermal systems were active in the Taseko Lakes Region, potential for a large-scale mineral deposit to occur in the region is high.

Many mineral occurrences have been identified in the region (Hollis et. al, 2007), but as of yet, none of the occurrences have been proven to be economic. The abundance of faults in the region may have inhibited the formation of larger deposits by permitting widespread, diffuse fluid flow throughout the region, thus dispersing economic minerals amongst many relatively small deposits rather than concentrating them in fewer, larger deposits.

### **3.9.2 Regional Comparisons**

Broad similarities exist between the deposits in this study, and more significant deposits in the region such as the Prosperity and Bralorne area deposits.

The Empress and Prosperity deposits are classified as porphyry copper deposits and hosted within Cretaceous intermediate coherent and volcanoclastic rocks (Heinrich, 1991). The Prosperity deposit is located proximal to the Yalakom Fault, the largest scale dextral fault in the region, which may have imposed structural controls on the emplacement of mineralizing intrusives and hydrothermal fluid flow important to the localization of mineralization at the deposit (Brommeland and Wober, 1999). There is no evidence to suggest that any faults played integral roles in the formation of the Empress deposit. Mineralization at the Prosperity deposit is connected to a porphyritic quartz diorite stock spatially associated with the deposit (Brommeland and Wober, 1999). This stock yielded a U-Pb zircon age of  $80 \pm 1.3$  Ma (Schiarizza and Riddell, 1997), whereas secondary biotite from the deposit has been dated at  $77.2 \pm 2.8$  Ma (Wolfhard, 1976), which is the interpreted age of mineralization. Therefore, Prosperity (~80-76 Ma) is younger than Empress (~87-88 Ma), indicating the deposit formed during separate phases of hydrothermal activity, but in broadly similar environments. Prosperity is located in the northern Taseko Lakes Region and represents a younger generation of magmatic-hydrothermal mineralization in the vicinity of Taseko Lakes.

Bralorne is classified as a mesothermal, vein-hosted, Au deposits that occur proximal to the contact between the SECB and the CPC. The Bralorne deposits are dominantly hosted by Permian intrusions (the Bralorne diorite and Soda granite) (Leitch et al., 1989). Therefore, host

rocks at both deposits are intrusive units that pre-date mineralization. Intrusions at Bralorne are mainly hosted by rocks of the Bridge River Terrane – an assemblage of allochthonous, metamorphosed oceanic volcanic and sedimentary rocks of Mississippian to Jurassic age (Schiarrizza et al. 1997). Therefore, Bralorne occurs within a metamorphic terrane as expected for mesothermal Au deposits, whereas Pellaire and Taylor-Windfall do not.

Mineralized veins at both Pellaire and Bralorne are hosted within fault zones with broadly similar orientations (dip ~55-70° towards the north) (Sanche, 2004). Ore mineralogy is similar between the deposits (pyrite, chalcopyrite, sphalerite, galena, tetrahedrite); however, Au is associated with Au-tellurides and inclusions in pyrite at Pellaire (Holtby, 1988), whereas it occurs as native Au at Bralorne (Ash et al., 2001). Veins at Bralorne are comprised of milky quartz ribboned with thin dark septae of slickensided sulphides, sericite and native Au (Leitch et al., 1989) and are interpreted to have formed in high-angle reverse faults due to fluid-pressure cycling processes described by Sibson et al. (1988). Quartz-carbonate-sericite-chlorite alteration envelopes are present around veins at Bralorne (Leitch et al., 1991). Pellaire possesses small halos of quartz ± carbonate alteration around veins, but alteration within the hydrothermal breccia is dominated by quartz-sericite-ankerite-siderite assemblages similar to those observed at the Bralorne deposits. Fluid inclusion evidence also suggests that both ore fluids were rich in CO<sub>2</sub> and at similar conditions during the formation of both deposits (T ~ 350°C and P ~ 175 MPa, salinity ~ 3 – 5 wt. % NaCl equiv.) (Leitch et al., 1991).

Mineralization at the Bralorne area deposits was constrained to 92 to 86 Ma and interpreted to be linked to sinistral and contractional deformation (Ash et al., 2001). However, recent work by Hart et al. (2008) suggests that the Bralorne deposits formed at 68 to 64 Ma. Leitch et al. (1989) suggest that mineralization may have been episodic and continued till as late as 45 Ma. Thus hydrothermal events at both deposits may have temporally overlapped, although Pellaire formed after the bulk of mineralization at Bralorne. Therefore, although Pellaire and Bralorne have many similarities, their lack of spatial and temporal association rules out any potential genetic relation between Bralorne and the deposits in this study.

Mineralization and hydrothermal systems were long lived in the Taseko Lakes region occurring from roughly 90 Ma to as late as 45 Ma. This is the same approximate time that the CPC was active (Rusmore and Woodsworth, 1991a), illustrating the strong connections that the CPC may have to many of the mineral deposits in the SECB.

### 3.10 CONCLUSIONS

The Taseko Lakes Region hosts markedly variable styles of Cu and Au mineralization as illustrated by the Empress, Taylor-Windfall and Pellaire deposits. All systems formed from magmatic dominated fluids of similar composition with variable inputs of meteoric waters. At least two separate generations of mineralization occurred in the southern Taseko Lakes Region, indicating magmatic-hydrothermal activity responsible for mineralization was prevalent in the area from about 89 to 85 Ma. Therefore, all three deposits formed in similar systems and illustrate the effects varying geologic settings and positioning within an overall system have on styles of mineralization. The indication of large-scale hydrothermal activity in the region during the Late Cretaceous also implies that there is significant potential for other magmatic-hydrothermal deposits to be present in the area.

Pellaire, Taylor-Windfall and Empress are all interpreted to have formed from fluid exsolved from the CPC. Mineralization also coincided with regional deformation in the SECB, which produced north and south-vergent contractional faults that focused exsolved fluids and aided the concentration of economic minerals at the Pellaire deposit and potentially also to the southeast of the study area at the Bralorne District deposits (Leitch et al., 1989). Fluid focusing and ore deposition occurred along the contact between the CPC and SECB due to local contrasts in permeability and host rock compositions at both the Empress and Pellaire deposits. Therefore, mineralization in the Taseko Lakes Region was aided by fluid focussing along contractional faults and the CPC-SECB contact. The SECB-CPC contact could be a significant trend along which economic minerals can be concentrated in the Taseko Lakes Region.

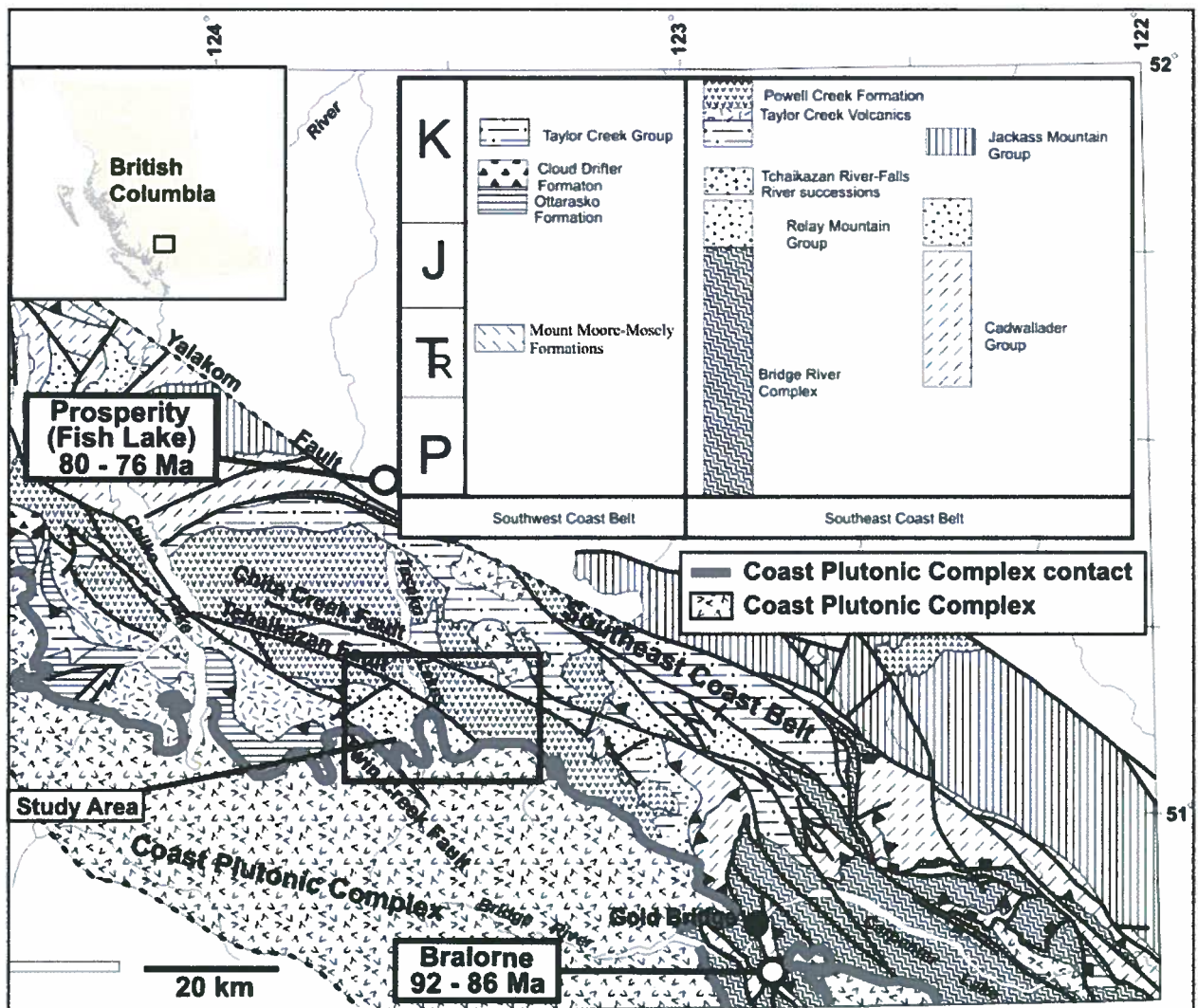
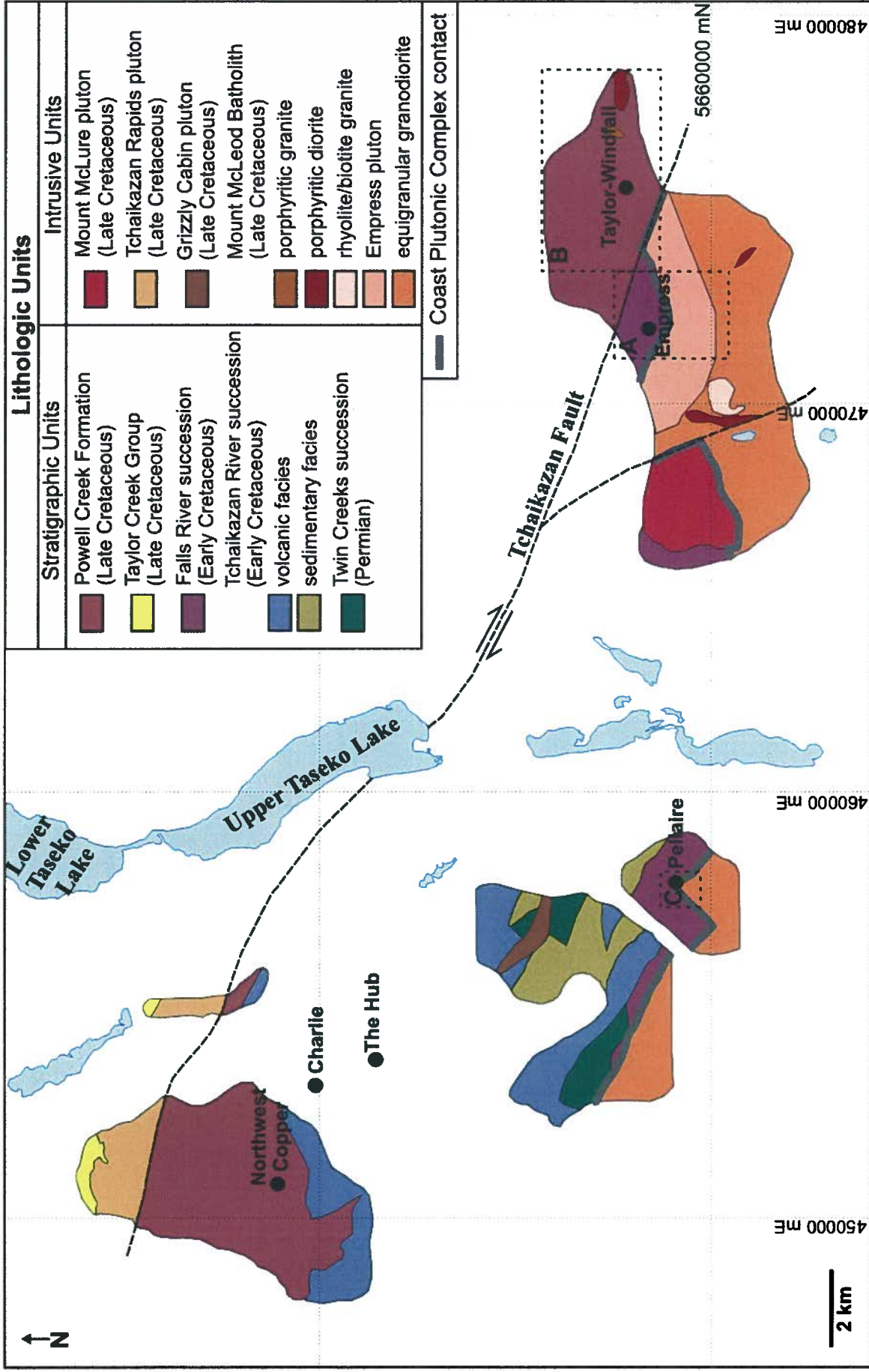


Figure 3.1 Regional geology of Taseko Lakes (modified from Israel et al., 2006), showing the locations of the study area, CPC and SECB as well as the approximate ages and locations of the Bralorne and Prosperity deposits (Wolfhard, 1976; Leitch et al., 1989). The solid box indicates the location of the map shown in Figure 3.4



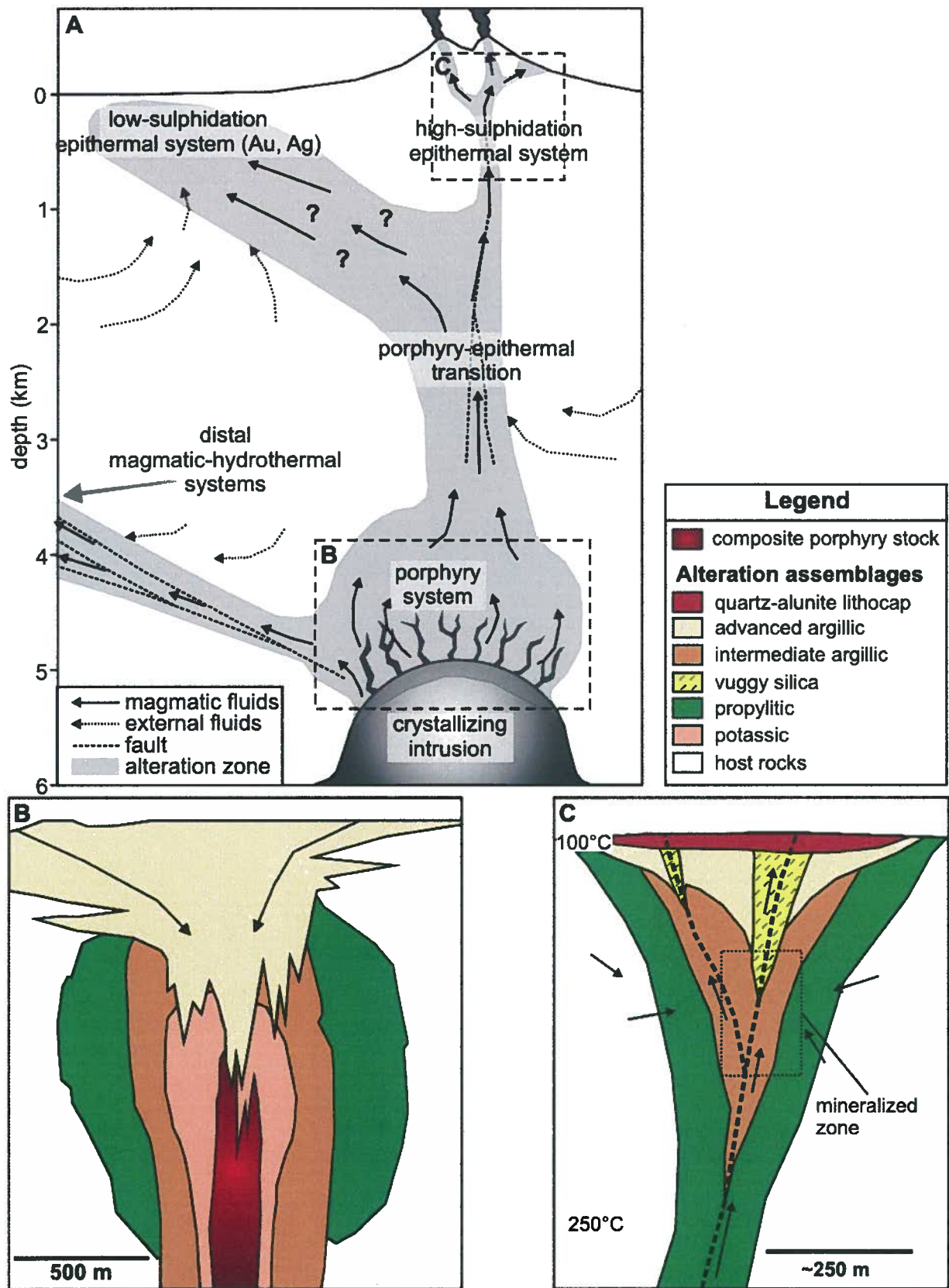


Figure 3.3 A) Cartoon illustrating the postulated deposit types potentially associated with a magmatic-hydrothermal system and their geometries with respect to the overall system. Environments of cartoons B and C are indicated by the dashed, labeled boxes. B) Schematic model of “typical” calc-alkaline porphyry systems. Arrows indicate the direction of non-magmatic fluid input (Modified from Lowell and Guilbert, 1970; Holiday and Cooke, 2007). C) Cartoon illustrating geometry, alteration zonation and fluid temperatures expected for typical high sulphidation epithermal systems (modified after Buchanan, 1981; Hedenquist et al., 1998; Hedenquist and Arribas, 1999).

**Table 3.1** Empress drill-hole data from the 1989 and 1990 drill programs by Westpine Metals Ltd. Contact depth and elevation refer to the contact between the Empress pluton and overlying country rock. Easting and northing coordinates are given in NAD 83 Zone 10. Holes logged and sampled in detail for this study are highlighted in grey. (Lambert, 1989; 1991)

hole ID	easting	northing	collar elevation (masl)	dip (°)	azimuth (°)	hole depth (m)	contact depth (m)	contact elevation (masl)
89-1	472020	5661445	1665	47	360	118.3	N/A	N/A
89-2	472020	5661440	1665	70	181	131.1	N/A	N/A
89-3	472100	5661440	1675	55	181	109.1	N/A	N/A
89-4	472020	5661565	1655	50	177	140.2	N/A	N/A
89-5	472160	5661470	1670	55	179	99.9	N/A	N/A
89-6	472030	5661350	1670	55	3	133.2	N/A	N/A
89-7	471870	5661470	1650	50	180	108.2	N/A	N/A
89-8	471930	5661595	1650	50	180	136.3	N/A	N/A
89-9	471930	5661665	1640	50	180	133.5	N/A	N/A
89-10	471965	5661615	1650	50	180	165.5	N/A	N/A
89-11	471860	5661535	1650	50	180	86	N/A	N/A
89-12	471890	5661625	1645	50	180	217.7	N/A	N/A
89-16	471860	5661410	1655	47	360	50.9	N/A	N/A
90-17	471850	5661660	1635	90	0	215.5	200.6	1434.4
90-18	471780	5661530	1650	90	0	191.2	185.6	1464.4
90-19	471930	5661480	1655	90	0	209.4	203.0	1452.0
90-20	471970	5661610	1650	90	0	217.1	213.7	1436.3
90-21	471820	5661590	1640	90	0	221.6	218.2	1421.8
90-22	471780	5661660	1635	90	0	211.3	207.0	1428.0
90-23	471740	5661600	1645	90	0	206.4	203.3	1441.7
90-24	471820	5661740	1625	90	0	197.3	184.1	1440.9
90-25	471740	5661460	1650	90	0	140.2	125.0	1525.0
90-26	471860	5661425	1655	50	178	87.5	83.8	1590.8
90-27	471860	5661400	1655	65	178	99.7	93.6	1570.2
90-28	472080	5661800	1615	90	0	133.2	119.8	1495.2
90-29	471930	5661670	1640	90	0	218.6	213.4	1426.6
90-30	471890	5661590	1650	90	0	223.5	220.4	1429.6
90-31	472020	5661570	1655	90	0	205.2	203.0	1452.0
90-32	471700	5661530	1650	90	0	180.8	151.8	1498.2
90-33	471700	5661660	1635	90	0	203.3	198.1	1436.9

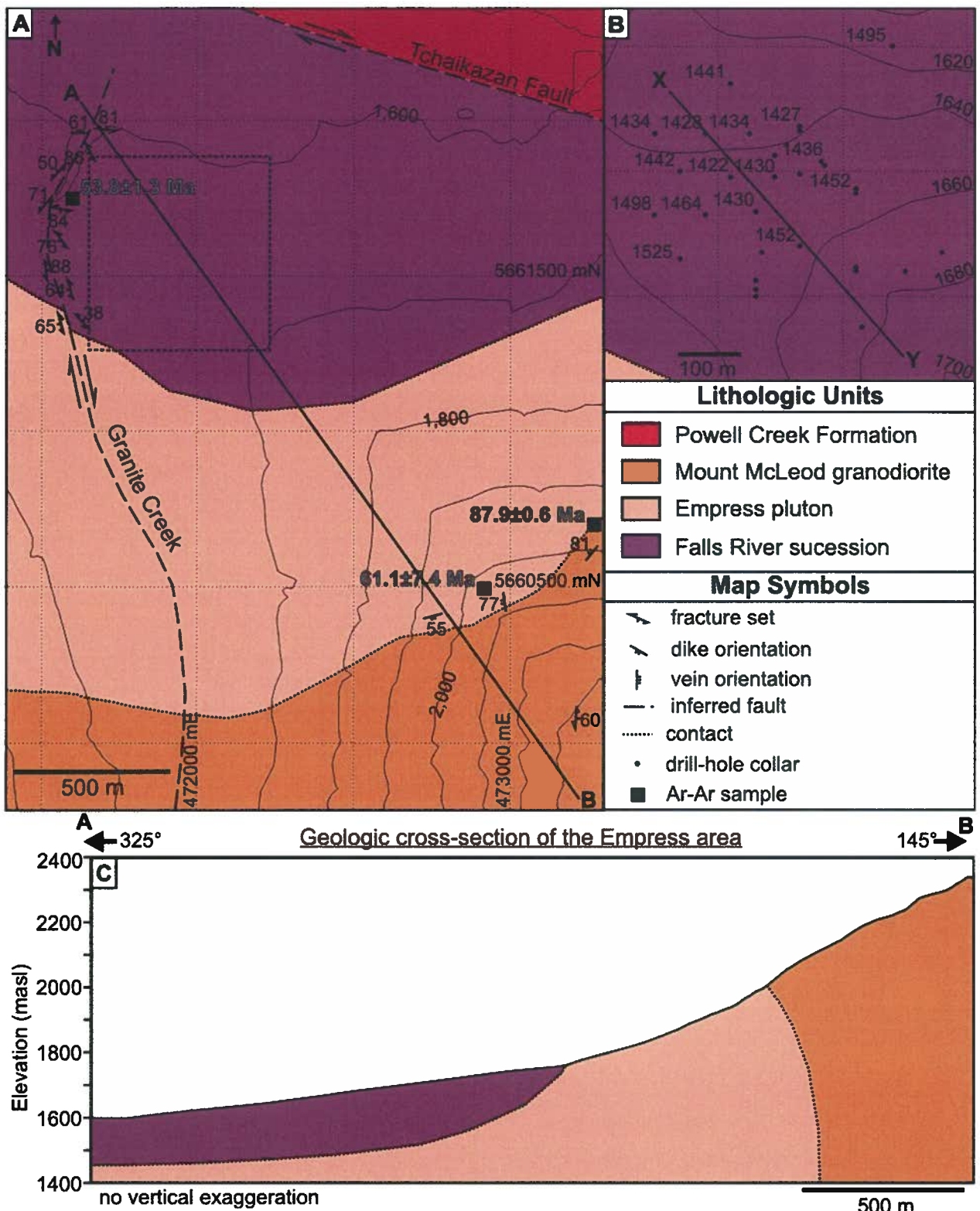
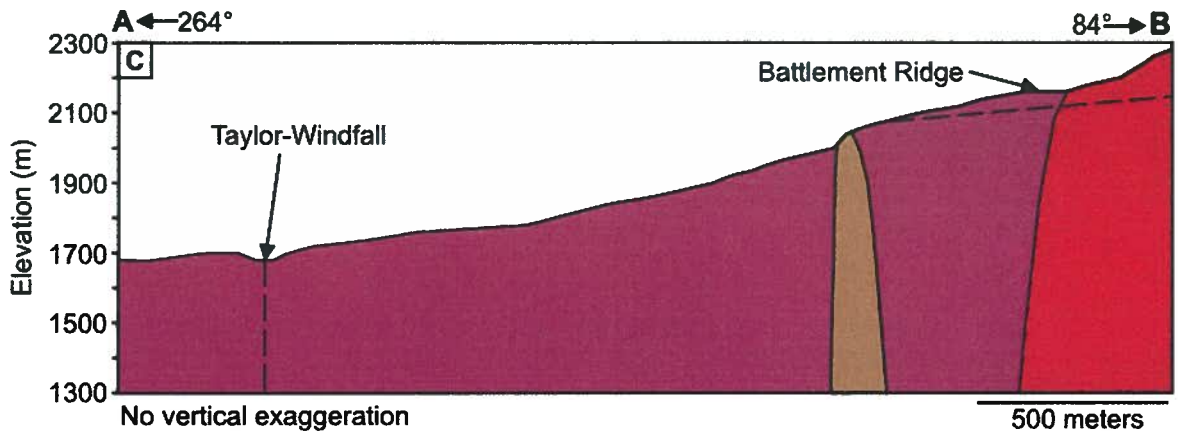
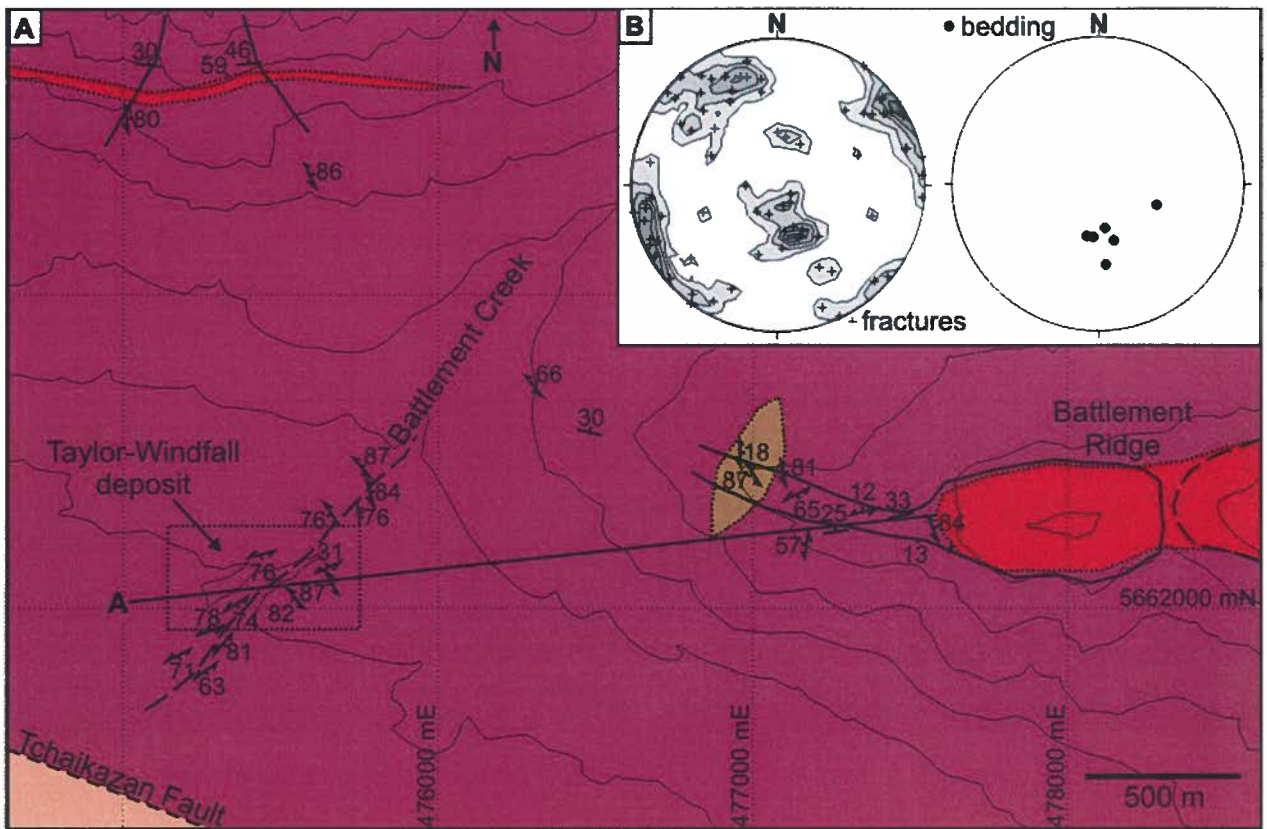


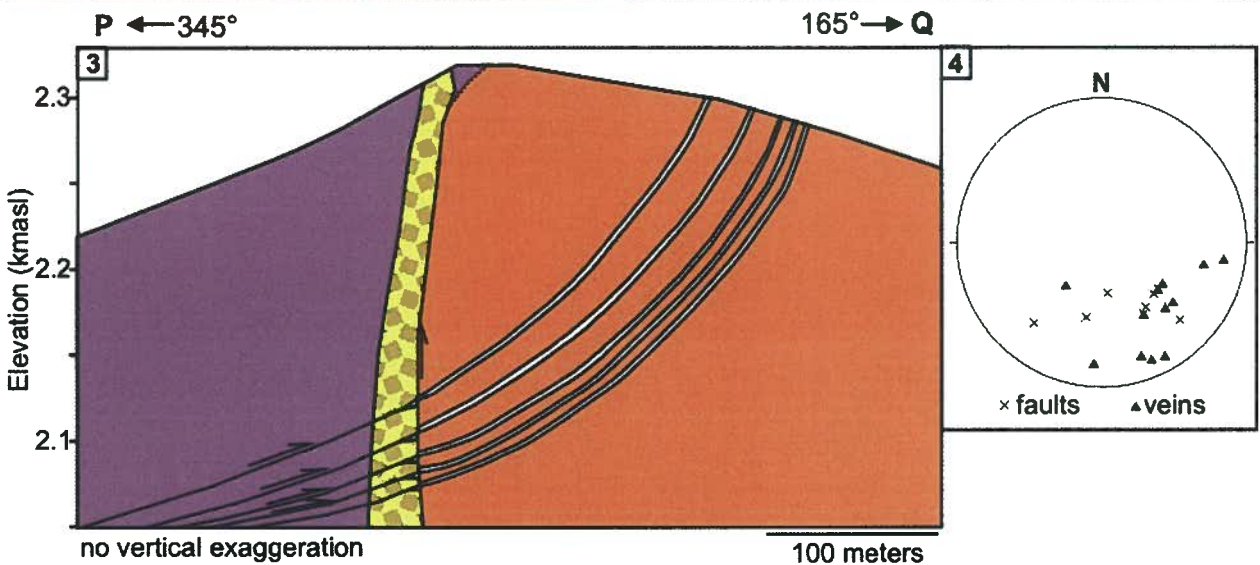
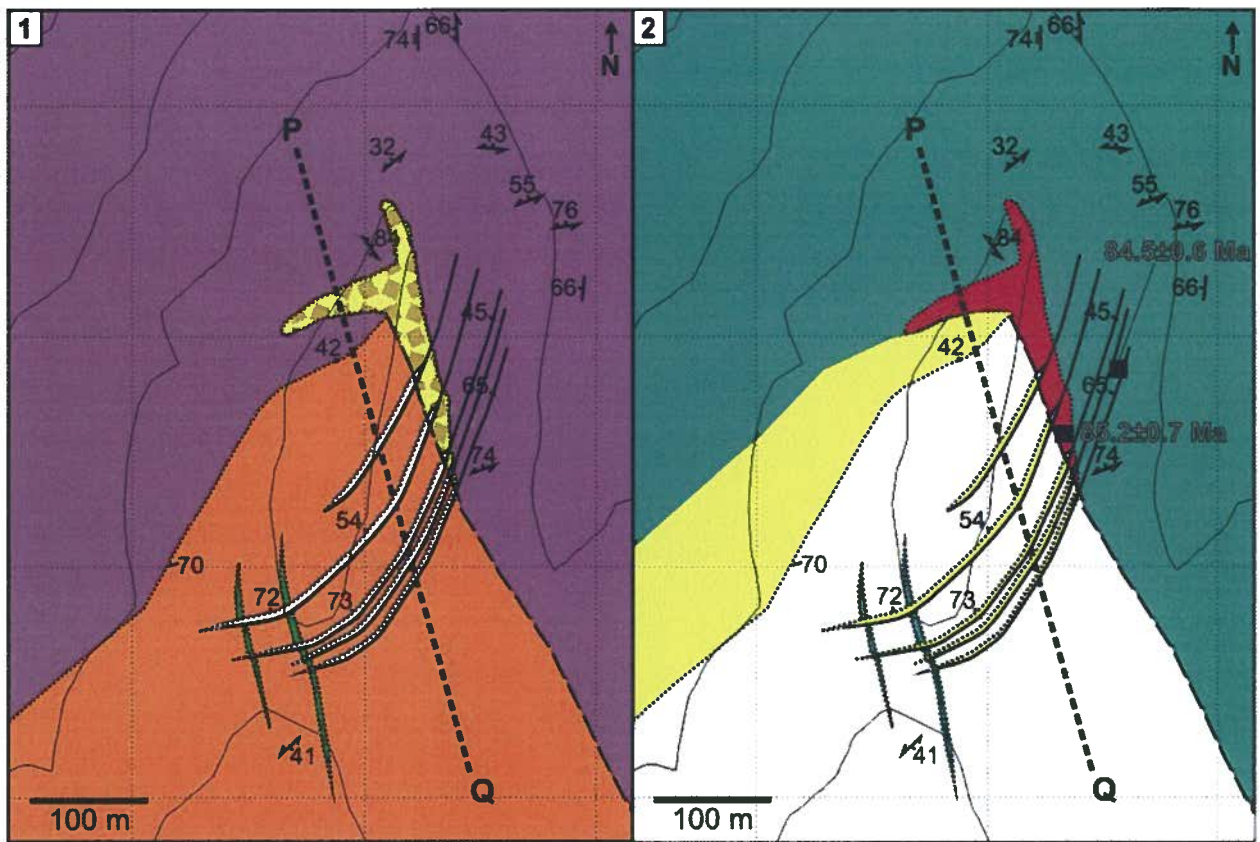
Figure 3.4 A) Geologic map of the Empress area (Location indicated by Box A on Figure 3.2). UTM coordinates are given in NAD 83 Zone 10 and contour intervals are 100 m and elevations are given in masl. Location of the map shown in B) is indicated by the dashed box, and the location of the cross-section shown in C) is indicated by line A-B. B) Geologic map of the Empress deposit. Elevations (masl) of the upper contact of the Empress pluton are indicated based on information from selected vertical drill-holes. Line X-Y indicates the location of the cross-section shown in Figure 3.10. C) Geologic cross-section of the Empress area. Locations and ages of geochronological samples from this study are indicated.





Lithologic Units	Map Symbols
porphyritic granite	fracture set
porphyritic diorite	bedding
Powell Creek Formation	vein orientation
Empress pluton	fault
	inferred fault
	contact

Figure 3.6 A) Geologic map of the Taylor-Windfall area (location indicated by box B on Figure 3.2) showing the location of the Taylor-Windfall deposit, Battlement Creek and Battlement ridge. Location of the cross-section shown in C) is indicated by line A-B. Approximate location of map (A) shown in Figure 3.5 is indicated by the dotted box. B) Equal area, lower hemisphere stereonet projections showing poles to fracture sets with density contours (left) and bedding measurements (right) in the vicinity of the Taylor-Windfall Deposit. C) Geologic cross-section of the Taylor-Windfall area.



Lithologic Units	Alteration Units	Map Symbols
quartz vein	least altered	fracture set
hydrothermal breccia	chlorite alteration	bedding
basaltic dikes	quartz-carbonate alteration	vein orientation
Mount McLeod granodiorite	quartz-sericite alteration	fault
Falls River succession		inferred fault
		contact
		Ar-Ar sample

Figure 3.7 1) Geologic map of the Pellaire property (location indicated by box C on Figure 3.2). Line PQ denotes the location of the cross-section shown in 3). 2) Alteration map of the Pellaire property. 3) Geologic cross-section of the Pellaire property. Note vein thickness is slightly exaggerated. Locations and ages of geochronological samples from this study are indicated. 4) Equal area, lower hemisphere stereonet projections showing poles to quartz veins and south-vergent faults in the vicinity of the Pellaire Deposit.

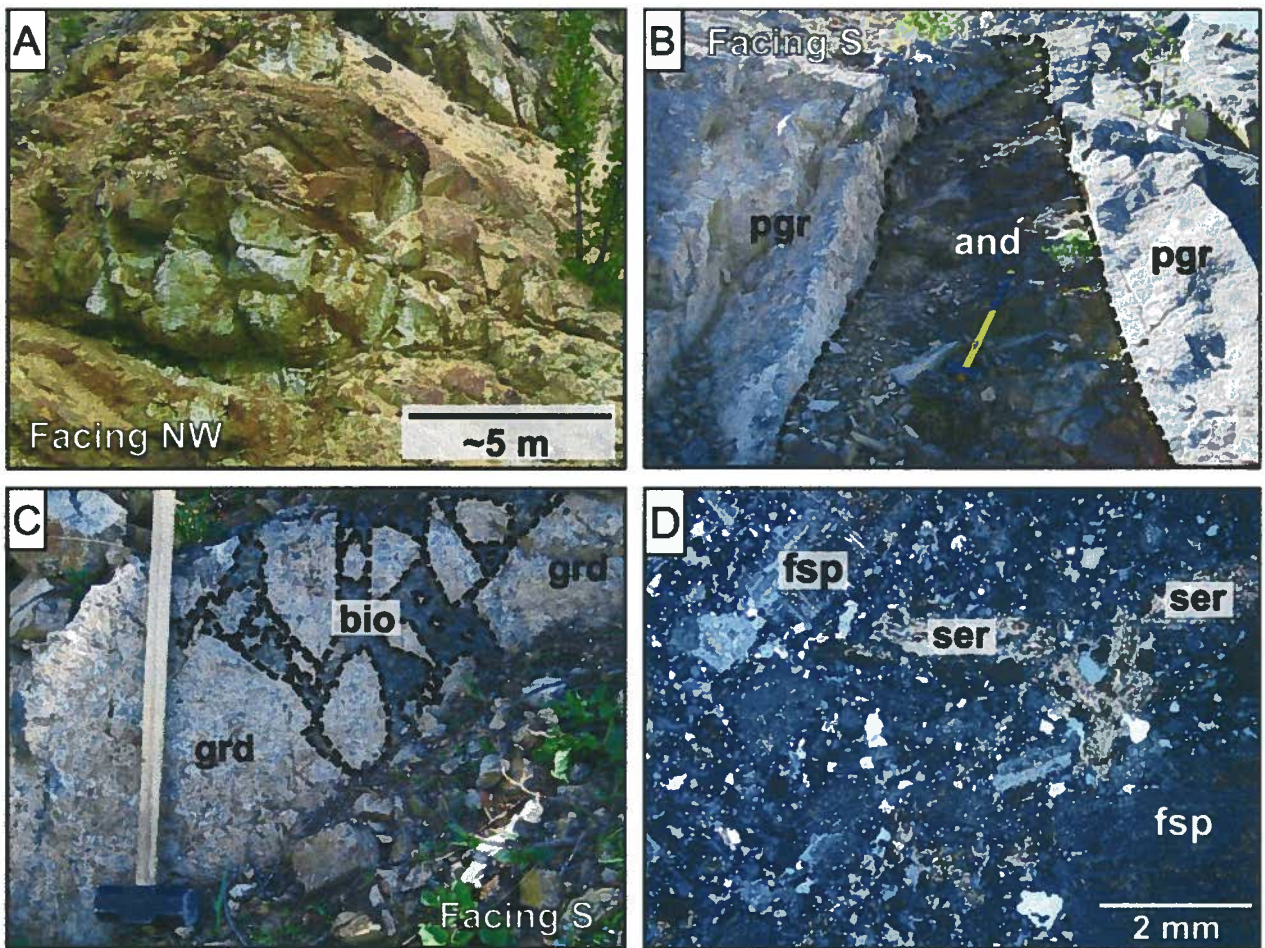


Figure 3.8 A) Bleached outcrop hosting Intense illite-pyrite altered andesite in gulley surrounding granite creek. B) Andesite dike cutting through porphyritic granite on the ridge to the southeast of Empress. C) Biotite cemented granodiorite boulder breccia on the ridge to the southeast of Empress. D) Sericite overprinting the porphyritic granite of the Empress Pluton (field of view = 7.8 mm). Abbreviations: and = andesite, bio = biotite, fsp = feldspar, grd = granodiorite, pgr = porphyritic granite, ser = sericite.

**Table 3.2 Summary of geochronological age data**

<b>Sample</b>	<b>Property</b>	<b>Description</b>	<b>Dating method</b>	<b>Mineral Separate</b>	<b>Age <math>\pm</math> 2<math>\sigma</math> (Ma)</b>	<b>Age type</b>
07-SB-GEO-02	Empress	Empress pluton	U-Pb	zircon	87.0 $\pm$ 1.4	concordant
07-SB-016	Empress	dacite from granite creek	<sup>40</sup> Ar- <sup>39</sup> Ar	biotite	53.8 $\pm$ 1.3	plateau
07-SB-006-2	Empress	andesite dike	<sup>40</sup> Ar- <sup>39</sup> Ar	hornblende	61.1 $\pm$ 7.4	plateau
07-SB-008	Empress	biotite from granodiorite breccia	<sup>40</sup> Ar- <sup>39</sup> Ar	biotite	87.93 $\pm$ 0.59	plateau
07-SB-073	Empress	rhyolite dike cutting granodiorite	<sup>40</sup> Ar- <sup>39</sup> Ar	biotite	91.45 $\pm$ 0.51	plateau
07-SB-CS-102	Empress	Empress pluton	<sup>40</sup> Ar- <sup>39</sup> Ar	biotite	87.87 $\pm$ 0.47	plateau
07-SB-CS-013	Empress	quartz-sericite alteration	<sup>40</sup> Ar- <sup>39</sup> Ar	muscovite	86.66 $\pm$ 0.50	plateau
	Taylor-					
07-SB-023-3	Windfall	foliated vuggy quartz rock	<sup>40</sup> Ar- <sup>39</sup> Ar	illite	89.3 $\pm$ 0.54	plateau
	Taylor-					
07-SB-020-2	Windfall	hydrothermal breccia matrix	<sup>40</sup> Ar- <sup>39</sup> Ar	illite	87.7 $\pm$ 1.1	plateau
07-SB-GEO-09	Pellaire	Mount McLeod granodiorite	U-Pb		83.2 $\pm$ 2.6	concordant
07-SB-173-1	Pellaire	hydrothermal breccia matrix	<sup>40</sup> Ar- <sup>39</sup> Ar	illite	85.16 $\pm$ 0.65	plateau
07-SB-136-7	Pellaire	fault gouge	<sup>40</sup> Ar- <sup>39</sup> Ar	illite	84.52 $\pm$ 0.58	plateau

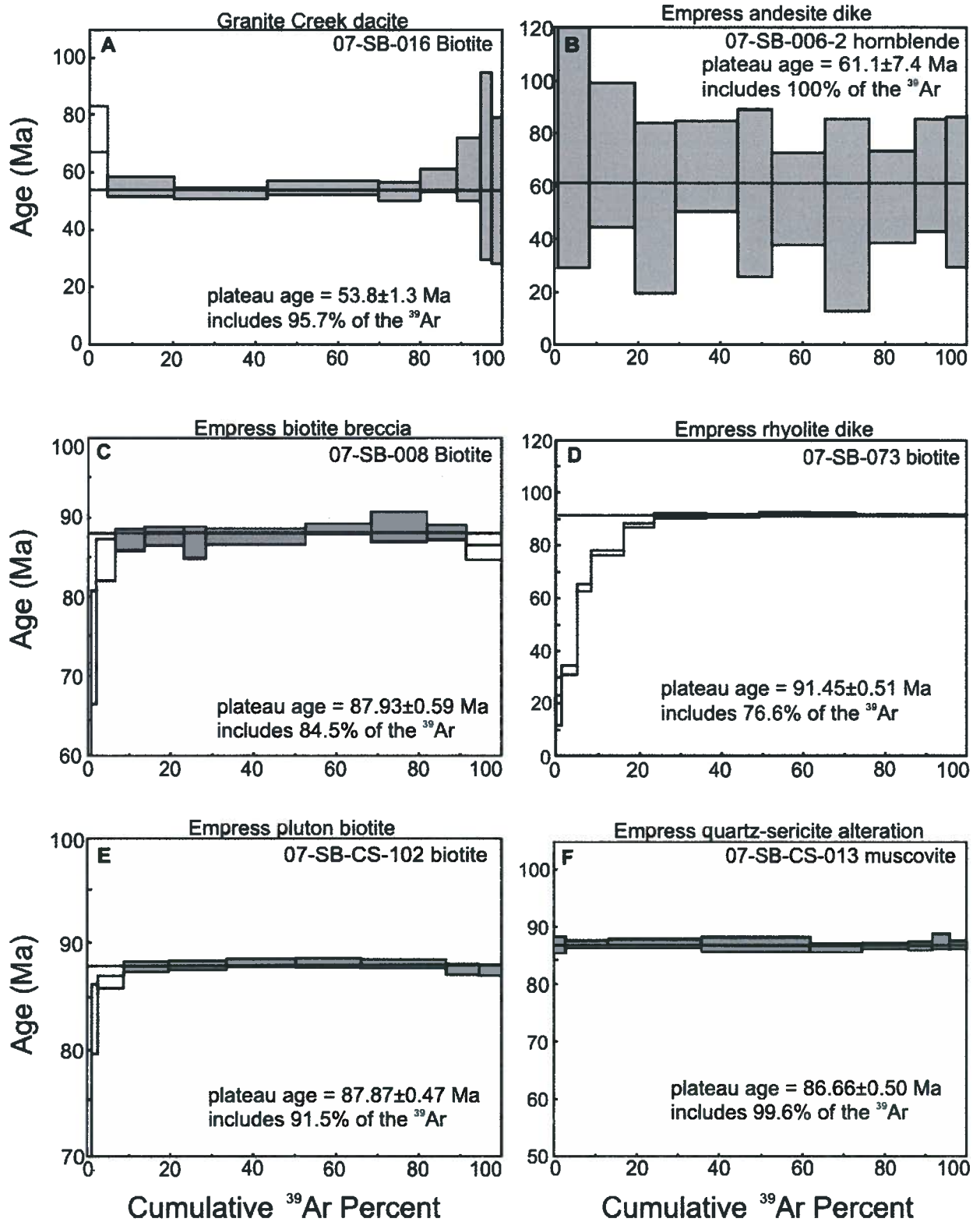


Figure 3.9 A) to F) Ar-Ar plateau ages of lithologic and alteration units in the southern Taseko Lakes area. The grey shaded boxes are included in the age calculation while the white boxes are rejected steps. Errors in box heights given at  $2\sigma$ . See text for analytical description and appendix A for complete data set.

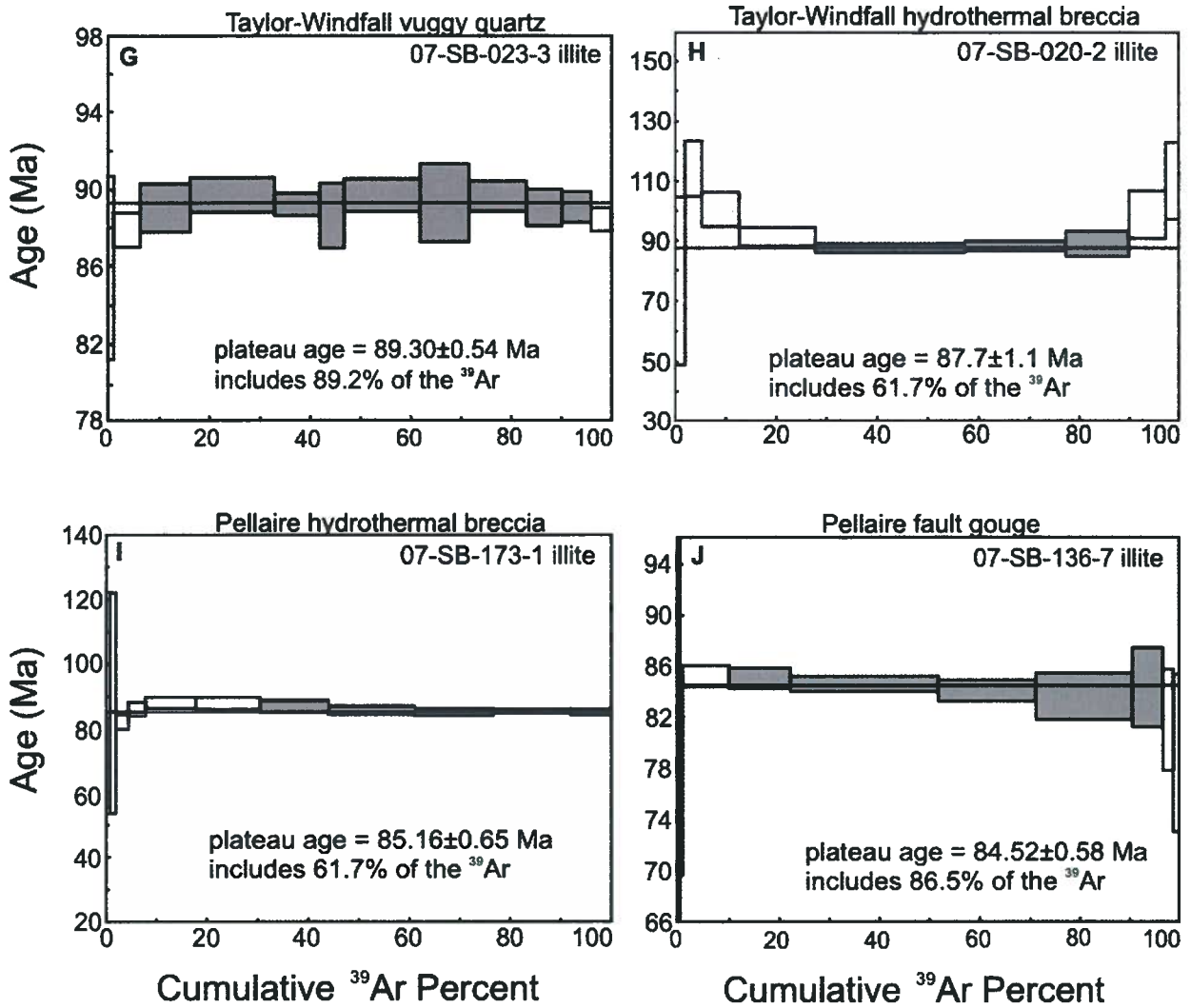


Figure 3.9 (cont'd) G) to J) Ar-Ar plateau ages of lithologic and alteration units in the southern Taseko Lakes area. The grey shaded boxes are included in the age calculation while the white boxes are rejected steps. Errors in box heights given at  $2\sigma$ . See text for analytical description and appendix A for complete data set.

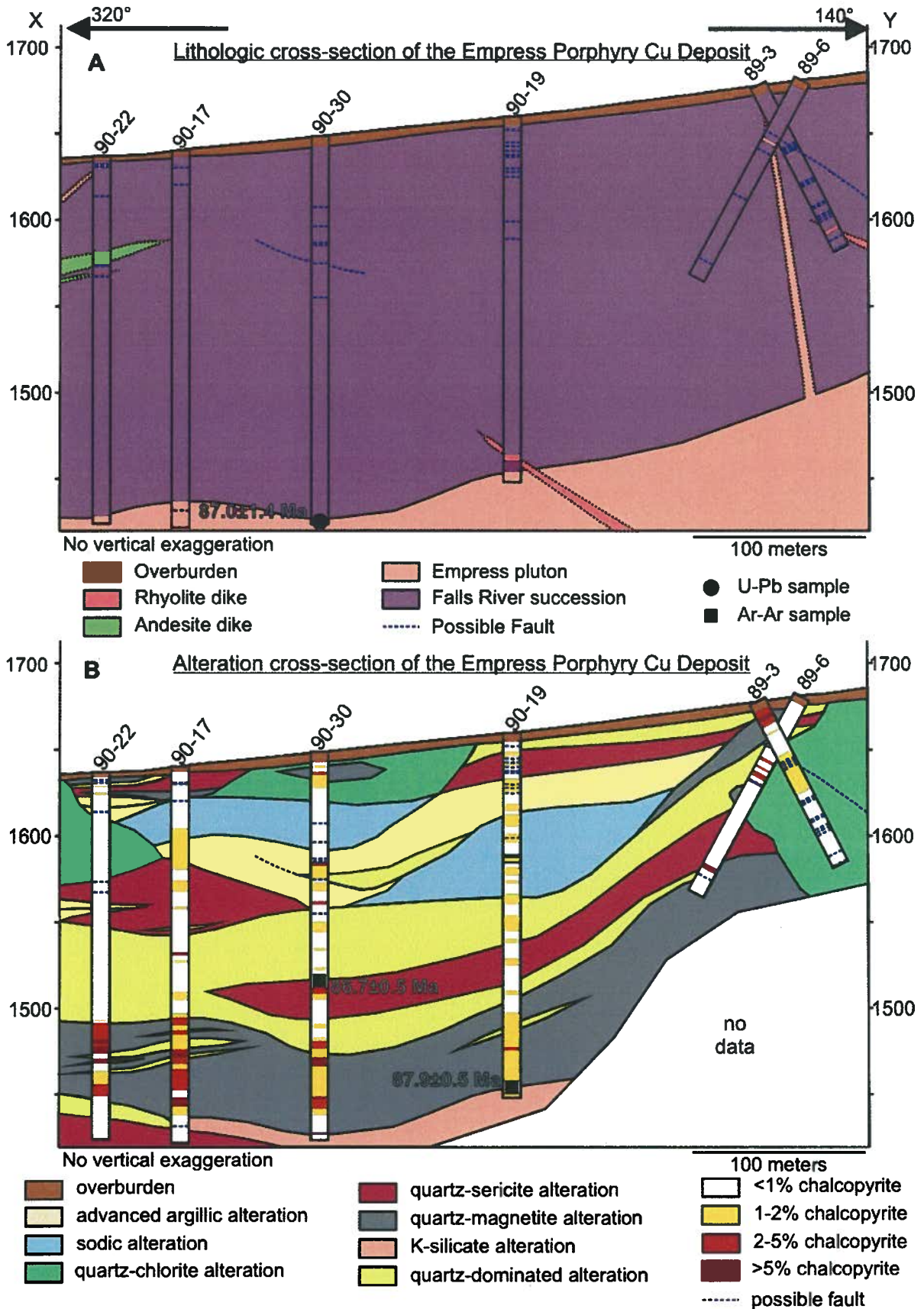


Figure 3.10 (A) Cross-section through the Empress deposit showing lithologic units. Dike and fault orientations are speculative due to the lack of oriented drill-core. (B) Cross-section through the Empress deposit showing alteration zones. Chalcopyrite grades are indicated within drill holes. Locations and ages of geochronological samples from this study are indicated. Cross-section locations indicated by line XY on Figure 3.4.

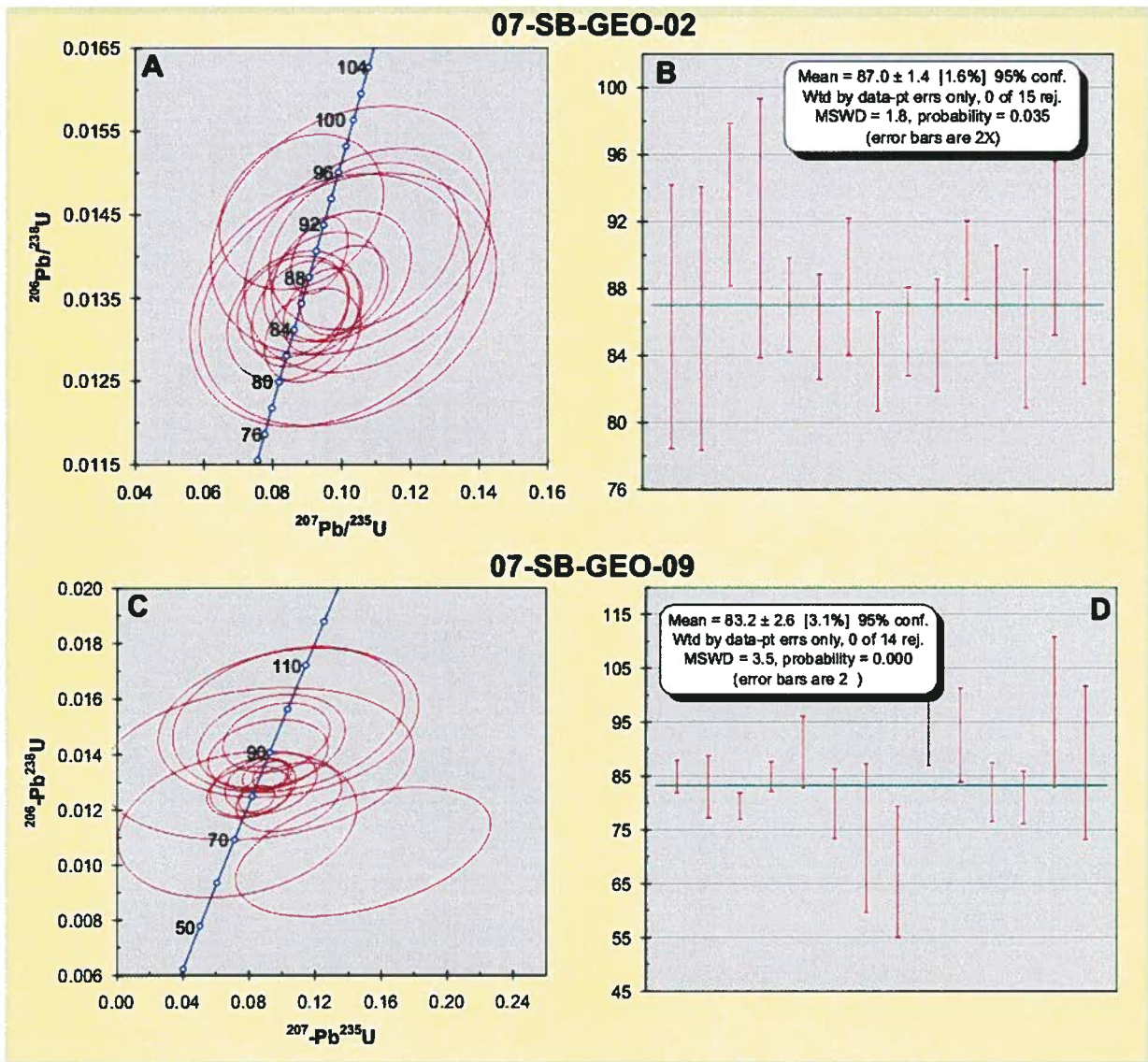


Figure 3.11 U-Pb data for samples indicated showing: A) U-Pb Concordia plots for zircon analysis (data presented in appendix and data point ellipses are  $2\sigma$ ) Ellipses represent the statistical 'concordia age' as calculated by ISOPLOT. The black line with white circles represents the Concordia curve with time (Ma) markers. B) Weighted average plots. Plots, ages, and errors were calculated using the ISOPLOT program of Ludwig (2003).

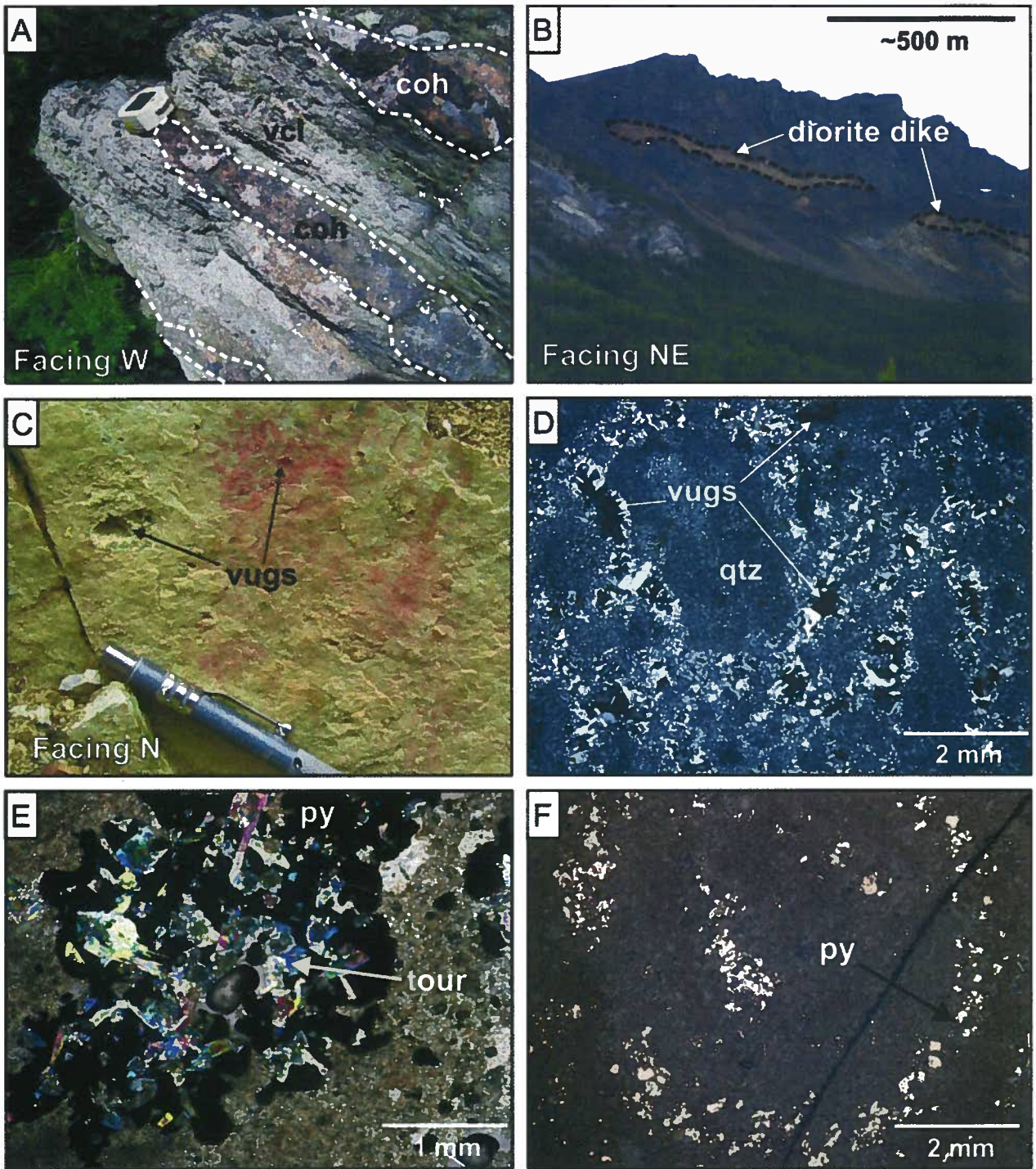


Figure 3.12 A) Coherent and volcanoclastic units from a pyroclastic surge deposit in the Powell Creek Formation. B) Altered porphyritic diorite dike cutting through rocks of the Powell Creek Formation on the ridge to the north of Battlement Creek. C) Vuggy silica altered rock. D) Cross-polarized light photomicrograph of vuggy silica alteration (field of view = 7.8 mm). E) Cross-polarized light photomicrograph of tourmaline occurring with pyrite (field of view = 3.9 mm). F) Reflected light photomicrograph of pyrite forming orbicule rim (field of view = 7.8 mm). Abbreviations: coh = coherent, py = pyrite, qtz = quartz, tour = tourmaline, vcl = volcanoclastic.

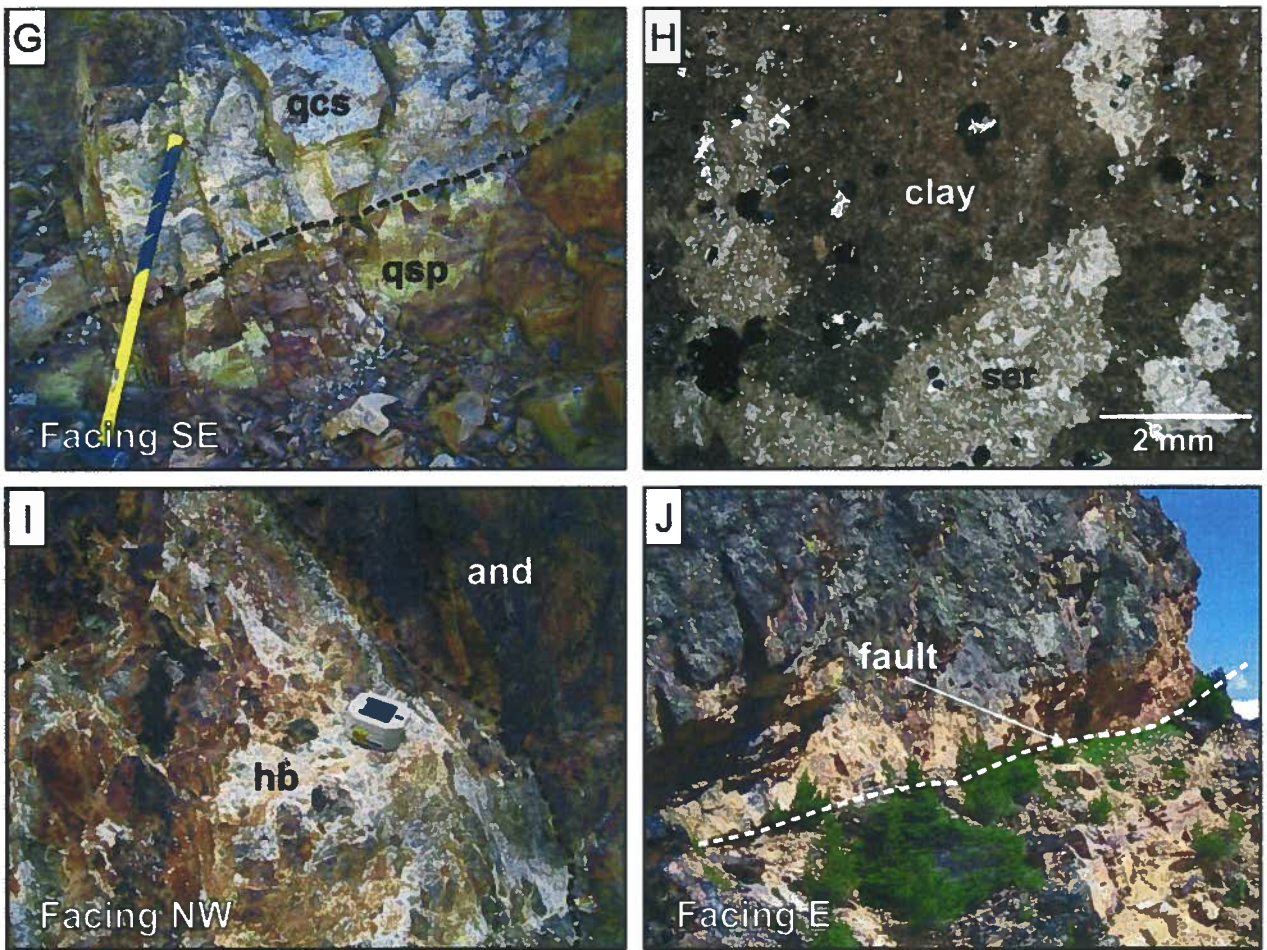


Figure 3.12 (cont'd) G) Fracture controlled quartz-sericite-pyrite and quartz-chlorite-sericite alteration. H) Blotchy, uneven sericite-advanced argillic-chlorite alteration field of view = 7.8 mm). I) Quartz-sericite-palygorskite cemented hydrothermal breccia. J) Low-angle fault hosting intense quartz-alunite alteration. Abbreviations: and = andesite, hb = hydrothermal breccia, qcs = quartz-chlorite-sericite alteration, qsp = quartz-sericite-pyrite alteration, ser = sericite.

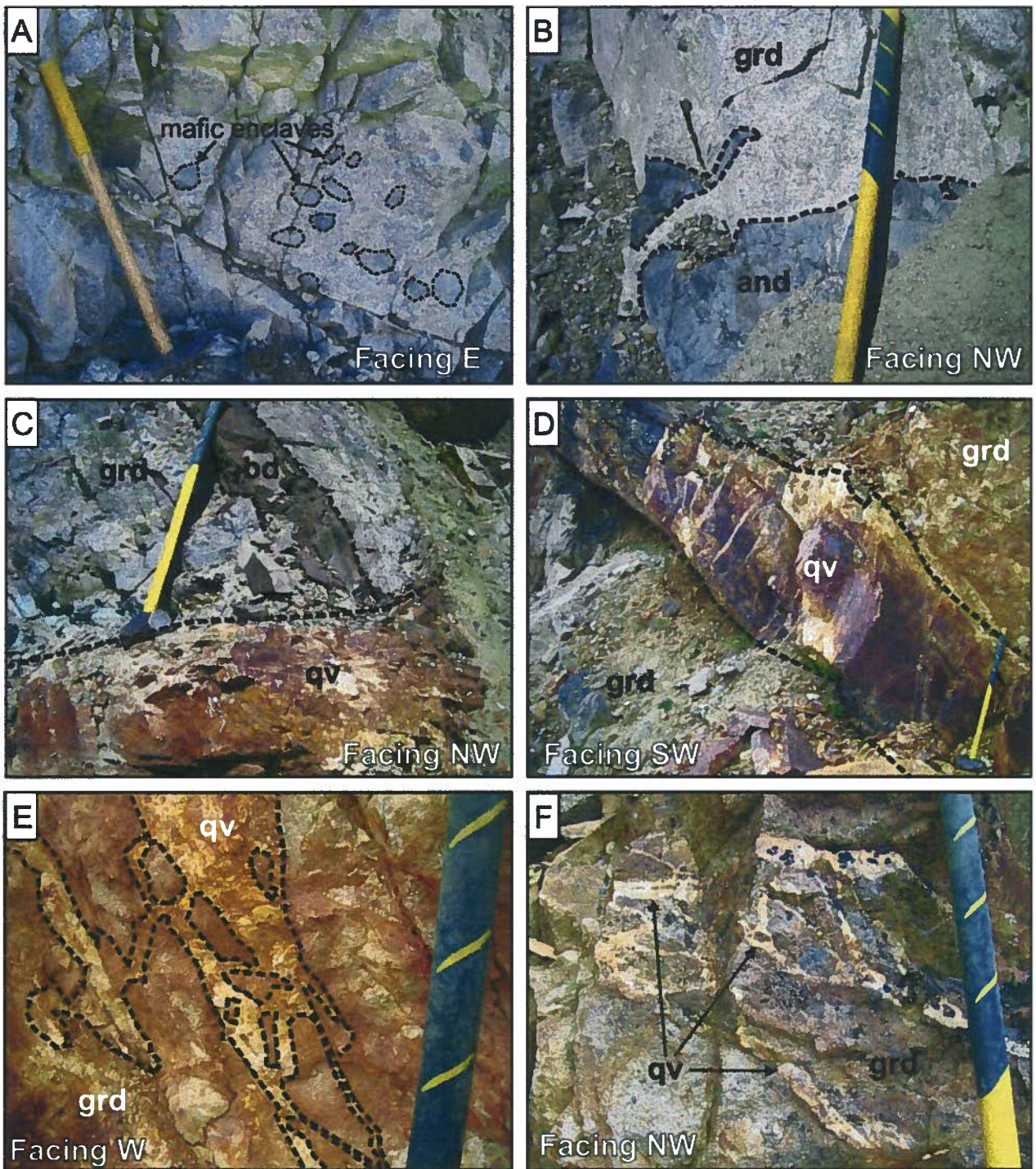


Figure 3.13 A) Outcrop of the Mount McLeod granodiorite containing mafic enclaves. B) Irregular, intrusive contact between the Mount McLeod granodiorite and the Falls River Succession. C) Basaltic dike cutting through the Mount McLeod Granodiorite, cut by quartz vein. D) One of the more prominent quartz veins on Pellaire. E) Brecciation of the hangingwall granodiorite above the quartz vein by quartz veining. F) Stockwork quartz veining in the hangingwall above a quartz vein. Abbreviations: and = andesite, bd = basaltic dike, grd = granodiorite, qv = quartz vein.

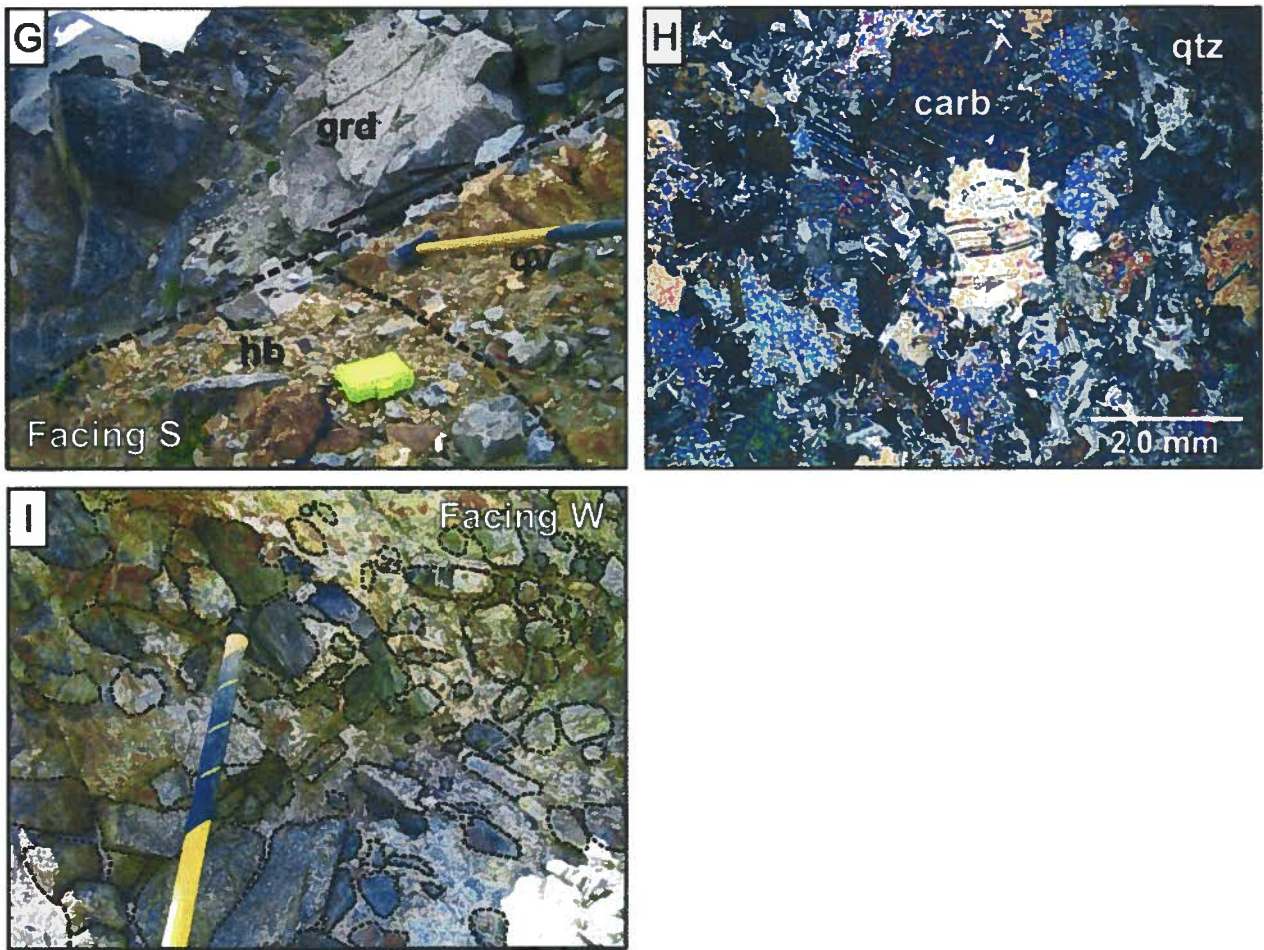


Figure 3.13 (cont'd) G) Quartz vein hosted within the hydrothermal breccia and cut and offset by the fault separating the breccia from the granodiorite. H) Cross-polarized light photomicrograph of Intense quartz-carbonate alteration in andesite (Field of view = 7.8 mm). I) Quartz-sericite-jarosite cemented polymictic hydrothermal boulder breccia. Abbreviations: carb = carbonate, grd = granodiorite, hb = hydrothermal breccia, qtz = quartz, qv = quartz vein.

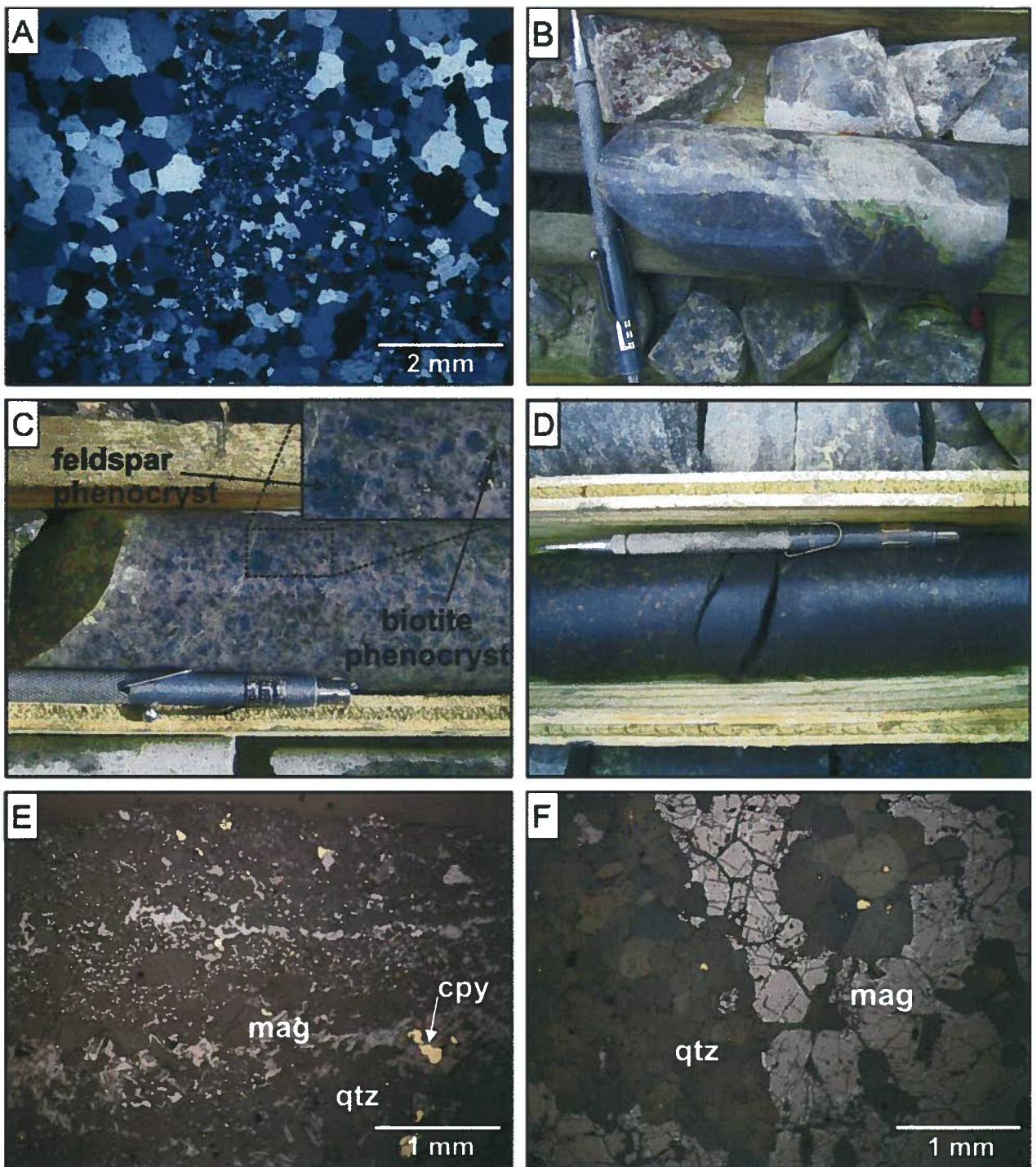


Figure 3.14 Photoplate of Empress alteration examples showing: A) Cross-polarized light photomicrograph of intermingling zones of fine and coarse grained quartz dominated alteration (field of view = 7.8 mm). B) Intermingling zones of light and dark grey quartz-dominated alteration. C) Potassium-silicate alteration within the Empress pluton. D) Massive magnetite alteration. E) Reflected light photomicrograph of magnetite-cemented quartz-dominated pebble breccia (field of view = 3.9 mm). F) Banded quartz-magnetite alteration (field of view = 3.9 mm). Abbreviations: cpy = chalcopryite, mag = magnetite, qtz = quartz.

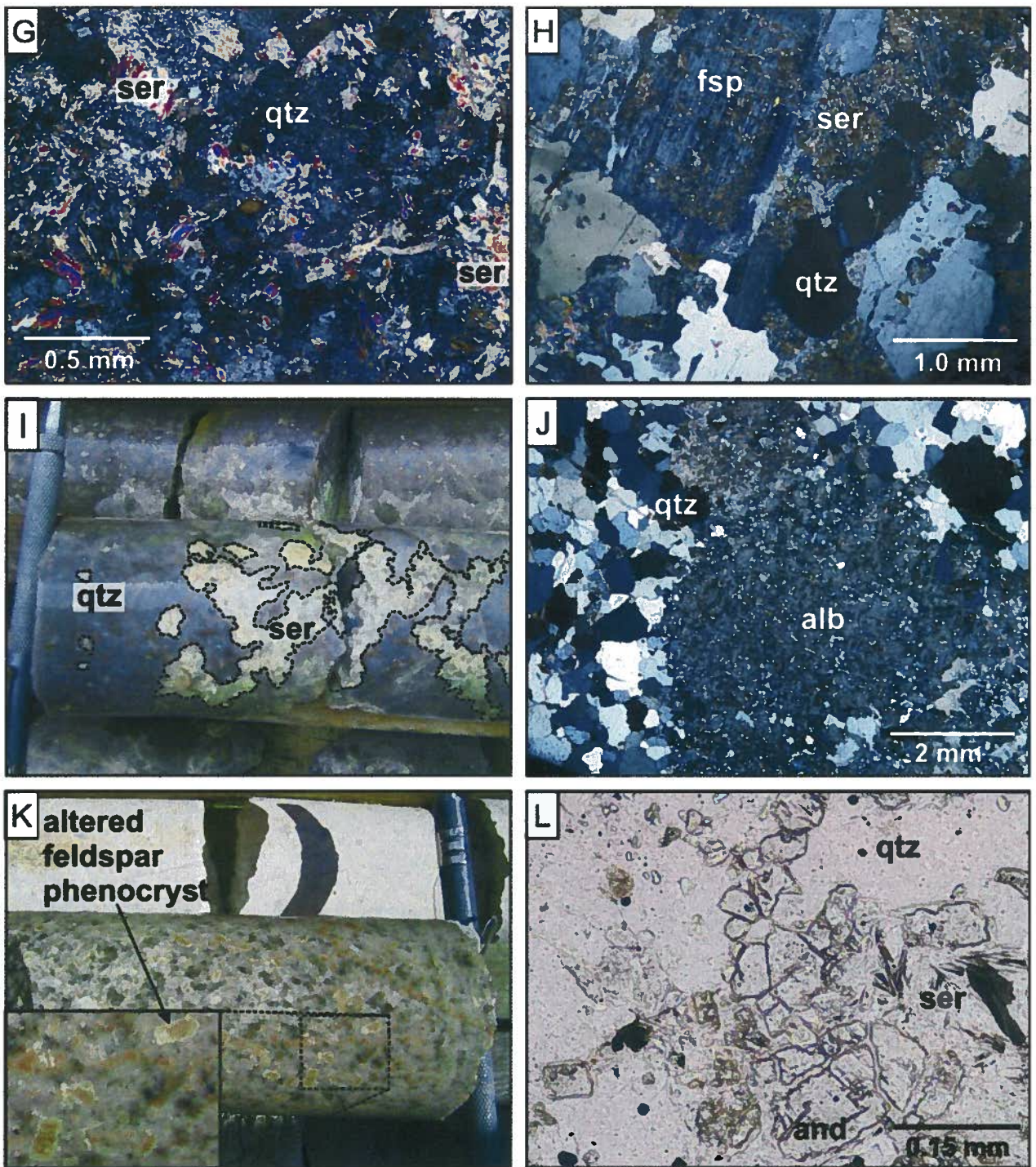


Figure 3.14 (cont'd) Photoplate of Empress alteration examples showing: G) Cross-polarized light photomicrograph of uniform quartz-sericite alteration (field of view = 2.0 mm). H) Cross-polarized light photomicrograph of sericite overprinting porphyritic granite (field of view = 3.9 mm). I) Patchy sericite occurring in quartz-dominated alteration. J) Cross-polarized light photomicrograph of blotchy fine-grained albitization of quartz-dominated alteration (field of view = 7.8 mm). K) Advanced argillic overprint of relatively fresh, porphyritic granite. Feldspar phenocrysts have been altered to kaolinite. L) Plane-polarized light photomicrographs of andalusite occurring in quartz-sericite alteration (field of view = 0.6 mm). Abbreviations: alb = albite, and = andalusite, fsp = feldspar, qtz = quartz, ser = sericite.

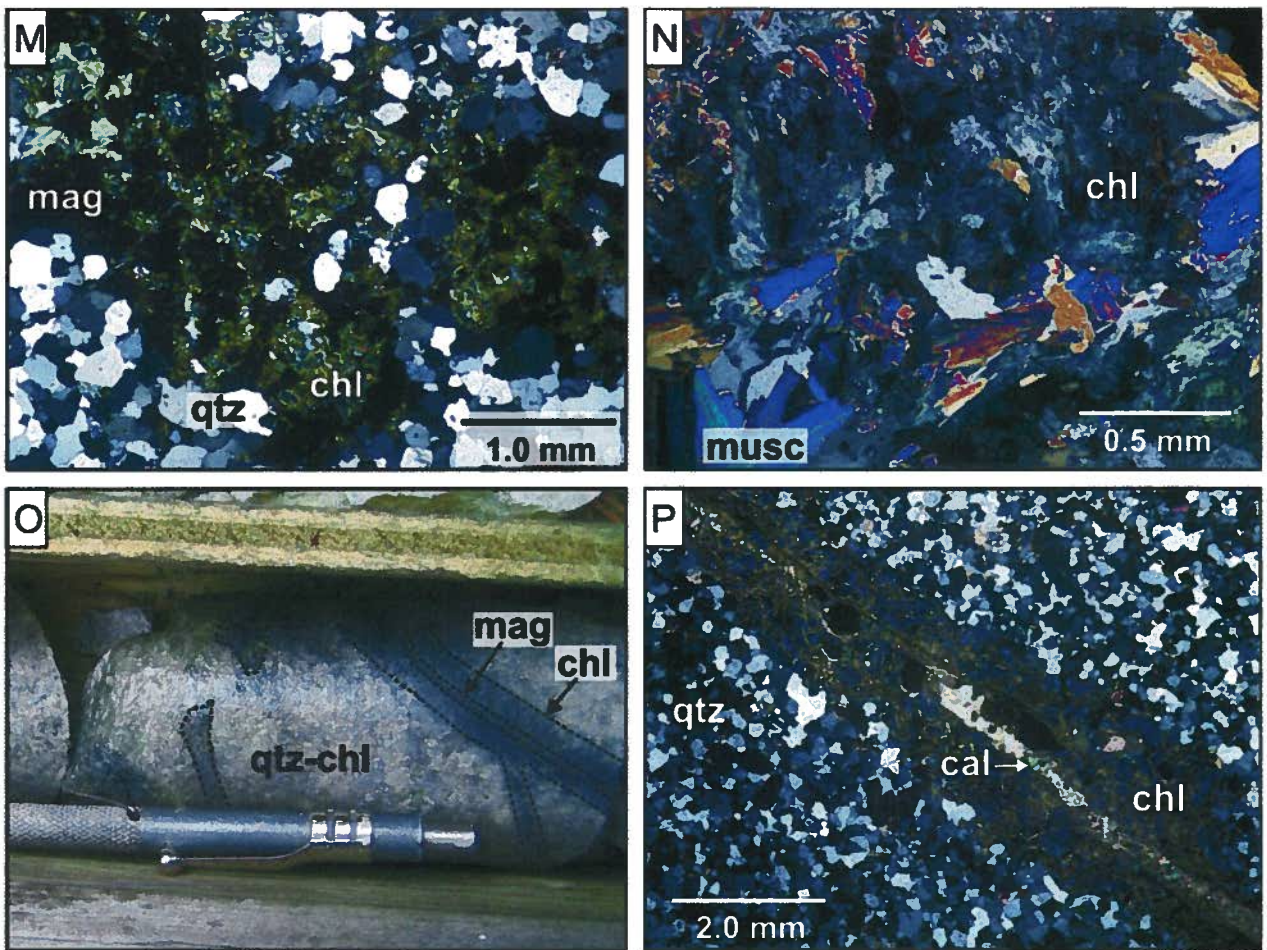


Figure 3.14 (cont'd) Photoplate of Empress alteration examples showing: M) Cross-polarized light photomicrograph of chlorite overprinting quartz-magnetite alteration (field of view = 3.9 mm). N) Cross-polarized light photomicrograph of chlorite overprinting quartz-sericite alteration (field of view = 2.0 mm). O) Chlorite-magnetite vein with chlorite halo cutting quartz-dominated alteration (field of view = 7.8 mm). P) Cross-polarized light photomicrograph of composite chlorite-calcite vein cutting quartz-dominated alteration (field of view = 7.8 mm). Abbreviations: cal = calcite, chl = chlorite, mag = magnetite, musc = muscovite, qtz = quartz.

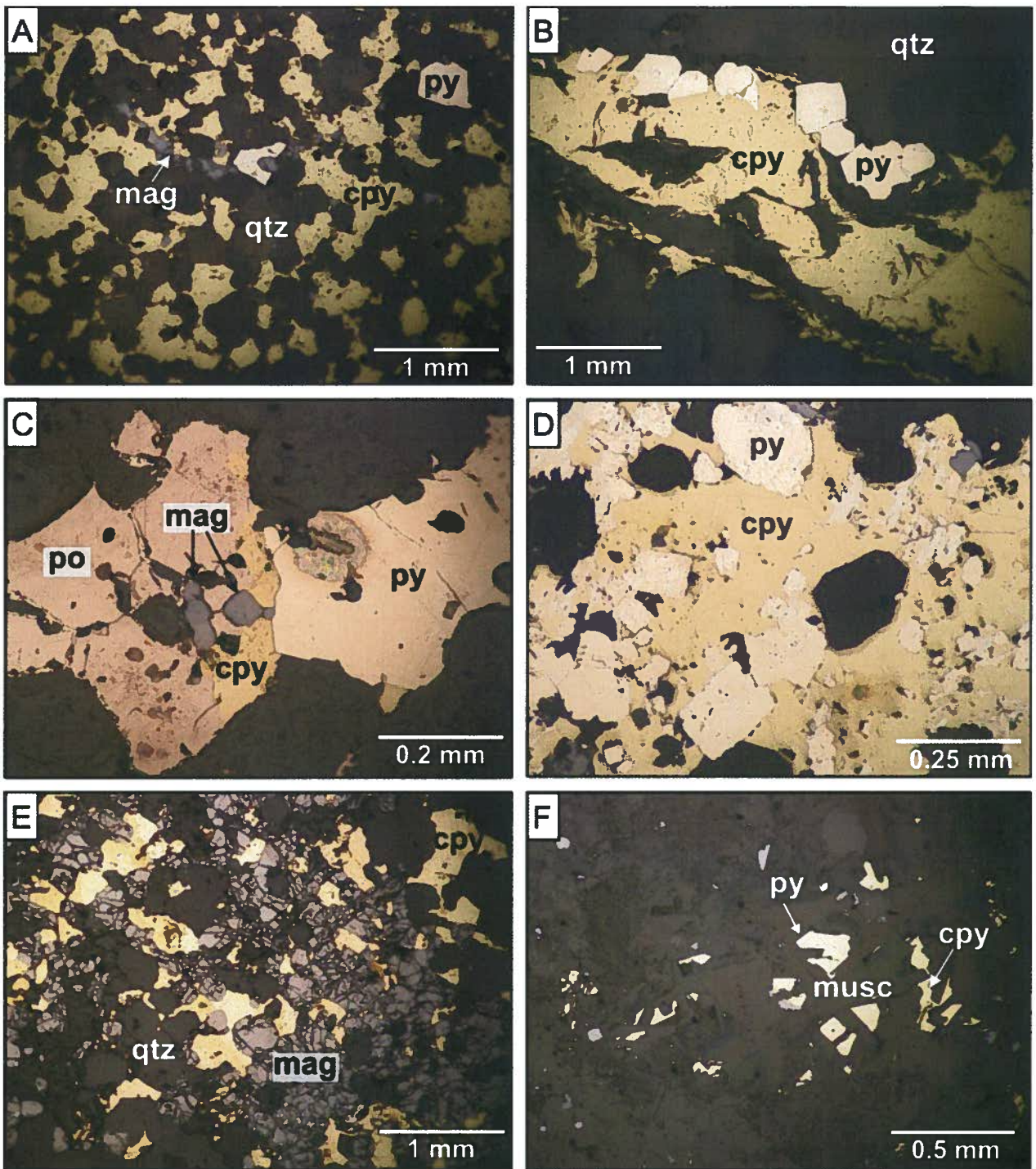
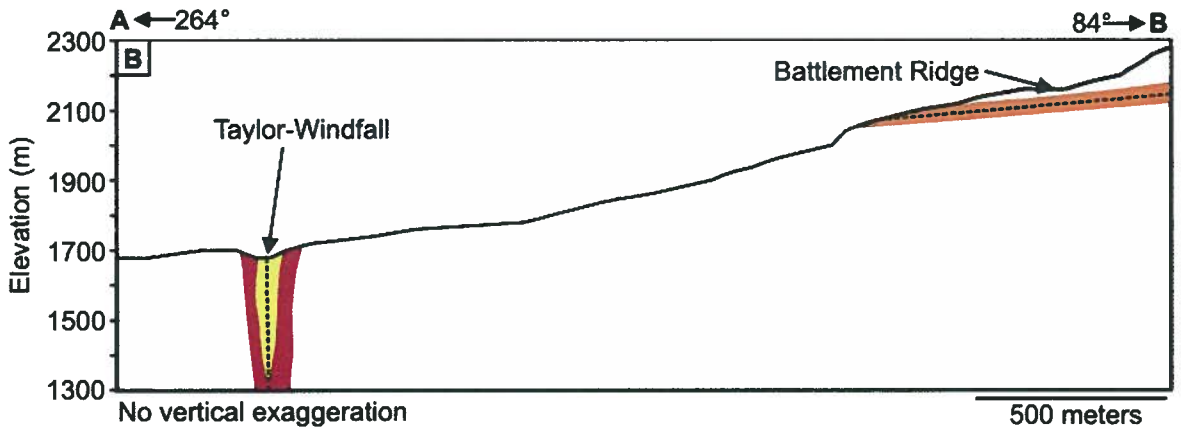
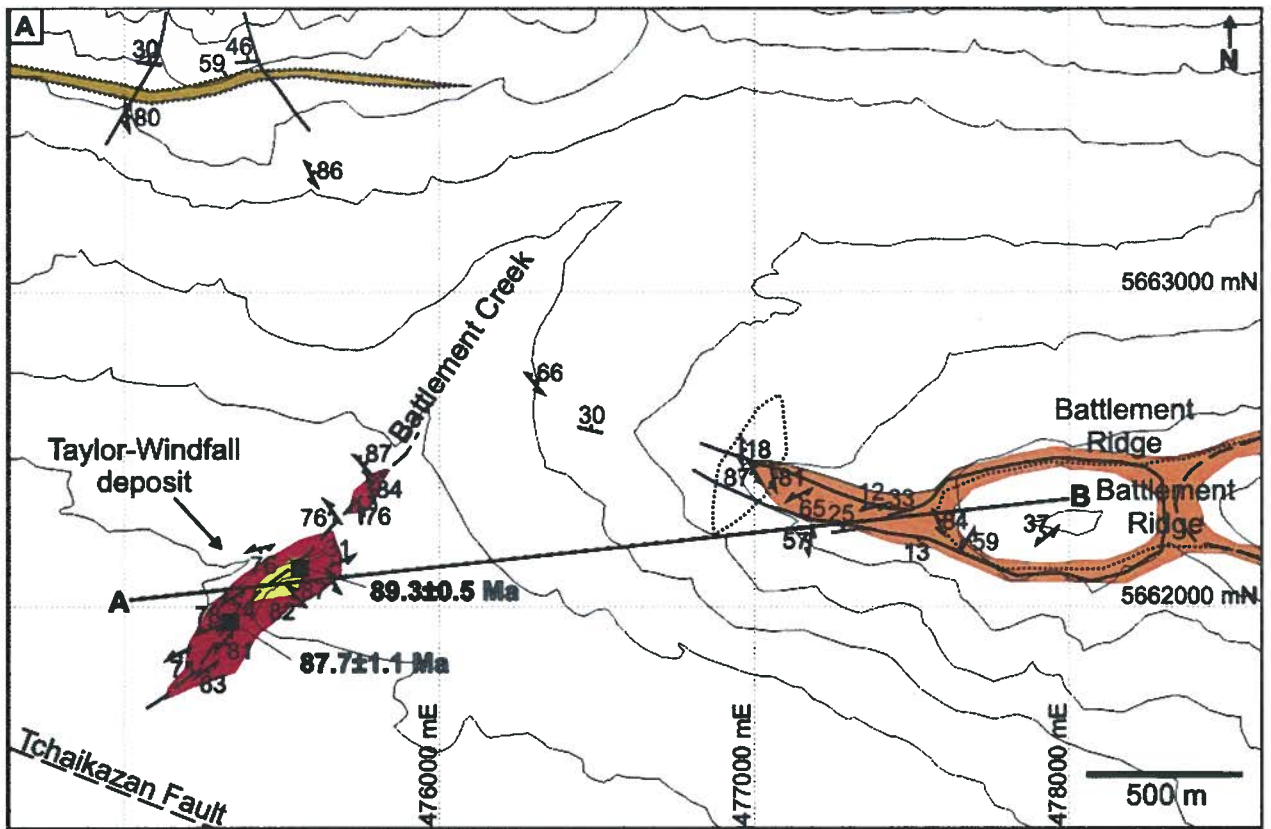


Figure 3.15 Reflected light photomicrographs showing: A) Uniform interstitial to net texture of chalcopyrite (field of view = 3.9 mm). B) Chalcopyrite-pyrite vein cutting quartz-dominated alteration (field of view = 3.9 mm). C) Pyrrhotite and chalcopyrite containing magnetite inclusions next to grain of pyrite (field of view = 0.8 mm). D) Net-textured chalcopyrite brecciating pyrite grains (field of view = 1.0 mm). E) Chalcopyrite occurring interstitially to quartz-magnetite alteration (field of view = 3.9 mm). F) Coarse muscovite crystals overprinting pyrite and chalcopyrite (field of view = 2.0 mm). Abbreviations: cpx = chalcopyrite, mag = magnetite, musc = muscovite, po = pyrrhotite, py = pyrite, qtz = quartz.



Alteration Units	Map Symbols
background alteration	fracture set
quartz-dickite alteration	bedding
quartz-alunite alteration	vein orientation
quartz-sericite ± chlorite ± pyrite ± argillic alteration	fault
vuggy silica alteration	inferred fault
	contact
	Ar-Ar sample

Figure 3.16 A) Alteration map of the Taylor-Windfall area (location indicated by box B on Figure 3.2) showing the location of the Taylor-Windfall deposit, Battlement Creek and Battlement ridge. Location of the cross-section shown in B) is indicated by line A-B. 2) Alteration cross-section of the Taylor-Windfall area. Locations and ages of geochronological samples from this study are indicated.

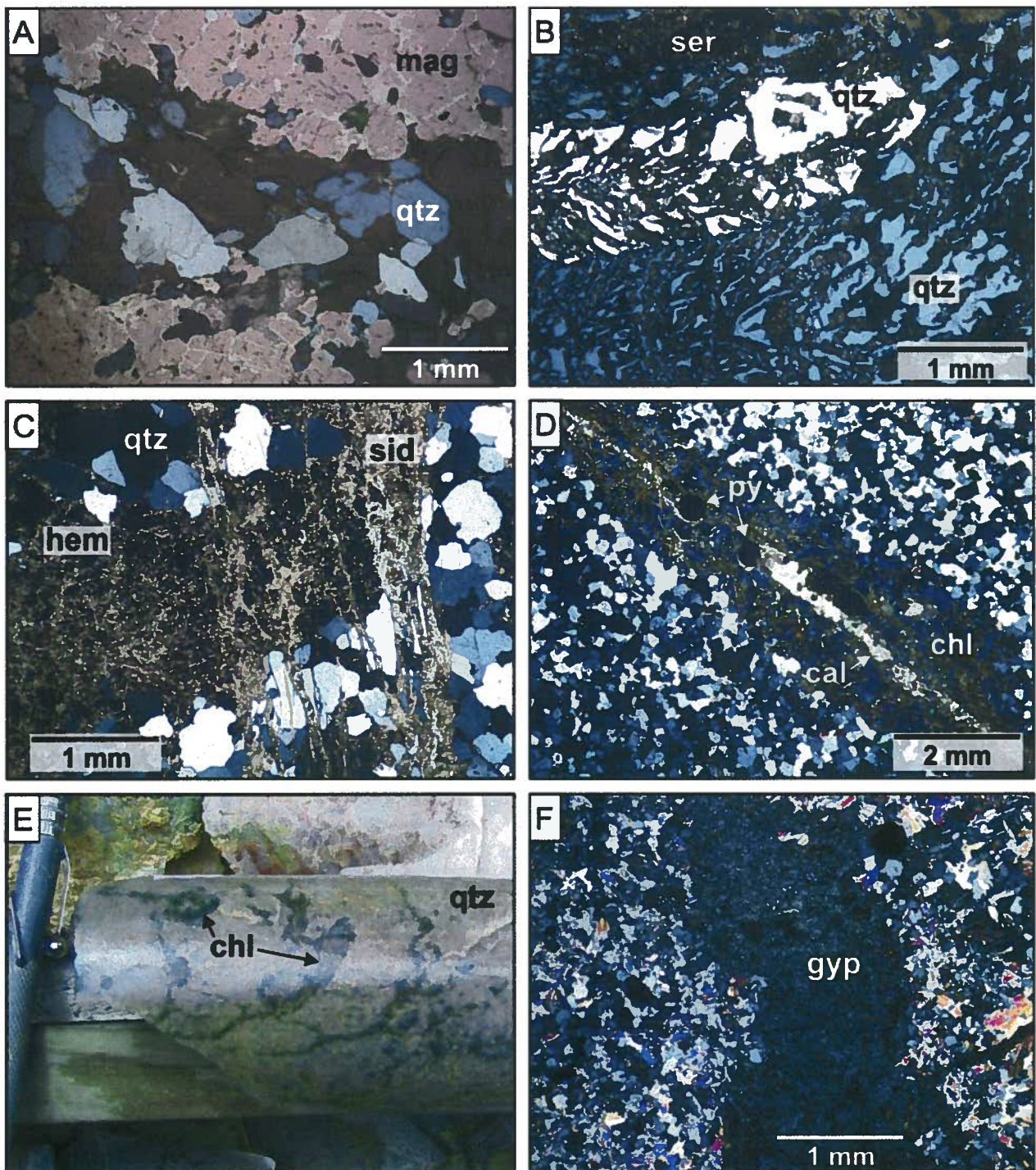


Figure 3.17 A) Reflected light photomicrograph of quartz vein running through magnetite-dominated alteration (field of view = 3.9 mm). B) Cross-polarized light photomicrograph of zebra-textured overprint of sericite-Fe-Oxide on main-stage quartz vein (field of view = 3.9 mm). C) Cross-polarized light photomicrograph of siderite overprinting hematite-cemented, quartz-dominated breccia (field of view = 3.9 mm). D) Cross-polarized Composite chlorite-calcite vein containing pyrite fragments cutting through quartz-chalcopyrite dominated rock (field of view = 7.8 mm). E) Dense chlorite veinlets cutting quartz-dominated alteration. F) Cross-polarized light photomicrograph of gypsum vein cutting through quartz-sericite altered rock (field of view = 3.9 mm).

Mineral		Mineralization stage							
		Pre	Early	Main	Late	Post			
alteration	high-T	quartz magnetite biotite K-feldspar rutile							
	Q-ser	hematite muscovite illite							
	sodic	albite paragonite montmorillonite							
	adv. argillic	andalusite pyrophyllite dickite kaolinite halloysite							
	Q-c	chlorite calcite							
	mineralization		pyrite bornite chalcopyrite pyrrhotite molybdenite						
		veining		quartz magnetite hematite siderite chlorite calcite gypsum/anhydrite					

Figure 3.18 Interpreted paragenesis for alteration minerals, sulphides and veins at the Empress deposit. Association of alteration minerals to respective alteration zones are indicated. Abbreviations: Q-ser = quartz-sericite alteration, adv. Argillic = advanced argillic alteration, Q-c = quartz-chlorite alteration. High-T alteration zones include quartz-dominated, quartz-magnetite and potassium silicate alteration.

Alteration zone	Mineral	Mineralization stage				
		Pre	Early	Main	Late	Post
high-T advanced argillic mineralization	quartz	[shaded bar]				
	corundum	[shaded bar]				
	andalusite	[shaded bar]				
quartz-sericite-pyrite alteration	tourmaline	[shaded bar]				
	ore minerals	[shaded bar]				
	pyrite	[shaded bar]				
low-T advanced argillic	pyrite	[shaded bar]				
	muscovite	[shaded bar]				
	illite	[shaded bar]				
	palygorskite	[shaded bar]				
	paragonite	[shaded bar]				
low-T advanced argillic	pyrophyllite	[shaded bar]				
	dickite	[shaded bar]				
	kaolinite	[shaded bar]				
	halloysite	[shaded bar]				
	chlorite	[shaded bar]				

Figure 3.19 Interpreted paragenesis Taylor-Windfall alteration minerals corresponding to specified alteration assemblages.

Event	Mineral	Mineralization stage		
		Pre	Main	Post
alteration	quartz siderite ankerite muscovite illite pyrite jarosite chlorite			
mineralization	ore minerals			
vein emplacement				
contractional faulting				

Figure 3.20 Interpreted paragenesis for alteration minerals, mineralization, vein emplacement and contractional faulting at the Pellaire deposit.

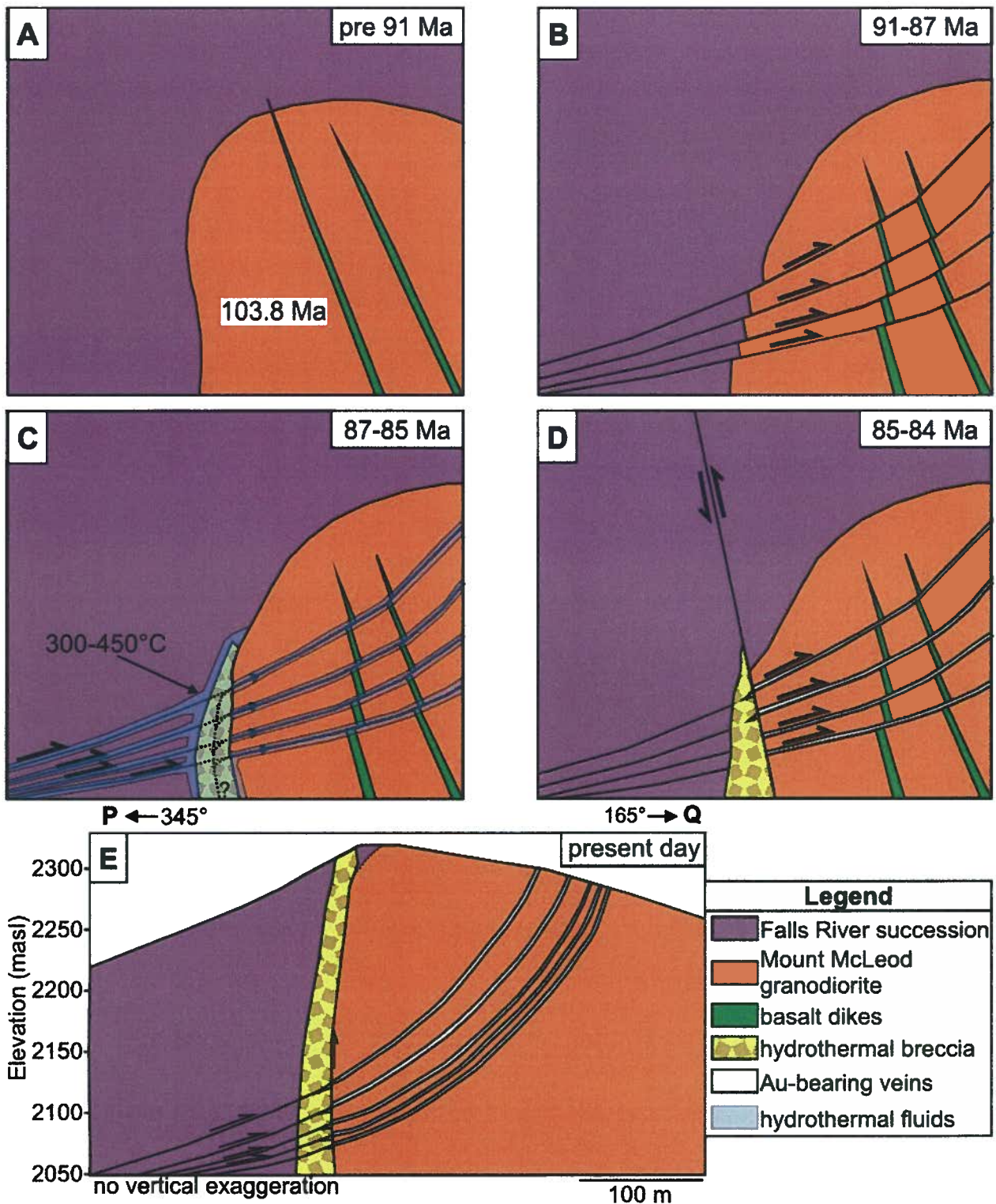


Figure 3.21 Cartoons illustrating the interpreted evolution of the Pellaire deposit. Approximate dates of events are indicated A) Mount McLeod granodiorite intrudes the Falls River Succession, and is subsequently intruded by basaltic dikes. B) South-vergent thrust faults form as a result of regional compressional deformation. C) Deep-seated magmatic or metamorphic hydrothermal fluids migrate upwards along newly formed north-vergent faults contact, resulting in the formation of the hydrothermal breccia. Dotted lines indicate potential fluid-flow paths. D) Quartz veins are emplaced and hydrothermal fluids cool and disappate, both north and south vergent faults remain active producing the faulted lower contacts of the quartz veins and the hydrothermal breccia-Mount McLeod granodiorite contact. E) Present day Geologic cross-section of the Pellaire deposit. Cross-section location indicated by line PQ on Figure 3.7.

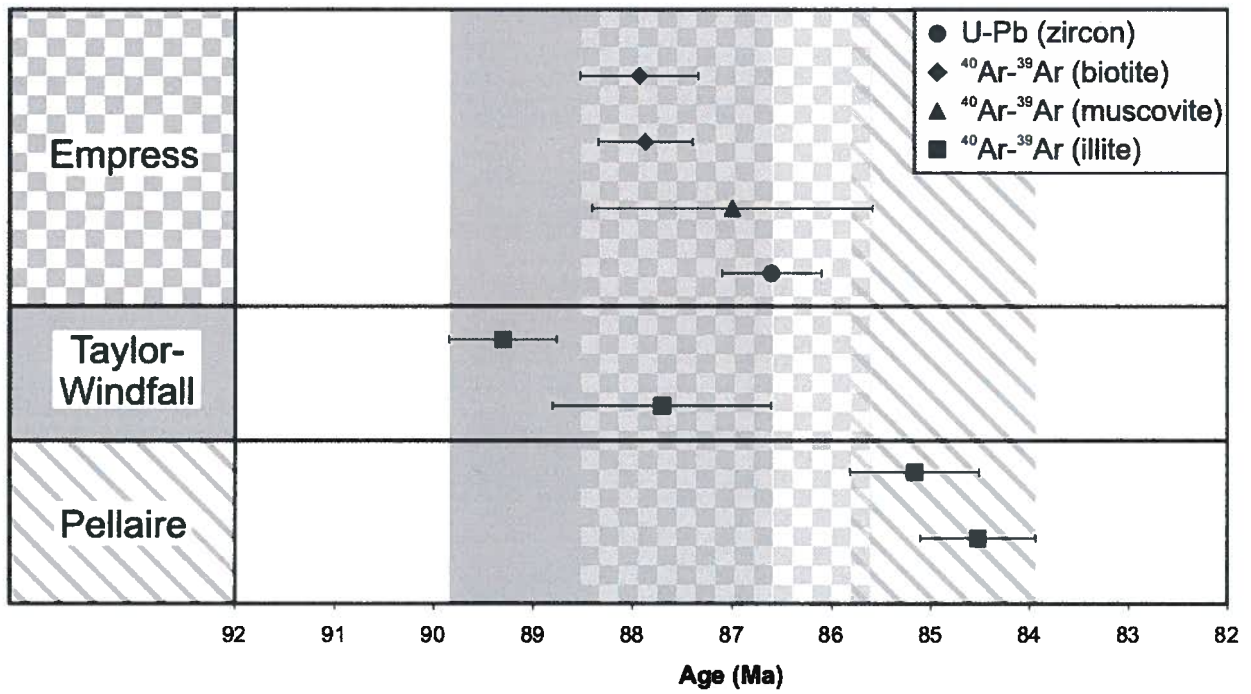


Figure 3.22 Summary of geochronological data for the Empress, Taylor-Windfall and Pellaire deposits. Shaded regions indicate maximum age range of mineralization for the deposits based on geochronology from this study.

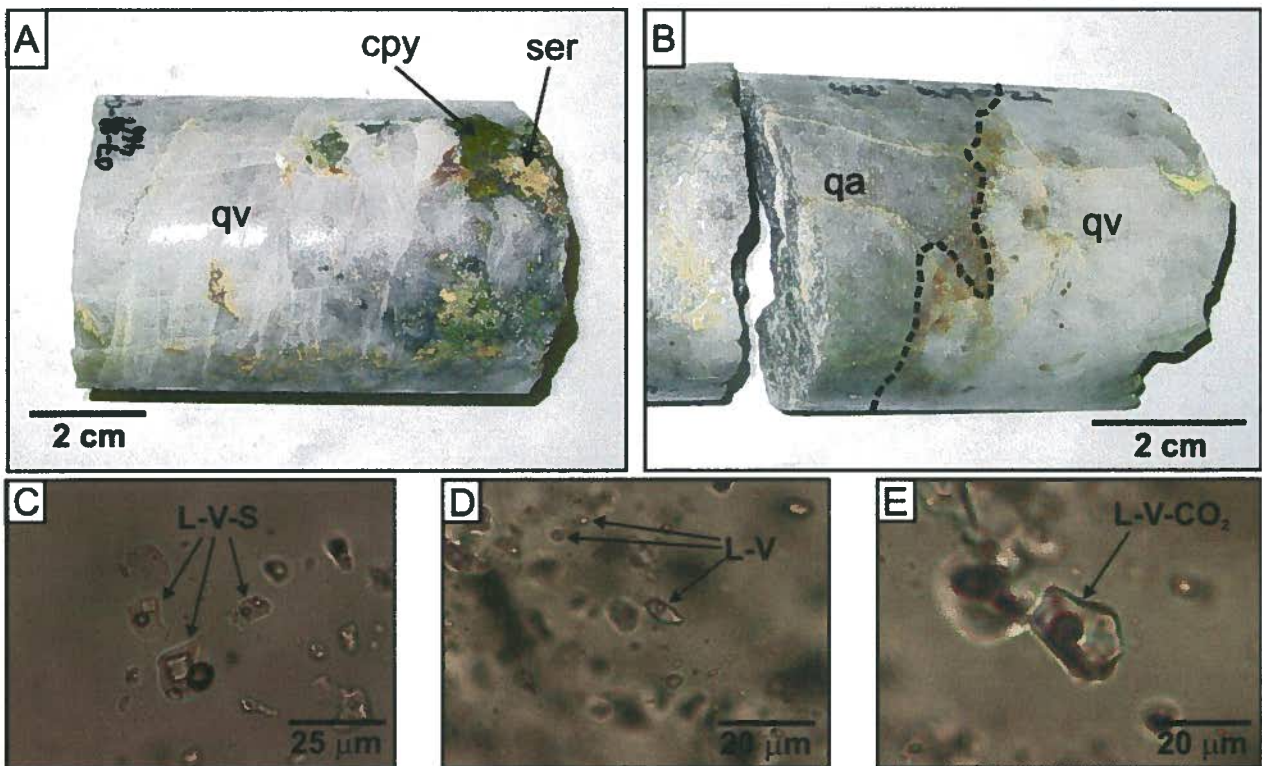
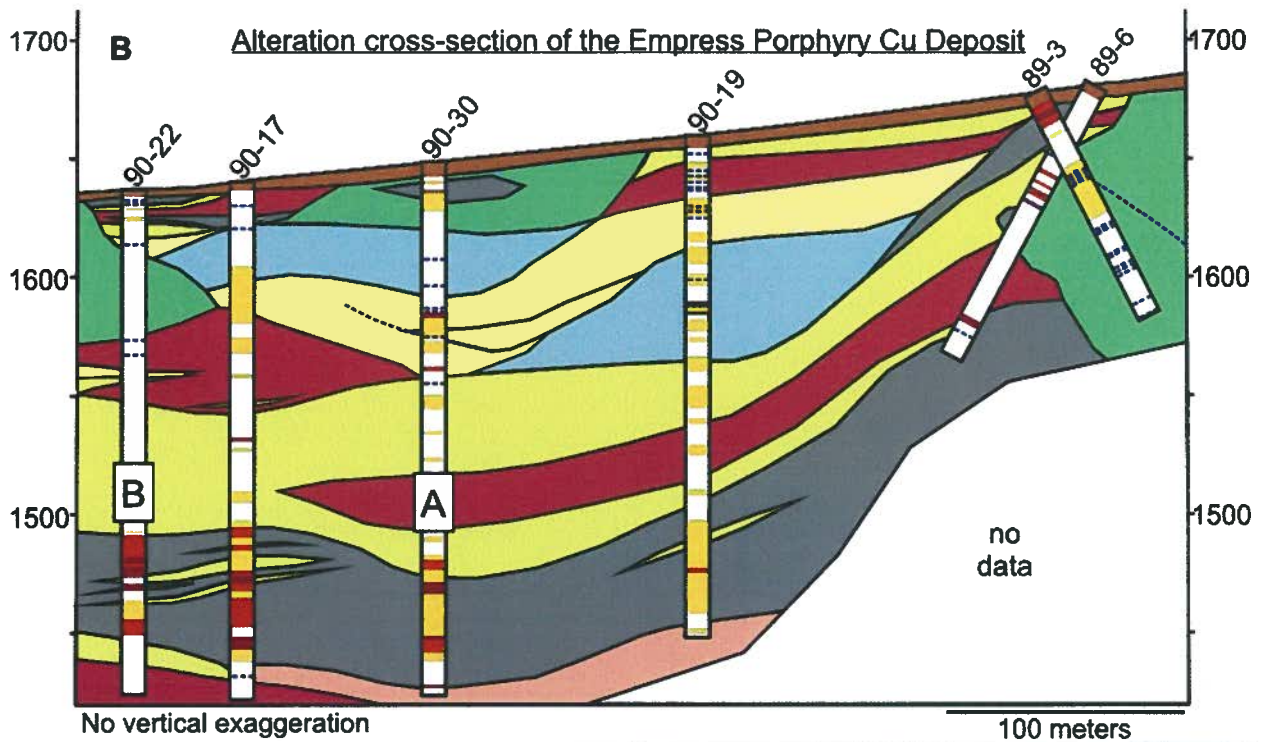
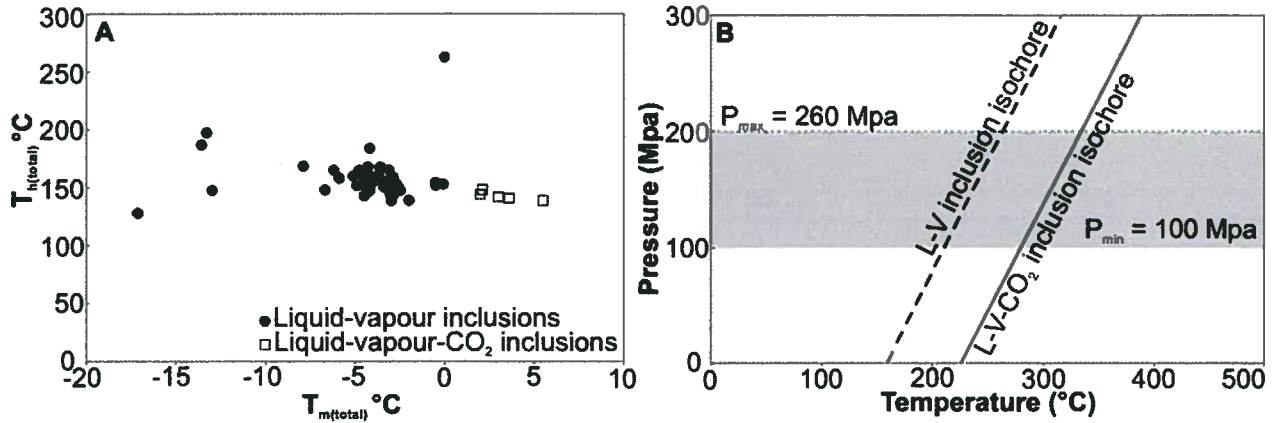
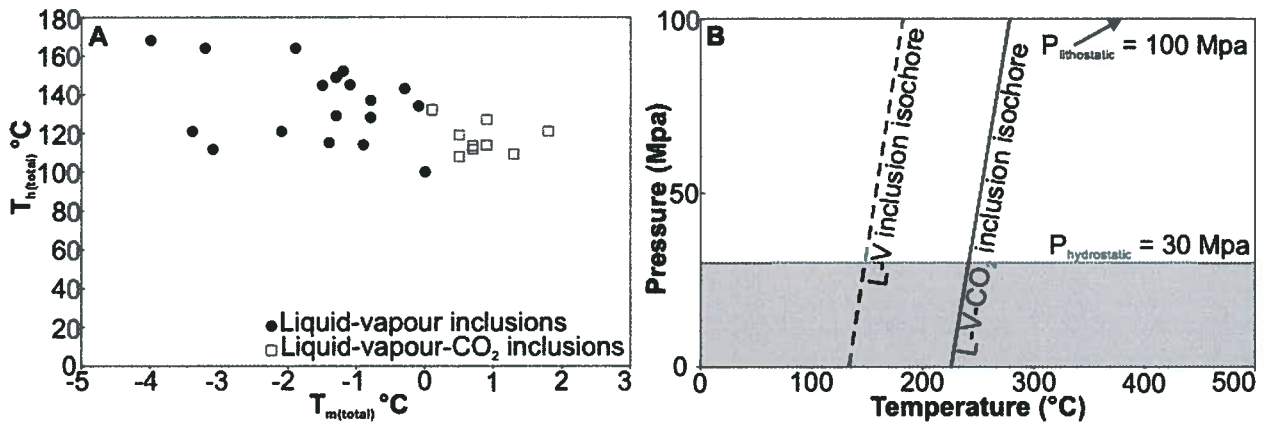


Figure 3.23 Cross-section of the Empress deposit (location indicated by line XY on Figure 3.4) showing locations of main-stage quartz veins analyzed using microthermometry. A) Photograph of sample 07-SB-CS-044. B) Photograph of sample 07-SB-CS-117. C) Photomicrograph of L-V-S fluid inclusions from sample 07-SB-CS-044. D) Photomicrograph of L-V fluid inclusions from sample 07-SB-CS-117. E) Photomicrograph of L-V-CO<sub>2</sub> fluid inclusion from sample 07-SB-CS-117.

### Empress fluid inclusion data



### Taylor-Windfall fluid inclusion data



### Pellaire fluid inclusion data

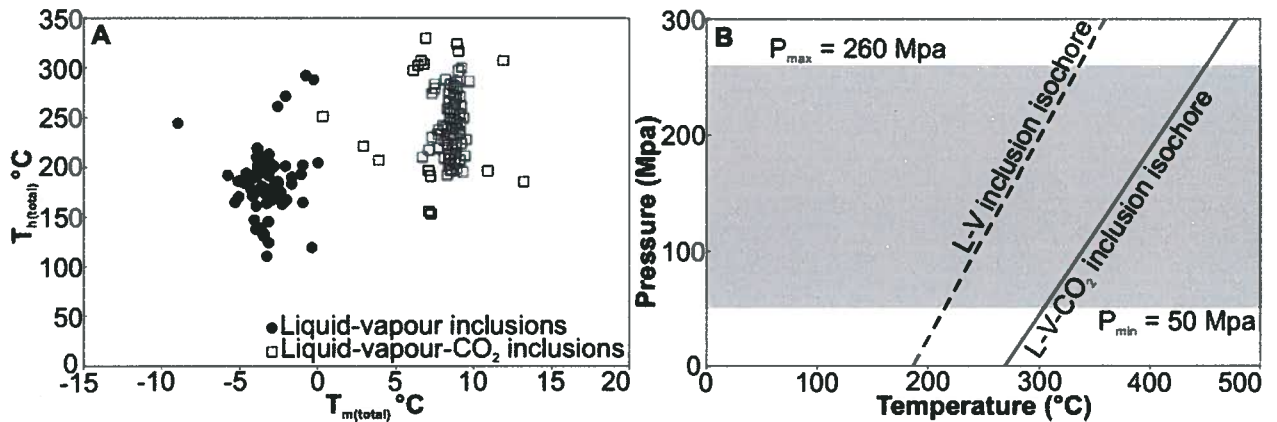


Figure 3.24 A) Total melting temperature versus Total homogenization temperature graph for Empress, Taylor-Windfall and Pellaire fluid inclusions. Total melting temperature corresponds to ice melting temperature for liquid-vapour inclusions, and clathrate melting temperature for liquid-vapour-CO<sub>2</sub> inclusions. B) Temperature versus pressure/depth chart showing calculated isochores for Empress, Taylor-Windfall and Pellaire fluid inclusions. Pressure constraints indicated by the shaded area are based on thermochronological data.

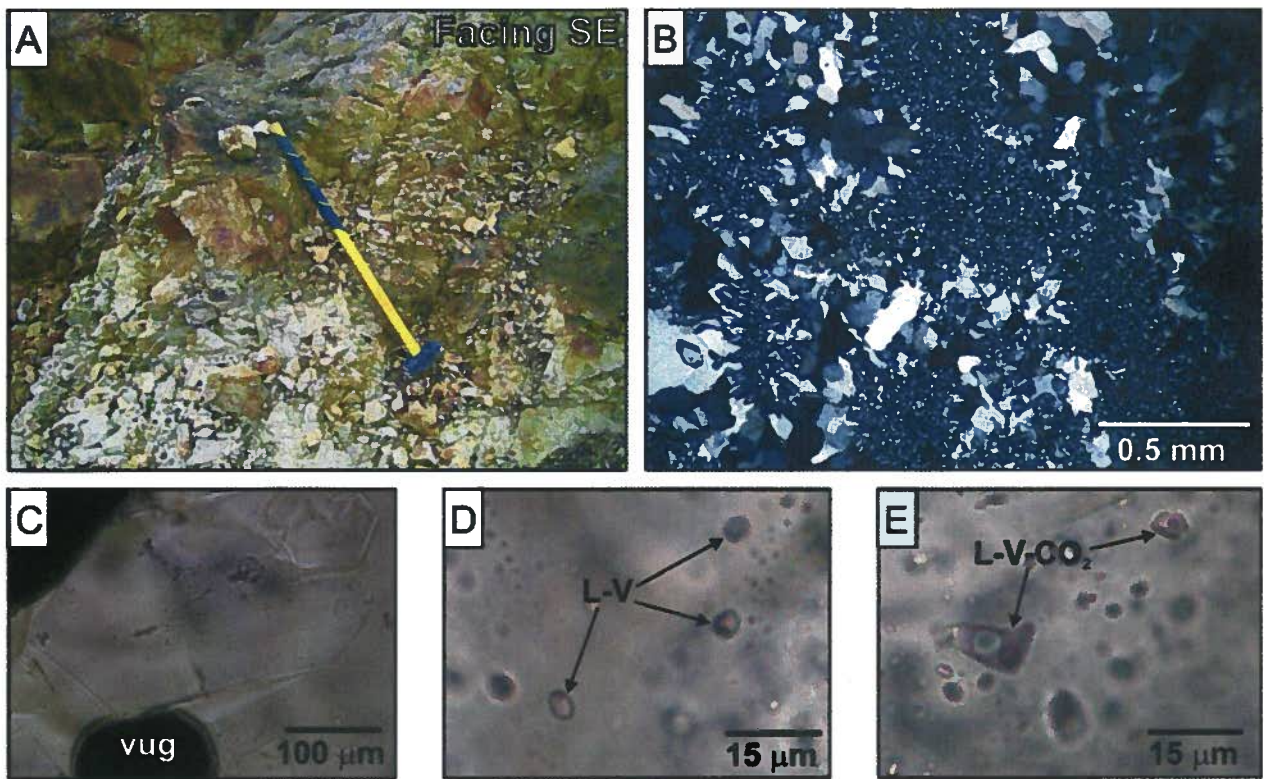


Figure 3.25 Photographs of Taylor-Windfall fluid inclusion samples: A) Outcrop of vuggy silica altered rock from which sample 07-SB-023-2 was sampled. B) Cross-polarized light photomicrograph of intense silica alteration in sample 07-SB-023-2. C) Plane-polarized light photo micrograph of euhedral quartz crystals containing sparse fluid inclusions surrounding a vuggy cavity (Field of view = 400  $\mu\text{m}$ ). D) Plane-polarized light photo micrograph of isolated L-V inclusions (Field of view = 60  $\mu\text{m}$ ). E) Plane-polarized light photo micrograph of relatively dense fluid inclusion cluster including L-V-CO<sub>2</sub> inclusions (Field of view = 60  $\mu\text{m}$ ).

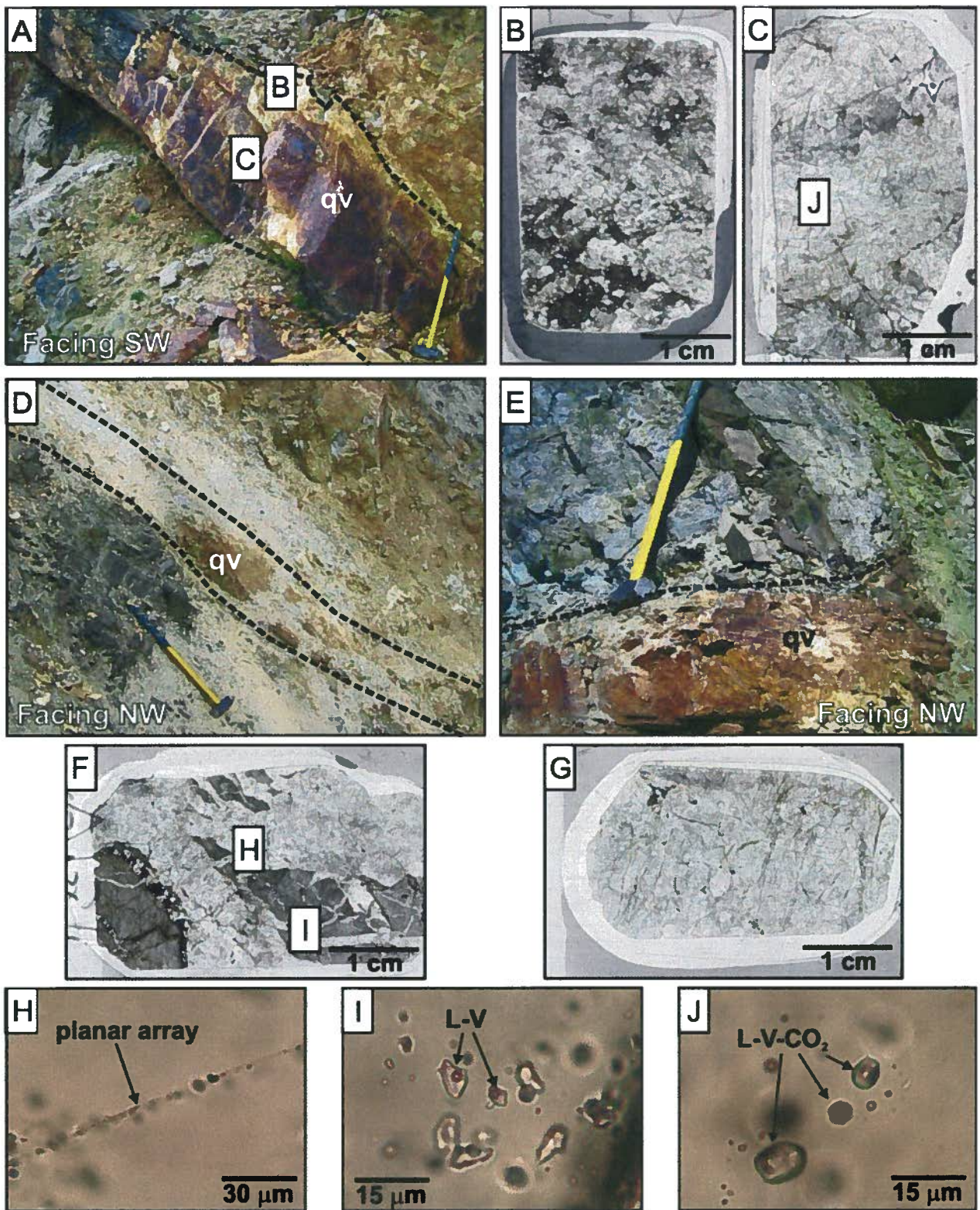


Figure 3.26 Photographs of Pellaire fluid inclusion samples: A) Quartz-vein outcrop showing sample locations for 07-SB-172-3 (B) and 07-SB-172-7 (C). B) Photograph of thin section 07-SB-172-3. C) Photograph of thin section 07-SB-172-7. Location of photomicrograph shown in J) is indicated. D) Quartz-vein outcrop from which sample 07-SB-136-1 was taken. E) Quartz-vein outcrop from which sample 07-SB-139-3 was taken. F) Photograph of thin section 07-SB-136-1. Location of photomicrographs shown in H) and I) are indicated. G) Photograph of thin section 07-SB-172-7. H) Plane-polarized light photomicrograph of planar array of monophasic liquid inclusions (field of view = 120  $\mu\text{m}$ ). I) Plane-polarized light photomicrograph of L-V inclusions (field of view = 60  $\mu\text{m}$ ). J) Plane polarized light photomicrograph of L-V-CO<sub>2</sub> inclusions (field of view = 60  $\mu\text{m}$ ).

**Table 3.3** Carbon and oxygen isotope data for post-mineralization calcite veins at the Empress deposit

Sample no.	Vein-type	Host Rock	$\delta^{13}\text{C}$ ‰ (V-PDB)	$\delta^{18}\text{O}$ ‰ (V-SMOW)
07-SB-CS-025	calcite (void fill)	quartz-sericite alteration	-12.148	9.700
07-SB-CS-072	calcite	advanced argillic alteration	-8.843	7.219
07-SB-CS-073	calcite	advanced argillic alteration	-8.922	10.992
07-SB-CS-107	calcite	andesite dike	-8.418	9.025
07-SB-CS-136	calcite	quartz-sericite alteration	-8.816	7.896
07-SB-CS-172	calcite	quartz-chlorite alteration	-9.593	12.361

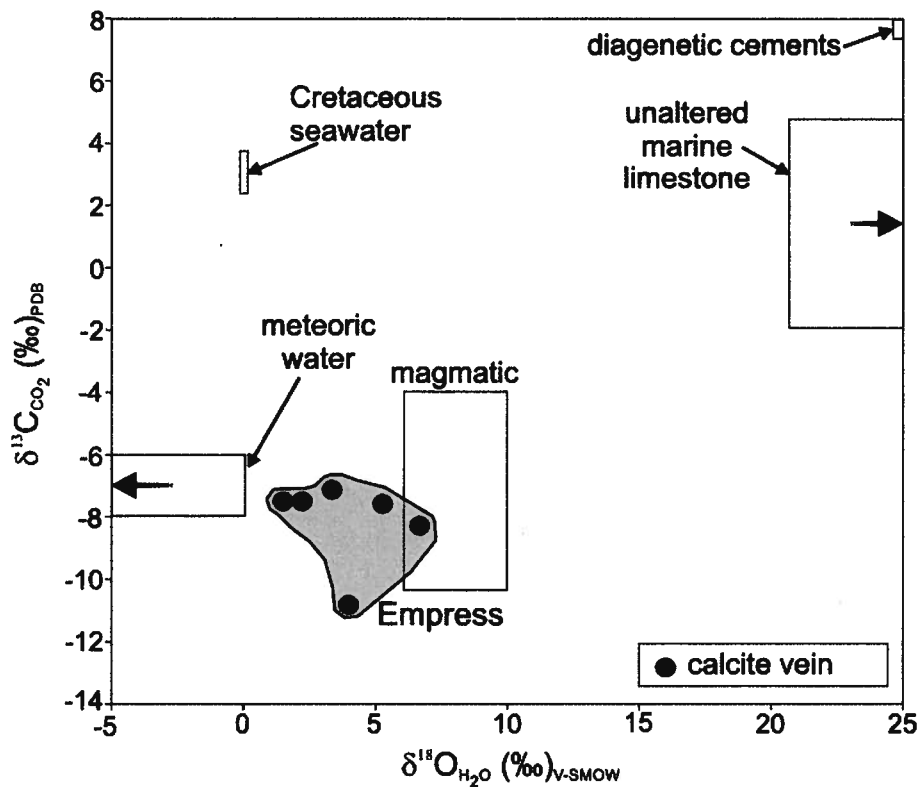


Figure 3.27 Oxygen and carbon isotopic data for calcite vein samples at the Empress deposit. Fields from Rollinson (1993) and Sharp (2006) and Cretaceous seawater values from Veizer et al. (1999). Oxygen values for meteoric water is poorly constrained due to the temperature and latitude dependence of oxygen fractionation, but is generally depleted in  $\delta^{18}\text{O}$  in hydrothermal environments (Rollinson, 1993). Samples suggest that fluids had a predominantly magmatic fluid source.  $\delta^{18}\text{O}_{\text{H}_2\text{O}}$  fractionation corrections calculated from Zheng (1994) at 250°C.  $\delta^{13}\text{C}_{\text{H}_2\text{O}}$  fractionation corrections calculated from Ohmoto and Rye (1979).

**Table 3.4** Oxygen isotope data for quartz-vein and quartz-magnetite samples

Sample no.	Property	Description	Sample type	Mineral	$\delta^{18}\text{O}$ ‰ (V-SMOW)
07-SB-CS-030	Empress	quartz vein cutting quartz-dominated alteration	quartz vein	quartz	8.4
07-SB-CS-117-2	Empress	quartz vein cutting quartz-magnetite alteration	quartz vein	quartz	8.5
07-SB-CS-126	Empress	quartz vein cutting quartz-dominated alteration	quartz vein	quartz	8.5
07-SB-023-2	Taylor-Windfall	vuggy quartz-pyrite altered rock	quartz vein	quartz	11.1
07-SB-171-1	Pellaire	quartz vein cutting granodiorite	quartz vein	quartz	9.6
07-SB-172-3	Pellaire	quartz vein contact at hangingwall contact	quartz vein	quartz	8.7
07-SB-172-7	Pellaire	quartz vein ~60cm below upper contact	quartz vein	quartz	9.4
07-SB-CS-052	Empress	blotchy quartz-magnetite alteration	altered rock	magnetite	6.6
07-SB-CS-052	Empress	blotchy quartz-magnetite alteration	altered rock	quartz	12.4
07-SB-CS-123	Empress	wavy layered quartz-magnetite alteration	altered rock	magnetite	6.8
07-SB-CS-123	Empress	wavy layered quartz-magnetite alteration	altered rock	quartz	7.3
07-SB-CS-150	Empress	uniform quartz-magnetite alteration	altered rock	magnetite	1.8
07-SB-CS-150	Empress	uniform quartz-magnetite alteration	altered rock	quartz	8

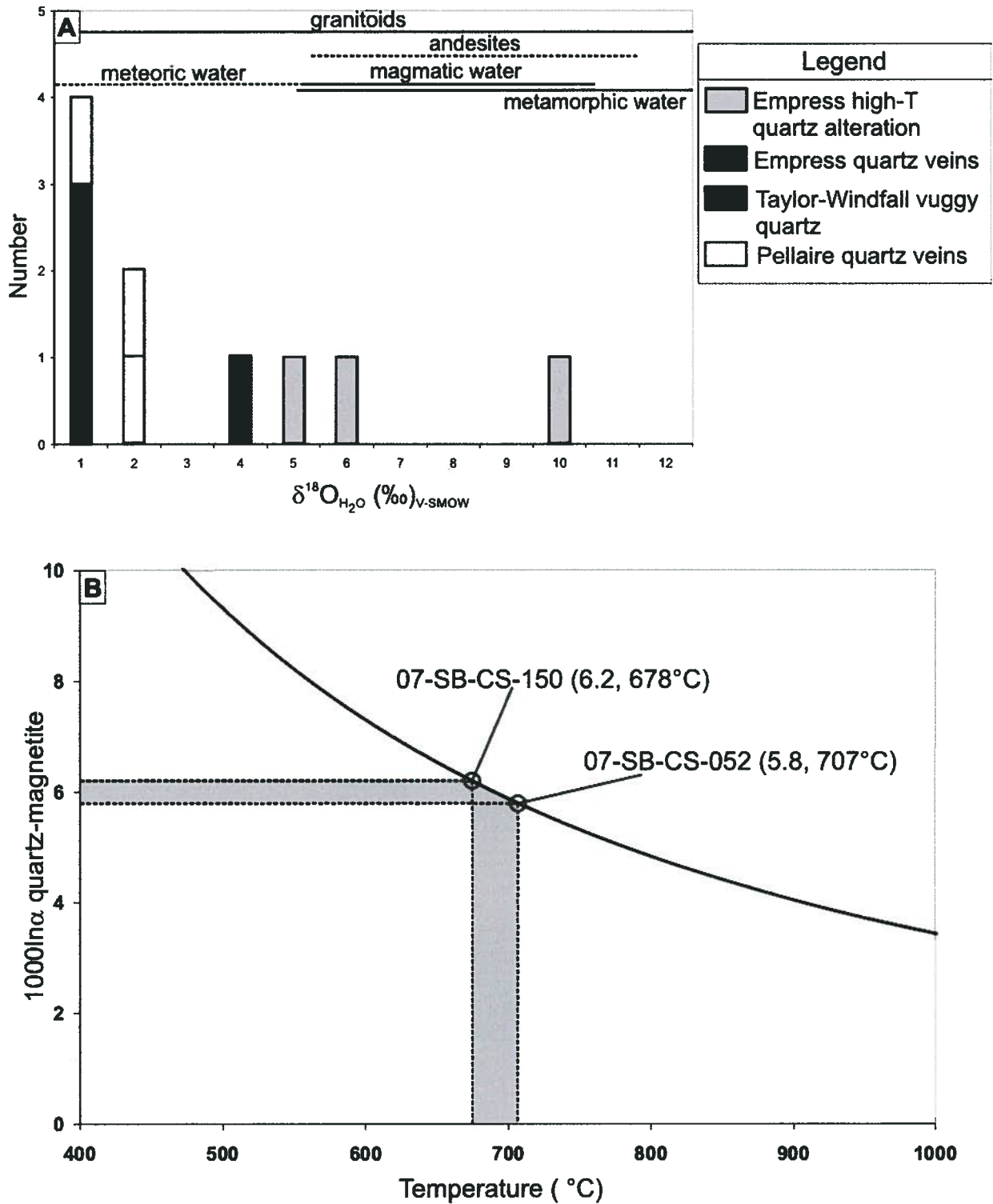


Figure 3.28 A) Oxygen isotope data from powdered quartz-vein and whole rock samples from Empress, Taylor-Windfall and Pellaire. Typical oxygen ranges for granitoids, andesites, magmatic waters and meteoric waters are also shown (Rollinson, 1993). Locations of numbered Pellaire samples are indicated on the photograph.  $\delta^{18}\text{O}_{\text{H}_2\text{O}}$  fractionation corrections calculated from Zheng (1993). B) Quartz-magnetite  $\delta^{18}\text{O}$  fractionation factors for Empress quartz-magnetite samples and corresponding temperatures based on quartz-magnetite fractionation geothermometry. Sample numbers followed by quartz-magnetite fractionation factors and corresponding temperatures are indicated for individual mineral pairs. Temperatures calculated using equations from Chiba et al. (1989).

**Table 3.5 Oxygen and hydrogen isotopic data for hydrous alteration minerals**

<b>Sample</b>	<b>Deposit</b>	<b>Mineral</b>	<b><math>\delta^{18}\text{O}</math> ‰ (V-SMOW)</b>	<b><math>\delta\text{D}</math> ‰ (V-SMOW)</b>
07-SB-CS-007	Empress	Chlorite	7.9	-81
07-SB-CS-012	Empress	Paragonite	8.1	-93
07-SB-CS-013	Empress	Muscovite	6.9	-79
07-SB-CS-025	Empress	Muscovite	7.3	-76
07-SB-CS-063	Empress	Illite	7.9	-77
07-SB-CS-085	Empress	Kaolinite	10.7	-97
07-SB-CS-102	Empress	Biotite	5.2	-101
07-SB-CS-127	Empress	Biotite	5.9	-93
07-SB-CS-153	Empress	Kaolinite	17.4	-80
07-SB-CS-196	Taylor-Windfall	Illite	10.0	-82
07-SB-023-3	Taylor-Windfall	Paragonite	7.8	-72
07-SB-136-6	Pellaire	Muscovite	5.5	-66
07-SB-139-7	Pellaire	Muscovite	6.1	-77

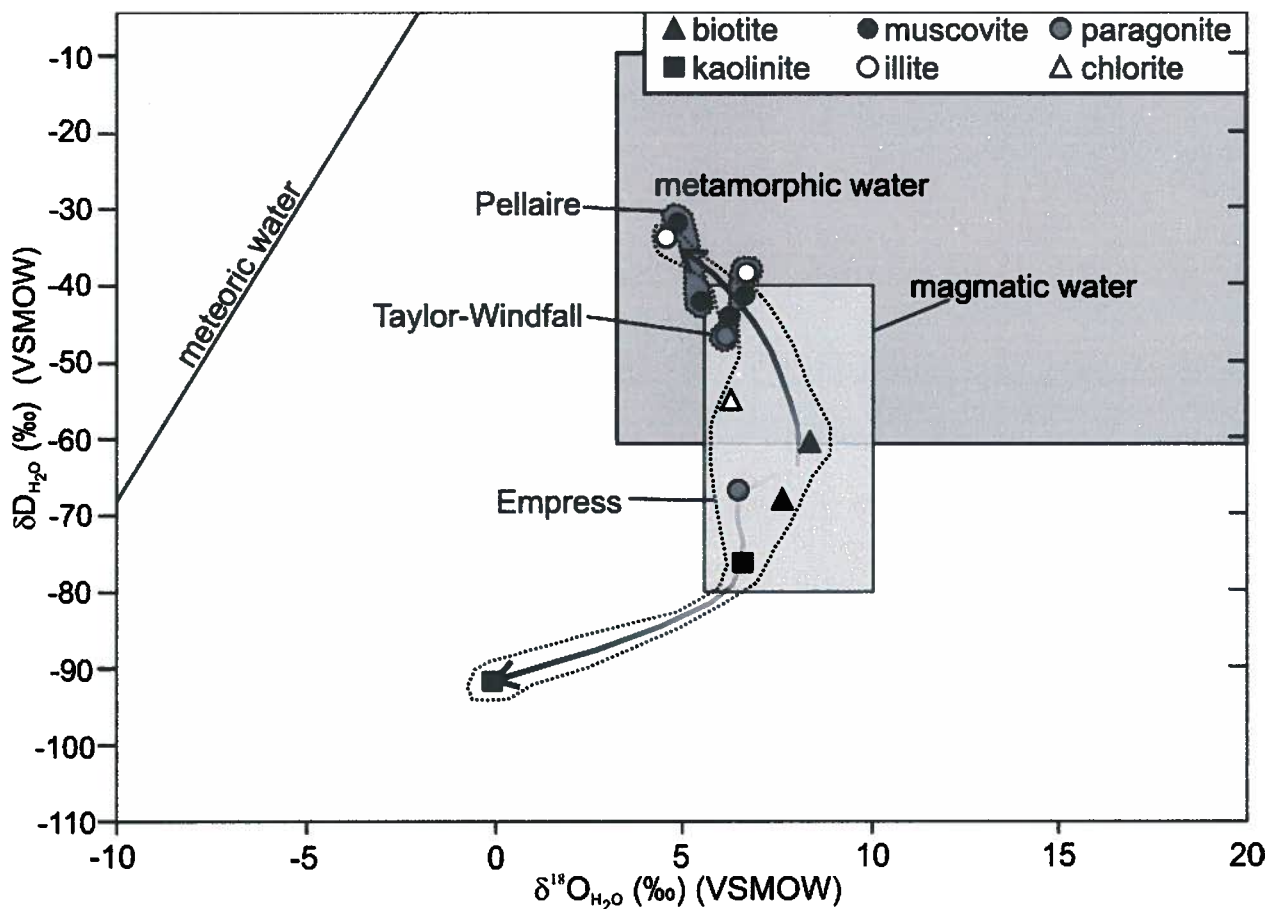


Figure 3.29  $\delta^{18}\text{O}$  versus  $\delta\text{D}$  plot of hydrous alteration mineral samples from Empress, Taylor-Windfall and Pellaire. Magmatic, metamorphic and meteoric water values are from Rollinson (1993). Regions of isotopic values for alteration minerals from each deposit are outlined by the dotted lines, Taylor-Windfall and Pellaire are shaded grey. Arrows indicate the interpreted fluid evolution path for Empress fluids.  $\delta^{18}\text{O}_{\text{H}_2\text{O}}$  fractionation corrections calculated from the following equations: Biotite, muscovite, paragonite, illite and kaolinite – Zheng (1993); chlorite – Cole (1985).  $\delta\text{D}_{\text{H}_2\text{O}}$  fractionation corrections calculated from the following equations: Biotite, muscovite and paragonite – Suzuoki and Epstein (1976); illite – Yeh (1980); kaolinite – Lambert and Epstein (1980); chlorite – Graham et al. (1987).

**Table 3.6 Summary of thermochronological age data**

<b>Sample</b>	<b>Property</b>	<b>Description</b>	<b>Thermochronometer</b>	<b>Age <math>\pm 2\sigma</math> (Ma)</b>	<b>T<sub>c</sub> (°C)</b>	<b>Depth (km)</b>
07-SB-GEO-02	Empress	Empress pluton	ZFT	92.5 $\pm$ 9.0	232	8
07-SB-GEO-02	Empress	Empress pluton	AFT	33.3 $\pm$ 5.0	116	4
07-SB-GEO-04	Empress	Mount McLeod granodiorite	ZFT	94.7 $\pm$ 9.6	232	8
07-SB-GEO-04	Empress	Mount McLeod granodiorite	AFT	40.8 $\pm$ 4.8	116	4
07-SB-GEO-12	Empress	Mount McLeod granodiorite	ZFT	94.7 $\pm$ 9.2	232	8
07-SB-GEO-12	Empress	Mount McLeod granodiorite	AFT	55.6 $\pm$ 6.6	116	4

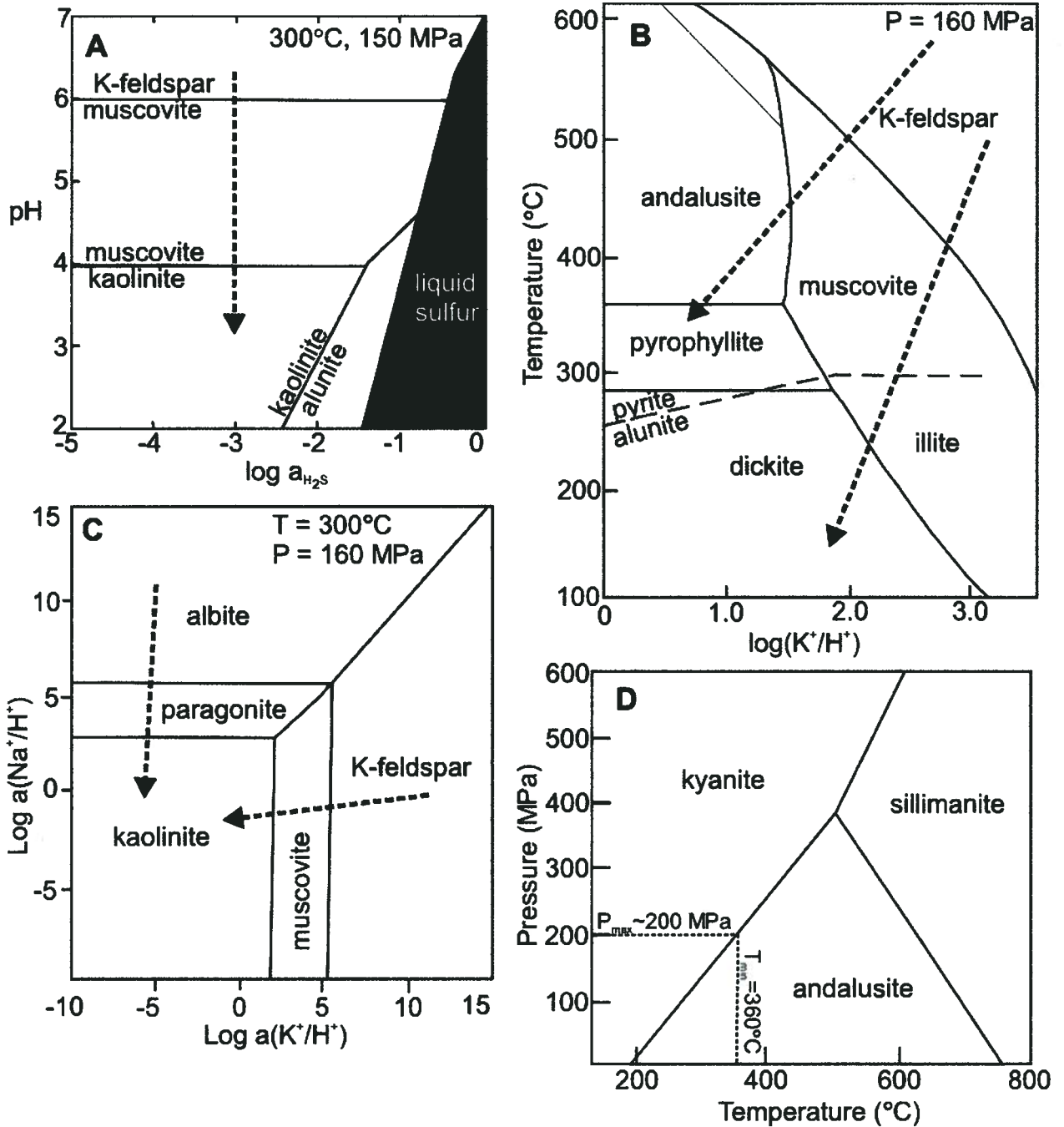


Figure 3.30 Mineral stability diagrams showing stability fields of specific minerals associated with indicated alteration assemblages at the Empress deposit. Dashed arrows indicate approximate physiochemical evolution of Empress fluids. A) Hydrothermal alteration mineral stabilities as a function of pH and  $\text{H}_2\text{S}$  concentration at 300°C and 150 MPa (modified from Gammons and Williams-Jones, 1997). B) The stability of Al-silicate minerals as a function of  $\text{K}^+/\text{H}^+$  mole ratios vs. temperature, at quartz saturation, and 160 MPa (calculated based on values from Anderson, 1996). The position of the pyrite-alunite coexistence line was estimated from thermodynamic data and relationships in active systems (Giggenbach, 1997). C) Phase relations in the ideal system Na-K-C-O-H-Al at 300°C and 160 MPa (calculated based on values from Anderson, 1996). D) P-T phase diagram for the ideal  $\text{Al}_2\text{O}_3\text{-SiO}_2$  system. Maximum pressure of formation of andalusite for peak hydrothermal conditions is indicated (calculated based on values from Anderson, 1996). Alteration zones are characterized by the following minerals: Potassium silicate alteration – K-feldspar; sodic alteration – albite, paragonite; quartz-sericite/intermediate argillic – muscovite, illite; advanced argillic – kyanite, sillimanite, andalusite, pyrophyllite, dickite, kaolinite, alunite.

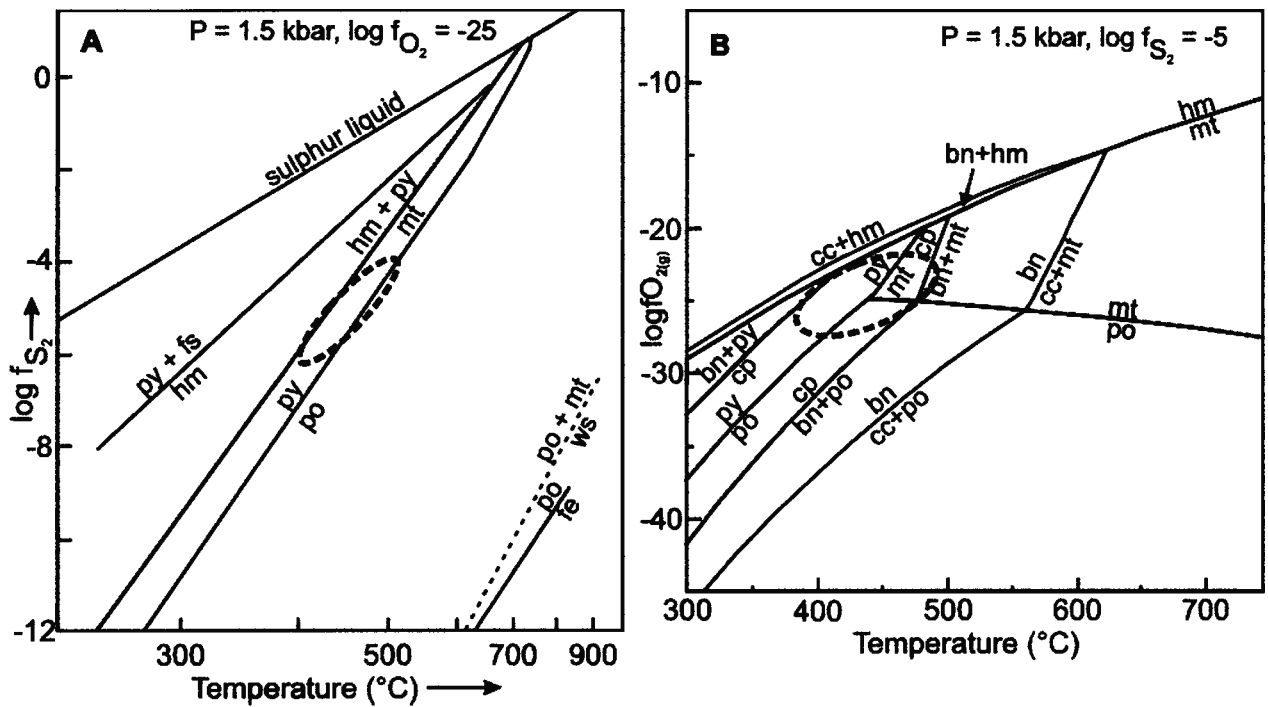


Figure 3.31 Mineral stability diagrams for Empress ore minerals. Approximate conditions of ore deposition are indicated by dashed circles. A) Temperature- $f_{\text{S}_2}$  diagram for the Fe-S-O system showing sulphidation states of ore-forming fluids. Approximate conditions of ore deposition at the Empress deposit are indicated by dashed zones. Sulphidation reactions calculated from Barton and Skinner (1979). B) Temperature- $f_{\text{O}_2(g)}$  diagram for the Cu-Fe-S-O system under feldspar-stable conditions (modified from Johnson et al., 1992). Stability fields or sulphide-oxide mineral assemblages observed at Empress are indicated by the shaded fields. Chalcopyrite and magnetite are not observed to have formed in equilibrium at Empress. Abbreviations: bn = bornite, cc = chalcocite, cp = chalcopyrite, fe = native iron, fs = ferrous sulphate, hm = hematite, mt = magnetite, po = pyrrhotite, py = pyrite, ws = wustite.

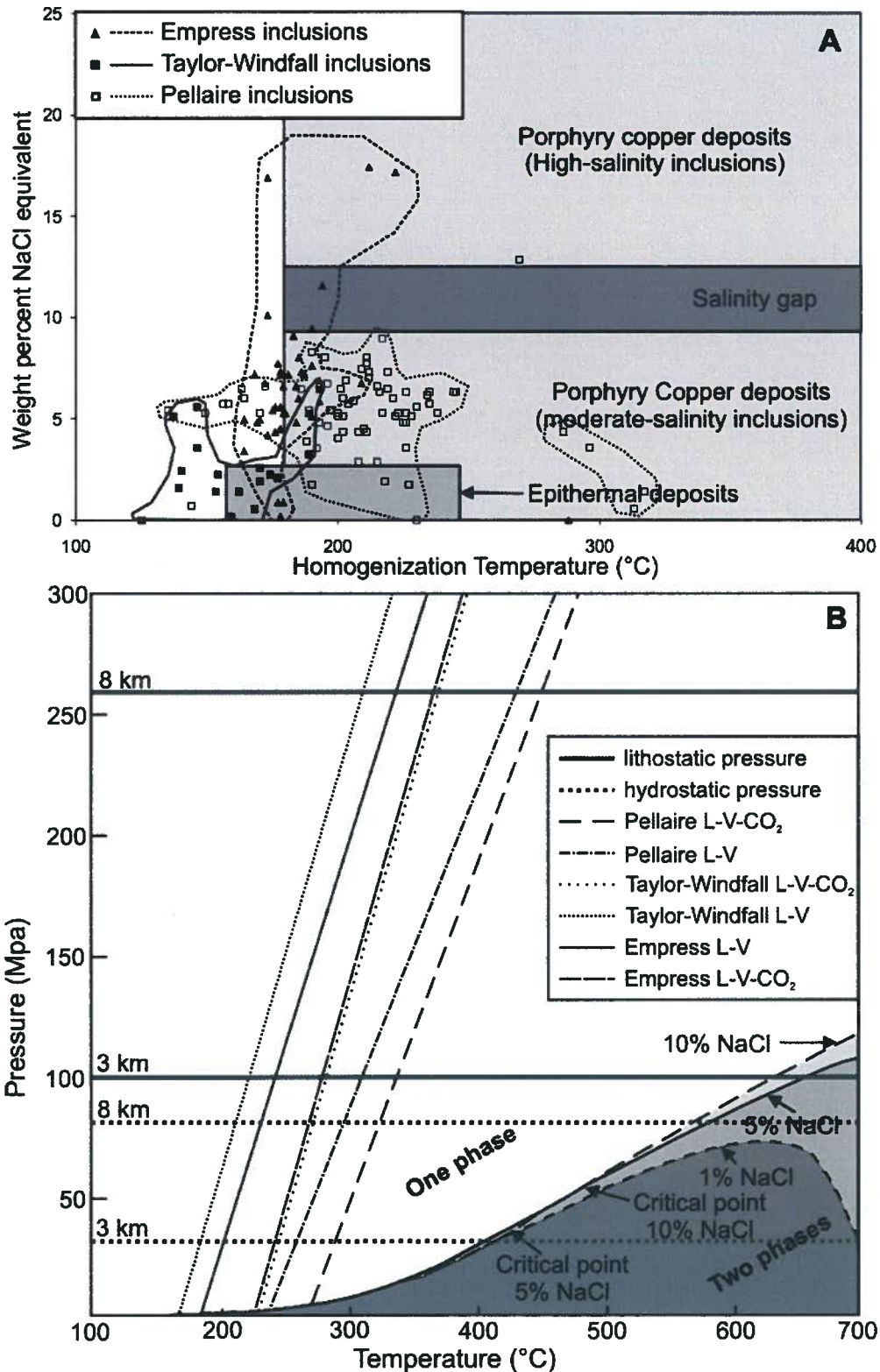


Figure 3.32 A) Salinity- $T_h$  graph comparing Empress, Taylor-Windfall and Pellaire L-V fluid inclusions with those characteristic of epithermal precious metal deposits and Potassium-silicate zones in porphyry Cu deposits. Porphyry Cu deposit fluids have been divided into moderate and high-salinity magmatic hydrothermal fluids (Modified from Vila et al., 1991). B) Curves limiting the stable existence of solutions with 1, 5 and 10% NaCl shown with isochores of Empress, Taylor-Windfall and Pellaire fluids. Moderate salinity fluids must not drop below the phase immiscibility curves during cooling and pressure release in order to prevent phase separation (Modified from Ahmad and Rose, 1980). Grey lines indicate maximum pressures based on maximum depth estimates of 8km for Empress and Pellaire and 3km for Taylor-Windfall for both lithostatic and hydrostatic pressure gradients (Hagemann and Brown, 1996).

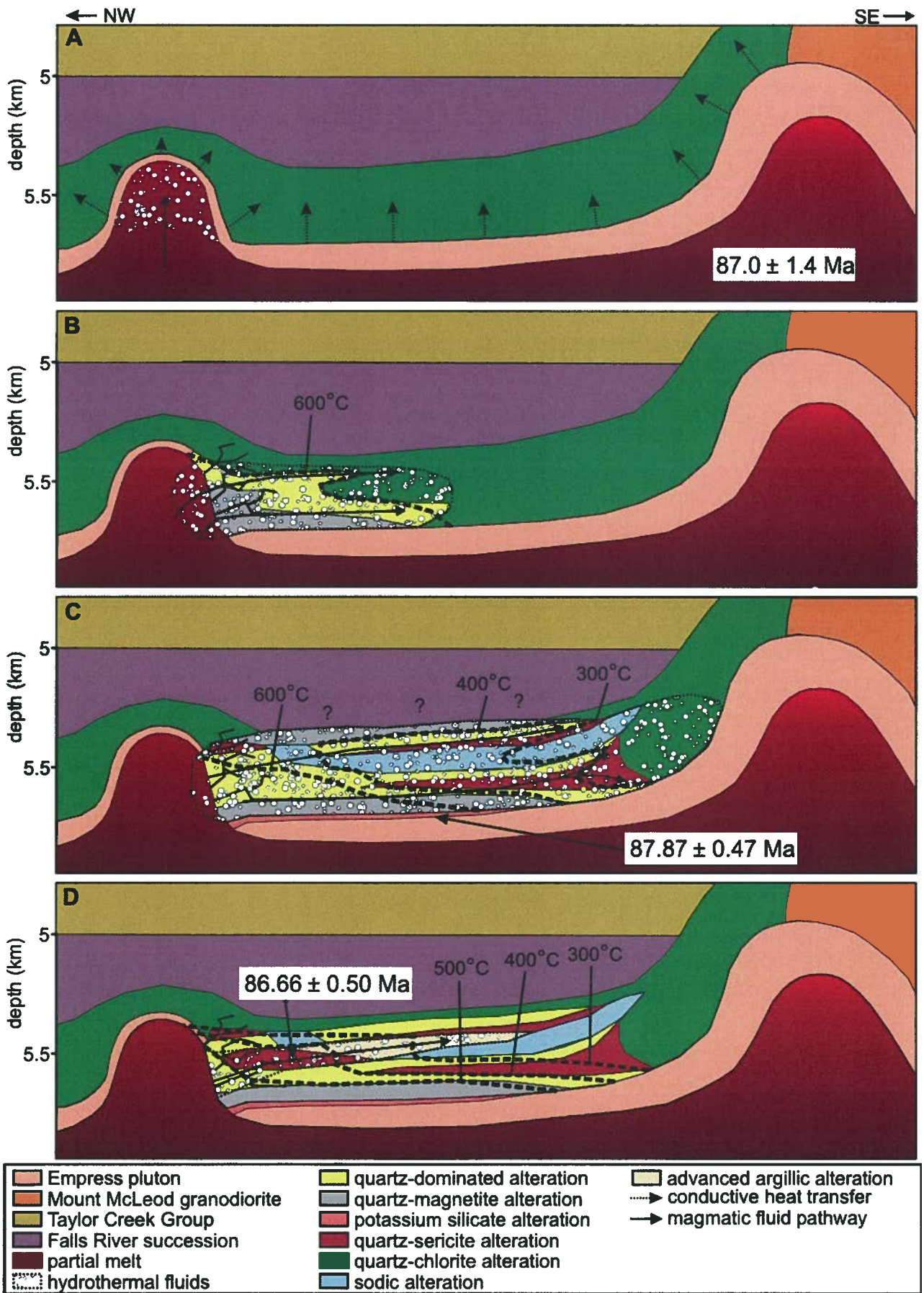


Figure 3.33 Cartoon cross-sections illustrating the proposed formational sequence of the Empress deposit. Depths are estimated based on regional stratigraphic data from Garver (1992), Schiarizza et al. (1997) and Israel et al. (2006) corroborated by AFT data. Geochronological ages are indicated for the Empress pluton and hydrothermal system. A) Initial emplacement of the Empress pluton causes contact metamorphism and dehydration of the overlying rocks in the Falls River succession. Fluids produced by dehydration reactions produce chlorite alteration halo surrounding the Empress pluton. Outer carapace of the pluton cools and crystallizes and hydrothermal fluids exsolved from magma pool in cupola protruding above main intrusive body. B) Hydrothermal fluids in cupola become overpressured and breach the outer crystalline carapace of the intrusion causing hydrofracturing and producing permeable conduits for fluid flow. Low-buoyancy magmatic fluids migrate laterally producing initial high-T quartz-dominated, quartz-magnetite and potassium silicate alteration. C) Fluids continue to migrate and mix with infiltrating connate waters producing sodic and quartz-sericite alteration. Migration of magmatic fluids controlled by the upper margin of the crystalline carapace of the Empress pluton and halted at sharp increase in slope of the pluton. D) Late stage magmatic fluids migrate through Empress system producing overprinting advanced argillic alteration on other alteration types.

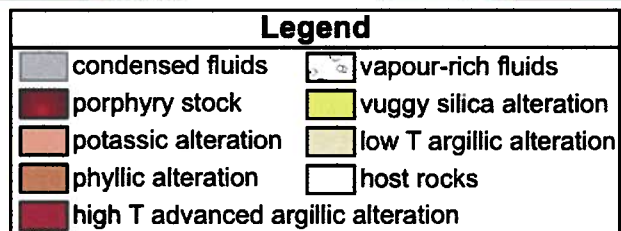
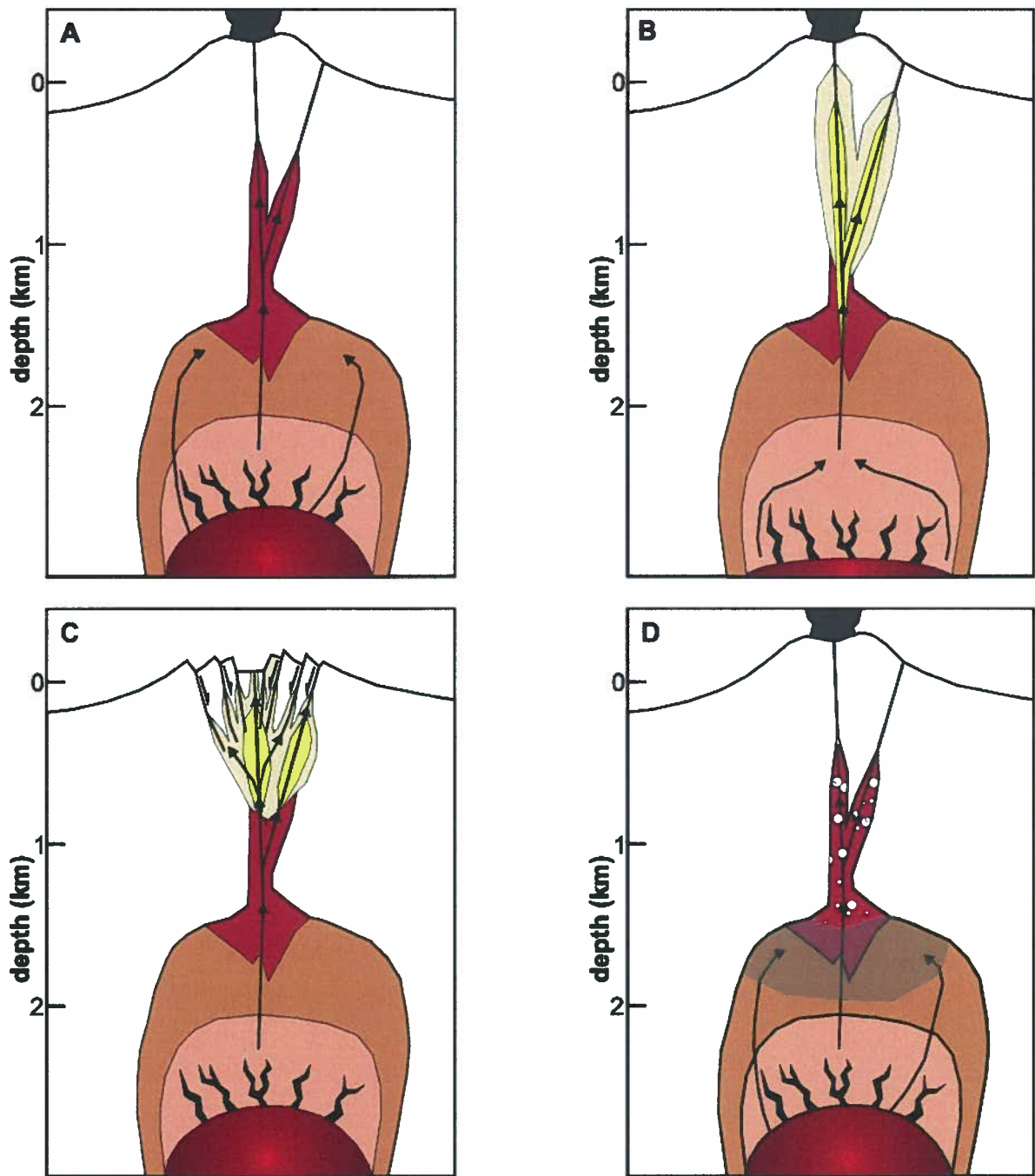


Figure 3.34 Cartoons illustrating the potential scenarios resulting in high-temperature porphyry-style alteration being overprinted by lower temperature epithermal-style alteration: A) Initial subvolcanic porphyry system develops forming typical potassic, phyllic and high temperature advanced argillic assemblages. B) Continued crystallization of porphyry stock results in downward migration of partial melt and source fluids. This causes telescoping of the hydrothermal system by the overprinting of the roof of the porphyry system by epithermal style alteration and mineralization. C) Sector collapse of the overlying volcanic edifice results in sharp drops in fluid temperatures and pressures causing rapid transition from porphyry to epithermal style alteration and mineralization. D) High-buoyancy, high-T vapour-dominated fluids ascend more rapidly than cooler, condensed aqueous fluids.

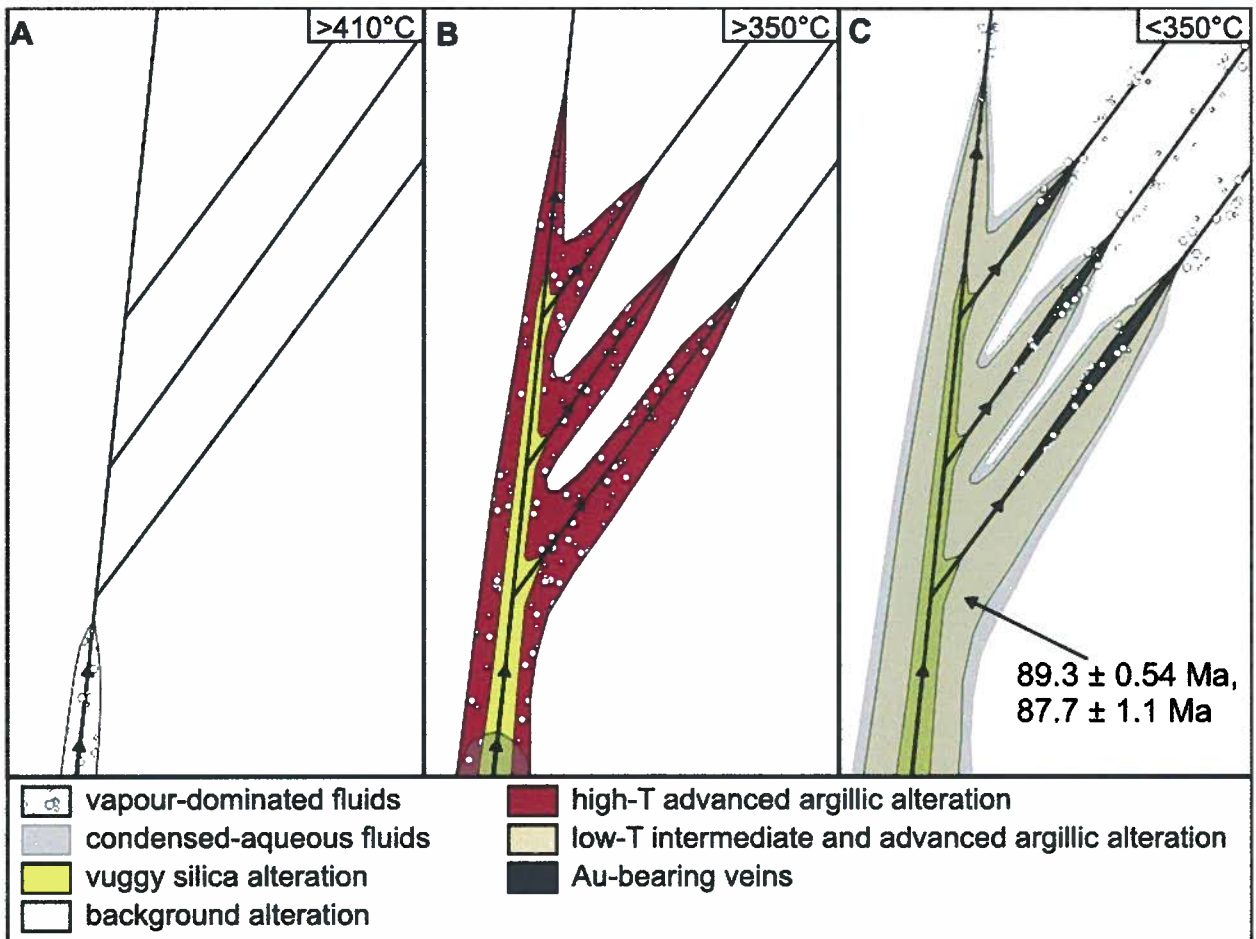


Figure 3.35 Cartoons illustrating the interpreted genetic model of the evolution of the Taylor-Windfall hydrothermal system. A) High-T ( $>410^{\circ}\text{C}$ ) vapour-dominated fluids ascend to Taylor-Windfall area along pre-existing fractures and faults. B) Acidic vapour dominated fluids continue vertical ascent while leaching wall rocks producing vuggy silica and high-T advanced argillic alteration. Vapour-dominated fluids cool to as low as  $350^{\circ}\text{C}$  and are followed by cooler, less buoyant, low-salinity condensed-aqueous fluids. C) Relatively cool ( $<350^{\circ}\text{C}$ ) condensed-aqueous fluids migrate through the Taylor-Windfall systems overprinting high-T advanced argillic alteration with low-T advanced argillic alteration and quartz-illite alteration. Aqueous fluids migrate into isolated fractures and precipitate gold, which may have been aided by boiling due to sharp pressure drops.  $^{40}\text{Ar}$ - $^{39}\text{Ar}$  dates of illite samples from Taylor-Windfall alteration are indicated

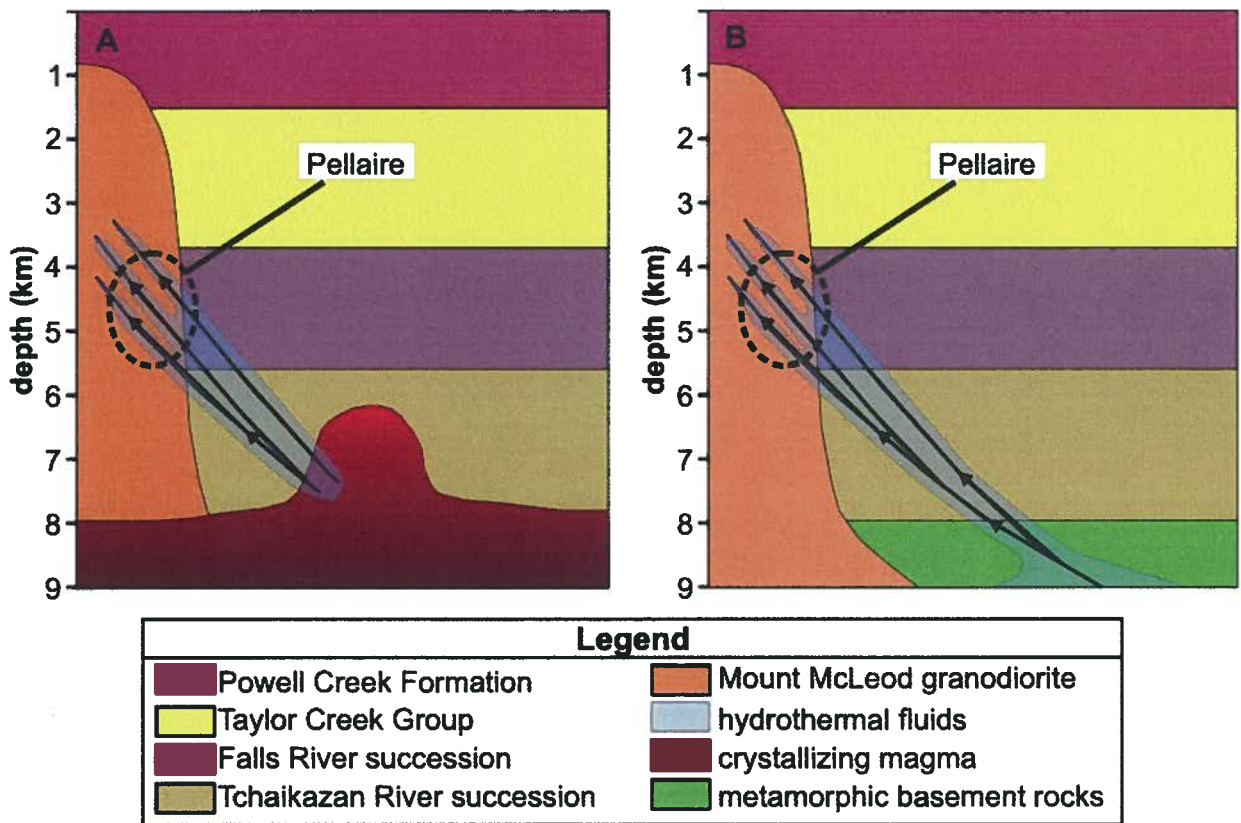


Figure 3.36 Cartoons illustrating the potential sources for mineralizing fluids at the Pellaire deposit. A) Deeper seated crystallizing intrusion exolves magmatic-hydrothermal fluids which ascend to Pellaire along pre-existing faults. B) Underlying crust undergoes dehydration during regional metamorphism, generating metamorphic fluids which ascend to Pellaire along pre-existing faults.

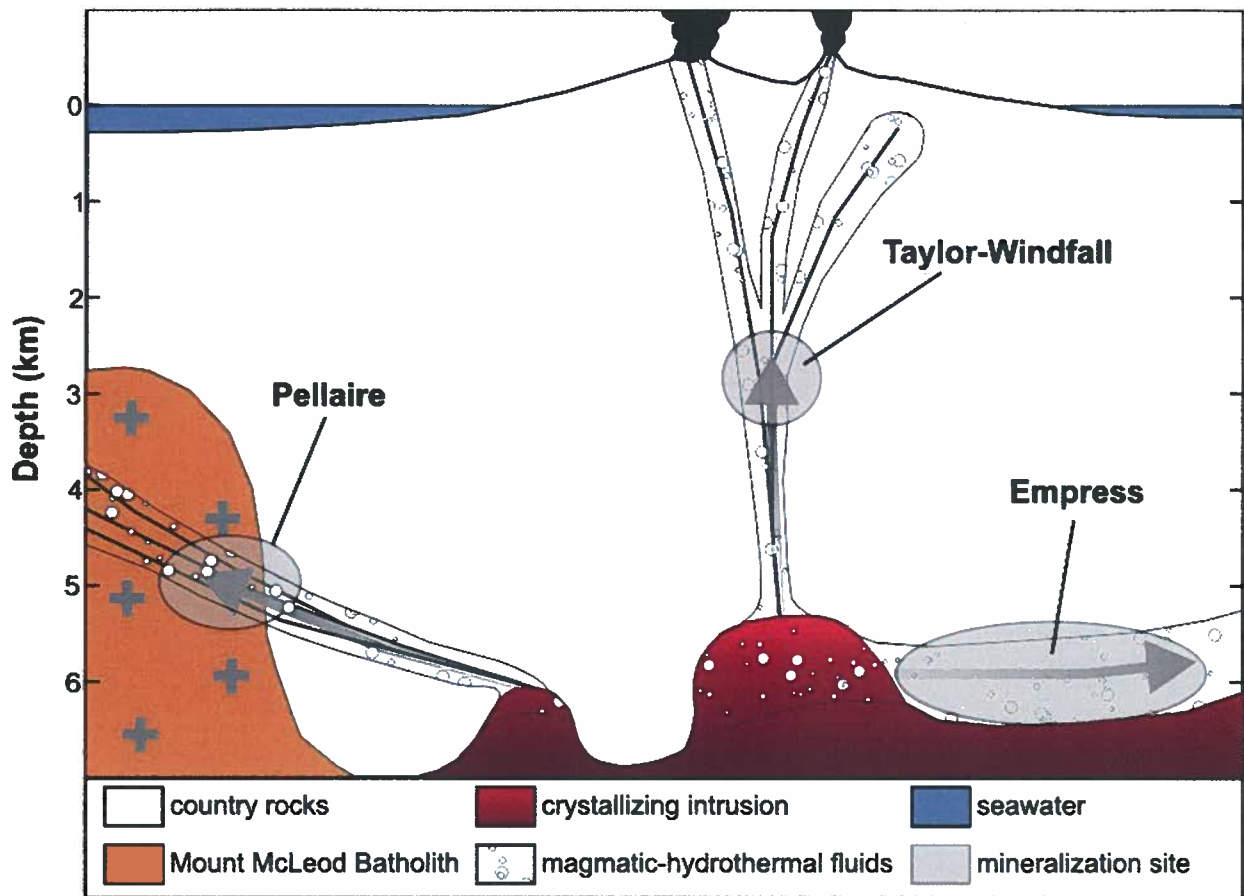


Figure 3.37 Cartoon illustrating the interpreted formational settings of the Empress, Taylor-Windfall and Pellaire deposits with respect to an overall magmatic-hydrothermal system centered on a crystallizing calc-alkaline intrusion.

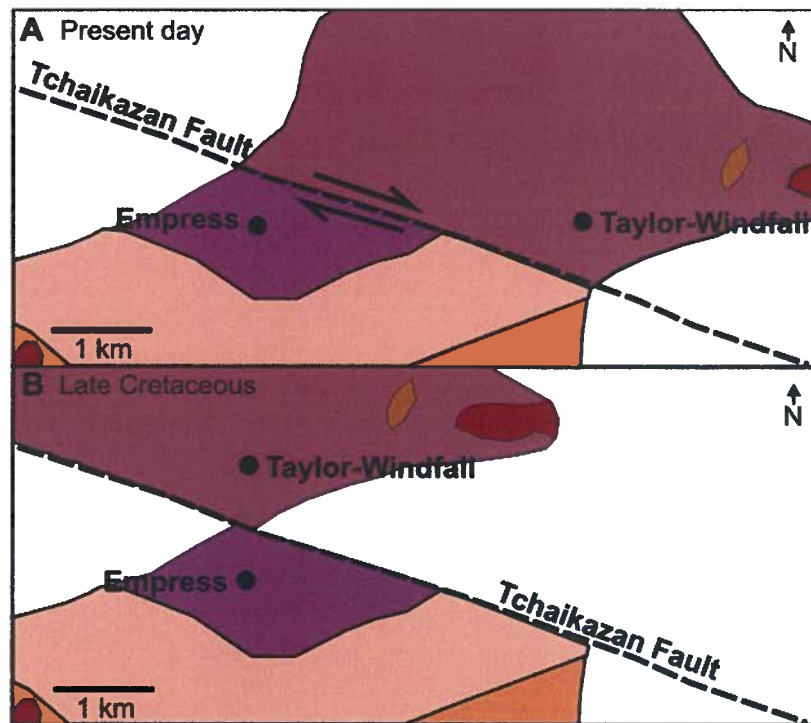


Figure 3.38 Geologic maps showing A) the present geometry of the Tchaikazan Fault, Empress and Taylor-Windfall deposits and B) The proposed geometry of the Empress and Taylor-Windfall deposits during the Late Cretaceous with roughly 3 km of Eocene dextral displacement removed on the Tchaikazan Fault.

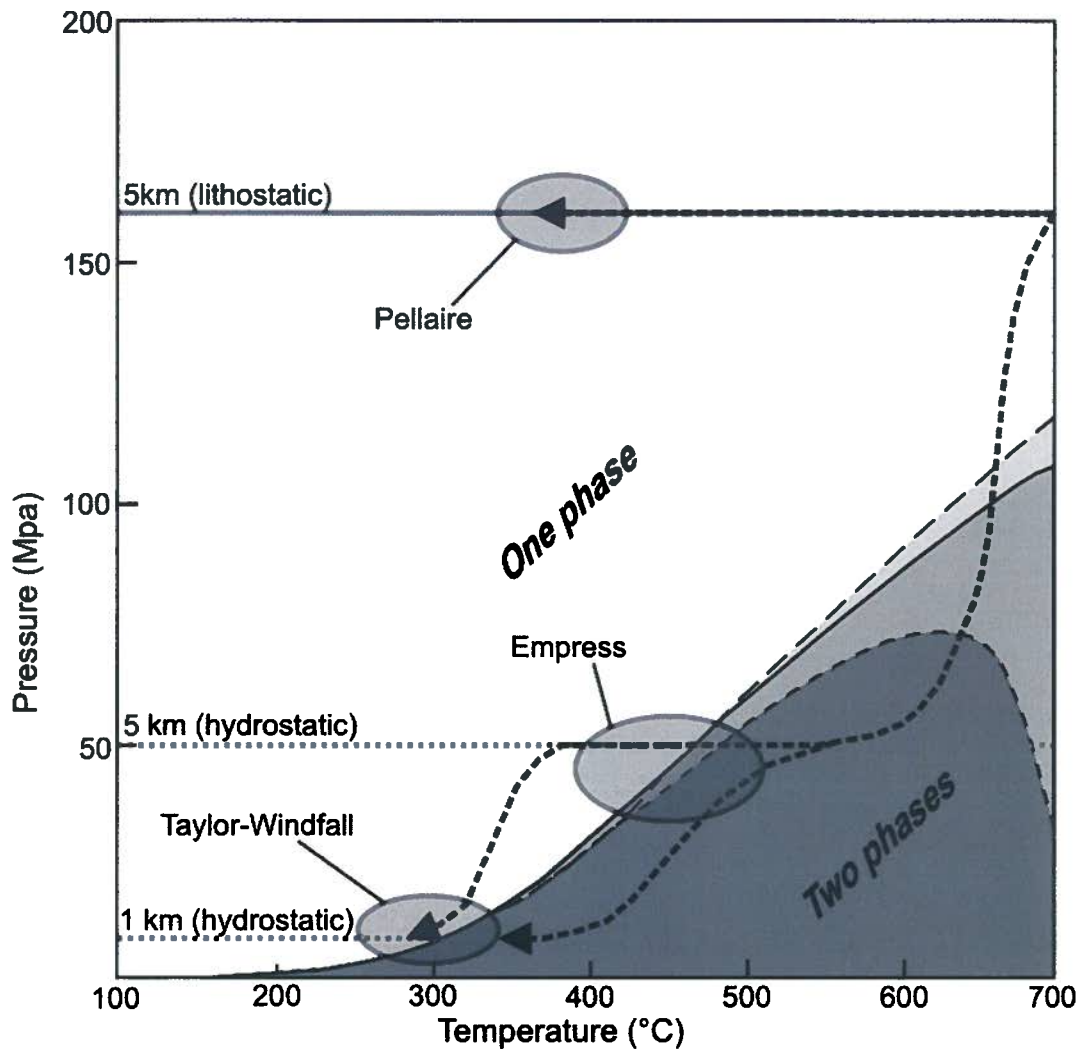


Figure 3.39 Pressure versus temperature graph with curves limiting the stable existence of solutions with 1, 5 and 10% NaCl showing the interpreted P-T evolution of fluids for the Empress, Taylor-Windfall and Pellaire hydrothermal systems. Estimated P-T conditions of mineralization are indicated by the shaded circles for each deposit. Hydrofracturing at Empress causes pressures to drop from lithostatic to hydrostatic. This pressure drop allows initial magmatic fluids to boil and separate into a low-salinity vapour phase and a hypersaline liquid phase. As the vapour phase cools, some vapour re-condenses back to a liquid phase. Both the vapour and condensed liquid phase ascend towards the surface along pre-existing faults and permeable zones. The vapour phase ascend more rapidly due to its higher buoyancy and generates high-T advanced argillic alteration at Taylor-Windfall. The condensed liquid phase follows the vapour phase, but has cooled and reacted more extensively with surrounding rocks due to its slower ascent. The condensed phase overprints high-T alteration at Taylor-Windfall and deposits gold into isolated fractures. Pellaire fluids may have come from a similar source as Empress and Taylor-Windfall fluids, but cooled under uniform lithostatic pressures, which prevented any phase separation of fluids. Pressures for hydrostatic and lithostatic conditions at estimated depths of the Empress (5 km), Pellaire (5 km) and Taylor-Windfall (1 km) systems are based off of lithostatic and hydrostatic pressure gradients from Hagemann and Brown (1996).

## CHAPTER IV

### CONCLUSIONS AND RECOMMENDATIONS FOR FUTURE RESEARCH

#### 4.1 CONCLUSIONS

The summary of the main conclusions of the overall study is provided below.

The Taseko Lakes Region hosts three separate generations of faults. The first generation of faults (D1) are characterized by sub-vertical sinistral-reverse faults and formed prior (>89 Ma) to the majority of mineralization at Taseko Lakes. The second generation (D2) of faults consists of moderate- to high-angle south (early) and north-vergent (late) contractional faults respectively, which formed relatively synchronously (~91-84 Ma) with much of the mineralization at Taseko Lakes, including the Pellaire deposit. Both types of these faults contain relatively ductile shear-fabrics suggesting fluid flow along the faults may have occurred simultaneously with deformation. The most recent generation of faults (D3) in the region are large-scale dextral faults (Schiarizza et al., 1997), including the Tchaikazan Fault, and were active until Eocene time. However, geochronological data from this study indicates that many faults, including the Northwest Copper and Mount McLure Faults, were active into the Tertiary. Thus the D3 deformational event likely gave rise to several varying styles of faulting. Thus D3 faults may be reactivated faults from the initial sinistral deformation event (Schiarizza et al., 1997). D3 formed after the majority of hydrothermal activity in the region, and thus could potentially cut pre-existing mineralization or focus Eocene hydrothermal fluids – however no mineralization appears to be associated with Eocene hydrothermal activity. Geochronological evidence from this study indicates that magmatic activity occurred in the region until 22 Ma.

Broad compositional and textural similarities between the country rocks of the Southeast Coast Belt (SECB) in the study area imply that no specific lithologic unit holds a greater affinity than the others to host mineralization. However, compositional and physical differences do exist between the intrusive rocks of the Coast Plutonic Complex (CPC) and the volcanic and sedimentary rocks of the SECB. Contrasting permeabilities between the two suites of rocks are interpreted to have focused flow directions of mineralizing fluids at both the Pellaire and Empress deposits. Because of this, there is significant potential for mineralization to occur along

the contact between the CPC and the SECB as evidenced by the occurrence of the Empress, Pellaire and Taylor-Windfall deposits proximal to this contact.

The Empress deposit is a developed porphyry Cu prospect. Mineralization occurred at approximately 88 to 87 Ma at depths of roughly 5 km when large volumes magmatic hydrothermal fluids from an unidentified source intrusion migrated laterally along a trough-shaped topographic low in the upper margin of the pre-existing Empress pluton. The low-permeability of the Empress pluton focussed fluids into the overlying country rocks of the Falls River succession. Thus fluid flow occurred dominantly parallel to the contact between the Empress pluton and overlying country rocks, producing intense subhorizontally zoned high-temperature (up to 700°C) phases of quartz-dominated, quartz-magnetite and potassium silicate alteration overprinted by later phases quartz-sericite, sodic, advanced argillic and quartz-chlorite alteration. Fluid inclusion and stable isotopic evidence suggests that hydrothermal fluids at the deposit were initially magmatic-dominated, but there was a gradual input of meteoric waters into the system over time.

The Taylor-Windfall deposit is a past-producing, intermediate to high-sulphidation epithermal Au deposit characterized by fracture controlled vuggy-silica, quartz-sericite  $\pm$  chlorite  $\pm$  pyrite and argillic alteration. Alteration and mineralization formed at about 89 to 87 Ma when hydrothermal fluids migrated upwards along a fault and fracture zones. An initial high-temperature vapour phase generated high-temperature corundum-andalusite and vuggy-silica alteration assemblages reported by Price (1986). The vapour phase was followed by a cooler, re-condensed vapour of similar composition that overprinted high-temperature assemblages with lower temperature intermediate and advanced argillic alteration. These two fluid phases may have originally been part of the same fluid phase, but separated when cooler parts of the vapour re-condensed during ascent. Mineralizing fluids were mainly magmatic in origin with some meteoric component. Mineralization is hosted in a sulphide-dominated and a tourmaline-dominated vein (Price, 1986). There is no evidence to indicate that boiling took place at Taylor-Windfall. A leached cap of fault-controlled quartz-alunite alteration occurs on the ridge above the deposit. More study is required to determine what relation, if any, the zone of quartz-alunite alteration has with the Taylor-Windfall system.

The Pellaire deposit is a past-producing gold-telluride deposit. Mineralization formed when magmatic fluids migrated distally from a crystallizing calc-alkaline intrusion along (D2) south-vergent faults. As fluids crossed from the Falls River succession into the Mount McLeod granodiorite they were cooled and disturbed from chemical equilibrium, which resulted in the

emplacement of quartz-veins in the south-vergent faults and deposition of ore minerals. A zone of hydrothermal brecciation separates the two rock units and may have been caused by high-fluid pressures or pre-existing faulting. Both cases would have arisen due to the competency contrast between the Falls River succession and Mount McLeod granodiorite. Mineralization occurred synchronously with deformation at 85 Ma.

Similarities in ages, fluid compositions and sources between the Empress, Taylor-Windfall and Pellaire deposits indicate they formed from similar magmatic-hydrothermal systems. The widespread occurrence of magmatic-hydrothermal mineralization in the southern Taseko Lakes Region suggests that hydrothermal systems much larger than the scales of the individual deposits were active in the region during approximately 89 to 85 Ma. Since the deposits are interpreted to have formed from similar systems, their varying characteristics illustrate the variability of mineralizing styles that can occur in magmatic-hydrothermal systems. This variability arises largely due to differing characteristics of pre-existing geology and the location of the deposits with respect to the overall system.

Thermochronological data indicates that rocks around Taseko Lakes were buried to depths greater than 4 km during the Late Cretaceous. However, the rocks were all exhumed to depths shallower than 4 km between 50 and 30 Ma.

In summary, Late Cretaceous magmatic-hydrothermal mineralization is abundant in the Taseko Lakes Region. Fluids responsible for mineralization were exolved from crystallizing intrusion related to the Coast Plutonic Complex. Evidence suggests that the hydrothermal systems in the region were large-scale, with fluid flow aided by the high concentration of faults in the area. The region has potential to host a variety of styles of magmatic-hydrothermal mineral deposits depending on the settings and conditions under which the deposits formed.

## 4.2 FURTHER WORK

This study has been a relatively broad-scale study of the Taseko Lakes Region. As a result there is significant room for more detailed study in many different areas.

1. More extensive core logging and sampling at the Empress Deposit would help to better understand the geometries and extents of observed mineralization and alteration zones.
2. More detailed and extensive mapping at Taylor-Windfall and Pellaire could further constrain the structural and alteration histories in the vicinities of the deposits. Access to many areas around the deposits was limited due to the steepness of the terrain. Ropes and climbing gear could aid in accessing some of these areas.
3. Access to the underground workings at both Taylor-Windfall and Pellaire would greatly aid in understanding the mineralization, alteration and structures at the deposits. Sampling of the ore minerals and ore-bearing veins could also open up avenues for more detailed textural, mineralogical and geochemical studies.
4. Re-Os dating of molybdenite from the Empress deposit could better constrain the age of mineralization for that deposit.
5.  $^{40}\text{Ar}$ - $^{39}\text{Ar}$  dating of alunite from Battlement Ridge could evaluate possible links between the quartz-alunite alteration zone and the Taylor-Windfall system.
6. A detailed Pb isotopic study of the sulphide minerals at each deposit and the intrusive phases in the region could better constrain the source of the metals and potentially provide more links between the deposits and any potential intrusions associated with mineralization.
7. Studies of mineral deposits elsewhere along the margins of the Coast Plutonic Complex (CPC) could assess the extent to the CPC can focus mineralization.

## REFERENCES

- Ahmad, S.N., and Rose, A.W. 1980. Fluid inclusions in porphyry and skarn ore at Santa Rita, New Mexico. *Economic Geology*, **75**: 229-250.
- Alderton, D.H.M., and Fallick, A.E. 2000. The Nature and Genesis of Gold-Silver-Tellurium Mineralization in the Metaliferi Mountains of Western Romania. *Economic Geology*, **95**: 495-516.
- Ames, D.E., Franklin, J.M., and Froese, E. 1991. Zonation of hydrothermal alteration at the San Antonio Gold Mine, Bissett, Manitoba, Canada. *Economic Geology*, **86**: 600-619.
- Anderson, G.M. 1996. *Thermodynamics of natural systems*. John Wiley & Sons, Inc. Toronto, Canada.
- Archibald, D.A., Glover, J.K., and Schiarizza, P. 1990. Preliminary Report on  $^{40}\text{Ar}/^{39}\text{Ar}$  geochronology of the Warner Pass, Noaxe Creek and Bridge River Map Areas (92O/2; 92J/15). *In Geological Fieldwork 1989*, B.C. Ministry of Energy, Mines and Petroleum Resources, Paper 1990-1: 34-51.
- Arribas, A., Hedenquist, J.W., Itaya, T., Okada, T., Concepción, R.A., and Garcia, J.S. 1995. Contemporaneous formation of adjacent porphyry and epithermal Cu-Au deposits over 300 ka in Northern Luzon, Philippines. *Geology*, **23**: 337-340.
- ASD 2005. RS<sup>3</sup>. Analytical Spectral Devices, Inc.
- ASD 2006. TerraSpec® User Manual. Analytical Spectral Devices, Inc.
- Ash, C.H., McDonald, R.W.J., and Reynolds, P.R. 2001. Relationships between ophiolites and gold-quartz veins in the North American Cordillera. *British Columbia Geological Survey, Bulletin 108*
- Bakker, R.J. 2002. CLATHRATES, package of computer programs for fluid inclusion studies.
- Barr, D.A., Fox, P.E., Northcote, K.E., and Preto, V.A. 1976. The alkaline suite porphyry deposits – a summary. *Canadian Institute of Mining and Metallurgy, Special Volume 15*: 359-367.
- Barton, Jr. P.B., and Skinner, B.J. 1979. Sulphide mineral stabilities. *In Geochemistry of hydrothermal ore deposits, Edited by Barnes, H.L.* John Wiley, New York, pp. 278-403.
- Bateman, A.M. 1914. Exploration between Lillooet and Chilko Lake, British Columbia. *In: Summary Report, 1912, Geological Survey of Canada*: 177-187.
- Beaudoin, G., and Therrien, P. 2008. *Stable Isotope Fractionation Calculator*. Department of Geology, Laval University.
- Bellamy, J., Arnold, R. 1985. Bralorne Mine project: Report on the 1984 exploration work, Bridge River Area, B.C. Geological Survey Branch Assessment Report 13617. E and B Explorations Inc, Vancouver B.C. 83 p.
- Bierwirth, P., Huston, D., Blewett, R. 2002. Hyperspectral mapping of mineral assemblages associated with gold mineralization in the Central Pilbara, Western Australia. *Economic Geology* **97**: 819-826.
- Bladh, K.W. 1982. The formation of goethite, jarosite, and alunite during the weathering of sulphide-bearing felsic rocks. *Economic Geology*, **77**: 176-184.
- Blevings, S.K., Kennedy, L.A., and Hickey, K.A. 2008. Controls on Copper and Gold Mineralization along the Contact between the Coast Plutonic Complex and the Southeast Coast Belt, Taseko Lakes Region, southwestern British Columbia (NTS 092O/04). *In: Geoscience BC Summary of Activities 2007, Geoscience BC, Report 2008-1*: 21-34.
- Boer, R.H., Meyer, F.M., Robb, L.J., Graney, J.R., Vennemann, T.W., and Kesler, S.E. 1995. Mesothermal-type mineralization in the Sabie-Pilgrim's Rest Gold Field, South Africa. *Economic Geology*, **90**: 860-876.

- Bowers, T.S., and Helgeson, H.C. 1985. FORTRAN programs for generating fluid inclusion isochors and fugacity coefficients for the system H<sub>2</sub>O-CO<sub>2</sub>-NaCl at high pressures and temperatures. *Computers and Geoscience* **11**: 203-213.
- Boyle, R.W. 1979. The geochemistry of gold and its deposits. Geological Survey of Canada, Bulletin **280**: 583.
- Brandon, M.T. Roden-Tice, M.K., and Garver, J.I. 1998: Late Cenozoic exhumation of the Cascadia accretionary wedge in the Olympic Mountains, Northwest Washington State. *Geological Society of America Bulletin*, **110**: 985-1009.
- Brathwaite, R.L., Simpson, M.P., Faure, K. and Skinner, D.N.B. 2001. Telescoped porphyry Cu-Mo-Au mineralisation, advanced argillic alteration and quartz-sulphide-gold-anhydrite veins in the Thames District, New Zealand. *Mineralium Deposita*, **36**: 623-640.
- Brimhall Jr., G.H., and Ghiorso, M.S. 1983. Origin and ore-forming consequences of the advanced argillic alteration process in hypogene environments by magmatic gas contamination of meteoric fluids. *Economic Geology*, **78**: 73-90.
- Brindley, G.W., and Brown, G. 1980. X-ray diffraction procedures for clay mineral identification. *In* Crystal structure of clay minerals and their X-ray identifications. *Edited by* Brindley, G.W., and Brown, G. Mineralogical Society Monograph **5**: 305-359.
- Brommeland, L.K., and Wober, G. 1999. Prosperity Gold-Copper Project, 1998 diamond drilling assessment report. Geological Survey Branch Assessment Report 25898. Taseko Mines Ltd, Vancouver, B.C. 185 p.
- Brown, P.E. 1992. FlinCor: Microsoft Windows fluid inclusion application. version 1.4
- Buchanan, L.J. 1981. Precious metal deposits associated with volcanic environments in Southwest Arizona. *Geological Society Digest*, **14**: 237-261.
- Chiba, H., Chacko, T., Clayton, R.N., and Goldsmith, J.R. 1989. Oxygen isotope fractionations involving diopside, forsterite, magnetite, and calcite: Application to geothermometry. *Geochimica et Cosmochimica Acta*, **53**: 2985-2995.
- Coish, R.A., Kretschmar, L.M., and Journeay, J.M. 1998. Geochemistry of the Miocene Mount Noel Volcanic Complex, British Columbia and comparison with the Columbia River basalt. *Journal of Volcanology and Geothermal Research*, **83**: 269-285.
- Colvine A.C., Fyon, J.A., Heather, K.B., Marmont, S., Smith, P.M., and Troop, D.G. 1988. Archean lode gold deposits in Ontario. Ontario Geological Survey Miscellaneous Paper **139**: p. 136.
- Cole, D.R. 1985. A preliminary evaluation of oxygen isotopic exchange between chlorite and water. *Geological Society of America Abstract with Programs*, **17**: p. 550.
- de Ronde, C.E.J., and Blattner, P. 1988. Hydrothermal alteration, stable isotopes, and fluid inclusions of the Golden Cross epithermal gold-silver deposit, Waihi, New Zealand. *Economic Geology*, **83**: 895-917.
- Dilles, J.H., and Einaudi, M.T. 1992. Wall-rock alteration and hydrothermal flow paths about the Ann-Mason Porphyry Copper Deposit, Nevada – A 6-Km vertical reconstruction. *Economic Geology*, **87**: 1963-2001.
- Dilles, J.H., Farmer, G.L., and Field, C.W. 1995. Sodium-calcium alteration due to non-magmatic saline fluids in porphyry copper deposits: Results for Yerington, Nevada. *In* Magmas, Fluids, and Ore Deposits: Mineralogical Association of Canada Short Course, **23**: 309-338.
- Dong, H., Hall, C.M., Halliday, A.N., Peacor, D.R., Merriman, R.J., and Roberts, B. 1997. <sup>40</sup>Ar/<sup>39</sup>Ar illite dating of Late Caledonian (Acadian) metamorphism and cooling of K-bentonites and slates from the Welsh Basin, U.K. *Earth and Planetary Science Letters*, **150**: 337-351.

- Driesner, T. and Geiger, S. 2007. Numerical simulation of multiphase fluid flow in hydrothermal systems. *Reviews in Mineralogy and Geochemistry*, **65**: 187-212.
- Drews-Armitage, S.P. 1996. Clay alteration and gold deposition in the genesis and Blue Star Deposits, Eureka County, Nevada. *Economic Geology*, **91**: 1383-1393.
- Duan, Z., Møller, N., and Weare, J.H. 1996. Prediction of the solubility of H<sub>2</sub>S in NaCl aqueous solution: an equation of state approach. *Chemical Geology* **130**: 15-20.
- Evans, A.M. 1993. *Ore Geology and Industrial Minerals*. Blackwell Science, Oxford, United Kingdom.
- Farley, K.A. 2000. Helium diffusion from apatite: general behaviour as illustrated by Durango fluorapatite. *Journal of Geophysical Research*, **105**: 2903-14.
- Field, C.W., Zhang, L., Dilles, J.H., Rye, R.O., Reed, M.H. 2005. Sulfur and oxygen isotopic record in sulphate and sulphide minerals of early, deep, pre-Main Stage porphyry Cu-Mo and late Main Stage base-metal mineral deposits, Butte district, Montana. *Chemical Geology, Geochemistry of Sulfate Minerals: A tribute to Robert O Rye*, **215**: 61-93.
- Fleischer, R.K., Price, P.B., Walker, R.M. 1975: *Nuclear Tracks in Solids*. Berkely: University of California Press: 605 pages.
- Fournier, R.O. 1999. Hydrothermal processes related to movement of fluid from plastic into brittle rock in the magmatic-epithermal environment. *Economic Geology*, **94**: 1193-1211.
- Friedman, R.M., Armstrong, R.L. 1995. Jurassic and Cretaceous geochronology of the southern Coast Belt, British Columbia 49° to 51°. *In* Miller DM, Busby C, Jurassic Magmatism and Tectonics of the North American Cordillera: Boulder, Colorado. Geological Society of America Special Paper **299**.
- Gammons, C.H., and Williams-Jones, A.E. 1997. Chemical mobility of gold in the porphyry-epithermal environment. *Economic Geology*, **92**: 45-59.
- Garver, J.I. 1989. Basin evolution and source terranes of Albian-Cenomanian Rocks in the Tyaughton Basin, Southern British Columbia: Implications for mid-Cretaceous tectonics in the Canadian Cordillera. Unpublished Ph.D. thesis, The University of Washington, Seattle, Washington. 227 pages.
- Garver, J.I. 1992. Provenance of Albian-Cenomanian Rocks fo the Methow and Tyaughton Basins, Southern British Columbia: a mid-Cretaceous link between North American and the Insular Terrane. *Canadian Journal of Earth Sciences*, **29**: 1274-1295.
- Giggenbach, W.F. 1997. The origin and evolution of magmatic-hydrothermal systems. *In* *Geochemistry of Hydrothermal Ore Deposits*, third edition, *edited by* Barnes, H.L. John Wiley & Sons Inc., Hoboken, NJ.
- Glover, J.K., and Schiarizza, P. 1987. Geology and Mineral Potential of the Warner Pass Map Area (92O/3). *In*: Geological Fieldwork 1986, B.C. Ministry of Energy, mines and Petroleum Resources, Paper **1987-1:1** 57-169.
- Glover, J.K., Schiarizza, P., Umhoefer, P.J., and Garver, J.I. 1987. Geology of the Warner Pass Map Area (92O/3). B.C. Ministry of Energy, Mines and Petroleum Resources, Open File **1987-3**.
- Glover, J.K., Schiarizza, P., and Garver, J.I. 1988a. Geology of the Noaxe Creek Map Area (92O/2). *In* Geological Fieldwork 1987. B.C. Ministry of Energy, Mines and Petroleum Resources, Paper **1988-1**: 105-123.
- Glover, J.K., Schiarizza, P., Garver, J.I., Umhoefer, P.J., and Tipper, H.W. 1988b. Geology and Mineral Potential of the Noaxe Creek Map Area (92O/2). B.C. Ministry of Energy, Mines and Petroleum Resources, Open File **1988-9**.
- Graham, C.M., Viglino, J.A., and Harmon, R.S. 1987. Experimental study of hydrogen-isotope exchange between aluminous chlorite and water and of hydrogen diffusion in chlorite. *American Mineralogist*, **72**: 566-579.

- Groves, D.I., Goldfarb, R.J., Gebre, M.M., Hagemann S.G., and Robert, F. 1998. Orogenic gold deposits; a proposed classification in the context of their crustal distribution and relationship to other gold deposit types. *Ore Geology Reviews*, **13**: 7-27.
- Groves, D.I., Goldfarb, R.J., Robert, F., and Hart, C.J.R. 2003. Gold Deposits in Metamorphic Belts: Overview of Current Understanding, Outstanding Problems, Future Research, and Exploration Significance. *Economic Geology*, **98**: 1-29.
- Gustafson, L.B., and Hunt, J.P. 1975. The Porphyry Copper Deposit at El Salvador, Chile. *Economic Geology* **70**: 857-912
- Hagemann, S.G., and Brown, P.E. 1996. Geobarometry in Archean lode-gold deposits. *European Journal of Mineralogy*, **8**: 937-960.
- Hanes, J.A. 1991. K-Ar and  $^{40}\text{Ar}/^{39}\text{Ar}$  geochronology: methods and applications. In *Applications of radiogenic isotope systems to problems in geology*. Edited by Heaman, L., and Ludden, J.N. Mineralogical Association of Canada, Short Course Handbook, **19**: 27-57.
- Harris, A.C. and Golding, S.D. 2002. New evidence of magmatic-fluid-related phyllic alteration: Implications for the genesis of porphyry Cu deposits. *Geology*, **30**: 335-338.
- Hart, C.J.R., Goldfarb, R.J., Ullrich, T.D., and Friedman, R. 2008. Gold, granites and geochronology: Timing of formation of the Bralorne-Pioneer gold orebodies and the Bendor batholith, southwestern British Columbia (NTS 092J/15). In *Geoscience BC, Summary of Activities 2007*, Geoscience BC, Report **2008-1**: 47-54.
- Hayba, D.O., and Ingebritsen, S.E. 1994. The computer model HYDROTHERM, a three-dimensional finite-difference model to simulate ground-water flow and heat transport in the temperature range of 0 to 1200C. U.S. Geological Survey Water-Res Invest Report, **94**: 12252.
- Hedenquist, J.W. 1987. Mineralization associated with volcanic-related hydrothermal systems in the circum-Pacific. *Transactions: 4<sup>th</sup> Circum Pacific Energy and Mineral Resources Conference*, Singapore. American Association of Petroleum Geologists: 513-524.
- Hedenquist, J.W., and Henley, R.W. 1985. Hydrothermal eruptions in the Waiotapu Geothermal System, New Zealand: Their origin, associated breccias and relation to precious metal mineralization. *Economic Geology*, **80**: 1640-1668.
- Hedenquist, J.W., and Arribas, A., Jr. 1999. The tops and bottoms of high-sulfidation epithermal ore deposits. Edited by Stanley, C.J., et al. *Mineral deposits: Processes to processing*. Proceedings of the Fifth Biennial SGA meeting and the Tenth Quadrennial IAGOD Symposium, London, England: 515-518.
- Hedenquist, J.W., and White, N.C. 2005. Epithermal gold-silver ore deposits: Characteristics, interpretation and exploration. Prospectors and Developers Association of Canada, short course notes.
- Hedenquist, J.W., Arribas, Jr., A., and Reynolds, T.J. 1998. Evolution of an intrusion-centered hydrothermal system: Far Southeast-Lepanto porphyry and epithermal Cu-Au deposits, Philippines. *Economic Geology*, **93**: 373-404.
- Heinrich, C.A. 2005. The physical and chemical evolution of low-salinity magmatic fluids at the porphyry to epithermal transition: a thermodynamic study. *Mineralium Deposita*, **39**: 864-889.
- Heinrich, C.A. 2007. Fluid-fluid interactions in magmatic-hydrothermal ore formation. *Reviews in Mineralogy and Geochemistry*, **63**: 363-387.
- Heinrich, S.M. 1991. Taseko Mines Assessment Report. Geological Survey Branch Assessment Report 22065. Taseko Mines Ltd., Vancouver, B.C. 35 p.
- Hemley, J.J. 1959. Some mineralogical equilibria in the system  $\text{K}_2\text{O}-\text{Al}_2\text{O}_3-\text{SiO}_2-\text{H}_2\text{O}$ . *American Journal of Science*, **257**: 241-270.

- Hemley, J.J., Hostetler, P.B., Gude, A.J., and Mountjoy, W.T. 1969. Some stability relations of alunite. *Economic Geology*, **64**: 599-612.
- Hemley, J.J., Montoya, J.W., Marinenko, J.W., and Luce, R.W. 1980. Equilibria in the system  $Al_2O_3$ - $SiO_2$ - $H_2O$  and some general implications for alteration/mineralization processes. *Economic Geology*, **75**: 210-228.
- Hezarkhani, A., and Williams-Jones, A.E. 1998. Controls of alteration and mineralization in the Sungun Porphyry Copper Deposit, Iran: Evidence from fluid inclusions and stable isotopes. *Economic Geology*, **93**: 651-670.
- Holiday, J.R. and Cooke, D. R. 2007. Advances in Geological Models and Exploration Methods for Copper  $\pm$  Gold Porphyry Deposits. Proceedings of Exploration 07: Fifth Decennial International Conference on Mineral Exploration, pp. 791-809.
- Hollis, L., Blevings, S.K., Chamberlain, C.M., Hickey, K.A., and Kennedy, L.A. 2007. Mineralization, alteration and structure of the Taseko Lakes region (NTS 092O/04), southwestern British Columbia: Preliminary analysis. In: Geoscience BC, Paper 2007-1: 297-307.
- Hollis, L., Hickey, K. and Kennedy, L.A. 2008. Mineralization and alteration associated with an hypothesized copper (molybdenum) porphyry system in the Taseko Lakes Region, southwestern British Columbia (NTS 092O/04). In Geoscience BC Summary of Activities, Geoscience BC, Report 2008-1: 55-66.
- Holtby, M.H. 1988. An assessment report of diamond drilling and underground development on the Lord 1 to 3 and Hi 1 to 4 claims. Geological Survey Branch Assessment Report 16864. Consolidated Silver Standards Limited, Vancouver, B.C. 108 p.
- Hurwitz, S., Kipp, K.L., Ingebritsen, S.E., and Reid, M.E. 2003. Groundwater flow, heat transport, and water table position within volcanic edifices: implications for volcanic processes in the Cascades Range. *Journal of Geophysical Research*, **108**: 2557.
- Husson, L., and Moretti, I. 2002. Thermal regime of fold and thrust belts – an application to the Bolivian sub Andean zone. *Tectonophysics*, **345**: 253-280.
- Israel, S. 2001. Structural and stratigraphic relationships within the Tchaikazan River area, southwestern British Columbia: implications for the tectonic evolution of the southeastern Coast Belt. Unpublished M.Sc. Thesis. University of British Columbia, Vancouver, B.C. 135 p.
- Israel, S., Schiarizza, P., Kennedy, L.A., Friedman, R.M., and Villeneuve, M.E. 2006. Evidence for Early to Late Cretaceous, sinistral deformation in the Tchaikazan River area, southwestern British Columbia: Implications for the evolution of the southeastern Coast Belt. In: Evidence for Major Lateral Displacements in the North American Cordillera. Geological Association of Canada Special Paper 46.
- Jeletzky, J.A., and Tipper, H.W. 1968. Upper Jurassic and Cretaceous rocks of Taseko Lakes map area and their bearing on the geological history of southwestern British Columbia. Geological Survey of Canada, Paper 67-54: 218 p.
- Jia, Y., and Kerrich, R. 1999. Nitrogen isotope systematics of mesothermal lode gold deposits: Metamorphic, granitic, meteoric water, or mantle origin? *Geology*, **27**: 1051-1054.
- John, D.A. 1989. Geologic setting, depths of emplacement, and regional distribution of fluid inclusions in the intrusions of the Central Wasatch Mountains, Utah. *Economic Geology*, **84**: 386-409.
- Johns, S.M., Kyser, T.K., and Hemlstaedt, H.H. 2006. Character of fluids associated with hydrothermal alteration and metamorphism of Palaeoproterozoic submarine volcanic rocks, Baffin Island, Nunavut, Canada. *Precambrian Research* **145**: 93-110.

- Johnson, J.W., Oelkers, E.H., and Helgeson, H.C. 1992. SUPCRT92: a software package for calculating the standard modal thermodynamic properties of minerals, gases, aqueous species and reactions from 1 to 5000 bars and 0 to 1000°C. *Computers and Geoscience*, **18**: 899-947.
- Journey, J.M., Friedman, R.M. 1993. The Coast Belt thrust system: evidence of Late Cretaceous shortening in southwest British Columbia. *Tectonics*, **12**: 756-775.
- Journey, J.M., and Mahoney, J.B. 1994. Cayoosh assemblage: Regional correlations and implications for terrane linkages in the Southern Coast Belt, British Columbia. *In Geological Survey of Canada, Current Research 1994-A*: 165-175.
- Kelley, K.D., Romberger, S.B., Beaty, D.W., Pontius, J.A., Snee, L.W., Stein, H.J., and Thompson, T.B. 1998. Geochemical and geochronological constraints on the genesis of Au-Te deposits at Cripple Creek, Colorado. *Economic Geology*, **93**: 981-1012.
- Kesler, S.E. 2005. Ore-forming fluids. *Elements*, **1**: 13-18.
- Ketcham, R.A., and Apatite to Zircon Inc. 2008. HeFTy. V. 1.5.6.
- Ketcham, R.A., Donelick R.A., and Carlson, W.D. 1999. Variability of apatite fission-track annealing kinetics. III. Extrapolation to geological time scales. *American Mineralogist*, **84**: 1235-1255.
- Lambert, E. 1989. Geochemical and diamond drilling program of the Taseko property. Unpublished company report. Westpine Metals Ltd., Vancouver B.C.
- Lambert, E. 1991. 1990 Diamond drill program of the Taseko property. Unpublished company report. Westpine Metals Ltd., Vancouver B.C.
- Lambert, S.J., and Epstein, S. 1980. Stable isotope investigations of an active geothermal system in Vales Caldera, Jemez Mountains, New Mexico. *Journal of Volcanology and Geothermal Research*, **8**: 111-129.
- Lane, R. 1983. Geological and geochemical assessment report on the Taseko property (Bluff Claims 1 and 2, Windfall C-G, Windfall #2 C-G, and Province C-G). Unpublished company report. Westmin Resources Ltd., Vancouver, B.C.
- Larson, P.B. 1987. Stable isotope and fluid inclusion investigations of epithermal vein and porphyry molybdenum mineralization in the Rico Mining District, Colorado. *Economic Geology* **82**: 2141-2157.
- Leitch, C.H.B., Dawson, K.M., and Godwin, C.I. 1989. Early Late Cretaceous-Early Tertiary gold mineralization: A galena lead isotope study of the Bridge River Mining Camp, Southwestern British Columbia, Canada. *Economic Geology*, **84**: 2226-2236.
- Leitch, C.H.B., Godwin, C.I., Brown, T.H., and Taylor, B.E. 1991. Geochemistry of mineralizing fluids in the Bralorn-Pioneer mesothermal gold vein deposit, British Columbia, Canada. *Economic Geology* **86**: 318-353.
- Lowell, J.D., and Guilbert, J.M. 1970. Lateral and vertical alteration-mineralization zoning in porphyry ore deposits. *Economic Geology*, **65**: 373-408.
- Ludwig, K. 2003. Isoplot 3.00 – a geochronological toolkit for Microsoft Excel. Berkeley Geochronological Center, **Special Publication 4**: 71p.
- Macdonald, A.J., and Spooner, E.T.C. 1981. Calibration of a Linkam TH 600 programmable heating-cooling stage for microthermometric examination of fluid inclusions. *Economic Geology* **76**: 1248-1258.
- MacKenzie, J.D. 1921. A Reconnaissance between Taseko Lake and Fraser River, British Columbia. *In Summary Report, 1920, Part A, Geological Survey of Canada*, pages 70-81.

- Markley, M.J., Teysiier, C., and Cosca, M. 2002. The relation between grain size and  $^{40}\text{Ar}/^{39}\text{Ar}$  date for Alpine white mica from the Siview-Mischabel Nappe, Switzerland. *Journal of Structural Geology*, **24**: 1937-1955.
- Martinez-Serrano, R.G. 2002. Chemical variations in hydrothermal minerals of the Los Humeros geothermal system, Mexico. *Geothermics*, **31**: 579-612.
- Maxson, J.A. 1996. A sedimentary record of Late Cretaceous tectonic restructuring of the North American cordillera: The Tyaughton–Methow basin, southwest British Columbia; Unpublished M.Sc. thesis. University of Minnesota
- McMillan, W.J., and Panteleyev, A. 1988. Porphyry copper deposits. *In* *Ore Deposit Models*. Edited by Roberts, R.G., and Sheahan, P.A. *Geoscience Canada*, **7**: 52-63.
- McLaren, G.P. 1990. A mineral resource assessment of the Chilko Lake planning area. BC Ministry of Energy, Mines and Petroleum Resources, Bulletin 81, 117 p.
- Milu, V., Milesi, J.P., and Leroy, J.L. 2004. Roşia Poieni copper deposit, Apuseni Mountains, Romania: advanced argillic overprint of a porphyry system. *Mineralium Deposita*, **39**: 173-188.
- Monger, J.H.W. 1999. Review of the Geology and Tectonics of the Canadian Cordillera. Notes for a short course, Sidney, British Columbia (February 24-25), 72 pages.
- Monger, J.H.W., and Journeay, J.M. 1994. Guide to the geology and tectonic evolution of the southern Coast Mountains. Geological Survey of Canada Open File **2490**.
- Monger, J.H.W., Price, R.A., and Templeman-Kluit, D.J. 1982. Tectonic accretion and the origin of the southern Coast Mountains. Geological Survey of Canada Open File **2490**.
- Monger, J.H.W., van der Heyden, P., Journeay, J.M., Evenchick, C.A. and Mahoney, J.B. 1994. Jurassic – Cretaceous Basins along the Canadian Coast Belt: their Bearing on pre-mid-Cretaceous Sinistral Displacements. *Geology*, **22**: 175-178.
- Mustard, P.S. and van der Heyden, P. 1994. Stratigraphy and sedimentology of the Tatla Lake – Bssel Creek Map Areas, West-central British Columbia; in *Current Research 1994-A*, Geological Survey of Canada, p. 95-104.
- Ohmoto, H., and Rye, R.O. 1979. Isotopes of sulphur and carbon. In *Geochemistry of hydrothermal ore deposits*. Edited by Barnes, H.L. Wiley, New York, pp.509-567.
- Oliver, J., 1986. Fluids expelled tectonically from orogenic belts: their role in hydrocarbon migration and other geologic phenomena. *Geology*, **14**: 99-102.
- Osborne, W. 1994. 1993-1994 Exploration Program on the Taseko Property. Unpublished company report. Westpine Metals, Ltd., Vancouver, B.C.
- Osborne, W. 1999. Report on the 1998 exploration program of the Taseko Property. Unpublished company report. Great Quest Metals, Ltd., Vancouver, B.C.
- Parrish, R.R. 1992. U-Pb Ages for Cretaceous Plutons in the Eastern Coast Belt, Southern British Columbia. *In* *Current Research, Part A*. Geological Survey of Canada **91-2**: 109-113.
- Passchier, C.W., and Trouw, R.A.J. 2005. *Microtectonics*. Springer-Verlag, Berlin, Germany.
- Perry, E.C., Jr., Tan, F.C., and Morey, G.B. 1973. Geology and Stable Isotope Geochemistry of the Biwabik Iron Formation, Northern Minnesota. *Economic Geology*, **68**: 1110-1125.
- Pezzot, E.T. 2005. Assessment report on the Pellaire project. Unpublished company report. Valor Resources Ltd., Vancouver, B.C.
- Post, J.L., and Crawford, S. 2007. Varied forms of palygorskite and sepiolite from different geologic systems. *Applied Clay Science*, **36**: 232-244.

- Price, G. 1986. *Geology and Mineralization, Taylor-Windfall Gold Prospect, British Columbia, Canada*. M.Sc. Thesis, Department of Geosciences, Oregon State University, Corvallis, Oregon.
- Proffett, J.M. 2003. *Geology of the Bajo de la Alumbrera Porphyry Copper-Gold Deposit, Argentina*. *Economic Geology*, **98**: 1535-1574.
- Reed, M.H. 1997. Hydrothermal alteration and its relationship to ore fluid composition. *In Geochemistry of Hydrothermal Ore Deposits*, third edition, *edited by Barnes, H.L.* John Wiley & Sons Inc., Hoboken, NJ.
- Reiners, P.W., and Brandon, M.T. 2006. Using thermochronology to understand orogenic erosion. *Annual Reviews of Earth and Planetary Science*, **34**: 419-466.
- Reiners, P.W., Spell T.L., Nicolescu, S., and Zanetti, K.A. 2004. Zircon (U-Th)/He thermochronometry: He diffusion and comparisons with  $^{40}\text{Ar}/^{39}\text{Ar}$  dating. *Geochimica et Cosmochimica Acta*, **68**: 1857-1887,
- Ren, S.K., Walshe, J.L., Paterson, R.G., Both, R.A., and Andrew, A. 1995. Magmatic and hydrothermal history of the porphyry-style deposits of the Ardlethan Tin Field, New South Wales, Australia. *Economic Geology*, **90**: 1620-1645.
- Renne, P.R., Swisher, C.C., Deino, A.L., Karner, D.B., Owens, T.L., and DePaolo, D.J. 1998. Intercalibration of standards, absolute ages and uncertainties in  $^{40}\text{Ar}/^{39}\text{Ar}$  dating. *Chemical Geology* **145**: 117-152
- Reyes, A.G. 1990. Petrology of Philippine geothermal systems and the application of alteration mineralogy to their assessment. *Journal of Volcanology and Geothermal Research*, **43**: 279-309.
- Richards, J. 2007. Tectonomagmatic controls on porphyry and epithermal Au deposits. *In Vancouver Mining Exploration Group. Gold deposits: Exploration and economics short course notes.*
- Rollinson, H. 1993. *Using geochemical data; evaluation, presentation, interpretation.* Longman Group UK, Ltd. London, United Kingdom.
- Rowins, S.M. 1999. Reduced porphyry copper-gold deposits: a newly recognized style of gold mineralization. *GSA abstracts with programs*, **A-92**.
- Rusmore, M.E. 1987. *Geology of the Cadwallader Group and the Intermontane-Insular superterrane boundary, Southwestern British Columbia.* *Canadian Journal of Earth Sciences*, **24**: 2279-2291.
- Rusmore, M.E., and Woodsworth, G.J. 1991a. Coast Plutonic Complex; a mid-Cretaceous contractional orogen. *Geology*, **19**; 941-944.
- Rusmore, M.E., and Woodsworth, G.J. 1991b. Distribution and tectonic significance of Upper Triassic terranes in the eastern Coast Mountains and adjacent Intermontane Belt, British Columbia. *Geological Society of America Special Paper* **343**.
- Rusmore, M.E., and Woodsworth, G.J. 1994. Evolution of the eastern Waddington Thrust Belt and its relation to the mid-Cretaceous Coast Mountains arc, western British Columbia. *Tectonics*, **13**: 1052-1067.
- Rye, R.O., Betke, P.M., and Wasserman, M.D. 1992. The stable isotope geochemistry of acid-sulfate alteration. *Economic Geology*, **87**: 225-262.
- Samson, I., Anderson, A., and Marshall, D. 2003. *Fluid Inclusions: Analysis and Interpretation.* Mineralogical Association of Canada, short course series volume **32**.
- Sanche, H.A. 2004. Report on the 2003 surface drilling on the Bralorne Pioneer Mine property, Cosmopolitan, Cosmopolitan Fraction and Mauser claims. Unpublished company report. Bralorne Pioneer Gold Mines Ltd., Vancouver, B.C. 51 p.
- Sand, L.B., Rustum, R., and Osborn, E.F. 1957. Stability relations of some minerals in the  $\text{Na}_2\text{O}-\text{Al}_2\text{O}_3-\text{SiO}_2-\text{H}_2\text{O}$  System. *Economic Geology*, **52**: 169-179.

- Schiarizza, P., and Garver, J.I. 1995. Guide to the Geology and Tectonic evolution of the Bridge River Area, Southeastern Coast Belt, Southwestern, British Columbia: A field guide to accompany days 2 and 3 of GAC/MAC Victoria '95 field trip A5. Geological Association of Canada - Mineralogical Association of Canada Annual Meeting, Victoria, B.C.
- Schiarizza, P., and Riddell, J. 1997. Geology of the Tatlayoko Lake – Beece Creek area (92N/8, 9, 10; 92O/5, 6, 12). *In* Interior Plateau Geoscience Project: Summary of Geological, Geochemical and Geophysical Studies. *Edited by* Diakow, L.J.
- Schiarizza, P., Gaba, R.G., Glover, J.K., Garver, J.I., Umhoefer, P.J. 1997. Geology and mineral occurrences of the Taseko – Bridge River Area. BC Ministry of Employment and Investment, Bulletin 100. 292 p.
- Seedorff, E., and Einaudi, M.T. 2004. Henderson porphyry molybdenum system, Colorado: II. Decoupling of introduction and deposition of metals during geochemical evolution of hydrothermal fluids. *Economic Geology*, **99**: 39-72.
- Sharp, Z. 2006. Stable Isotope Geochemistry. Pearson Prentice Hall, Upper Saddle River, N.J.
- Shimizu, T., Matsueda, H., Ishiyama, D., and Matsubaya, O. 1998. Genesis of epithermal Au-Ag mineralization of the Koryu Mine, Hokkaido, Japan. *Economic Geology*, **93**: 303-325.
- Sibson, R.H., Robert, F., and Poulsen, K.H. 1988. High-angle reverse faults, fluid-pressure cycling, and mesothermal gold-quartz deposits. *Geology*, **16**: 551-555.
- SII 2002. SpecMin Pro version 3.1. Spectral International Inc.
- Sillitoe, R.H. 1994. Erosion and collapse of volcanoes – causes of telescoping in intrusion-centered ore deposits. *Geology*, **22**: 945-948.
- Sillitoe, R.H. 1995. Exploration of porphyry copper lithocaps. In: Pacific Rim Congress 95:19-22 November 1995, Auckland, New Zealand, proceedings: Carlton South, The Australasian Institute of Mining and Metallurgy, pp. 527-532.
- Simon, G., Kesler, S.E., Essene, E.J., and Chryssoulis, S.L. 2000. Gold in porphyry copper deposits: Experimental determination of the distribution of gold in the Cu-Fe-S system at 400 to 700°C. *Economic Geology*, **95**: 259-270
- Smith, A.L. 1998. Report on the 1998 Program of Regional Geochemical Sampling and Geological Reconnaissance of the Lord River Project. Unpublished company report. Pellaire Gold Mines, Ltd., Vancouver, B.C.
- Spry, P.G., Paredes, M.M., Foster, F., Truckle, J.S., and Chadwick, T.H. 1996. Evidence for a genetic link between gold-silver telluride and porphyry molybdenum mineralization at the Golden Sunlight Deposit, Whitehall, Montana: fluid inclusion and stable isotope studies. *Economic Geology*, **91**: 507-526.
- Squire, R.J., Herrman, W., Pape, D., and Chalmers, D.I. 2007. Evolution of the Peak Hill high-sulfidation epithermal Au-Cu deposit, eastern Australia. *Mineralium Deposita*, **42**: 489-503.
- Stoffregen, R. 1987. Genesis of acid-sulphate alteration and Au-Cu-Ag mineralization at Summitville, Colorado. *Economic Geology*, **82**: 1575-1591.
- Suzuoki, T., and Epstein, S. 1976. Hydrogen isotope fractionation between OH-bearing minerals and water. *Geochimica et Cosmochimica Acta*, **40**: 1229-1240.
- Symons, D.T.A., Harris, M.J., Gabites, J.E., and Hart, C.J.R. 2000. Eocene (51 Ma) end to northward translation of the CPC: paleomagnetism and K-Ar dating of the White Pass Dikes. *Tectonophysics*, **326**: 93-109.

- Thompson, A.J.B., Hauff, P.L., and Robitaille, A.J. 1999. Alteration mapping in exploration: Application of short-wave infrared (SWIR) spectroscopy. *Society of Economic Geologists Newsletter* **39**: 1, 16–27
- Tipper, H.W. 1963. Geology, Taseko Lakes, British Columbia (92-O). Map 29-1963. Geological Survey of Canada.
- Tipper, H.W. 1978. Taseko Lakes (92O) Map Area, Geological Survey of Canada Open File 534.
- Ulrich, T., and Heinrich, C.A. 2001. Geology and alteration geochemistry of the porphyry Cu-Au deposit at Bajo de la Alumbrera, Argentina. *Economic Geology* **96**:1719, correctly reprinted in 2002 **97**: 1863-1888.
- Umhoefer, P.J., and Schiarizza, P. 1996. Latest Cretaceous to Early Tertiary dextral strike-slip faulting on the southeastern Yalakom fault system, southeastern Coast Belt, British Columbia. *Geological Society of America Bulletin* **108**: 768-785.
- Umhoefer, P.J., Rusmore, M.E., and Woodsworth, G.J. 1994. Contrasting tectonostratigraphy and structure in the Coast Belt near Chilko Lake, British Columbia: Unrelated terranes or an arc – back-arc transect?. *Canadian Journal of Earth Sciences*, **31**: 1700-1713.
- Umhoefer, P.J., Schiarizza, P., Robinson, M. 2002. Relay Mountain Group, Tyaughton - Methow Basin, southwest British Columbia: A major Middle Jurassic to Early Cretaceous terrane overlap assemblage. *Canadian Journal of Earth Sciences*, **43**: 1143-1167.
- Veizer, J., Ala, D., Azmy, K., Bruckschen, P., Buhl, D., Bruhn, F., Carden, G.A.F., Diener, A., Ebner, S., Godderis, Y., Jasper, T., Korte, C., Pawelek, F., Podlaha, O.G., and Strauss, H. 1999.  $^{87}\text{Sr}/^{86}\text{Sr}$ ,  $\delta^{13}\text{C}$  and  $\delta^{18}\text{O}$  evolution of Phanerozoic seawater. *Chemical Geology*, **161**: 59-88.
- Vila, T., Sillitoe, R.H., Betzhold, J., Viteri, E. 1991. The porphyry gold deposit at Marte, Northern Chile. *Economic Geology* **86**: 1271-1286.
- Wallier, S., Rey, R., Kouzmanov, K., Pettke, T., Heinrich, C.A., Leary, S., O'Connor, G., Tămaş, C.G., Vennemann, T., and Ulrich, T. 2006. Magmatic fluids in the breccia hosted epithermal Au-Ag deposit of Roşia Montană. *Economic Geology*, **101**: 923-954.
- Watanabe, Y., and Hedenquist, J. 2001. Mineralogic and stable isotope zonation at the surface over the El Salvador porphyry copper deposit, Chile. *Economic Geology*, **96**: 1775-1797.
- White, N.C., and Hedenquist, J.W. 1990. Epithermal environments and styles of mineralization: Variations and their causes, and guidelines for exploration. *Journal of Geochemical Exploration*, **36**: 445-474.
- White, N.C., and Hedenquist, J.W. 1995. Epithermal gold deposits: Styles, characteristics and exploration. *SEG newsletter*, **23**: 1, 9-13.
- White, S. 1975. The effects of strain on the microstructures, fabrics and deformation mechanisms in quartzites. *Philosophical Transactions of the Royal Society of London*, **283**: 69-86.
- Williams-Jones, A.E., and Heinrich, C.A. 2005. Vapor transport of metals and the formation of magmatic-hydrothermal ore deposits. *Economic Geology*, **100**: 1287-1312.
- Wolfhard, M.R. 1976. Fish Lake. In: *Porphyry Deposits of the Canadian Cordillera*, Sutherland BA, ed. Canadian Institute of Mining and Metallurgy, **Special Volume 15**: 317-322.
- Yardley, B.W.D. 2005: Metal concentrations in crustal fluids and their relationship to ore formation. *Economic Geology*, **100**: 613-632.
- Yeh, H.W. 1980. D/H ratios and late-stage dehydration of shales during burial. *Geochimica et Cosmochimica Acta*, **44**: 341-352.

- Zhang, Y.G., and Frantz, J.D. 1989. Experimental determination of the compositional limits of immiscibility in the system  $\text{CaCl}_2\text{-H}_2\text{O-CO}_2$  at high temperatures and pressures using synthetic fluid inclusions. *Chemical Geology* **74**: 289-308.
- Zhang, X., Nesbitt, B.E., and Muehlenbachs, K. 1989. Gold mineralization in the Okanagan Valley, Southern British Columbia: Fluid inclusion and stable isotope studies. *Economic Geology* **84**: 410-424.
- Zheng, Y.F. 1993. Calculation of oxygen isotope fractionation in hydroxyl-bearing silicates. *Earth Planetary Science Letters*, **120**: 247-263.
- Zheng, Y.F. 1994. Oxygen isotope fractionation in metal monoxides. *Mineralogical Magazine*, **58A**: 1000-1001.

## **Appendix A: Short-wavelength infrared (SWIR) Spectra**

Figure A.1 Sample SWIR spectra for indicated samples and minerals

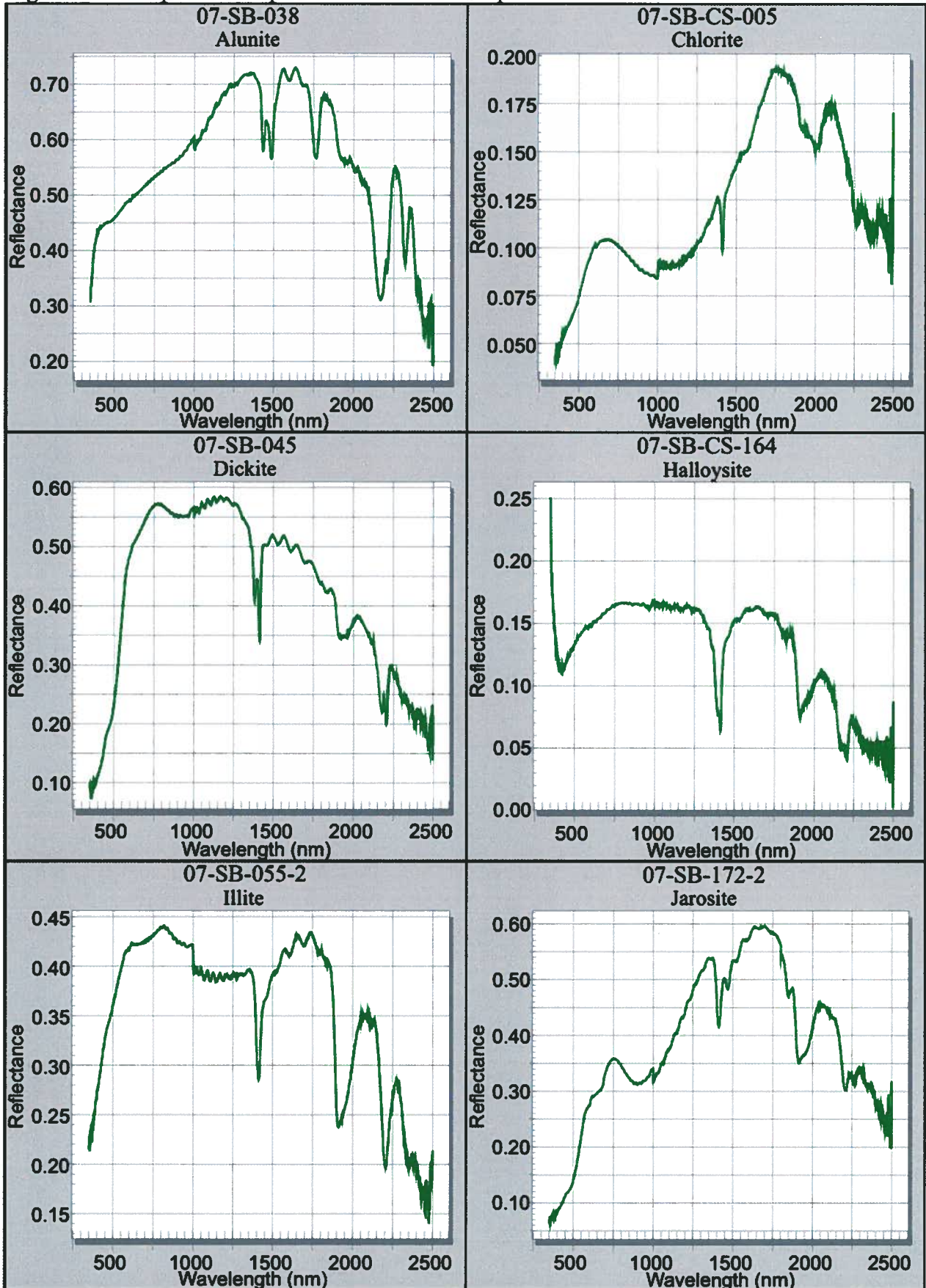
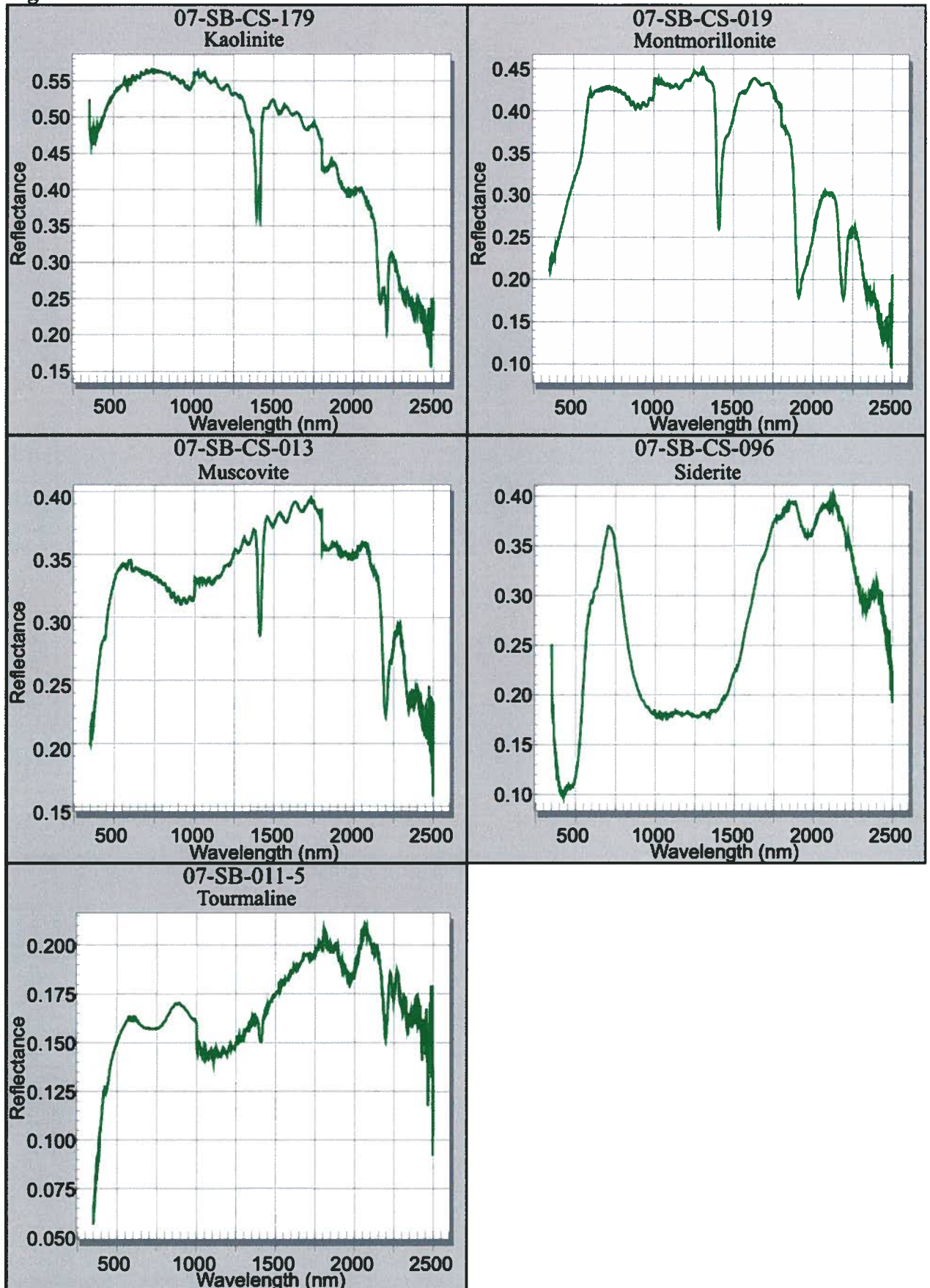


Figure A.1 Cont.



## **Appendix B: Geochronological Data**

## B1. $^{40}\text{Ar}$ - $^{39}\text{Ar}$ Geochronology

Mineral separates from 20 separate samples were hand-picked, washed in acetone, dried, wrapped in aluminum foil and stacked in an irradiation capsule with similar-aged samples and neutron flux monitors (Fish Canyon Tuff sanidine (FCs), 28.02 Ma (Renne et al., 1998)).

The samples were irradiated on January 4 through January 6, 2007 at the McMaster Nuclear Reactor in Hamilton, Ontario, for 90 MWH, with a neutron flux of approximately  $6 \times 10^{13}$  neutrons/cm<sup>2</sup>/s. Analyses (n=48) of 16 neutron flux monitor positions produced errors of <0.5% in the J value.

The samples were analyzed at the Noble Gas Laboratory, Pacific Centre for Isotopic and Geochemical Research (PCIGR), University of British Columbia, Vancouver, BC, Canada. The mineral separates were step-heated at incrementally higher powers in the defocused beam of a 10W CO<sub>2</sub> laser (New Wave Research MIR10) until fused. The gas evolved from each step was analyzed by a VG5400 mass spectrometer equipped with an ion-counting electron multiplier. All measurements were corrected for total system blank, mass spectrometer sensitivity, mass discrimination, radioactive decay during and subsequent to irradiation, as well as interfering Ar from atmospheric contamination and the irradiation of Ca, Cl and K (Isotope production ratios:  $(^{40}\text{Ar}/^{39}\text{Ar})_{\text{K}} = 0.0302 \pm 0.00006$ ,  $(^{37}\text{Ar}/^{39}\text{Ar})_{\text{Ca}} = 1416.4 \pm 0.5$ ,  $(^{36}\text{Ar}/^{39}\text{Ar})_{\text{Ca}} = 0.3952 \pm 0.0004$ ,  $\text{Ca}/\text{K} = 1.83 \pm 0.01$  ( $^{37}\text{Ar}_{\text{Ca}}/^{39}\text{Ar}_{\text{K}}$ )).

Ages were determined by plateau (spectrum) and inverse correlation plots using Isoplot ver.3.09 (Ludwig, 2003). Errors are quoted at the 2-sigma (95% confidence) level and are propagated from all sources except mass spectrometer sensitivity and age of the flux monitor.

The results are summarized in Table 2.1 and 3.2 and plateau age plots are shown in Figure 2.13 and 3.12.

**Table B.1**  $^{40}\text{Ar}$ - $^{39}\text{Ar}$  geochronological data  
Laser<sup>1</sup>  
Power

(%)	Isotope Ratios							Age $\pm 2\sigma$		
	$^{40}\text{Ar}/^{39}\text{Ar}$	$^{38}\text{Ar}/^{39}\text{Ar}$	$^{37}\text{Ar}/^{39}\text{Ar}$	$^{36}\text{Ar}/^{39}\text{Ar}$	Ca/K	Cl/K	$\%^{40}\text{Ar}$		$\%^{39}\text{Ar}$	$^{40}\text{Ar}^*/^{39}\text{ArK}$
06-SB-025-1 Biotite, $J = 0.010126 \pm 0.000008$ ; volume $^{39}\text{ArK} = 467.87$ ; integrated age = $84.23 \pm 0.58$ ( $2\sigma$ )										
2	11.883 $\pm$ 0.009	0.048 $\pm$ 0.065	0.050 $\pm$ 0.068	0.032 $\pm$ 0.069	0.316	0.007	71.09	0.87	3.045 $\pm$ 0.648	54.78 $\pm$ 11.49
2.3	4.354 0.016	0.027 0.073	0.044 0.040	0.006 0.059	0.846	0.003	32.2	4.09	2.735 0.117	49.28 2.08
2.6	5.755 0.020	0.017 0.052	0.190 0.021	0.004 0.041	4.42	0	13.04	16.12	4.916 0.116	87.64 2.02
2.8	5.314 0.004	0.014 0.024	0.003 0.049	0.001 0.074	0.041	0	4.66	26.81	4.990 0.031	88.92 0.55
3	5.664 0.004	0.016 0.034	0.003 0.054	0.002 0.042	0.029	0	9.8	15.39	5.006 0.036	89.22 0.63
3.2	7.237 0.006	0.022 0.028	0.009 0.070	0.008 0.046	0.074	0.002	29.24	5.79	4.949 0.111	88.22 1.94
3.4	6.346 0.006	0.024 0.047	0.012 0.060	0.006 0.061	0.145	0.002	24.84	5.54	4.583 0.117	81.85 2.04
3.8	5.849 0.009	0.033 0.021	0.044 0.028	0.007 0.046	0.926	0.004	32.13	7.95	3.841 0.104	68.84 1.83
4.5	6.165 0.020	0.022 0.041	0.089 0.025	0.005 0.028	2.045	0.002	20.95	17.42	4.790 0.116	85.44 2.03
06-SB-025-1 Illite, $J = 0.010122 \pm 0.000008$ ; volume $^{39}\text{ArK} = 1410.67$ ; integrated age = $85.64 \pm 0.46$ ( $2\sigma$ )										
2	16.040 $\pm$ 0.007	0.065 $\pm$ 0.040	0.021 $\pm$ 0.051	0.045 $\pm$ 0.025	0.094	0.01	80.36	0.62	3.004 $\pm$ 0.319	54.04 $\pm$ 5.65
2.3	7.413 0.006	0.030 0.027	0.011 0.045	0.013 0.025	0.199	0.003	50.61	3.98	3.581 0.099	64.23 1.75
2.5	5.014 0.016	0.016 0.027	0.026 0.037	0.002 0.057	0.592	0	12.02	8.68	4.338 0.083	77.53 1.46
2.7	5.147 0.013	0.013 0.040	0.011 0.037	0.001 0.098	0.201	0	2.69	4.67	4.895 0.070	87.24 1.22
3	5.013 0.014	0.013 0.026	0.014 0.032	0.001 0.062	0.318	0	3.06	16.66	4.801 0.070	85.60 1.21
3.2	5.118 0.012	0.013 0.040	0.010 0.029	0.000 0.135	0.21	0	1.17	9.6	4.983 0.062	88.77 1.09
3.4	5.065 0.012	0.012 0.027	0.005 0.037	0.000 0.109	0.109	0	0.79	14.06	4.961 0.063	88.39 1.09
3.6	5.109 0.018	0.013 0.031	0.002 0.062	0.000 0.098	0.032	0	1.45	16.34	4.974 0.091	88.62 1.59
3.8	5.016 0.014	0.013 0.025	0.002 0.037	0.000 0.095	0.038	0	1.07	15.92	4.902 0.070	87.36 1.21
4	5.110 0.004	0.013 0.023	0.004 0.035	0.001 0.094	0.057	0	1.79	9.45	4.943 0.027	88.07 0.46
06-SB-030 Biotite, $J = 0.010103 \pm 0.000006$ ; volume $^{39}\text{ArK} = 828.97$ ; integrated age = $88.69 \pm 1.29$ ( $2\sigma$ )										
2	52.980 $\pm$ 0.009	0.075 $\pm$ 0.048	0.075 $\pm$ 0.054	0.176 $\pm$ 0.029	0.743	0.006	95.84	0.34	2.016 $\pm$ 1.438	36.38 $\pm$ 25.69
2.3	77.207 0.012	0.070 0.054	0.053 0.048	0.252 0.024	0.951	0.002	96.08	1.27	2.953 1.779	53.04 31.48
2.6	53.253 0.014	0.050 0.033	0.082 0.026	0.170 0.021	1.766	0.001	93.99	3.64	3.148 1.029	56.48 18.18
2.9	15.163 0.026	0.023 0.034	0.204 0.029	0.036 0.033	4.574	0	68.56	7.13	4.681 0.408	83.37 7.10

3.1	8.207	0.030	0.017	0.057	0.192	0.032	0.012	0.041	4.288	0	37.85	7.93	4.971	0.237	88.40	4.11
3.3	6.548	0.031	0.015	0.044	0.148	0.035	0.005	0.041	3.377	0	18.89	8.48	5.158	0.192	91.64	3.32
3.5	6.786	0.029	0.016	0.039	0.105	0.032	0.006	0.040	2.382	0	22.42	10.2	5.134	0.190	91.23	3.29
3.7	6.037	0.023	0.014	0.025	0.030	0.024	0.003	0.034	0.687	0	13.3	23.54	5.150	0.131	91.51	2.27
3.9	5.811	0.025	0.014	0.035	0.028	0.028	0.003	0.032	0.632	0	10.73	16.04	5.079	0.140	90.28	2.42
4.1	5.952	0.011	0.015	0.031	0.030	0.032	0.003	0.058	0.644	0	10.32	9.06	5.174	0.076	91.93	1.31
4.3	6.118	0.010	0.018	0.024	0.049	0.027	0.003	0.069	1.08	0.001	11.06	5.71	5.207	0.088	92.50	1.52
4.7	6.134	0.005	0.020	0.032	0.031	0.027	0.003	0.042	0.674	0.001	11.88	6.66	5.200	0.051	92.37	0.89

06-SB-030 Muscovite, J = 0.010098±0.000006; volume <sup>39</sup>Ar<sub>K</sub> = 264.82; integrated age = 90.59±2.75 (2σ)

2	314.293	±0.009	0.214	±0.028	0.055	±0.063	1.073	±0.019	0.83	0	100.99	2.27	-3.125	±5.409	-57.85	±101.75
2.3	33.545	0.005	0.033	0.027	0.037	0.029	0.098	0.017	0.787	0	86.04	16.95	4.613	0.482	82.15	8.40
2.6	8.788	0.011	0.016	0.043	0.049	0.022	0.012	0.034	1.084	0	36.33	21.45	5.440	0.141	96.48	2.43
2.8	8.678	0.005	0.015	0.052	0.034	0.028	0.011	0.023	0.724	0	34.27	16.85	5.511	0.081	97.70	1.39
3.1	9.058	0.005	0.016	0.047	0.030	0.029	0.012	0.029	0.644	0	37.7	15.83	5.449	0.110	96.63	1.91
3.4	6.349	0.004	0.014	0.027	0.028	0.031	0.003	0.067	0.604	0	10.97	18.54	5.423	0.071	96.19	1.22
3.7	6.319	0.006	0.015	0.084	0.051	0.032	0.004	0.069	1.066	0	9.37	8.12	5.246	0.091	93.12	1.58

06-SB-082-4 Illite, J = 0.010117±0.000008; volume <sup>39</sup>Ar<sub>K</sub> = 3738.87; integrated age = 60.54±0.13 (2σ)

2	4.588	±0.005	0.017	±0.043	0.019	±0.033	0.006	±0.058	0.298	0	37.05	0.79	2.746	±0.111	49.44	±1.97
2.2	3.709	0.005	0.018	0.041	0.017	0.039	0.003	0.046	0.344	0.001	19.4	1.57	2.885	0.041	51.90	0.72
2.5	3.607	0.006	0.016	0.021	0.014	0.020	0.001	0.027	0.312	0	8.3	4.51	3.245	0.023	58.27	0.41
2.7	3.671	0.005	0.013	0.015	0.011	0.022	0.001	0.046	0.237	0	3.77	7.9	3.481	0.020	62.44	0.34
2.9	3.631	0.005	0.013	0.017	0.010	0.017	0.000	0.051	0.231	0	2.63	8.97	3.485	0.019	62.52	0.34
3.1	3.516	0.006	0.013	0.014	0.009	0.022	0.000	0.062	0.211	0	2.35	10.7	3.385	0.021	60.75	0.36
3.3	3.488	0.005	0.013	0.014	0.007	0.019	0.000	0.048	0.17	0	1.88	12.69	3.376	0.018	60.60	0.32
3.5	3.498	0.007	0.013	0.016	0.008	0.023	0.000	0.079	0.172	0	2.26	11.93	3.373	0.026	60.53	0.46
3.7	3.487	0.005	0.013	0.014	0.007	0.013	0.000	0.045	0.168	0	2.28	15.51	3.364	0.017	60.38	0.29
3.9	3.496	0.004	0.013	0.020	0.007	0.021	0.000	0.070	0.162	0	2.14	10.81	3.373	0.016	60.54	0.29
4.1	3.495	0.005	0.014	0.019	0.009	0.025	0.000	0.097	0.203	0	1.85	7.21	3.376	0.019	60.59	0.33
4.3	3.482	0.005	0.013	0.014	0.009	0.019	0.000	0.082	0.197	0	1.78	7.4	3.367	0.018	60.43	0.32

06-SB-119 Hornblende, J = 0.010108±0.000006; volume <sup>39</sup>Ar<sub>K</sub> = 278.12; integrated age = 21.96±0.66 (2σ)

2	41.936	±0.013	0.094	±0.077	0.135	±0.053	0.145	±0.041	1.877	0.012	98.34	0.81	0.587	±1.726	10.68	±31.29
---	--------	--------	-------	--------	-------	--------	-------	--------	-------	-------	-------	------	-------	--------	-------	--------

2.2	7.413 0.012	0.032 0.100	0.034 0.064	0.022 0.088	0.353	0.003	73.72	2.28	1.479 0.563	26.77 10.11
2.5	3.542 0.008	0.027 0.053	0.023 0.053	0.009 0.041	0.343	0.003	56.99	5.76	1.208 0.105	21.90 1.88
2.8	4.503 0.005	0.056 0.035	0.028 0.036	0.012 0.039	0.538	0.009	70.94	10.11	1.168 0.134	21.17 2.42
3.1	2.605 0.011	0.320 0.018	0.228 0.021	0.006 0.042	5.088	0.07	45.67	12.99	1.227 0.073	22.23 1.31
3.4	3.011 0.010	0.548 0.013	0.570 0.016	0.008 0.029	12.885	0.123	54.4	20.49	1.263 0.070	22.88 1.26
3.7	2.003 0.014	0.657 0.019	0.688 0.020	0.005 0.033	15.589	0.149	33.74	32.23	1.225 0.053	22.19 0.96
4	1.893 0.031	0.579 0.038	0.480 0.037	0.005 0.074	10.728	0.13	11.19	6.97	1.170 0.113	21.21 2.03
4.5	1.800 0.037	0.522 0.041	0.342 0.041	0.004 0.073	7.63	0.117	16.94	8.36	1.090 0.101	19.76 1.82

06-SB-243 Hornblende, J = 0.010138±0.000010; volume <sup>39</sup>Ar<sub>K</sub> = 152.72; integrated age = 61.83±5.47 (2σ)

2	730.212±0.011	0.748±0.067	0.809±0.051	2.496±0.022	9.291	0.061	100.77	0.33	-5.667±14.706	-106.75±285.37
2.3	225.179 0.015	0.207 0.039	0.387 0.029	0.762 0.023	7.551	0.011	100	3.21	-0.028 4.966	-0.52 90.85
2.5	75.350 0.026	0.087 0.049	0.383 0.035	0.247 0.031	7.719	0.006	96.46	4.55	2.626 2.037	47.40 36.29
2.7	96.383 0.032	0.092 0.047	0.318 0.042	0.316 0.036	6.445	0.004	96.67	6.07	3.174 3.172	57.14 56.22
2.9	38.019 0.031	0.046 0.080	0.305 0.037	0.118 0.035	6.323	0.002	90.72	8.99	3.480 1.218	62.54 21.52
3.1	16.365 0.014	0.027 0.054	0.299 0.020	0.044 0.033	6.453	0.001	76.74	12.57	3.740 0.440	67.14 7.75
3.3	5.169 0.012	0.041 0.035	0.311 0.016	0.007 0.048	6.757	0.006	27.36	10.53	3.578 0.105	64.29 1.86
3.5	5.289 0.007	0.061 0.030	0.283 0.020	0.007 0.071	6.093	0.01	28.43	9.59	3.595 0.150	64.59 2.64
3.7	4.864 0.007	0.061 0.019	0.264 0.017	0.005 0.041	5.818	0.011	23.35	19.89	3.617 0.069	64.97 1.22
3.9	6.811 0.009	0.070 0.058	0.343 0.021	0.012 0.058	7.325	0.012	42.87	6.83	3.684 0.211	66.15 3.72
4.3	7.243 0.010	0.074 0.026	0.597 0.022	0.014 0.035	13.295	0.013	46.73	11.33	3.740 0.154	67.14 2.72
4.8	6.741 0.007	0.050 0.052	0.904 0.017	0.013 0.080	20.084	0.008	36.49	6.1	4.050 0.305	72.60 5.36

07-SB-006-2 Hornblende, J = 0.005281±0.000012; volume <sup>39</sup>Ar<sub>K</sub> = 11.22; integrated age = 61.31±8.57 (2σ)

2	98.9836±0.0452	0.1408±0.1097	3.4691±0.3219	0.3122±0.0649	10.073	0.014	91.2	7.65	8.249±5.118	76.93±46.73
2.2	94.7466 0.0239	0.2117 0.0420	10.6679 0.1100	0.3015 0.0326	31.19	0.032	91.53	11.02	7.776 2.935	72.60 26.86
2.4	75.0539 0.0294	0.0761 0.2175	19.3985 0.0359	0.2465 0.0492	57.337	0.002	92.21	9.94	5.611 3.458	52.68 31.99
2.6	51.6429 0.0239	0.0664 0.1545	14.1676 0.0814	0.1584 0.0365	41.513	0.004	85.25	15.32	7.281 1.827	68.07 16.77
2.8	32.0338 0.0386	0.0536 0.1332	1.9955 1.3590	0.0923 0.1234	5.772	0.004	76.82	8.26	6.145 3.382	57.62 31.21
3	20.0191 0.0160	0.0467 0.2724	1.0684 0.9435	0.0505 0.1251	3.136	0.004	63.73	12.95	5.950 1.874	55.82 17.31
3.3	22.4588 0.0145	0.1264 0.1204	2.0005 0.4880	0.0619 0.2088	5.895	0.022	70.61	10.59	5.311 3.848	49.90 35.66
3.6	15.7164 0.0218	0.0811 0.1241	2.0538 0.5198	0.0365 0.1711	6.051	0.013	48.02	11.34	6.033 1.862	56.58 17.19
3.9	21.5293 0.0389	0.0760 0.2486	2.5406 0.6788	0.0547 0.1393	7.509	0.011	55.68	7.82	6.937 2.248	64.91 20.66
4.5	27.7321 0.0204	0.0672 0.1880	0.2590 7.3508	0.0792 0.1294	0.733	0.007	66.8	5.11	6.232 3.053	58.42 28.16

07-SB-008 Biotite, J = 0.005279±0.000010; volume <sup>39</sup>Ar<sub>K</sub> = 313.21; integrated age = 86.87±0.54 (2σ)

2	65.0406±0.0504	0.2466±0.2248	0.0608±0.6091	0.2453±0.1677	0.126	0.041	109.51	0.12	-5.055±11.884	-48.79±116.28
2.2	47.5998 0.0260	0.2013 0.2047	0.0614 0.5798	0.1464 0.1259	0.152	0.036	86.05	0.24	5.688 5.425	53.38 50.16
2.4	38.0111 0.0232	0.2178 0.1123	0.0441 0.4461	0.1161 0.0795	0.111	0.041	86.55	0.38	4.520 2.658	42.54 24.72
2.6	22.7371 0.0298	0.1965 0.0549	0.0096 0.7995	0.0510 0.0507	0.023	0.04	63.14	1.3	7.883 0.780	73.56 7.13
2.8	14.5317 0.0101	0.1808 0.0284	0.0060 0.2827	0.0185 0.0483	0.016	0.038	35.57	4.58	9.093 0.284	84.58 2.58
3	10.9922 0.0056	0.1713 0.0245	0.0041 0.0923	0.0056 0.0845	0.011	0.036	12.58	6.92	9.361 0.150	87.02 1.36
3.2	11.0318 0.0060	0.1722 0.0239	0.0046 0.1787	0.0055 0.0702	0.013	0.036	12.92	9.53	9.416 0.128	87.52 1.16
3.4	13.2418 0.0071	0.1681 0.0360	0.0040 0.0694	0.0133 0.0534	0.01	0.035	27.56	5.26	9.325 0.221	86.70 2.01
3.6	13.8467 0.0062	0.1830 0.0128	0.0043 0.0403	0.0149 0.0211	0.012	0.038	31.41	23.88	9.411 0.110	87.47 1.00
3.8	11.4494 0.0051	0.1637 0.0172	0.0038 0.1694	0.0065 0.0236	0.011	0.034	15.75	15.86	9.520 0.069	88.46 0.63
4	11.5726 0.0112	0.1638 0.0228	0.0034 0.1419	0.0068 0.0857	0.009	0.034	16.3	13.42	9.544 0.207	88.68 1.88
4.2	11.2074 0.0059	0.1638 0.0204	0.0043 0.1091	0.0059 0.0487	0.012	0.034	13.89	9.66	9.464 0.103	87.96 0.94
4.4	12.1022 0.0056	0.1615 0.0173	0.0067 0.0938	0.0098 0.0289	0.018	0.034	22.51	8.84	9.194 0.100	85.50 0.91

07-SB-016 Biotite, J = 0.005278±0.000010; volume <sup>39</sup>Ar<sub>K</sub> = 65.29; integrated age = 55.49±1.71 (2σ)

2	18.7040±0.0146	0.0494±0.0905	0.6612±0.0483	0.0410±0.0716	1.846	0.005	52.23	4.26	8.039±0.873	74.97± 7.98
2.2	9.8517 0.0219	0.0628 0.0462	0.9219 0.0274	0.0151 0.0740	2.595	0.01	37.25	16.08	5.838 0.368	54.75 3.40
2.4	8.8814 0.0224	0.0593 0.0424	1.3897 0.0278	0.0126 0.0437	3.917	0.01	34.27	22.64	5.576 0.223	52.33 2.06
2.6	9.1457 0.0233	0.0647 0.0411	2.1199 0.0268	0.0129 0.0532	5.983	0.011	34.23	26.87	5.796 0.268	54.36 2.48
2.8	7.3584 0.0340	0.0728 0.0704	0.4957 0.0347	0.0079 0.1154	1.387	0.013	13.26	10.18	5.655 0.354	53.06 3.27
3	7.5753 0.0349	0.0696 0.0807	1.2956 0.0397	0.0078 0.1554	3.651	0.012	8.67	9.06	6.069 0.436	56.89 4.02
3.3	8.4599 0.0268	0.1488 0.0602	2.9906 0.0304	0.0115 0.3439	8.477	0.03	7.09	5.61	6.500 1.202	60.85 11.06
3.6	9.4975 0.0240	0.1839 0.0915	4.2771 0.0372	0.0190 0.6221	12.215	0.036	-1.26	2.73	6.616 3.571	61.92 32.86
4	10.1023 0.0335	0.5759 0.0636	4.9073 0.0378	0.0249 0.3677	14.042	0.128	18.29	2.57	5.687 2.771	53.36 25.62

07-SB-020-2 Illite, J = 0.005277±0.000008; volume <sup>39</sup>Ar<sub>K</sub> = 48.17; integrated age = 91.38±1.37 (2σ)

2	93.4472±0.0159	0.3481±0.0850	1.2744±0.0380	0.2922±0.0383	3.674	0.064	90.76	2.02	8.187±3.072	76.31±28.04
2.2	31.3261 0.0199	0.2259 0.0860	0.7948 0.0433	0.0669 0.0535	2.283	0.045	56.03	3.28	12.343 1.040	113.84 9.29
2.4	15.8354 0.0197	0.1282 0.0696	0.7097 0.0257	0.0183 0.1089	2.038	0.025	24.59	7.42	10.818 0.629	100.16 5.67
2.6	13.7309 0.0114	0.0421 0.0654	0.2760 0.0238	0.0138 0.0769	0.791	0.006	24.26	14.95	9.818 0.334	91.12 3.02
2.8	11.8595 0.0054	0.0400 0.0521	0.1515 0.0215	0.0085 0.0587	0.434	0.006	17.89	29.43	9.399 0.158	87.33 1.43
3	10.3071 0.0101	0.0336 0.0236	0.1575 0.0348	0.0032 0.1525	0.45	0.004	2.55	19.79	9.474 0.176	88.01 1.59

3.2	11.4531 0.0104	0.0346 0.1285	0.1967 0.0255	0.0070 0.2105	0.562	0.004	9.37	12.49	9.558 0.450	88.77 4.08
3.4	13.1022 0.0066	0.0545 0.1163	0.5003 0.0225	0.0095 0.3135	1.434	0.009	8.28	7.4	10.646 0.886	98.61 7.99
4	31.3748 0.0182	0.2511 0.0988	2.5906 0.0327	0.0694 0.0673	7.486	0.051	57.66	3.21	11.898 1.427	109.85 12.78

07-SB-023-3 Illite, J = 0.005282±0.000012; volume <sup>39</sup>Ar<sub>K</sub> = 670.67; integrated age = 89.19±0.41 (2σ)

2	14.6575±0.0075	0.0234±0.1538	0.0010±1.5094	0.0198±0.0894	0	0.001	34.04	1.27	9.233±0.528	85.90±4.80
2.2	10.3988 0.0053	0.0153 0.0559	0.0021 0.5957	0.0035 0.0821	0.003	0	7.48	5.34	9.447 0.099	87.85 0.90
2.4	9.8428 0.0042	0.0134 0.0515	0.0010 0.5592	0.0010 0.4599	0.001	0	1.53	9.81	9.575 0.140	89.01 1.27
2.6	9.7696 0.0043	0.0139 0.0485	0.0003 0.3058	0.0004 0.7563	0	0	0.36	16.66	9.649 0.099	89.68 0.90
2.7	9.8039 0.0047	0.0137 0.0361	0.0009 0.2420	0.0008 0.1808	0.001	0	0.88	9.07	9.593 0.064	89.17 0.58
2.8	9.9669 0.0162	0.0231 0.2093	0.0012 0.2227	0.0018 0.1882	0	0.002	2.39	4.73	9.529 0.186	88.59 1.69
2.9	9.8188 0.0046	0.0146 0.0324	0.0008 0.3787	0.0006 0.4714	0.001	0	0.82	15.02	9.648 0.093	89.67 0.84
3	9.7757 0.0047	0.0147 0.0940	0.0012 0.3260	0.0007 1.1160	0.002	0	0.56	9.76	9.603 0.224	89.26 2.03
3.1	9.7650 0.0044	0.0138 0.0420	0.0009 0.2919	0.0005 0.5378	0.001	0	0.15	11.3	9.643 0.086	89.62 0.78
3.2	9.7743 0.0045	0.0152 0.0585	0.0013 0.3316	0.0008 0.3901	0.002	0	0.5	7.04	9.576 0.106	89.02 0.96
3.1	9.8141 0.0047	0.0151 0.0492	0.0016 0.5425	0.0010 0.2429	0.002	0	0.65	5.83	9.579 0.087	89.04 0.79
3.6	9.9585 0.0050	0.0149 0.0854	0.0026 0.3596	0.0019 0.0817	0.004	0	2.3	4.19	9.508 0.068	88.40 0.61

07-SB-073 Biotite, J = 0.005277±0.000008; volume <sup>39</sup>Ar<sub>K</sub> = 637.42; integrated age = 86.18±0.28 (2σ)

2	24.9631±0.0115	0.1677±0.0684	0.5206±0.0315	0.0777±0.0453	1.565	0.031	86.3	0.2	2.844±1.035	26.88±9.71
2.2	11.3218 0.0255	0.2546 0.0388	0.4210 0.0440	0.0330 0.0598	1.256	0.054	82.35	0.83	1.793 0.611	16.99 5.77
2.4	8.6646 0.0160	0.2193 0.0290	0.1245 0.0342	0.0178 0.0301	0.371	0.046	59.04	3.72	3.426 0.184	32.32 1.72
2.6	9.1234 0.0145	0.2152 0.0155	0.0288 0.0394	0.0079 0.0405	0.085	0.046	22.87	3.32	6.811 0.152	63.70 1.40
2.8	9.8421 0.0089	0.2283 0.0205	0.0219 0.0286	0.0053 0.0407	0.065	0.049	14.79	7.89	8.261 0.103	76.98 0.94
3	10.2304 0.0064	0.2408 0.0157	0.0164 0.0429	0.0028 0.0463	0.049	0.052	6.66	7.41	9.408 0.073	87.41 0.66
3.2	10.2246 0.0100	0.2437 0.0134	0.0239 0.0414	0.0013 0.0514	0.071	0.053	2.99	12.71	9.818 0.103	91.13 0.93
3.4	10.2077 0.0053	0.2436 0.0137	0.0307 0.0193	0.0013 0.0742	0.091	0.053	2.87	12.96	9.815 0.061	91.10 0.55
3.6	10.1654 0.0068	0.2429 0.0148	0.0364 0.0374	0.0009 0.1200	0.108	0.053	1.71	12.17	9.887 0.076	91.75 0.68
3.8	10.1328 0.0052	0.2417 0.0121	0.0363 0.0175	0.0008 0.1759	0.108	0.052	1.42	11.36	9.880 0.067	91.69 0.61
4.2	10.0928 0.0030	0.2417 0.0152	0.0298 0.0253	0.0007 0.0661	0.089	0.052	1.67	27.43	9.857 0.034	91.48 0.31

07-SB-093 Hornblende, J = 0.005276±0.000008; volume <sup>39</sup>Ar<sub>K</sub> = 272.84; integrated age = 45.39±0.94 (2σ)

2	67.8668±0.0484	0.1873±0.2676	1.9447±0.9790	0.2140±0.1071	5.734	0.03	90.8	0.37	5.792±6.235	54.31±57.59
2.2	68.9592 0.0164	0.1522 0.0800	1.1779 0.6011	0.2141 0.0972	3.457	0.022	90.7	0.77	6.180 6.095	57.89 56.18

2.4	33.3566±0.0137	0.1242±0.0521	1.2313±0.3234	0.0971±0.0475	3.612	0.021	84.54	1.68	4.960±1.321	46.60±12.25
2.6	21.4287±0.0130	0.0799±0.1028	0.4365±0.2445	0.0538±0.0657	1.277	0.013	72.37	2.47	5.678±1.033	53.25±9.54
2.9	14.6488±0.0180	0.0449±0.3287	0.2597±1.7357	0.0384±0.2654	0.757	0.005	72.84	1.4	3.576±3.009	33.72±28.11
3.2	10.2782±0.0071	0.0848±0.0983	0.7521±2.2202	0.0204±0.1623	2.203	0.015	52.52	2.45	4.478±0.979	42.13±9.10
3.5	9.5467±0.0183	0.1145±0.1005	1.0681±0.3279	0.0177±0.2642	3.132	0.022	43.13	1.52	4.682±1.389	44.02±12.90
3.8	8.0170±0.0067	0.4479±0.0192	4.3420±0.0253	0.0137±0.2749	12.782	0.1	37.8	3.63	4.646±1.117	43.69±10.38
4.1	5.5745±0.0137	0.5257±0.0181	5.9566±0.0189	0.0052±0.0284	17.557	0.118	12.27	32.49	4.837±0.082	45.46±0.76
4.4	5.0916±0.0134	0.4855±0.0199	6.1458±0.0182	0.0037±0.0321	18.118	0.109	4.42	40.29	4.820±0.075	45.30±0.70
4.7	5.2462±0.0086	0.4276±0.0135	5.9902±0.0152	0.0042±0.0581	17.659	0.096	5.34	12.93	4.823±0.085	45.34±0.79

07-SB-102-1 Illite, J = 0.005282±0.000012; volume <sup>39</sup>Ar<sub>K</sub> = 1637.37; integrated age = 49.11±0.31 (2σ)

2	8.4678±0.0064	0.0246±0.0619	0.0140±1.0925	0.0095±0.0274	0.04	0.002	32.28	3.37	5.635±0.088	52.91±0.81
2.2	6.5631±0.0093	0.0149±0.0298	0.0108±0.8802	0.0031±0.0341	0.032	0	13.62	11.73	5.611±0.065	52.69±0.60
2.4	5.7502±0.0129	0.0133±0.0154	0.0113±0.2460	0.0009±0.0407	0.033	0	4.44	21.06	5.445±0.073	51.16±0.68
2.5	5.6127±0.0132	0.0130±0.0275	0.0156±0.5938	0.0008±0.0445	0.046	0	3.78	11.2	5.338±0.073	50.17±0.68
2.6	5.4434±0.0157	0.0128±0.0350	0.0159±0.2833	0.0007±0.0658	0.047	0	2.96	10.54	5.218±0.085	49.05±0.79
2.7	5.4018±0.0083	0.0145±0.1634	0.0092±1.7713	0.0017±0.6166	0.027	0	8.36	5.61	4.863±0.321	45.76±2.98
2.9	5.3918±0.0189	0.0134±0.0511	0.0192±0.4599	0.0009±0.0894	0.057	0	4.43	10.47	5.089±0.103	47.86±0.95
3.1	5.5045±0.0057	0.0134±0.0509	0.0152±0.5594	0.0017±0.0576	0.045	0	8.27	6.81	4.971±0.042	46.76±0.39
3.3	5.4801±0.0058	0.0143±0.0169	0.0056±1.0242	0.0019±0.0914	0.016	0	9.15	5.71	4.893±0.060	46.03±0.55
3.5	5.4869±0.0047	0.0150±0.0364	0.0247±0.2524	0.0019±0.1271	0.073	0	9.2	5.85	4.898±0.076	46.08±0.71
3.7	5.6066±0.0057	0.0158±0.0459	0.0063±1.5104	0.0024±0.0782	0.018	0	11.52	4.54	4.864±0.064	45.76±0.59
4	6.1604±0.0052	0.0171±0.0732	0.0054±2.7789	0.0044±0.0571	0.015	0	19.27	3.1	4.855±0.078	45.68±0.73

07-SB-136-7 Illite, J = 0.005273±0.000008; volume <sup>39</sup>Ar<sub>K</sub> = 419.52; integrated age = 84.20±0.52 (2σ)

2	15.2708±0.0158	0.0252±0.2489	1.5961±0.0245	0.0280±0.1005	4.506	0	39.72	0.84	8.308±0.859	77.36±7.83
2.2	9.9801±0.0071	0.0134±0.0912	1.8382±0.0159	0.0038±0.0556	5.184	0	6.7	9.47	9.169±0.092	85.18±0.84
2.4	9.3743±0.0067	0.0130±0.0616	0.3922±0.0214	0.0011±0.1903	1.103	0	0.92	12.14	9.151±0.087	85.02±0.79
2.6	9.2479±0.0068	0.0131±0.0716	0.2427±0.0171	0.0006±0.1146	0.683	0	0.72	29.43	9.103±0.066	84.58±0.60
2.8	9.1487±0.0058	0.0137±0.0675	0.0655±0.0257	0.0004±0.6063	0.183	0	0.01	19.35	9.045±0.093	84.06±0.84
3	9.1013±0.0053	0.0131±0.0693	0.0673±0.0359	0.0004±1.5185	0.19	0	0.05	19.36	8.995±0.200	83.60±1.82
3.2	9.3293±0.0066	0.0119±0.0809	0.0195±0.1039	0.0013±0.8924	0.052	-0.001	0.19	6.24	9.073±0.341	84.31±3.10
3.5	9.8155±0.0106	0.0151±0.2008	0.0525±0.1052	0.0049±0.2912	0.139	-0.001	4.11	2.07	8.793±0.437	81.77±3.97
3.9	10.4757±0.0147	0.0241±0.0985	0.1687±0.0426	0.0096±0.2343	0.462	0.001	8.53	1.1	8.504±0.680	79.14±6.19

07-SB-158 Biotite, J = 0.005273±0.000008; volume <sup>39</sup>Ar<sub>K</sub> = 63.99; integrated age = 81.10±2.39 (2σ)

2	157.1470±0.0807	0.9700±0.2105	3.1117±0.1038	0.5008±0.1534	9.834	0.202	71.9	0.2	41.030±24.677	353.34±193.00
2.2	339.2586±0.0199	1.1047±0.0733	2.9997±0.0474	1.1288±0.0426	8.801	0.204	95.5	0.59	15.641±13.522	142.97±118.83
2.4	27.2542±0.0110	0.6387±0.0315	1.9329±0.0206	0.0851±0.1014	5.469	0.14	85.09	4.1	3.764±2.582	35.45±24.09
2.6	13.9451±0.0224	0.3293±0.0829	0.5078±0.0354	0.0387±0.1040	1.414	0.07	70.74	5.5	3.620±1.199	34.12±11.19
2.8	19.6116±0.0102	0.2788±0.0297	0.3622±0.0534	0.0488±0.0735	1.003	0.058	66.23	6.3	6.169±1.063	57.75±9.79
3	11.6532±0.0116	0.2031±0.0575	0.1981±0.0375	0.0330±0.0607	0.549	0.042	78.74	13.45	2.317±0.588	21.90±5.53
3.2	12.6826±0.0103	0.2144±0.0193	0.3583±0.0265	0.0092±0.1574	1	0.045	12.45	12.26	10.490±0.445	97.13±4.02
3.4	12.0060±0.0101	0.2419±0.0255	0.7777±0.0192	0.0057±0.2363	2.186	0.052	3.69	12.43	10.902±0.418	100.84±3.76
3.6	12.3884±0.0081	0.6147±0.0202	2.2487±0.0152	0.0078±0.2900	6.35	0.138	10.09	17.8	10.715±0.679	99.16±6.11
3.8	12.4693±0.0119	0.8217±0.0190	4.5379±0.0168	0.0096±0.1669	12.851	0.187	12.98	20.83	10.525±0.496	97.44±4.47
4	13.1318±0.0156	0.4650±0.0258	5.3225±0.0211	0.0111±0.2223	15.136	0.103	3.34	6.54	11.524±0.766	106.42±6.87

07-SB-173-1 Illite, J = 0.005272±0.000008; volume <sup>39</sup>Ar<sub>K</sub> = 363.32; integrated age = 85.73±0.65 (2σ)

2	36.7505±0.0163	0.1628±0.0621	0.2199±0.0570	0.1008±0.0523	0.624	0.029	78.38	0.6	7.417±1.523	69.20±13.94
2.2	25.6034±0.0209	0.1047±0.1496	0.1524±0.0735	0.0554±0.2305	0.434	0.018	61.18	1.16	9.436±3.782	87.59±34.26
2.4	14.5419±0.0178	0.0388±0.0999	0.1082±0.0526	0.0197±0.0276	0.309	0.005	36.92	2.62	8.792±0.250	81.74±2.27
2.6	12.2837±0.0194	0.0289±0.0869	0.0761±0.0574	0.0105±0.0389	0.217	0.003	21.83	3.4	9.235±0.236	85.77±2.14
2.8	10.9056±0.0174	0.0221±0.0443	0.0518±0.0231	0.0049±0.0461	0.148	0.002	11.73	9.92	9.461±0.187	87.81±1.69
3	10.2788±0.0207	0.0181±0.0432	0.0405±0.0387	0.0028±0.0354	0.116	0.001	6.84	12.54	9.431±0.205	87.54±1.86
3.2	9.9001±0.0201	0.0185±0.0406	0.0307±0.0411	0.0018±0.0762	0.088	0.001	4.23	13.63	9.343±0.198	86.74±1.79
3.4	9.7225±0.0143	0.0161±0.0534	0.0276±0.0446	0.0018±0.1045	0.079	0	4.31	16.98	9.185±0.146	85.31±1.33
3.6	9.7415±0.0070	0.0167±0.0653	0.0252±0.0445	0.0020±0.1469	0.072	0.001	4.99	15.63	9.130±0.110	84.81±1.00
3.8	9.9442±0.0065	0.0184±0.0560	0.0310±0.0403	0.0026±0.0455	0.089	0.001	6.66	15.47	9.157±0.071	85.06±0.65
4	10.3018±0.0061	0.0187±0.0364	0.0380±0.0577	0.0040±0.0659	0.109	0.001	9.44	8.04	9.130±0.098	84.81±0.89

07-SB-CS-013 Muscovite, J = 0.005282±0.000012; volume <sup>39</sup>Ar<sub>K</sub> = 505.99; integrated age = 86.70±0.45 (2σ)

2	20.5739±0.0182	0.0534±0.0848	0.3704±0.0407	0.0459±0.0719	1.1	0.006	57.55	0.38	7.570±0.975	70.73±8.93
2.2	10.9467±0.0125	0.0186±0.0748	0.6394±0.0184	0.0059±0.0532	1.91	0.001	11.28	2.59	9.328±0.156	86.77±1.41
2.4	9.9001±0.0056	0.0178±0.0447	0.3009±0.0174	0.0020±0.0824	0.906	0.001	4.35	10.26	9.338±0.073	86.86±0.66
2.6	9.7285±0.0082	0.0156±0.0278	0.2809±0.0171	0.0013±0.0539	0.846	0	3.07	22.31	9.349±0.081	86.96±0.74
2.8	9.5358±0.0149	0.0150±0.0455	0.0890±0.0230	0.0006±0.0629	0.268	0	1.29	26.27	9.336±0.141	86.84±1.28

3	9.4962 0.0081	0.0145 0.0592	0.0077 0.0607	0.0007 0.1095	0.023	0	1.13	12.47	9.268 0.080	86.23 0.72
3.2	9.5343 0.0050	0.0149 0.0363	0.0105 0.0681	0.0007 0.0931	0.031	0	1.04	11	9.304 0.052	86.55 0.47
3.4	9.6054 0.0062	0.0148 0.0597	0.0083 0.0462	0.0010 0.1686	0.024	0	0.95	5.97	9.304 0.078	86.55 0.71
3.6	9.7391 0.0120	0.0166 0.1101	0.0081 0.0816	0.0012 0.2443	0.023	0	0.68	4.17	9.389 0.147	87.32 1.33
4	9.5949 0.0065	0.0144 0.0740	0.0181 0.0775	0.0009 0.1489	0.054	0	0.02	4.56	9.318 0.075	86.68 0.68

07-SB-CS-102 Biotite, J = -0.005281 ± 0.000012; volume  $^{39}\text{Ar}_K = 677.5$ ; integrated age =  $87.35 \pm 0.27$  ( $2\sigma$ )

2	58.9953 ± 0.0814	0.3215 ± 0.2919	0.6886 ± 0.1398	0.1893 ± 0.0946	2.003	0.06	82.07	0.04	7.238 ± 3.650	67.67 ± 33.50
2.2	14.1338 0.0298	0.1728 0.1407	0.6720 0.0510	0.0431 0.0535	1.966	0.034	79.49	0.22	2.159 0.600	20.45 5.65
2.4	13.1582 0.0131	0.1994 0.0480	3.6431 0.0194	0.0312 0.0426	10.728	0.041	59.87	0.55	4.700 0.395	44.23 3.68
2.6	13.8633 0.0098	0.2828 0.0245	0.9194 0.0168	0.0175 0.0670	2.694	0.061	33.08	1.46	8.897 0.361	82.83 3.29
2.8	10.1420 0.0049	0.2468 0.0186	0.0192 0.0475	0.0029 0.0516	0.056	0.053	7.02	6.22	9.277 0.064	86.29 0.59
3	9.6687 0.0051	0.2359 0.0160	0.0032 0.0792	0.0007 0.0929	0.009	0.051	1.29	10.84	9.436 0.053	87.73 0.48
3.2	9.5987 0.0046	0.2361 0.0118	0.0023 0.0413	0.0004 0.0658	0.006	0.051	0.54	13.97	9.453 0.045	87.89 0.41
3.4	9.6113 0.0042	0.2352 0.0150	0.0027 0.0885	0.0004 0.0813	0.008	0.051	0.52	16.6	9.477 0.042	88.10 0.38
3.6	9.6188 0.0044	0.2352 0.0115	0.0024 0.1005	0.0004 0.1365	0.007	0.051	0.55	15.77	9.479 0.046	88.12 0.42
3.8	9.6119 0.0043	0.2354 0.0097	0.0020 0.0613	0.0004 0.1330	0.006	0.051	0.7	20.6	9.469 0.045	88.03 0.40
4	9.5993 0.0042	0.2328 0.0139	0.0020 0.1120	0.0006 0.1802	0.006	0.05	0.56	8	9.411 0.052	87.51 0.47
4.2	9.6112 0.0052	0.2366 0.0178	0.0050 0.0571	0.0007 0.1163	0.015	0.051	0.38	5.75	9.402 0.056	87.43 0.50

<sup>1</sup> As measured by laser in % of full nominal power (10W)

## B2. U-Pb Geochronology

Laser ablation ICP-MS dating has recently been established as a routine procedure at the PCIGR. Zircons are separated from their host rocks using conventional mineral separation methods. Approximately 25 of the coarsest, clearest, most inclusion-free grains are selected from each sample, mounted in an epoxy puck along with several grains of internationally accepted the ~1100 Ma FC-1 standard zircon, and brought to a very high polish. The grains are examined using a stage-mounted cathodoluminescence unit, which makes it possible to detect the presence of altered zones or older inherited cores within the zircon. High-quality portions of each grain, free of alteration, inclusion, or cores, are selected for analysis. The surface of the mount is then washed for ~10 minutes with dilute nitric acid and rinsed in high purity water. Analyses are carried out using a New Wave 213 nm Nd-YAG laser coupled to a Thermo Finnigan Element2 high-resolution ICP-MS. Ablation takes place within a New Wave “Supercell” ablation chamber which is designed to achieve very high efficiency entrainment of aerosols into the carrier gas. Helium is used as the carrier gas for all experiments and gas flow rates, together with other parameters such as torch position, are optimized prior to beginning a series of analyses. A 25 micron spot with 40% laser power is used, making line scans rather than spot analyses in order to avoid within-run elemental fractions. Each analysis consists of a 7-second background measurement (laser off) followed by a ~28-second data acquisition period with the laser firing. A typical analytical session consists of four analyses of the standard zircon, followed by four analyses of unknown zircons, two standard analyses, four unknown analyses, etc., and finally four standard analyses. Data are reduced using the GLITTER software marketed by the GEMOC group at Macquarrie University in Sydney, Australia, which automatically subtracts background measurements, propagates all analytical errors, and calculates isotopic ratios and ages. The time resolved signal from each analysis is carefully examined, and portions of the signal that are interpreted to reflect the effects of post-crystallization Pb-loss and/or the presence of older inherited zircon cores are excluded from calculation of the final isotopic ratios. Interpreted crystallization ages are based on a weighted average of the calculated  $^{206}\text{Pb}/^{238}\text{U}$  ages for 8-20 individual analyses from each sample. Errors for the final interpreted age for each sample are given at the 2 sigma level using the method of Ludwig (2003). Results from this study are summarized in tables 2.1 and 3.2, Concordia plots are shown in figures 2.9 and 3.14.

**Table B2. U-Pb Laser Ablation geochronology data**

Sample no. & rock type	Fraction	Isotopic Compositions (1 $\sigma$ )			Isotopic Ages (1 $\sigma$ )		
		$^{207}\text{Pb}/^{206}\text{Pb}$	$^{207}\text{Pb}/^{235}\text{U}$	$^{206}\text{Pb}/^{238}\text{U}$	$^{207}\text{Pb}/^{206}\text{Pb}$	$^{207}\text{Pb}/^{235}\text{U}$	$^{206}\text{Pb}/^{238}\text{U}$
06-SB-	1	0.06748(0.01342)	0.1235(0.0244)	0.01375(0.00061)	852.7(366.27)	118.2(22.06)	88.1(3.87)
GEO-2	2	0.04072(0.01073)	0.07548(0.01986)	0.01392(0.00052)	0.1(260.98)	73.9(18.75)	89.1(3.3)
Tchaikazan	3	0.04865(0.00569)	0.09442(0.0112)	0.01467(0.00038)	131.2(254.2)	91.6(10.39)	93.9(2.44)
Rapids	4	0.04741(0.0019)	0.09263(0.00439)	0.01434(0.00021)	69.3(93.17)	90(4.08)	91.8(1.31)
pluton	5	0.05785(0.00884)	0.10877(0.01674)	0.01358(0.00046)	524(304.25)	104.8(15.33)	87(2.94)
	6	0.05686(0.00341)	0.10548(0.00699)	0.01363(0.00027)	485.6(127.98)	101.8(6.42)	87.3(1.7)
450078E	7	0.04743(0.00313)	0.09126(0.00661)	0.01405(0.00027)	70.3(150.45)	88.7(6.15)	89.9(1.68)
5675682N	8	0.05086(0.00191)	0.2307(0.01153)	0.03313(0.00051)	234.3(84.29)	210.8(9.51)	210.1(3.17)
	9	0.04809(0.00193)	0.2345(0.01264)	0.03363(0.00055)	103.8(92.42)	213.9(10.4)	213.2(3.45)

Sample no. & rock type	Fraction	Isotopic Compositions (1 $\sigma$ )			Isotopic Ages (1 $\sigma$ )		
		$^{207}\text{Pb}/^{206}\text{Pb}$	$^{207}\text{Pb}/^{235}\text{U}$	$^{206}\text{Pb}/^{238}\text{U}$	$^{207}\text{Pb}/^{206}\text{Pb}$	$^{207}\text{Pb}/^{235}\text{U}$	$^{206}\text{Pb}/^{238}\text{U}$
07-SB-	1	0.05645 (0.0100)	0.10192 (0.0176)	0.01348 (0.0006)	470 (350)	98.5 (16.2)	86.3 (3.9)
GEO-02	2	0.05288 (0.0093)	0.0967 (0.0166)	0.01347 (0.0006)	324 (355)	93.7 (15.4)	86.2 (3.9)
Empress	3	0.04599 (0.0051)	0.08833 (0.0097)	0.01453 (0.0004)	0.1 (245)	85.9 (9.0)	93 (2.4)
pluton	4	0.05594 (0.0092)	0.10262 (0.0166)	0.01431 (0.0006)	450 (329)	99.2 (15.2)	91.6 (3.9)
	5	0.09943 (0.0521)	0.09235 (0.0381)	0.01575 (0.0054)	1614 (750)	89.7 (35.4)	100.7 (34.4)
	6	0.05426 (0.0029)	0.10065 (0.0053)	0.01359 (0.0002)	382 (115)	97.4 (4.9)	87 (1.4)
471890E	7	0.04565 (0.0035)	0.086 (0.0066)	0.01339 (0.0003)	0.1 (157)	83.8 (6.20)	85.7 (1.6)
5661590N	8	0.05479 (0.0046)	0.09987 (0.0082)	0.01376 (0.0003)	404 (177)	96.7 (7.6)	88.1 (2.1)
	9	0.0484 (0.0031)	0.09153 (0.0057)	0.01305 (0.0002)	119 (143)	88.9 (5.3)	83.6 (1.5)
	10	0.05238 (0.0026)	0.09456 (0.0047)	0.01334 (0.0002)	302 (111)	91.7 (4.4)	85.4 (1.3)
	11	0.04803 (0.0032)	0.08788 (0.0057)	0.01331 (0.0003)	101 (150)	85.5 (5.4)	85.2 (1.7)
	12	0.04837 (0.0018)	0.09359 (0.0034)	0.01401 (0.0002)	118 (85)	90.8 (3.1)	89.7 (1.2)
	13	0.05108 (0.0039)	0.09466 (0.0071)	0.01363 (0.0003)	245 (165)	91.8 (6.5)	87.2 (1.7)
	14	0.04721 (0.0044)	0.08607 (0.0079)	0.01328 (0.0003)	59.3 (208)	83.8 (7.3)	85 (2.1)
	15	0.05623 (0.0060)	0.10653 (0.0112)	0.01412 (0.0004)	461 (222)	102.8 (10.3)	90.4 (2.6)

Sample no. & rock type	Fraction	Isotopic Compositions (1σ)			Isotopic Ages (1σ)		
		$^{207}\text{Pb}/^{206}\text{Pb}$	$^{207}\text{Pb}/^{235}\text{U}$	$^{206}\text{Pb}/^{238}\text{U}$	$^{207}\text{Pb}/^{206}\text{Pb}$	$^{207}\text{Pb}/^{235}\text{U}$	$^{206}\text{Pb}/^{238}\text{U}$
16		0.05667 (0.0078)	0.10745 (0.0146)	0.01395 (0.0006)	478 (280)	103.6 (13.3)	89.3 (3.5)
Sample no. & rock type	Fraction	Isotopic Compositions (1σ)			Isotopic Ages (1σ)		
		$^{207}\text{Pb}/^{206}\text{Pb}$	$^{207}\text{Pb}/^{235}\text{U}$	$^{206}\text{Pb}/^{238}\text{U}$	$^{207}\text{Pb}/^{206}\text{Pb}$	$^{207}\text{Pb}/^{235}\text{U}$	$^{206}\text{Pb}/^{238}\text{U}$
07-SB-	1	0.04917 (0.0040)	0.08577 (0.0068)	0.01293 (0.0004)	156 (179)	83.6 (6.3)	82.8 (2.2)
GEO-08	2	0.0539 (0.0031)	0.09765 (0.0055)	0.01325 (0.0002)	367 (125)	94.6 (5.1)	84.8 (1.5)
Mount	3	0.05335 (0.0035)	0.09994 (0.0064)	0.01356 (0.0003)	344 (140)	96.7 (5.9)	86.8 (1.7)
McLeod	4	0.05276 (0.0063)	0.10519 (0.0124)	0.014 (0.0005)	319 (251)	101.6 (11.4)	89.6 (3.1)
pluton	5	0.0485 (0.0010)	0.09108 (0.0019)	0.01322 (0.0001)	124 (49)	88.5 (1.8)	84.7 (0.7)
	6	0.05196 (0.0047)	0.09666 (0.0086)	0.01416 (0.0004)	284 (195)	93.7 (8.0)	90.6 (2.4)
	7	0.04449 (0.0037)	0.08692 (0.0071)	0.01375 (0.0003)	0.1 (107)	84.6 (6.6)	88 (1.9)
466760E	8	0.04677 (0.0042)	0.08947 (0.0080)	0.01371 (0.0003)	37.1 (202)	87 (7.4)	87.8 (1.9)
5660115N	9	0.05321 (0.0069)	0.1029 (0.0131)	0.01422 (0.0005)	338 (269)	99.4 (12.1)	91 (3.0)
	10	0.05691 (0.0066)	0.31355 (0.0374)	0.04142 (0.0016)	487 (237)	276.9 (28.9)	261.6 (9.7)
	11	0.03405 (0.0178)	0.0675 (0.0352)	0.01518 (0.0011)	0.1 (280)	66.3 (33.5)	97.1 (7.0)
	12	0.04587 (0.0087)	0.09742 (0.0183)	0.01624 (0.0007)	0.1 (396)	94.4 (17.0)	103.8 (4.6)
	13	0.0726 (0.0165)	0.12884 (0.0283)	0.01384 (0.0011)	1003 (403)	123.1 (25.5)	88.6 (6.8)
	14	0.04952 (0.0044)	0.0927 (0.0080)	0.01363 (0.0004)	173 (193)	90 (7.5)	87.3 (2.2)
	15	0.04193 (0.0135)	0.09905 (0.0316)	0.01773 (0.0013)	0.1 (429)	95.9 (29.2)	113.3 (8.0)
	16	0.0572 (0.0062)	0.11164 (0.01176)	0.01335 (0.00047)	499 (222)	107.5 (10.7)	85.5 (3.0)
Sample no. & rock type	Fraction	Isotopic Compositions (1σ)			Isotopic Ages (1σ)		
		$^{207}\text{Pb}/^{206}\text{Pb}$	$^{207}\text{Pb}/^{235}\text{U}$	$^{206}\text{Pb}/^{238}\text{U}$	$^{207}\text{Pb}/^{206}\text{Pb}$	$^{207}\text{Pb}/^{235}\text{U}$	$^{206}\text{Pb}/^{238}\text{U}$
07-SB-	1	0.05169 (0.0033)	0.09012 (0.0057)	0.01325 (0.0002)	272 (140)	87.6 (5.3)	84.9 (1.5)
GEO-09	2	0.0557 (0.0069)	0.09336 (0.0113)	0.01296 (0.0005)	440 (254)	90.6 (10.5)	83 (2.9)
Mount	3	0.04748 (0.0025)	0.08487 (0.0044)	0.01239 (0.0002)	72.5 (122)	82.7 (4.2)	79.4 (1.2)
McLeod	4	0.05165 (0.0027)	0.09398 (0.0048)	0.01326 (0.0002)	270 (115)	91.2 (4.4)	84.9 (1.4)
granodiorite	5	0.04844 (0.0079)	0.09158 (0.0148)	0.01398 (0.0005)	121 (345)	89 (13.8)	89.5 (3.3)
	6	0.06508 (0.0083)	0.1043 (0.0130)	0.01246 (0.0005)	777 (249)	101 (11.9)	79.8 (3.2)
	7	0.05015 (0.0207)	0.07288 (0.0296)	0.01147 (0.0011)	202 (751)	71.4 (28.0)	73.5 (6.9)
468272E	8	0.10339 (0.0230)	0.14907 (0.0315)	0.01048 (0.0010)	1686 (363)	141 (27.8)	67.2 (6.1)

5659568N	9	0.05319 (0.0008)	0.39555 (0.0062)	0.05609 (0.0004)	337 (32)	338 (4.5)	352 (2.5)
	10	0.05226 (0.0072)	0.0968 (0.0132)	0.0146 (0.0005)	297 (288)	93.8 (12.2)	93.4 (3.2)
	11	0.04874 (0.0096)	0.0936 (0.0182)	0.01447 (0.0007)	135 (407)	90.9 (16.9)	92.6 (4.4)
	12	0.04767 (0.0062)	0.0825 (0.0106)	0.01281 (0.0004)	81.9 (283)	80.5 (9.9)	82 (2.8)
	13	0.04431 (0.0058)	0.08024 (0.0104)	0.01264 (0.0004)	0.1 (201)	78.4 (9.8)	81 (2.4)
	14	0.05943 (0.0188)	0.10395 (0.0323)	0.01514 (0.0011)	583 (569)	100 (29.7)	96.8 (7.0)
	15	0.0488 (0.0224)	0.0851 (0.0387)	0.01366 (0.0011)	138 (826)	82.9 (36.2)	87.5 (7.1)
	16	0.05995 (0.0169)	0.104 (0.0286)	0.01526 (0.0011)	602 (514)	101 (26.3)	97.6 (6.8)

## **Appendix C: Microthermometric Data**

### **C. Methodology**

Microthermometric measurements were made using Linkam THMSG 600 stages at the University of British Columbia and Simon Fraser University. Precision is  $\pm 0.2^{\circ}\text{C}$  for temperatures below  $30^{\circ}\text{C}$  and  $\pm 3.0^{\circ}\text{C}$  for temperatures above  $30^{\circ}\text{C}$  (Macdonald and Spooner, 1981). NaCl equivalent salinities were calculated by measuring the final melting temperature of ice in liquid-vapour-rich (halite-undersaturated) inclusions. Isochores were calculated from the Zhang and Frantz (1989) equation using FlinCor software (Brown, 1992).

Inclusions were identified and classified based on classification schemes presented in Samson et al. (2003). Estimation of compositions of inclusions containing  $\text{CO}_2$  was aided by ICE software (Bakker, 2002) using the Duan et al. (1996) equation of state. These estimations are calculated based on both the proportions of phases present in the inclusions and measured melting and homogenization temperatures. Isochores for Liquid-vapour and liquid-vapour- $\text{CO}_2$  inclusions were calculated using Flincor software (Brown, 1992) using the Zhang and Frantz (1989) and Bowers and Helgeson (1985) equations respectively. These isochores were calculated in order to estimate a pressure correction for the trapped inclusions (Samson et al., 2003).

Table C.1 Microthermometric data for Taylor-Windfall fluid inclusions

Slide	Chip	Inclusion	Type	T <sub>Nice</sub>	T <sub>micc</sub>	T <sub>meq</sub>	T <sub>E</sub>	T <sub>Hot</sub>	T <sub>NCO2</sub>	T <sub>mCO2</sub>	Salinity
07-SB-023-2	2	1	L-V	-41	-1.3		-1.3	129			2.24
07-SB-023-2	2	2	L-V	-40	-1.9		-4.5	164			3.23
07-SB-023-2	2	3	L-V	-39	-1.5		-1.6	145			2.57
07-SB-023-2	2	5	L-V	-35	-0.8		-0.8	128			1.40
07-SB-023-2	2	8	L-V	-36	-0.1		-0.1	134			0.18
07-SB-023-2	2	9	L-V	-40	-1.1		-1.1	145			1.91
07-SB-023-2	3	3	L-V	-43	-3.4		-3.4	121			5.56
07-SB-023-2	3	4	L-V	-45	-1.4		-1.4	115			2.41
07-SB-023-2	3	5	L-V	-45	0		0	100			0.00
07-SB-023-2	3	7	L-V	-42	-2.1		-2.1	121			3.55
07-SB-023-2	3	8	L-V	-40	-0.9		-0.9	114			1.57
07-SB-023-2	5	1	L-V	-40	-0.8		-0.8	137			1.40
07-SB-023-2	5	2	L-V	-38	-1.3		-1.3	149			2.24
07-SB-023-2	5	4	L-V	-41	-3.1		-5.6	112			5.11
07-SB-023-2	5	5	L-V	-43	-4		-6.1	168			6.45
07-SB-023-2	5	7	L-V	-46	-3.2		-3.2	164			5.26
07-SB-023-2	5	8	L-V	-37	-0.3		-0.3	143			0.53
07-SB-023-2	5	9	L-V	-39	-1.2		-1.2	152			2.07
07-SB-023-2	2	4	L-V-CO2	-44		1.3	1.3	109			
07-SB-023-2	2	6	L-V-CO2	-37	-2	1.2	1.2				3.39
07-SB-023-2	2	7	L-V-CO2	-41	-1.7	0.7	0.7	113			2.90
07-SB-023-2	2	10	L-V-CO2	-42		0.5	0.5				
07-SB-023-2	2	11	L-V-CO2	-39	-0.8	0.9	0.9	127			1.40
07-SB-023-2	3	1	L-V-CO2	-42	-1.1	1.8	1.8	121			1.91
07-SB-023-2	3	2	L-V-CO2	-41		0.9	0.9	114			
07-SB-023-2	3	6	L-V-CO2	-44		0.5	0.5	108			
07-SB-023-2	5	3	L-V-CO2	-44		0.7	0.7	112			
07-SB-023-2	5	6	L-V-CO2	-39	-0.9	1	1				1.57
07-SB-023-2	5	10	L-V-CO2	-42		0.1	0.1	132			
07-SB-023-2	5	11	L-V-CO2	-45	-1.5	0.5	0.5	119			2.57

**Table C.2 Microthermometric Data for Empress fluid inclusions**

Slide	Chip	Inclusion	Type	T <sub>Nice</sub>	T <sub>inice</sub>	T <sub>incla</sub>	T <sub>E</sub>	T <sub>Htot</sub>	T <sub>NCO2</sub>	T <sub>mCO2</sub>	Salinity
07-SB-CS-044	2	1	L-V	-40	-3.3			150			5.41
07-SB-CS-044	2	2	L-V	-37	-0.1			153			0.18
07-SB-CS-044	2	4	L-V	-39	-3.7		-9.2	160			6.01
07-SB-CS-044	2	5	L-V	-37	-4.1			159			6.59
07-SB-CS-044	2	8	L-V	-40	-2.7		-17.7	153			4.49
07-SB-CS-044	2	9	L-V	-41	-3.2		-18.2	154			5.26
07-SB-CS-044	2	10	L-V	-42	-4.5			162			7.16
07-SB-CS-044	2	11	L-V	-54	-7.9		-17.7	169			11.57
07-SB-CS-117	1	1	L-V	-45.2	-3		-11.2	139			4.96
07-SB-CS-117	1	2	L-V	-45	-3		-9.4	145			4.96
07-SB-CS-117	1	3	L-V	-44.8	-4.6		-10.2	161			7.31
07-SB-CS-117	1	4	L-V	-45	-4.9		-8.8	152			7.72
07-SB-CS-117	1	5	L-V	-45	-2.9		-10	144			4.80
07-SB-CS-117	1	6	L-V	-44.8	-2.9		-13.5	159			4.80
07-SB-CS-117	1	7	L-V	-44.5	-3.1		-12.6	165			5.11
07-SB-CS-117	1	11	L-V	-49	-4.2		-28	147			6.74
07-SB-CS-117	1	13	L-V	-47.5	-2		-28	139			3.39
07-SB-CS-117	4	1	L-V	-37	-6.7		-2.1	148			10.11
07-SB-CS-117	4	2	L-V	-31	0			263			0.00
07-SB-CS-117	4	4	L-V	-38	-13		-2.4	148			16.88
07-SB-CS-117	4	5	L-V	-45	-0.5		-0.6	154			0.88
07-SB-CS-117	4	6	L-V	-40	-5.2		-5.7				8.14
07-SB-CS-117	4	9	L-V	-40	-0.5			152			0.88
07-SB-CS-117	4	10	L-V	-41	-3.6		-17	168			5.86
07-SB-CS-117	4	11	L-V	-40	-6.2		-11.4	165			9.47
07-SB-CS-117	4	12	L-V	-40	-4.1		-13.5	154			6.59
07-SB-CS-117	4	13	L-V	-43	-5.9		-10.2	158			9.08
07-SB-CS-117	4	14	L-V	-43	-5.1		-10	160			8.00
07-SB-CS-117	4	15	L-V	-41	-3.4		-10.3	153			5.56
07-SB-CS-117	4	17	L-V	-42	-3.4		-12	151			5.56
07-SB-CS-117	4	18	L-V	-39	-2.5		-10.1	148			4.18
07-SB-CS-117	4	19	L-V	-38	-4.5		-13.5	156			7.16
07-SB-CS-117	9	1	L-V	-40	-4.5		-17	143			7.16
07-SB-CS-117	9	2	L-V	-50	-17.1		-29	128			20.28

Table C.2 Cont.

Slide	Chip	Inclusion	Type	T <sub>Nice</sub>	T <sub>nlce</sub>	T <sub>ncia</sub>	T <sub>E</sub>	T <sub>ftot</sub>	T <sub>NCO2</sub>	T <sub>mCO2</sub>	Salinity
07-SB-CS-117	9	3	L-V	-39	-4.5		-16	153			7.16
07-SB-CS-117	9	4	L-V	-39	-4.3		-19	168			6.88
07-SB-CS-117	9	5	L-V	-40	-4.2		-16	184			6.74
07-SB-CS-117	9	6	L-V	-41	-4.8		-21.5	165			7.59
07-SB-CS-117	9	7	L-V	-46.1	-13.6		-22.5	187			17.42
07-SB-CS-117	9	8	L-V	-44.9	-13.3		-22	197			17.15
07-SB-CS-117	9	9	L-V	-33.3	-4.6		-25	153			7.31
07-SB-CS-117	9	10	L-V	-38.3	-2.6		-17.7	151			4.34
07-SB-CS-117	9	11	L-V	49	-3.2		-18.7	155			5.26
07-SB-CS-044	2	3	L-V-CO2	-36	-1.3	0.5					
07-SB-CS-044	2	6	L-V-CO2	-39		2		145			
07-SB-CS-044	2	7	L-V-CO2	-40	-2.1	2.3					
07-SB-CS-044	2	12	L-V-CO2	-37	-1.9	3.6		141			
07-SB-CS-117	1	12	L-V-CO2	-35	-0.9	3		142			
07-SB-CS-117	4	3	L-V-CO2	-46	-1.7	5.5		139			
07-SB-CS-117	4	16	L-V-CO2	-47	-0.2	2.1		148			

**Table C.3** Microthermometric data for Pellaire fluid inclusions

Slide	Chip	Inclusion	Type	T <sub>Nice</sub>	T <sub>nice</sub>	T <sub>incla</sub>	T <sub>E</sub>	T <sub>Htot</sub>	T <sub>NCO2</sub>	T <sub>mCO2</sub>	Salinity
07-SB-136-1	1	2	L-V	-41	0		-5.1	205			0.00
07-SB-136-1	1	3	L-V	-40	-2.1		-2.1	201			3.55
07-SB-136-1	1	5	L-V	-38	-3.9		-10.5	219			6.30
07-SB-136-1	1	6	L-V	-38	-1.7		-3.2	190			2.90
07-SB-136-1	1	13	L-V	-36	-1		-5.6	202			1.74
07-SB-136-1	1	15	L-V	-9							0.00
07-SB-136-1	4	4	L-V	-39	-3.1		-3.6	175			5.11
07-SB-136-1	4	11	L-V	-40	-3.3		-11	164			5.41
07-SB-136-1	4	12	L-V	-39	-3.3		-11	172			5.41
07-SB-136-1	4	13	L-V	-39	-3.3		-11	172			5.41
07-SB-136-1	10	1	L-V	-39	-3.6		-5.9	181			5.86
07-SB-136-1	10	2	L-V	-40	-3.5		-5.7				5.71
07-SB-136-1	10	3	L-V	-36	-2.4		-3.7	175			4.02
07-SB-136-1	10	4	L-V	-37	-2.6		-2.7	177			4.34
07-SB-136-1	10	5	L-V	-38	-3.2		-6.1	175			5.26
07-SB-136-1	10	6	L-V	-37	-2.6		-2.8	186			4.34
07-SB-136-1	10	9	L-V	-37	-2.7		-5	185			4.49
07-SB-136-1	10	10	L-V	-35	-3.9			191			6.30
07-SB-136-1	10	11	L-V	-36	-2.6		-2.9	183			4.34
07-SB-136-1	10	16	L-V	-41	-3.4		-3.7				5.56
07-SB-136-1	10	17	L-V	-38	-3.7		-6.8	196			6.01
07-SB-136-1	10	18	L-V	-38	-3.7		-6.8	177			6.01
07-SB-136-1	16	1	L-V	-39	-2.6			261			4.34
07-SB-136-1	16	2	L-V	-39	-2.9		-3.8	168			4.80
07-SB-136-1	16	3	L-V	-44	-2.1		-3	271			3.55
07-SB-136-1	16	13	L-V	-40	-5		7.7				7.86
07-SB-136-1	16	18	L-V	-38	-3.1		-3.5	197			5.11
07-SB-139-3	10	4	L-V	-40	-4.6		-8.7	194			7.31
07-SB-139-3	10	11	L-V	-41	-3.1		-3.9	177			5.11
07-SB-139-3	10	12	L-V	-40	-4.4		-6.1	187			7.02
07-SB-139-3	10	16	L-V	-39	-3.5		-5.6	179			5.71
07-SB-139-3	10	17	L-V	-38	-4.7		-9	184			7.45
07-SB-139-3	10	18	L-V	-38	-4.2		-8.7	171			6.74
07-SB-139-3	10	19	L-V	-38	-5.1			186			8.00

Table C.3 Cont.

Slide	Chip	Inclusion	Type	T <sub>Nice</sub>	T <sub>Nice</sub>	T <sub>meia</sub>	T <sub>E</sub>	T <sub>Hist</sub>	T <sub>NCO2</sub>	T <sub>mCO2</sub>	Salinity
07-SB-139-3	10	20	L-V	-38	-4.3			178			6.88
07-SB-139-3	15	7	L-V	-52	-3.9		-5.4	210			6.30
07-SB-139-3	15	9	L-V	-50	-9			244			12.84
07-SB-139-3	15	14	L-V	-50	-2.9			201			4.80
07-SB-172-3	3	2	L-V	-40	-4.1		-4.5	147			6.59
07-SB-172-3	3	3	L-V	-37	-3.7		-4	139			6.01
07-SB-172-3	3	6	L-V	-39	-3.5		-3.9				5.71
07-SB-172-3	3	10	L-V	-40	-3.5		-3.7	131			5.71
07-SB-172-3	4	1	L-V	-40	-3.3		-5	110			5.41
07-SB-172-3	4	3	L-V	-40	-3.5		-4.9	133			5.71
07-SB-172-3	4	4	L-V	-39	-4		-5	138			6.45
07-SB-172-3	4	8	L-V	-42							0.00
07-SB-172-3	4	10	L-V	-41	-4.6			187			7.31
07-SB-172-3	4	11	L-V	-40	-4.9			186			7.72
07-SB-172-3	4	13	L-V	-36	-3.2		-3.9	145			5.26
07-SB-172-3	4	15	L-V	-40	-3.2		-4.1	124			5.26
07-SB-172-3	8	4	L-V	-45	-0.8		-1.1	292			1.40
07-SB-172-3	8	5	L-V	-38	-2.1			167			3.55
07-SB-172-3	8	6	L-V	-41	-1		-1.1	165			1.74
07-SB-172-3	8	11	L-V	-41	-1.7		-1.7	183			2.90
07-SB-172-3	8	12	L-V	-43	-2.8		-2.8	171			4.65
07-SB-172-3	8	17	L-V	-43	-2.3		-2.5	163			3.87
07-SB-172-7	1	2	L-V	-42	-3.1		-3.4	203			5.11
07-SB-172-7	1	4	L-V	-38	-2.9		-3.4	200			4.80
07-SB-172-7	1	8	L-V	-42	-3.8		-4	209			6.16
07-SB-172-7	1	10	L-V	-41	-3.4			205			5.56
07-SB-172-7	1	12	L-V	-39	-3.5		-3.9	210			5.71
07-SB-172-7	1	14	L-V	-41	-3.2		-3.7	213			5.26
07-SB-172-7	1	17	L-V	-42	-4			194			6.45
07-SB-172-7	1	18	L-V	-54	-4.1		-4.4	190			6.59
07-SB-172-7	1	19	L-V	-43	-3.9		-4.2	201			6.30
07-SB-172-7	1	21	L-V	-38	-3.9		-5.9	220			6.30
07-SB-172-7	7	5	L-V	-38	-0.3		-0.3	288			0.53
07-SB-172-7	7	6	L-V	-38	-0.8		-0.8				1.40

Table C.3 Cont.

Slide	Chip	Inclusion	Type	T <sub>Nice</sub>	T <sub>Nice</sub>	T <sub>meta</sub>	T <sub>E</sub>	T <sub>Htot</sub>	T <sub>NCO2</sub>	T <sub>mCO2</sub>	Salinity
07-SB-172-7	7	17	L-V	-39	-1.2		-1.7				2.07
07-SB-172-7	10	1	L-V	-43	-0.4		-3.9	119			0.70
07-SB-172-7	10	2	L-V	-39	-1.1		-3.8	193			1.91
07-SB-172-7	10	6	L-V	-41	-5.3			165			8.27
07-SB-172-7	10	7	L-V	-42	-4			176			6.45
07-SB-172-7	10	9	L-V	-41	-3.6		-4				5.86
07-SB-172-7	10	10	L-V	-43	-3.2		-3.5	198			5.26
07-SB-172-7	10	11	L-V	-44	-5.8		-6.3	192			8.94
07-SB-172-7	10	13	L-V	-46	-3.2			201			5.26
07-SB-172-7	10	14	L-V	-45	-5.1		-5.4	170			8.00
07-SB-172-7	10	15	L-V	-40	-3.2			192			5.26
07-SB-172-7	10	16	L-V	-42	-4		-4.9	161			6.45
07-SB-139-3	15	12	L-V-CO2	-48	-1	2.9	1	221			
07-SB-136-1	1	7	L-V-CO2	-40		8.6	1.7				
07-SB-136-1	4	14	L-V-CO2	-42		0.3		251			
07-SB-136-1	1	1	L-V-CO2	-34	-3.2	8.7	-3.2	241			
07-SB-136-1	1	4	L-V-CO2	-39		8.6	7.3	236			
07-SB-136-1	1	8	L-V-CO2	-40	-0.2	8.7	8.6	267	-105		
07-SB-136-1	1	9	L-V-CO2	-41	-6.5	8.6	7.5	233	-102		
07-SB-136-1	1	10	L-V-CO2	-40					-101	-56.8	
07-SB-136-1	1	11	L-V-CO2	-41		8.5	7.1	246			
07-SB-136-1	1	12	L-V-CO2	-39		8.9		245			
07-SB-136-1	1	14	L-V-CO2	-34	-3.4	8.9	-3.4	244			
07-SB-136-1	1	16	L-V-CO2	-40		8.8	0.6	285	-103		
07-SB-136-1	1	17	L-V-CO2	-40		9	5.9	297	-102	-54	
07-SB-136-1	1	18	L-V-CO2	-39		8.7			-103		
07-SB-136-1	1	19	L-V-CO2	-40		9.2		299	-102	-56	
07-SB-136-1	4	1	L-V-CO2	-39		8.9	8.4	279			
07-SB-136-1	4	2	L-V-CO2	-34		8.9	8.8	285			
07-SB-136-1	4	3	L-V-CO2	-34		8.4	8.1	274			
07-SB-136-1	4	5	L-V-CO2	-37	-3.5	8.7	-3.5	281			
07-SB-136-1	4	6	L-V-CO2	-38		9.2	9				
07-SB-136-1	4	7	L-V-CO2	-40		9	8.7	317			
07-SB-136-1	4	8	L-V-CO2	-40		8.5	7.9	266			

Table C.3 Cont.

Slide	Chip	Inclusion	Type	T <sub>Nice</sub>	T <sub>nlce</sub>	T <sub>mcla</sub>	T <sub>E</sub>	T <sub>Hot</sub>	T <sub>NCO2</sub>	T <sub>mCO2</sub>	Salinity
07-SB-136-1	4	9	L-V-CO2	-39		8.9		324			
07-SB-136-1	4	10	L-V-CO2	-41	-4.5	8.2	-4.5	240			
07-SB-136-1	4	15	L-V-CO2	-41		8.8	7.7				
07-SB-136-1	4	16	L-V-CO2	-39		8.5	6	269			
07-SB-136-1	4	17	L-V-CO2	-39		8.6	5.9	263			
07-SB-136-1	4	18	L-V-CO2	-40		8.4	7.9	273			
07-SB-136-1	10	7	L-V-CO2	-39		8.5	7.9	241	-102	-52	
07-SB-136-1	10	8	L-V-CO2	-39		8.6	7.8	223	-103	-51	
07-SB-136-1	10	12	L-V-CO2	-38		9		235			
07-SB-136-1	10	13	L-V-CO2	-38		8.8		262			
07-SB-136-1	10	14	L-V-CO2	-40		7.9					
07-SB-136-1	10	15	L-V-CO2	-34		9.1		271			
07-SB-136-1	10	19	L-V-CO2	-40		8.8	7.7	264	-102	-52	
07-SB-136-1	16	4	L-V-CO2	-40		8.8		270			
07-SB-136-1	16	5	L-V-CO2	-40		8.8		256			
07-SB-136-1	16	6	L-V-CO2	-40	-2.1	8.7		221			
07-SB-136-1	16	7	L-V-CO2	-41		8.4		268			
07-SB-136-1	16	8	L-V-CO2	-39		8.4		263			
07-SB-136-1	16	9	L-V-CO2	-40		9		260			
07-SB-136-1	16	10	L-V-CO2	-42		8.2					
07-SB-136-1	16	11	L-V-CO2	-44		8		241			
07-SB-136-1	16	12	L-V-CO2	-41		8.3		259	-102	-52	
07-SB-136-1	16	14	L-V-CO2	-42		7.7		233	-103	-52	
07-SB-136-1	16	15	L-V-CO2	-39		8.5					
07-SB-136-1	16	16	L-V-CO2	-40		7.3	5.7	230			
07-SB-136-1	16	17	L-V-CO2	-34		8.5	8.1	208	-103		
07-SB-139-3	10	1	L-V-CO2	-39		8.8	8.5	258	-102	-51	
07-SB-139-3	10	2	L-V-CO2	-38		9	8.7	253	-102	-52	
07-SB-139-3	10	3	L-V-CO2	-38		8.5	8.1	250			
07-SB-139-3	10	5	L-V-CO2	-39		8.7	7.1	281			
07-SB-139-3	10	6	L-V-CO2	-36		8.9	7.6	258	-102	-51	
07-SB-139-3	10	7	L-V-CO2	-38		8.8		255	-102	-51	
07-SB-139-3	10	8	L-V-CO2	-39		9.1		253	-102	-51	
07-SB-139-3	10	9	L-V-CO2	-39		9		257	-102	-51	

Table C.3 Cont.

Slide	Chip	Inclusion	Type	T <sub>Nice</sub>	T <sub>nlce</sub>	T <sub>mcla</sub>	T <sub>E</sub>	T <sub>Hot</sub>	T <sub>NCO2</sub>	T <sub>mCO2</sub>	Salinity
07-SB-139-3	10	10	L-V-CO2	-39		9.2	6.5	261			
07-SB-139-3	10	13	L-V-CO2	-38		9.2		223			
07-SB-139-3	10	14	L-V-CO2	-34		8.6	7.2	272	-102	-51	
07-SB-139-3	10	15	L-V-CO2	-38		8.5		268	-102	-51	
07-SB-139-3	15	1	L-V-CO2	-41.1	-2.2	7.1	-2.2	155			
07-SB-139-3	15	2	L-V-CO2	-33.5	-10.9	9.1	-10.9	242			
07-SB-139-3	15	3	L-V-CO2	-43.7		7.2		153			
07-SB-139-3	15	4	L-V-CO2	-41.2		11.1	3.5				
07-SB-139-3	15	5	L-V-CO2	-41.9		8.1	6.4				
07-SB-139-3	15	6	L-V-CO2	-49	-2.1	8.8	2.1	235			
07-SB-139-3	15	8	L-V-CO2	-56	-0.9	8.4	5.4	203			
07-SB-139-3	15	10	L-V-CO2	-54		10.9		196			
07-SB-139-3	15	11	L-V-CO2	-49	-4.6	8.7	-4.6	233			
07-SB-139-3	15	13	L-V-CO2	-45		7.1	2.6	217			
07-SB-139-3	15	15	L-V-CO2	-54		9.4	3.8	211			
07-SB-139-3	15	16	L-V-CO2	-54		9.5	8.6	227			
07-SB-139-3	15	17	L-V-CO2	-52		8.3	7.9	222			
07-SB-139-3	15	18	L-V-CO2	-51	-0.1	9.1	0.4	207			
07-SB-172-3	3	1	L-V-CO2	-42		7.1		196			
07-SB-172-3	3	4	L-V-CO2	-39		8.8		214	-101	-52	
07-SB-172-3	3	5	L-V-CO2	-41		8.1		209	-102	-54	
07-SB-172-3	3	9	L-V-CO2	-42		8					
07-SB-172-3	3	11	L-V-CO2	-43		8.5	8.5	196	-102	-54	
07-SB-172-3	3	12	L-V-CO2	-42		7.2	7.2	191	-103	-51	
07-SB-172-3	4	2	L-V-CO2	-24	-4.6	7.9	-4.6				
07-SB-172-3	4	5	L-V-CO2	-40		8.8	8.8	220			
07-SB-172-3	4	6	L-V-CO2	-40		3.9	3.7	207			
07-SB-172-3	4	7	L-V-CO2	-39		8.9	8.6	237			
07-SB-172-3	4	9	L-V-CO2	-37		8.9		241			
07-SB-172-3	4	12	L-V-CO2	-38		6.7		210	-102	-52	
07-SB-172-3	4	14	L-V-CO2	-43		21.5					
07-SB-172-3	8	1	L-V-CO2	-42		8.1	7.8	227			
07-SB-172-3	8	2	L-V-CO2	-45		7.3	7.1				
07-SB-172-3	8	3	L-V-CO2	-44		9.7	9.4	286	-101	-51	

**Table C.3 Cont.**

Slide	Chip	Inclusion	Type	T <sub>Nice</sub>	T <sub>micc</sub>	T <sub>incla</sub>	T <sub>E</sub>	T <sub>Hot</sub>	T <sub>inCO2</sub>	T <sub>mCO2</sub>	Salinity
07-SB-172-3	8	7	L-V-CO2	-45		8	7.5				
07-SB-172-3	8	8	L-V-CO2	-38		8.9		254			
07-SB-172-3	8	9	L-V-CO2	-34		9.1		261			
07-SB-172-3	8	10	L-V-CO2	-42		8.2		230			
07-SB-172-3	8	13	L-V-CO2	-43		8	7.7				
07-SB-172-3	8	14	L-V-CO2	-43		7.7		219	-102	-52	
07-SB-172-3	8	15	L-V-CO2	-42		8.3	7.3	229	-103	-52	
07-SB-172-3	8	16	L-V-CO2	-42		8.4		232			
07-SB-172-3	8	18	L-V-CO2	-42	-0.5	8.2	7.7	288			
07-SB-172-3	8	19	L-V-CO2	-40		8.6	8.1				
07-SB-172-7	1	1	L-V-CO2	-40		8.7	8.3	256			
07-SB-172-7	1	3	L-V-CO2	-43		8.9	8.6				
07-SB-172-7	1	5	L-V-CO2	-44		8.8	8.5	243			
07-SB-172-7	1	6	L-V-CO2	-44		8.9		198	-101	-52	
07-SB-172-7	1	7	L-V-CO2	-40		8.6		217	-102	-51	
07-SB-172-7	1	9	L-V-CO2	-35		9	8.1				
07-SB-172-7	1	11	L-V-CO2	-44		9.3					
07-SB-172-7	1	13	L-V-CO2	-43		8.4	8.1	271			
07-SB-172-7	1	15	L-V-CO2	-41	-1.1	9.2	8.8				
07-SB-172-7	1	16	L-V-CO2	-39	-0.4	7.7	7.1	237			
07-SB-172-7	1	20	L-V-CO2	-41		9.3	8.1	249			
07-SB-172-7	1	22	L-V-CO2	-39		8.8	8.5	204			
07-SB-172-7	1	23	L-V-CO2	-39		8.5	8.1	283			
07-SB-172-7	7	1	L-V-CO2	-42		8.7	8.5	234			
07-SB-172-7	7	2	L-V-CO2	-42		8.3	8.2	192			
07-SB-172-7	7	3	L-V-CO2	-45		13.2		185			
07-SB-172-7	7	4	L-V-CO2	-45		8.4	8.3	213			
07-SB-172-7	7	7	L-V-CO2	-45	-3.9	6.9		330			
07-SB-172-7	7	8	L-V-CO2	-44		6.8		304			
07-SB-172-7	7	9	L-V-CO2	-45		7.5		279			
07-SB-172-7	7	10	L-V-CO2	-44		11.9		307			
07-SB-172-7	7	11	L-V-CO2	-43		6.6		307			
07-SB-172-7	7	12	L-V-CO2	-37		6.4	6.2	303			
07-SB-172-7	7	13	L-V-CO2	-45	-3.1	6.1	5.9	298			

Table C.3 Cont.

Slide	Chip	Inclusion	Type	T <sub>Nice</sub>	T <sub>mice</sub>	T <sub>mela</sub>	T <sub>E</sub>	T <sub>Hot</sub>	T <sub>NC02</sub>	T <sub>mCO2</sub>	Salinity
07-SB-172-7	7	14	L-V-CO2	-44		7.3	7.1	274			
07-SB-172-7	7	15	L-V-CO2	-42		7.5	7.2	283			
07-SB-172-7	7	16	L-V-CO2	-35		8.5	8.1	255	-105	-53	
07-SB-172-7	7	18	L-V-CO2	-34		8.7	8.4	249			
07-SB-172-7	7	19	L-V-CO2	-43		7.7	6.5				
07-SB-172-7	10	3	L-V-CO2	-42		9					
07-SB-172-7	10	4	L-V-CO2	-43		9.3		195			
07-SB-172-7	10	5	L-V-CO2	-42		9	8.6	207			
07-SB-172-7	10	8	L-V-CO2	-43	-2.6	9.1	8.8	235			
07-SB-172-7	10	12	L-V-CO2	-40		8.1	8	226			

Abbreviations: T<sub>Nice</sub>: Temperature of ice nucleation, T<sub>mice</sub>: Temperature of ice melting, T<sub>mela</sub>: Temperature of clathrate melting, T<sub>E</sub>: Eutectic temperature, T<sub>Hot</sub>: Total homogenization temperature, T<sub>NC02</sub>: Temperature of CO<sub>2</sub> nucleation, T<sub>mCO2</sub>: Temperature of CO<sub>2</sub> melting